THESIS FOR THE DEGREE OF DOCTOR OF PHILOSOPHY

Characterisation of Multifunctional Nanomaterials for Electronics Thermal Management and Sintering Applications

Abdelhafid Zehri

CHALMERS
UNIVERSITY OF TECHNOLOGY

Department of Microtechnology and Nanoscience

CHALMERS UNIVERSITY OF TECHNOLOGY

Gothenburg, Sweden 2021

Characterisation of Multifunctional Nanomaterials for Electronics Thermal Management and Sintering Applications
Abdelhafid Zehri
ISBN 978-91-7905-590-5

Doktorsavhandlingar vid Chalmers tekniska högskola
Ny serie nr 5057
ISSN ISSN 0346-718X

Department of Microtechnology and Nanoscience (MC2)
Chalmers University of Technology
SE-412 96 Gothenburg
Sweden
Telephone + 46 (0)31-772 1000

Cover: Yin and Yang concept put in the context of thermal management and graphene coated copper nanoparticles. The image shows a sphere with hexagonal lattice representing graphene that coats the metallic core and symbolizes the Yin, while the Yang is covering half of the sphere and represented with the red color.

Printed by Chalmers Reproservice
Gothenburg, Sweden 2021

Abstract

The science of manipulating materials at their nanoscale level is nowadays allowing endless possibilities to disrupt the current limitations on the conventional production processes and products. In electronics, the need for more capable thermal management strategies led to the exploration of advanced approaches and focus on new materials and allowed to push further the thermal dissipation capabilities of each generation of products. In this thesis, we investigate different thermal management concepts and propose new solutions based on carbon and metallic nanomaterials, while we explore the possibility to combine the size effect with the composition effect of the nanoscale materials.

Due to their high surface to volume ratio, nanoscale particles show different thermodynamics properties that led to their potential implementation in electronics fabrication processes. More specifically, silver nanoparticles (Ag NPs) have been under focus in recent years for applications to replace lead-free solder and contribute to energy saving. Due to a poor trade-off between the process parameters, the production costs, and the reliability of the silver related application, different strategies are being suggested to optimize its applications. In this present study, we investigate multiple sintering parameters of Ag NPs and use the nanoscale effect in a hybrid approach for the sintering of microscopic powder. The results of the sintering parameters are correlated to the density of the samples and their properties in terms of thermal and electrical conductivity. While the sintering of Ag NPs occurs at low temperatures and allows to obtain relatively high densities, the thermal and electrical properties are still limited and the increase in the temperature and fraction of the NPs higher than 400 degrees and 2wt.% has a much-pronounced effect to improve the physical properties of the samples.

The sintering of Ag NPs was also explored in this thesis to propose a novel approach to use graphene foam as a heat sink. While graphene is known for its outstanding physical, chemical, and mechanical properties, its integration as a practical solution in electronics is still missing. The use of Ag NPs in this work allowed to successfully attach the 3D graphene foam on its substrate and further improve both its mechanical and thermal properties by coating the graphene with Ag NPs. Also, the integration of Ag NPs as a die-attach for the 3D porous structure allowed its further use as a container for Phase Change Materials (PCM). Different amounts of PCM were introduced in the lightweight foam and the junction temperature of the hot spot was correlated to the power and the presence of the PCM. We found that graphene foam presents a real advantage for its use in thermal dissipation strategies.

2D graphene material is developed herein as a coating for micro-and nanoscale particles. Using Chemical Vapor Deposition (CVD) and Arc Discharge (AD) methods, we introduce the possibility to produce graphene coating on copper particles for application in thermal management. In addition, we explore the possibility to introduce a doping effect on the coated NPs to further study its effect on the thermal performances of NPs. The morphology and the composition of the coating were investigated and correlated with the bottom-up production process of CVD and AD. The thermal conductivity and chemical stability of the produced particles were studied for their use as fillers in thermally conductive pastes and additives water-based nanofluids. The thermal properties of the different systems were linked to the fraction of the additives and nanofillers. The graphene-coated particles were found to have a multifunctional effect. In both micro-and nanoscale particles, the graphene coating was found to act as a corrosion resistance that stabilizes the metallic core of the particles. The graphene coating also was found to act as a carbon source to reduce the microparticles in a bimodal powder at high temperatures. Finally, the encapsulation of the nanoscale powder allowed to observe a melting point depression related to the composition of the core of the nanoparticles and their nanoscale size.

In an effort to combine the size effect of the nanoparticles and their compositions, different alloyed nanoparticles were produced using AC. The morphology, the composition, and their sintering properties were compared to highlight their composition effect. The produced nanopowders were also used as a sintering aid in the spark plasma sintering approach (SPS) and the results show a positive contribution of the nanopowders in the reduction of the sintering temperature and the densification of the samples. An additional effect is also reported and arises from the possibility to use those particles to fine-tune the chemical composition of the bimodal particles.

Keywords: Low Temperature Sintering, Graphene Foam, Thermal Management, Nanofluids, Graphene Coated Nanoparticles, Thermally Conductive Adhesive, Spark Plasma Sintering, Alloy Based Nanoparticles, Arc Discharge.

List of publications

Appended papers and manuscripts

This thesis is based on the following appended papers and manuscripts:

A. **Low-Temperature Sintering Bimodal Micro Copper-Nano Silver for Electrical Power Devices**
Zehri, A., Ye, L., & Liu, J.
7th Electronic System-Integration Technology Conference (ESTC)., Dresden, Germany (2018), doi: 10.1109/ESTC.2018.8546502.

B. **High Porosity and Light Weight Graphene Foam Heat Sink and Phase Change Material Container for Thermal Management**
Zehri, A., Kabiri Samani, M., Gutierrez Latorre, M., Nylander, A., Nilsson, T., Fu, Y., Wang, N., Ye, L., & Liu, J.
Nanotechnology, 31(42), (2020), doi: 10.1088/1361-6528/aba029.

C. **Manufacturing Graphene-Encapsulated Copper Particles by Chemical Vapor Deposition in a Cold Wall Reactor**
Chen, S., Zehri, A., Wang, Q., Yuan, G., Liu, X., Wang, N., & Liu, J.
Chemistry Open, 8(1), 58–63, (2019), doi: 10.1002/open.201800228.

D. **Exploring Graphene Coated Copper Nanoparticles as a Multifunctional Nanofiller for Micro-Scaled Copper Paste**
Zehri, A., Nilsson, T., Fu, Y., Liu, J.
23rd European Microelectronics and Packaging Conference and Exhibition, EMPC 2021, Gothenburg, Sweden, (2021). Accepted.

E. **Graphene-Coated Copper Nanoparticles for Thermal Conductivity Enhancement in Water-Based Nanofluid**
Zehri, A., Nylander, A., Ye, L., & Liu, J.
22nd European Microelectronics and Packaging Conference and Exhibition, EMPC 2019, Pisa, Italy, (2019). doi: 10.23919/EMPC44848.2019.8951883.

F. **Graphene Oxide and Nitrogen-Doped Graphene Coated Copper Nanoparticles in Water-Based Nanofluids for Thermal Management in Electronics**
Zehri A., Nylander, A., Nilsson, T., Ye, L., Fu, Y., Liu, J.
Journal of Nanofluids, (2021), accepted.

G. **Characterisation of Nanosized Low Carbon Steel Alloy Based Nanopowder As a Sintering Aid For Spark Plasma Sintering process**
Zehri A., Zhang Y., Aboulfadl H., Cao Y., Sögaard C., Ye L., Palmqvist A., A., Nyborg L., Nilsson T.M.J., Fu F., Liu J. Manuscript.

Other contributions

The following selection of contribution is appended to the thesis due to overlap or being outside the scope of the thesis:

Multiple growth of graphene from a pre-dissolved carbon source
Fazi, A., Nylander, A., Zehri, A., Sun, J., Malmberg, P., Ye, L., Liu, J., & Fu, Y.
Nanotechnology, 31(34), 345601, (2020), doi: 10.1088/1361-6528/ab9040.

Graphene related materials for thermal management. 2D Materials
Fu, Y., Hansson, J., Liu, Y., Chen, S., Zehri, A., Kabiri Samani, M., Wang, N., Ni, Y., Zhang, Y., Zhang, Z.-B., Wang, Q., Li, M., Lu, H., Sledzinska, M., Sotomayor Torres, C. M., Volz, S., Balandin, A. A., Xu, X., & Liu, J.
2D Materials, 7(1), (2020), doi: 10.1088/2053-1583/ab48d9.

Thermally conductive and electrically insulating PVP/Boron nitride composite films for heat spreader
Liu, Y., Wang, N., Ye, L., Zehri, A., Nylander, A., Nkansah, A., Lu, H., & Liu, J.
Proceedings–IMAPS Nordic Conference on Microelectronics Packaging, NORDPAC 2019, 1–5, (2019), doi: 10.23919/NORDPAC.2019.8760352.

Surface modification of graphene for use as a structural Fortifier in water-borne epoxy coatings
Liu, Y., Xia, C., Zehri, A., Ye, L., Wang, N., Zhmud, B., Lu, H., & Liu, J.
Coatings, 9(11). (2019), doi: 10.3390/coatings9110754.

Mechanical behaviour of sintered silver nanoparticles reinforced by SiC microparticles
Long, X., Li, Z., Lu, X., Guo, H., Chang, C., Zhang, Q., Zehri, A., Ke, W., Yao, Y., Ye, L., & Liu, J.
Materials Science & Engineering A: Structural Materials: Properties, Microstructure and Processing, 744, 406–414, (2019), doi: 10.1016/j.msea.2018.12.015.

The influence of sintering process on thermal properties of nano-silver paste
Lu, X., Zhang, Q., Zehri, A., Ke, W., Huang, S., Zhou, C., Xia, W., Wu, Y., Ye, L., & Liu, J. 2018
19th international conference on electronic packaging technology (ICEPT), 1157–1160, (2018), doi: 10.1109/ICEPT.2018.8480545.

Surface analysis of iron and steel nanopowder. Surface and Interface Analysis
Manchili, S. K., Shvab, R., Zehri, A., Ye, L., Hryha, E., Liu, J., & Nyborg, L.
Surface and Interface Analysis, 50(11), 1083-1088–10886, (2018), doi: 10.1002/sia.6465.

Effect of nanopowder addition on the sintering of water-atomized iron powder
Manchili, S. K., Wendel, J., Zehri, A., Liu, J., Hryha, E., & Nyborg, L.
Metallurgical and Materials Transactions A: Physical Metallurgy and Materials Science, 51(9), 4890–4901, (2020), doi: 10.1007/s11661-020-05891-1.

Fabrication and characterization of graphene based film
Shi, Y., Ye, L., Zehri, A., Logothetis, N., Su, P., Wang, N., & Liu, J.
IMAPS Nordic Conference on Microelectronics Packaging, NordPac 2017, Goteborg, Sweden, 18-20 June 2017, 162–166, (2017). doi: 10.1109/NORDPAC.2017.7993185.

Improved interfacial bonding strength and reliability of functionalized graphene oxide for cement reinforcement applications
Wang, N., Wang, S., Tang, L., Ye, L., Cullbrand, B., Zehri, A., Tebikachew, B. E., & Liu, J.
Chemistry - A European Journal, 26(29), 6561–6568. (2020), doi: 10.1002/chem.201904625.

Graphene fibres: towards high mechanical, thermal and electrical properties state of art
Zehri, A., Hansson, J., Ye, L., Fu, Y., & Liu, J.
Proceedings–IMAPS Nordic Annual Conference 2016, Tonsberg, Norway, 5-7 June 2016.

Mechanical property and reliability of bimodal nano-silver paste with Ag-coated SiC particles
Zhang, Q., Zehri, A., Liu, J., Ke, W., Huang, S., Gutierrez Latorre, M., Wang, N., Lu, X., Zhou, C., Xia, W., Wu, Y., Ye, L., & Liu, J.
Soldering and Surface Mount Technology, 31(4), 193–202, (2019), doi: 10.1108/SSMT-05-2018-0014.

Abbreviation

2D	**2-Dimensional**
3D	**3-Dimensional**
AFM	**Atomic Force Microscopy**
APT	**Atomic Probe Tomography**
CI	**Cast iron**
CNT	**Carbon Nanotube**
DSC	**Differential Scanning Calorimetry**
EG	**Ethelene glycol**
FTIR	**Fourier Transform Infra-Red**
GCP	**Graphene coated particle**
GF	**Graphene Foam**
GO	**Graphene oxide**
HTF	**Heat Transfer Fluid**
IC	**Integrated Circuit**
LCS	**Low carbon steel**
NG	**Nitrogen-doped graphene**
NP	**Nanoparticle**
QNM	**Quantitative Nano Mechanics**
SEM	**Scanning Electron Microscopy**
TCA	**Thermally conductive adhesive**
TCA	**Thermally conductive Adhesive**
TEM	**Transmission Electron Microscopy**
TGA	**thermogravimetric**
Tj	**Junction temperature**
XPS	**X-ray Photoelectron Spectroscopy**
XRD	**X-ray Diffraction**

Table of Contents

Chapter 1

1. Introduction: Tiny Particles For a Big World

Nanomaterials are the new building blocks in the hand of the material scientist. These units of atoms offer nowadays a large variety of properties that can be tuned in many ways for diverse applications. Many processing methods have been developed and different aspects related to the nano realm are being investigated in modern science to push the boundaries of the possible to the limits of physics. In this chapter, a brief overview of the potential of nanoscale materials and technology is discussed within the context of contemporary technologies and their limitations. Throughout this chapter, we show that indeed it is a big world driven by the progress that leads to solutions which in turn bring up newer issues, and the answer today more than ever might be in these low scale materials.

1.1 Background

Where there is life, there is progress. As conscious living, we strive to improve our living conditions as the very essence of our existence and drive the socio-economic activity as long as we exist. The same existence is not only made possible as a way of survival but also in a way to optimise life quality. In such a context, electronics components and devices can have most of the credits for the transformations the world went through in the last 70 years. Since the emergence of the first Integrated circuits (IC) in the 1950s, the field of electronics has not stopped changing and driving technological revolutions to change the world. In the electronics sector, such evolution is driven by the increase of the performances of the electronic device that confers multifunctionality and efficiency. In different applications, the reduction in Size, the Weight of the device, its Power, and Cost (SWaP-C) is the driving force from a generation to the next. From highly sensitive applications, such as space and defence, to more common commercial consumer electronics including smart phones, laptop computers and electric vehicles, robustness and performance are key that focus the effort of science and engineering to come up with new concepts and products.

It is difficult to look back at the evolution of the electronic sector and the trend in the evolution of the number of transistors without referring to Moor's vision. In 1965, Gordon Moore presented what has been for many decades the basis for the roadmaps in the development of microchips and performances [1]. As a consequence different parameters related to the SWAP-C would induce the doubling of the transistor number every 18 to 24 months [2], [3]. And it is today, still, we see the electronic packaging technology continues to move in the direction of ultrahigh density with Very Large Systems Integrations (VLSI) leading to rapid miniaturisation of the electronic component with high frequency, and high-power densities. Moore also predicted new packaging solutions will be introduced and will no longer be constrained to the 2-dimensional (2D) dimension. Advanced packaging today deals with board-level integration and chip-level integration 3D packaging that includes Multi-Chip Modules (MCM) [4] and System-in-Package (SiP) [5]. Figure 1-1 shows the evolution of the SiP technology with the considerable increase in the IO counts and promise more functionalities and capabilities.

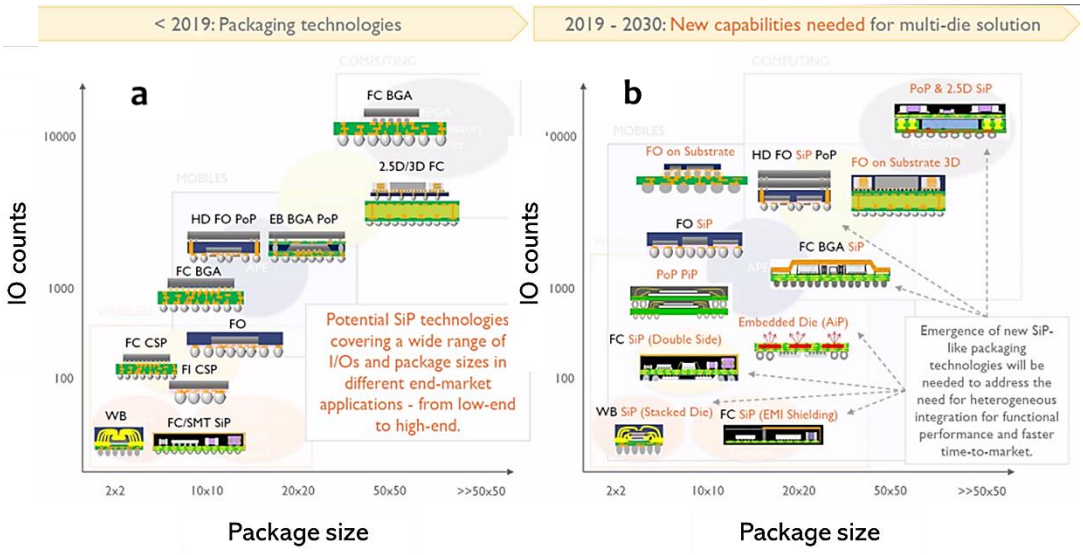

Figure 1-2: SiP technology roadmap showing the increase in the number of the IOs (a) before 2019 and (b) until 2030. Source Yole development.

The trend in the increase of the functionality of the integrated circuits led to the miniaturization of modern electronics, and the advances in the field of electronics resulted in a significant increase in the integration density (cf. figure 1-2). Processors shrank in size and price and largely expanded in terms of integration and functionalities. The downsizing of computers with millions of components was predicted to be a source of issue for heat dissipation. And it is today more than ever the heat management of billions of electronics components has become a limitation rather than an optimisation issue with heat fluxes projected over 300W/cm^2 [6]. In today's massive computing capabilities, such an effect is accompanied by an impressive increase in the development of the power density and the temperature of the processor. New advanced materials also point to the possibility for faster computing to overcome silicon technology limitations. Effort in the industry shows high potential for new materials-based chips such in the case of GaN and SiN [7], but all of this comes with a price. A further increase in the power densities and a substantial increase in the temperature of the processors is expected and need to be tackled.

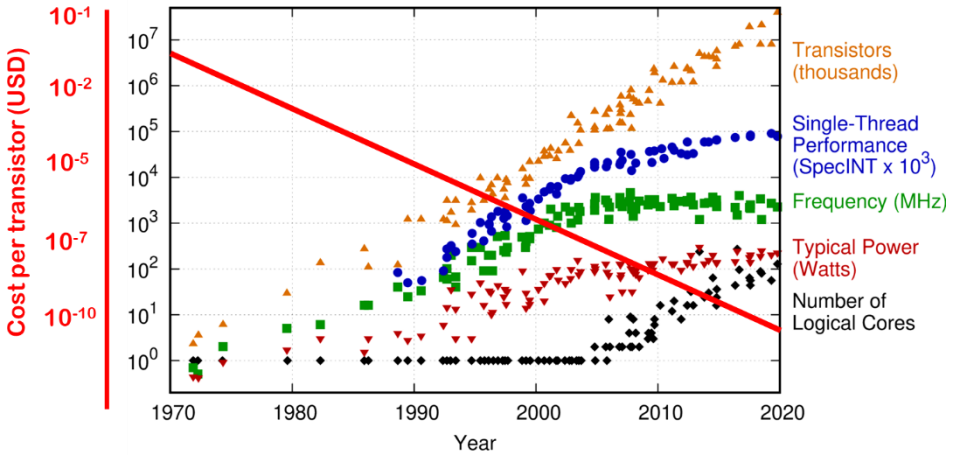

Figure 1-1: Evolution of the microprocessors trend in the last decades. Adopted from karlrupp.com and tapeop.com.

On the other hand and in the modern social context, energy efficiency and environmental issues are becoming of high priorities for a more ecocentric view of exploiting the natural resources. We have reached critical times where actions are needed to reduce our environmental impact for the sake of the person writing this thesis, the people reading it, and 'those who will come after' them. Figure 1-3.a shows the European Commission strategy[1]

[1] *European Commission 2050 strategic vision/source: dw.com, (accessed November 2021).*

to reduce greenhouse gas emissions in the next decades where the direct impact of industrial activity is estimated to be as high as 22%. While for many centuries, the manufacturing activity relied on a set of processes to give functionality to the products, the focus nowadays is made on the sustainability in manufacturing process and technology, where the complexity of parts should not necessarily come with a large impact on the environment. As simple as a product can be, its production does not necessarily come without an impact on the environment. Bridging old manufacturing and modern productions, one particular manufacturing process has always been at the edge of production efficiency and environmental impact. Powder Metallurgy (PM) has been known for many

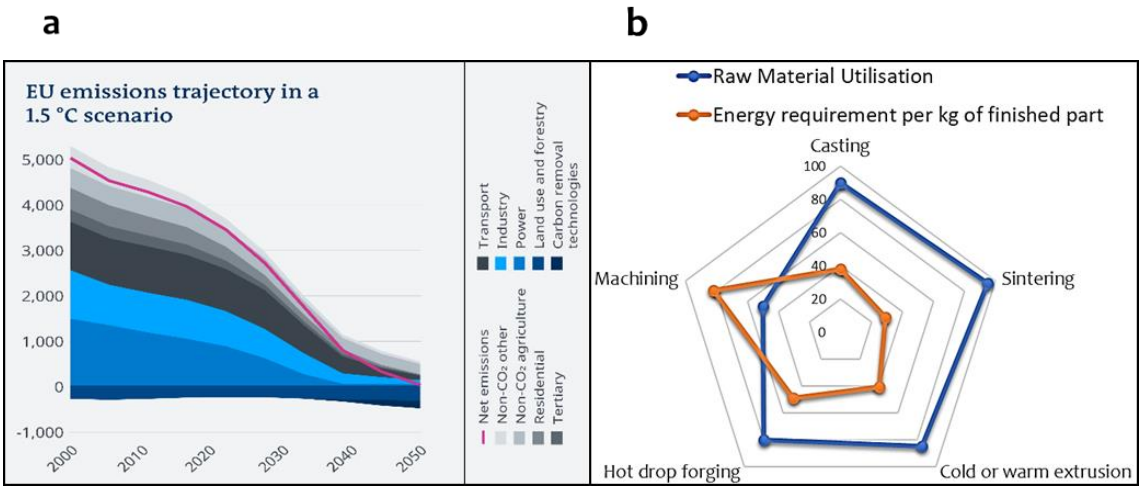

Figure 1-3: (a) Net-zero, EU strategy for the greenhouse gas emission development,(b) Comparison between different manufacturing processes, source (EPMA website).

centuries to provide excellent alternatives for the production of parts where complex shapes are made with minimum material waste and energy consumption[2]. PM holds a large fraction of the conventional manufacturing and is based on the possibility to compact powders into their parts shapes before consolidating them at the proper temperature that can be as low as half of their melting point. However, such a process is believed to hold more promises to become even more energy efficient with a possible reduction in sintering temperatures. As high as a third of the energy consumption in the process of PM is reserved to the sintering process, and any possible reduction in the energy allocated to this consolidation step might benefit highly to our engagement where, 'those who will come after' can have their chances to strive and solve even more complicated issues, perhaps dealing with thermal management of new concepts of electronics instead of being stuck on issues around surviving to the next day.

1.2 Nanomaterials and Nanotechnology

Nanoscale materials and technologies are the world of small, but big effects! Whether it is on the natural or synthetic material, humankind has been around and used nanomaterials since early ages. From Egyptian and Chinese civilizations to Ancient Roman times, colloidal gold and silver were used for their metaphysical healing effect and the coating and decoration of metallic and ceramics objects. What differs the old practices from their contemporary ones nowadays is the fact that nanomaterials entered the laboratory and paved the way to the birth of nanotechnology as a field of science. Various synthetic methods and characterisation procedures were suggested in a way to understand and non-stochastically exploit the nanoscale effect of these materials. It is at that moment that nanomaterials moved away from the metaphysical concept, and it is at that moment that humankind started learning 'how to handle' these nanoscale materials.

[2] *Comparison between different manufacturing processes/ source: epma.com, (accessed October 2021).*

As much as it is difficult to write about the trend of the electronics sector without referring to G. Moore, it is difficult to mention nanoscale technologies and materials without mentioning Richard Feynman and his early invitation[3] to enter the world of small. It is all to the honour of the sharp vision of the renowned physicist that a large part of today's research and science turns around the implementation of nanotechnology and that this thesis treats subjects he pointed to more than 60 years earlier. The pronounced speech by the professor saw an exponential-like trend of a chain of discoveries where nanoscale concepts led to new nanoscale achievement that led to newer nanoscale concepts in their turn, and we stand today on the verge of the mass production of transistors built on 3nm nodes in the next generations of daily life electronics. Beyond the possibility to produce such miniaturized devices, and the manipulation of matter at its lowest building blocks, issues related to heat density were a direct consequence that the bright scientist identified well back then.

Nanoscale technologies and materials often relate to a size range between 1 to 100 nanometres. In science, that definition is rather linked to the critical size of each material to display properties, which are fundamentally different from their counterpart. The nano realm lies at the heart of many fields joining physics, chemistry, and materials science - and the size-dependent disrupted properties arise from the surface and quantum size effect. The condensed matter of size lower than 100nm has shown intriguing properties compared to their counterparts bulk material with [8]: a lower melting point, higher wettability, enhanced chemical reaction, faster sintering kinetics, higher electrical resistivity, superparamagnetic properties, microwave absorption and localised surface plasmon resonances. They are being developed for many applications and can be ideal candidates They are ideal candidates as catalysts [9], sintering aids [10], microwave absorption magnetic for recording media [11], magnetic fluids [12], conducting ink/paste [13], and additives for heat transfer in fluids [14].

It is common in many studies that treat the field of nanoscale materials and technologies to introduce nanomaterials with the example of the division of the bulk gold. A large gold piece is periodically cut into smaller parts and each division is said to occur without changing its core value until it reaches a point where the small pieces start behaving in a way that differs from the initial bulk material. These new extremely tiny pieces of gold have a completely different set of properties and become much more valuable, again, if one knows 'how to handle' them. Such change is, of course, not intrinsically related to the gold atoms only and affects most physical and mechanical and chemical properties. For instance, copper nanoparticles smaller than 50 nm are considered super hard materials and do not exhibit the same malleability and ductility as bulk copper. Gold nanoparticles appear deep red to black in solution. In addition, these tiny pieces also possess a high number of atoms at the surface and result in non-negligible surface energy that provides new thermodynamical states. Melting point depression of metallic nanoparticles was found to be highly sensitive to the size and morphology of the particles, especially at values below 20nm [15]. Moreover, work on a broader range of nanoparticles including gold [16], silver [17], copper [18], nickel [19] revealed a higher densification activity at the nanoscale level with an inverse proportional trend with the size of the particle. The same high number of atoms at the surface results in surface areas with a large number of sites to attach functional groups that are used in drugs delivery in medicine. Furthermore, those tiny gold particles will behave differently depending on the way they are made. If instead of cutting periodically a bulky piece to the nano dimension, these tiny particles were produced by adding atoms to form them as a bottom-up method, their properties would be different. The amorphous polymorph calcium carbonate exists in a metastable structure at the nanoscale and presents much higher adsorption properties used in medicine [20].

In reference to the above-mentioned example of gold, the way these tiny particles of gold are cut might result in another set of properties. Modern science showed that, in addition to the size that matters in the field of nanomaterials, the variation in the shape results in different surface areas. In addition to their size, those tiny pieces of gold if cut into different shapes. In addition to their size, those tiny pieces of gold if were cut into different shapes would display different characteristics. The variation in the shape of the nanoparticles was reported to result in different antibacterial efficiency. Now, if those initial bulk of gold included a fraction of other atoms, its physical, mechanical, and chemical properties will not be different only at the microscale, but also once cut into tiny units. In recent years, an additional degree of freedom came to be added to the nano realm. Similarly to the bulk material, the composition of the particles is expected to provide a whole new panoply of properties.

[3] *Plenty of Room at the Bottom, talk presented by Richard P. Feynman to the American Physical Society in Pasadena, December 1959.*

Theoretical approaches of the additional degree of freedom showed potential to fine-tune the physicochemical properties of the nanoparticles through chemical composition tailoring [21][22]. From binary alloyed nanomaterial [23]–[30] to ternary and multi-element alloyed nanomaterials, the promise is here, the manipulation of material at their nanoscale level will make the difference in our daily life and it is about giving a new degree of freedom for engineering materials to match their applications.

Graphene is a nanomaterial that made the headlines years and keeps in the last and the interest of many research groups around the world. Graphene is no different from the tiny particles of gold. In the bulk, graphene sheets form a graphitic structure with millions of sheets at the microscopic scale. Graphite is known for some great properties that rewarded its integration in a large variety of applications. With the same magic that happens when using graphite pencil to write this sentence, the mechanical exfoliation of graphite results in thin flakes that approach the nanoscale dimensions. With the decreasing the properties of graphite slowly and gradually change and become the long-coveted 2D materials. No different from gold, those tiny and thin sheets behave differently depending on the way they are sensitive to their structures. And again not different from gold, those thin sheets show different properties depending on their composition when the carbon atoms are bonded to other chemical elements.

1.3 Research objective

The objective of the present research work aims at exploring the possibility to introduce new multifunctional nanomaterials for thermal management in electronics and low-temperature manufacturing. Metallic and carbon nanomaterials are developed, and the properties of those materials are investigated. The size effect of the nanoparticles is exploited to investigate the possibility to sinter silver nanoparticles as a sintering aid for electronic applications, and as a die attach for heat sink involving 3D-graphene foam. In the later approach, our work proposes a new approach to integrating the graphene foam as a phase change container and a heat sink. Through this work, our effort also aims at exploring the possibility to manufacture a new class of materials by using graphene as a surface coating of metallic micro- and nanoparticles and investigate their potentials multifunctional effect as fillers as paste and additives for water-based nanofluids. Finally, we investigated the possibility of surface dope the coated nanoparticles and studied their thermal properties as an additive for nanofluids used in thermal management. On the other hand, due to their high surface energy, nanoscale particles are expected to show higher diffusion kinetics that we investigate herein to decrease the processing temperature and the energy consumption behind the production of functional parts. We focus on developing nanopowders for sintering in an attempt to combine the size effect of the nanopowder with the chemical composition of the nanoparticles. Using the arc discharge method, cast iron-based nanopowder was produced and its thermodynamic properties investigated with a sintering approach of spark plasma sintering. In this thesis, we join our effort to the research discipline around nanomaterials to explore their different aspects with a step forwards in terms of production and integration of new nanomaterials to tackle issues around the thermal management in electronics and the possibility to use nanomaterials for low-temperature manufacturing. As we see nanomaterials providing a wide variety of properties with a large effect that stems for their small dimensions, we look at the possibility to exploit these properties and combine them to rise the potential to solve a multitude of issues. In this thesis, we ask questions such as:

- Can nanoscale materials be integrated further into the heat dissipation of modern electronics?
- How can graphene-based materials benefit from new structures of fillers and is it possible to use modern production solutions to manufacture even more advanced graphene fillers?
- How can non-conventional manufacturing processes benefit from the use of nanoscale materials and their?

Herein, nanomaterials based on graphene and metallic particles are developed and investigated for a multi-functional effect to solve state of the art industrial and daily used issues. Figure 1-4 shows a representative schematic of the structure of this work.

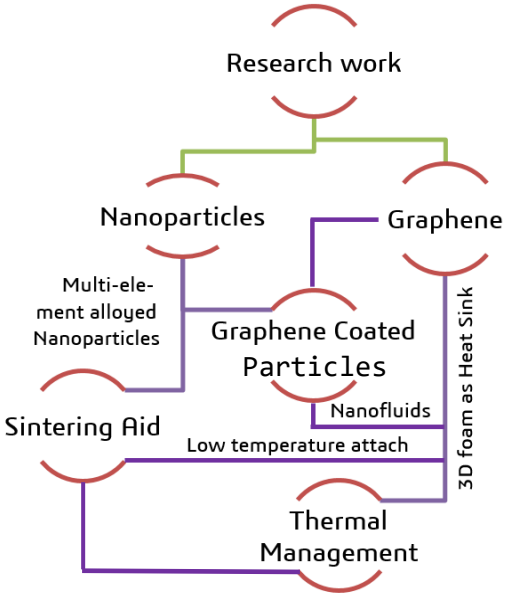

Figure 1-4: Structure of this thesis work.

1.4 The outline of the thesis

This thesis addresses the production and development of nanomaterials for thermal managements application in electronics and low-temperature manufacturing. The work includes the production of nanomaterials, their processing, and their characterisation. Novel ways of integrating graphene in the thermal management strategy are explored in terms of high porosity heat sinks and micro- and nano-scale fillers. In addition, novel work including multi-element-based nanopowder is explored using the non-conventional sintering method and its potential use in the manufacturing of functional parts.

The thesis is written in six chapters. The first chapter gives a general overview of the value of nanomaterials in the modern industrial and technological context. Chapter two is reserved for different notions and definitions that relate the properties of nanomaterials to the scope of this thesis. In chapter three, we explore the use of the nanoscale effect of silver nanoparticles for application in thermal management as a sintering aid material for copper powder and the integration of high porosity graphene foam. We report on different processing parameters and the potential of graphene foam to be used in the heat dissipation of modern electronics with an additional function to host PCM material. In chapter four, graphene is introduced as a surface coating for micro- and nano-scale copper particles for thermal management. Using two different production methods, the produced particles have been studied as fillers to improve the thermal transport properties of the host matrix. The properties and the contribution of the fillers are discussed in the application of thermally adhesive paste and nanofluids used in electronics cooling. In chapter five, the combination of size effect and chemical composition effect for the sintering of nanoparticles is explored. Using a combination of a top-down and bottom-up approach, alloy-based nanopowder is characterized and processed to evaluate its potential as a sintering aid. The results in terms of density and processing parameters are discussed. Chapter six gives a brief summary of the important results and final notes as future insights.

Chapter 2

2. Nanomaterials: Modern Solutions For Modern Issues

In the next industrial revolution, which has already begun, a large focus is put on our ability to produce more advanced concepts and technologies based on extremely intelligent systems for energy and materials efficiency manufacturing. Such vision relies in large part on the development of advanced materials and technologies where nanoscale materials are part of the equation as in 'the next big thing is small'. Beyond the nanotechnological hype, nanomaterials are expected to have a significant impact within and across disciplines in research and techno-economic sectors. As already mentioned, thanks to their tuneable physico-chemical properties, nanomaterials are at the centre of the cutting-edge technologies and sustainable manufacturing processes era. The condensed matter within the critical range of nanoscale dimension shows intriguing properties compared to their counterparts' bulk material. In the modern context, new sintering technics were developed where the integration of nanomaterial is being investigated. Thanks to their low processing temperatures, nanomaterials allow energy- and cost-efficient approaches. The high surface area to volume ratio of the nanocrystalline accounts for their high reactivity and driving force for sintering and make them promising candidates.

On the other hand, nanomaterials-based thermal management approaches have been suggested as solutions for the continuous increase in the power densities of electronic devices. Thanks to the high number of atoms and free electrons at the surface of the nanomaterials, an effort is put to integrate metallic and carbon nanomaterials in the next generation of thermal management solutions. The thermal management in computers product dominated the market[4] and are expected to maintain that position with the ever-growing capabilities and functionalities with an increase from 10.85 billion USD to a projected 18.50 billion USD between the period of 2019 and 2027[5]. With the trend in autonomous driving and electric vehicles, more complex systems are being integrated and the need for thermal approaches is resulting in significant and continuous growth. Recent ambitions, space tourism and the privatisation of the industry resulted in new heavier demands on the electronic packages where the thermal management using advanced approach becomes critical for the development of these segments.

In the last two decades, a new class of materials came to see the light of microscopes. The carbon-based 2-dimensional (2D) graphene showed outstanding properties and gave rise to new fields of science. In addition to its intrinsic properties, graphene layering, composition, and twisting sparked endless promises for many applications. While this wonder material is still wandering around for integrations in our daily life, research is going in full swing for the development of concepts, processes and production methods that can go in hand with the potential of graphene and nanoscale material.

In this chapter, different notions related to the work undergone in this thesis are presented. From metallic to carbon nanomaterials, the properties of the nanoscale materials are explained and linked to their potential to solve modern issues that obscure the continued progress of today reality and tomorrow's technologies. Throughout this chapter, we show that indeed it is a big world driven by the progress that leads to issues, and the answer might exist around the small world, where carbon is closely related.

2.1 Thermal Management and Nanoscale solutions

The development of the electronics device depends largely on a set of concepts and technologies that allows the electronics device to perform its tasks efficiently. While the manufacturing of the compound is purely linked to the progress in the Fab capabilities and the assembly lines, the performance and the reliability of the latter depends, in many ways, on the operating conditions and the working environment. In the field of electronics packaging, it is well known that the temperature rise has a critical effect on computing efficiency and its life cycle.

[4] *Data collected from: thermal management technologies industry/ source: grandviewresearch.com / (accessed August 2021)*

[5] *Data collected from: Thermal Management Market Size And Forecast/ source: verifiedmarketresearch.com* (accessed September 2021)

In fact, in the reliability of electronics, 10 degrees=1/2, is a rule of thumb that is commonly used to refer to the effect of the increase of temperature by 10 degrees results in the reduction of the product lifetime by half. The heat generated by electronic devices and their circuitry must be dissipated to maintain the Tj at an acceptable value and prevent premature failures while insuring high performances. To satisfy the junction temperature requirements in terms of performance and reliability, improvements in cooling technologies are required.

2.1.1 Electronic packaging in the thermal management strategy

In practice, the development challenges on the thermal management approach are driven by the decrease in the SWaP-C of the package. As much pressure is put on the IC level development with increase performances, pressures are also put on the electronic packaging to ensure functionality and the system reliability. The electronic packaging requires a constant focus on controlling the Tj of the system, matching the coefficient of thermal expansion of materials, the reduction of the thermal resistance between the different materials. In the electronic packaging the IC is connected to the different component through several levels of interconnections that allows the signal conduction but also fill more tasks such as ensuring mechanical robustness and heat dissipation through the solid connection and to the environment (cf. Figure 2-1). Subsequently, different thermal management strategies have been developed to solve the issues related to temperature increase in every packaging level (cf. Figure 2-2).

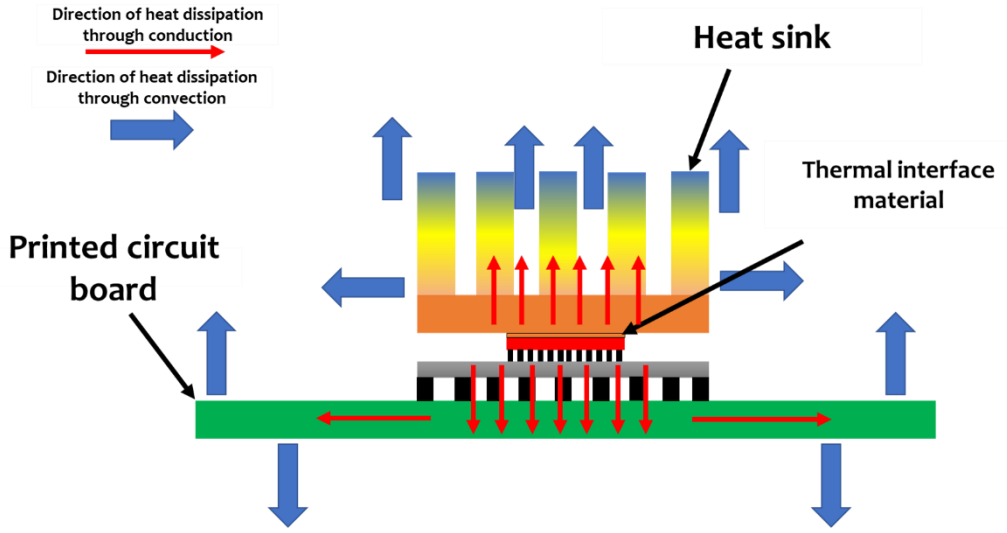

Figure 2-1: Basic heat dissipation mechanisms in the electronic package.

Three different thermal management levels can in general be distinguished. In the first where the IC is packaged into a module, the heat dissipation relies on heat conduction through the solid. Such heat is ideally evacuated to the device environment where is dissipated through additional mechanisms and is dominated by high-heat flux and miniaturization issues [31]. At this level, the solid phase connecting the different components play an important role in efficiently spreading the heat to the outer environment. In the second level, board-level thermal management involves the transport of large amounts of heat and the use of the Printed Circuit Board (PCB) to spread the heat from the chip package to the chassis or electronic system [32]. In the third level, System-level thermal management implies the heat dissipation from the chassis of the system heat exchanger. In the module-level thermal management, the improvement of heat flow between the IC and outer part of the package is the most effective way to lower the chip temperature. Such an approach relies on the use of high conductivity material that guarantees both mechanical robustness and high heat transport. In the board-level and system-level thermal management, it is the combination of conduction based and convection-based concepts that help maintain

acceptable temperature values. It is common to use a conventional air-cooled heat sink and heat exchanger to force air flow and pumped liquid loops.

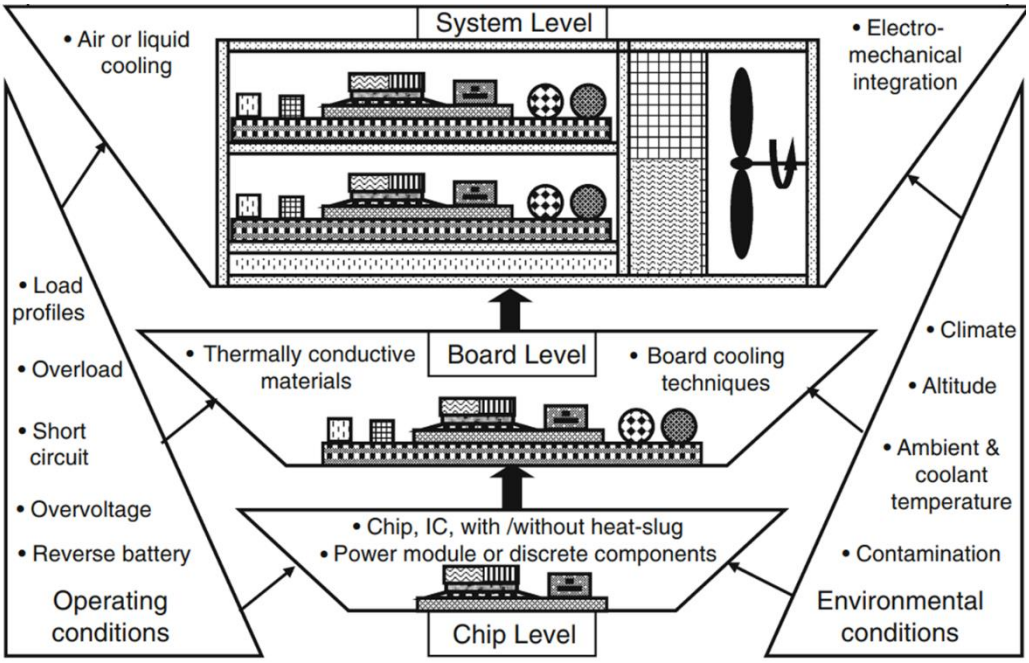

Figure 2-2: Thermal management strategies at different level of the electronic package. Adopted from [32].

Throughout the past decades, conventional approaches based on high conductivity metals were replaced with more advanced techniques and high performances materials to overcome the challenges of next-generation Ultra-High-Power Device (UHPD) thermal management strategies. In the next subsections, we detail concepts and definitions about new and advanced heat dissipation methods that are currently developed for the new generation of electronics and are directly linked to the subject of this thesis, where the need for carbon-based materials and solutions can be highly beneficial.

2.1.2 Thermal management strategies

Throughout the last decades, new materials and technologies have been steadily introduced to keep the Tj under a critical temperature and improve the thermal dissipation capabilities of the electronics system. Currently, the heat flux might exceed 300W/cm^2 and the need for ultra-high-device thermal materials is being developed. The main methods for the heat dissipation of the thermal loads generated by the electronics devices include passive and active approaches. These methods can be further classified into solid cooling, liquid cooling, refrigeration cooling, thermoelectric cooling, and latent heat-based cooling with different efficiency and capabilities related to the intrinsic properties of the materials and the mechanism of heat transfer involved.

Passive cooling techniques rely on the integration of a heat spreader or a heat sink into an electronics package. Without the need for a power assistance dissipation mechanism, this approach is often practical but is largely limited in terms of cooling and requires access to materials with good properties and/or large space to increase their efficiencies. Passive cooling includes heat sinks, latent heat, thermoelectric cooling, and heat spreader and can use both air and liquid medium to keep a reasonable condition on the package. In contrast, active cooling solutions require external assistance to dissipate the heat from the electronic system to its environment. They are more complex but provide much larger performances than in the case of passive heat sinks and heat spreaders for example. Similarly, the active cooling can use both solid and fluid media with some additional conditions on the package design. Commonly used methods for active cooling revolve around the use of air/liquid jet impingement, forced air/liquid convection, spray cooling and refrigerator cooling [33].

2.1.2.1 Advanced Thermally conductive adhesives

Adhesives are used in electronic packaging to ensure both mechanical adhesion between different packaging parts, and as functional material to transfer the electrical signal and the heat. Their primary task of such passive application is to provide the structural connection but also to play an important role in dissipating the heat from the IC- and board- levels to the outer surfaces of the package. The thermally conductive adhesives are usually formed by dispersing micron-sized high thermal conductivity fillers with different compositions, sizes and shapes [34]. Those conductive adhesives are found to provide many advantages, such as few processing steps with low processing temperatures and low-cost fine pitch interconnection capability [35].

As fillers, metallic materials have attracted tremendous research interests due to their unique electrical, thermal and mechanical properties to form electrical or thermal conductive paths [36]. Fillers of noble metals, such as silver [37] and gold [38], were intensively studied because of their promising electrical and thermal conductivities together with excellent anti-oxidation properties. However, widespread applications of such metal particles are limited due to their high cost. Copper stands out of the family of metallic materials for its electrical and thermal conductivity of Cu that are comparable to Ag, with a superior anti-electromigration [39] and a fraction of the price of silver (i.e.,1kg of copper cost around 1% of the cost of silver[6]). However, the challenge to applying bare fine Cu particles is that they will be easily oxidized to form Cu_2O within several hours when they are exposed to air at room temperature [40]. The formation of copper oxidation not only reduces the electrical conductivity but also results in a degradation in thermal conductivity [41].

Nowadays, nanoscale particles offer advanced properties with mild processing due to their high surface area to volume ratio characteristics and sintering that occurs at considerably lower temperatures [42], [43]. In the case of silver, sintering at temperature as low as room temperature achieved a value of 20% of electrical conductivity of the bulk silver [44] and nanoscale silver pastes sintered at 280°C resulted in thermal conductivity of ~240 W/mK with a bonding strength between 21 and 38MPa [45]. Other work on copper-silver nanopaste at relatively low sintering temperatures resulted in high electrical conductivities [46] that are combined with high shear strength [47]. To prevent the issue related to high surface to volume ratio and consequent porosity at low pressure and temperature results in higher creep effects and reduce the reliability of the component [48], [49], the bimodal approach was investigated by mixing micro and nanosized particles of copper [50]–[52], and achieved a difference of 50% of porosity comparatively to pure copper Nanoparticles (NPs) [53], and a volume resistivity corresponding to $28x10^{-6}$ Ω.cm for an optimal formulation of 20% micro flakes copper mixed with 80% copper nanoparticles [54].

Despite higher efficiency of the properties of the metal-based approaches, limitations related to the processing conditions, cost and final properties still hinder their further integration of nanoscale materials in the electronics roadmap [55]. As an alternative to silver screen-printing processing, the encapsulation of the copper particles by additional metals and alloys as an oxidation protection diffusion barrier was suggested. The addition of solders [56] and low melting temperature alloys [57] were explored and resulted in superior properties in the efficiency of the solar panel system at low temperatures. Also, due to their high surface energy, metallic nanoparticles (NPs) such as Ag, Cu and Au are being investigated as mono- and multiple size model integration. The results show the possibility to produce high-density materials at low processing temperatures (~250°C) while resulting in improved physical and mechanical properties. The monomodal size Ag NPs powder for instance was sintered at temperature as low as 240°C and resulted in high shear strength [58], while sub-10nm Cu paste sintering free particles resulted in resistivity of 1.2×10^{-2} Ω.cm [59]. Hybrid solutions based on multielement materials were also explored. Sintering of Ag NPs was used as a densification aid mixed with microscopic powder [60], [61]. However, the use of a hybrid approach usually results in the interdiffusion effect that leads to the growth of intermetallic compounds and Kirkendall voids [62].

[6] *Data collected from: Price of copper and gold / source: goldpricez.com/ (accessed October 22nd, 2021)*

2.1.2.2 Heat sinks

Heat sinks are common active or passive heat dissipation strategies employed in many applications to transport excess heat from the hot spots of the IC to the ambient. Its basic concept is centred around the possibility to increase the surface area of high thermal conductivity materials with its environment. The efficiency in the heat dissipation capabilities relies on the optimized conjugated heat transport mechanisms, namely conduction and convection. Large effort into the optimisation of the thermal performances of heat sinks led to the development of the hydrothermal design and the materials aiming at increasing the heat transfer area or/and the heat transfer coefficients [63], [64]. The focus on the structural designs produced pin fin heat sinks with different shapes, which was later improved into the development of flat fin heat sinks and a large variety of augmentations with the introduction of geometrical modifications [65]. When the total heat dissipation is critical, the optimal plate-fin heat sink is more efficient than the optimal pin fin heat sink, while, in contrast, the optimal pin fin heat sink dissipates more heat per unit weight than the optimal plate-fin heat sink. The optimisation of the heat removal in the case of fin heat sinks is also affected by other parameters such as the inclination of the fins and their orientation [66].

In terms of materials, heat sinks are commonly made of high conductivity metals. As the material is used to absorb heat from the hot side, copper might seem largely favoured but industrial application tends to integrate aluminium as, in addition to the heat transfer performance, and the heat removal per unit weight is also an important consideration. While the development of materials for application as a heat sink is limited compared to the numerous geometrical parameters, carbon materials turned to be a good alternative for such applications. Combining both good thermal properties and lightweight, this class of materials generated interest for their integration in the thermal management strategies and will be developed further in the next chapter.

Further optimisation of the heat transfer surface area per unit fluid flow volume resulted in the production of microchannels. These heat sinks usually integrate micron-sized channels that offer large surface areas and a very high heat transfer rate with optimized geometries [67]. However, the increase in the surface area through the downsizing of channels and the channels is not always optimal. The decrease in the size of these channels results in the reduction of the hydraulic diameter which results in the increase of the Reynolds number, the Nusselt number, and heat transfer rates but also the increased pressure and requires usually higher pressures to transfer cooling fluid through the microchannels [68]. A compromise is usually on the hydrothermal properties and their working conditions. An example of such structure can be found in metallic foams in combination with a phase change material (PCM). While offering a good compromise between high levels of heat dissipation with limited power and cost, this passive approach also combines low density and light weight, high surface area to volume [69] and high mechanical properties [70]. More specifically, the thermal properties of these foams were found to be directly related to the intrinsic thermal conductivity of the solid phase first, but also the porosity level [71][72]–[80],[81] and the nature of the filler or the fluid flowing through it [82]. For instance, the effective thermal conductivity of nickel open-cell foam was found to be 1.26W/m.K [83], while those of aluminum and copper foams were measured up to 6 W/m.K [84][85] and 22.71W/m.K [78] with high thermal performances as a heat sink [86] at densities levels of 93.4%, 90.98% and 94.2%, respectively [87].

2.1.2.3 Phase change material

Phase Change Materials (PCM) are latent heat storage materials that change their physical state when the thermal energy absorption/release takes place during melting/solidification. When the temperature is increased, the phase change is endothermic and the PCMs absorbs the heat to break their chemical bonds as it changes from solid to liquid, liquid to gas, solid to gas, or solid to solid. For instance, during the heating step, the material stores energy that results in its fusion when the phase change temperature is reached. The temperature remains constant, and the latent energy used is equivalent to the capacity of energy storage of the PCM. The process can also be exothermic when reverse-phase changes happen at decreasing temperatures. Upon cooling, the process of solidification allows this family of materials to restore the stored energy in the reversible process. The phase transition allows the storage of a large amount of heat and results in a slow change in temperature that is usually exploited in electronics thermal management. A large variety of materials have been studied and explored as PCM. The PCMs can be found as organic, inorganic, and eutectic materials with different melting/solidification temperatures and energy storage [88],[89], and organic PCM such as paraffin are among the most used due to

their low melting temperature and high latent heat of fusion (cf. Figure 2-3). As different materials have different melting/solidification properties, a large variety of materials with a long-range of phase change temperatures can be covered.

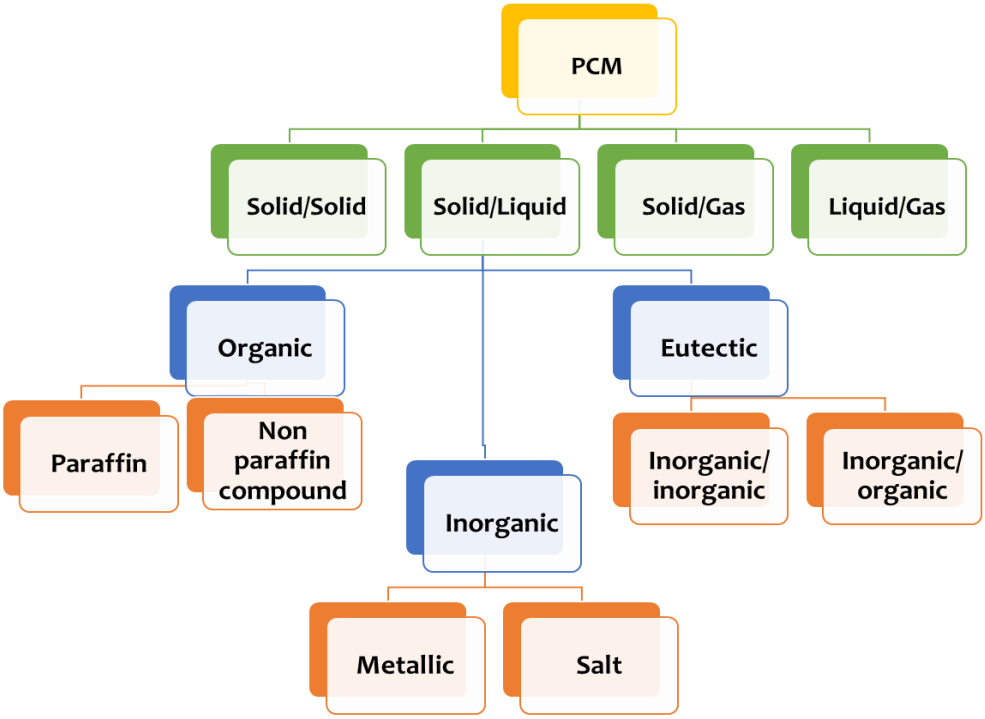

Figure 2-3: Different types of phase change materials. Reproduced from [88].

In electronics, the passive approach in thermal management is based on latent energy storage where the heat is released or absorbed during a phase change from solid to liquid to gas and verse versa. However, the thermal conductivity of paraffin grades is low and different approaches are deployed to enhance their thermal properties. Nanoparticle-enhanced phase change materials have been extensively studied with different types of nanoparticles, concentrations, and dispersion methods [90][91]. Such combination was found in the PCM properties from a different perspective with an increase in the thermal conductivity [92], and the phase change properties [93], However, despite the positive impact on the thermal properties, the introduction of these 'tiny' particles in the PCM matrix was found to have a limited effect. The stability of the NPs within the organic matrix was a bottleneck [94]. In addition to offering a template to strengthen the mechanical properties of the PCM, the non-movable matrix on the other hand shows promising improvement in the thermal properties.

Combination of heat sinks and phase change material

Recent developments to optimize the integration of PCM in thermal management led to the use of heat sinks as non-movable solid containers. The composite concept combines mutual benefits with large latent heat, high thermal conductivity, high porosity, and lightweight materials [95]. As PCMs generally possess low thermal conductivity and might reduce considerably the capability of the thermal design to dissipate the heat, the encapsulation that is usually in the form of a heat exchanger seals the PCM and enhance the heat transfer with the increase of the large surface area. Metallic heat sinks are usually used as they possess an intrinsic high thermal conductivity. As in the case of the nanofillers mentioned above, such high thermal conductivity results in a temperature homogeneity in the thermal design [96], and also limits the undercooling effect during solidification [97]. In addition, such encapsulation helps also in limiting the volume change during the phase change while positively impacting its melting/solidification properties. The synergy between the PCM and the heat sinks depends on a variety of parameters related to the geometry of the containers, their material [98], their designs [99], their orientations [100] and their filling factor [101]. Such parameters include the porosity of the heat sink

and its pore density, the thermal conductivity of the PCM and the container and the orientation of the composite material with the heat source.

The effort into combining the high thermal conductivity and high porosity foam with paraffin for thermal dissipation in electronics resulted in a mutual improvement in the thermal properties of the organic filler and the metallic matrix. PCM plays a role in the improvement of the thermal behaviour of the foams through the enhancement of the heat transfer at the pore level and the improvement of the convection at the interface of the liquid phase with the absorbed heat [102], [103], [104], with a strong effect on the melting front shape [102], [103]. On the other hand, the 3D porous structure improved the melting/solidification process with homogeneous nucleation of the paraffin and reduced void formation within the PCM to increase the effective heat transfer [97], while reducing the effect of the inclination of the PCM on the thermal response [105]. A trade-off is usually reported between the different parameters in the selection of the PCM and the high porosity material. The increase in the porosity level and the decrease in pores size and in the thermal conductivity of the foam results in extending the melting time of the PCM, and the application of a small amount of PCM results in a negligible effect on the thermal energy storage of the system [106]–[108]. As of the case of the heat sink material, the thermal conductivity of copper foam reached a 200% enhancement comparatively with pure PCM [109], and a temperature drop of up to 30% was reported in the case of aluminium foam [102], [110]. Nickel foam was also filled with PCM and achieved a temperature reduction of 24% [111], while the latter enhanced the PCM thermal conductivity by 23-fold by growing graphene on its surface [112].

2.1.2.4 Fluid based cooling and nanofluids

Fluid based heat dissipation solutions rely on the circulation of a fluid that comes into contact with the hot components. The heat removal in this case is done through the absorption of the thermal energy by a high-capacity dielectric coolant and is transmitted to other media. Fluid-based cooling finds applications with both passive and active approaches [114]. In the case of heat sinks, a large fraction of the thermal transport lies on the efficiency of the heat transfer with the fluid, where liquid-based media can have thermal capabilities as high as 1200 times the performances of air. Air cooling has been around for half a century, and while its legacy will not come to end any time soon, the large limitation of the air-cooling technologies is slowly giving space for new technologies based on liquid. Different liquid heat dissipation technologies saw the light with a variety of liquids employed to sustain the increase in the heat densities of high-power electronics devices. Due to superior thermal properties, Newtonian fluids are circulated within the system with relatively low pressure and low flow rates that require simple equipment [113]–[115]. Single-phase fluid solutions were first introduced as a first step to further improve the thermal management of the working fluid including water. The hydrogen bonds in water are at the origin of what makes this liquid vital to life, but also, it is these bonds that confer to water the highest thermal conductivity in all liquid that does not exceed 0.62 W/m.K at room temperature. Figure 2-4 shows the magnitude of heat transfer coefficient for different approaches for different liquid cooling methods.

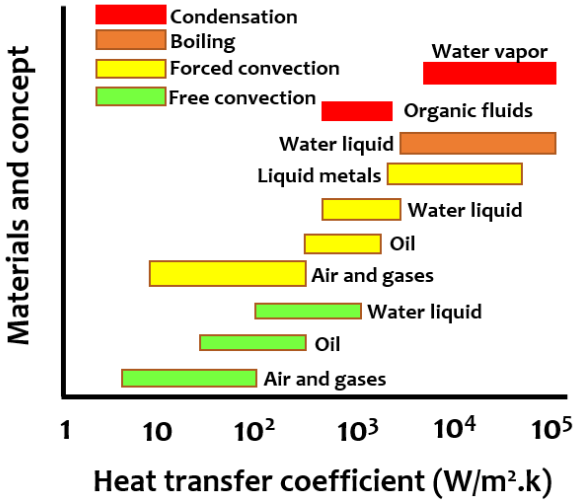

Figure 2-4: Range of heat transfer coefficients for different fluid. Reproduced from [114].

However, with thermal properties that well exceed that of air, the thermal conductivity of fluid quickly hit its limitations. To overcome these limits, Maxwell integrated the solid phase into the fluid, and already back then, found that the addition of solid inclusion in the liquid phase increased the thermal properties of the whole fluid to result in fluid with improved conductivity. It was only until 1994 that the first work on integrating nanomaterials as inclusions came to reality and the concept for multiphase fluid saw the light. The integration of these tiny particles in the liquid-based was reported to modify the thermophysical properties of the fluids and resulted in nanofluids with better thermal properties compared to the base fluid [118][119]. Large examples of materials classes have been studied as nanofillers such as nitrides and oxides ceramics [117][118], pure metals [119] and carbon materials [120]. Higher heat and mass transfer coefficients are reported [121] with relatively lower pressure drop [122], and a varied effect that depends on the base fluids, the nanoparticles' material class and morphologies [123]–[127]. In addition, other effects can emerge from the possible use of secondary additives [130][131], and the temperature of the fluids and the concentration of the fillers that affect the nature and the amplitude of the particle and fluid interaction [130][131]. Due to several factors affecting the practices around research in NFs, a consensus on the effect of the nanofillers is difficult to achieve. However, a trend of an increase in the thermal conductivity and an improved heat transfer coefficient is reported with the increase in the temperature and the fraction of the solid nanofiller [134].

Such nanoscale dimension makes it also possible to create suspensions of nanoparticles. The heat transfer of the nanoscale inclusion and the base fluids are directly related to the static and dynamic conditions of the particles, the particle and fluid interaction, and the nano layering mechanism around the nanofillers [80]. Many theories have been developed to explain the correlation between the thermal conductivity variation and the presence of dispersed nanoparticles. Studies have suggested the increase of thermal conductivity in nanofluids can be explained by [128]:

i. Increase in thermal transfer due to nanoparticles free motion (i.e., Brownian motion).

ii. Nanoconvection in the fluid.

iii. Agglomeration of nanoparticles.

iv. Increased interatomic interactions that lead to an increase in thermal energy transfer.

v. Layer-like ordered liquid molecules around the solid.

vi. Ballistic phonon transport of heat through solid nanoparticles.

The properties of the nanofluids enumerated above depend directly on the homogeneity of the dispersion and the stability of the nanofillers and give rise to a high degree of complexity that relates to [138]: the nanoparticles, their concentration, their size, their shape, the temperature of the fluid, and interaction between the nanoparticles and their host. Generally, metal oxides are used as dispersed particles in the base fluid because of their chemical stability. The nature of the interaction between the base fluid and the nanoparticles defines the efficiency of the heat transfer. The conjugated mechanisms involved in the heat transfer in the nanofluids depends on the compatibility between the solid and liquid phase at their interface. More importantly, most of the thermophysical properties cited here are directly connected to the stability of the particles in dispersion that are defined as their tendency to resist the adhesion together and not form aggregates. This tendency is directly dictated by the type of interaction between the colloidal nanoparticles (i.e., attractive and repulsive nature of the forces) [139]. According to the types of repulsion, two kinds of mechanisms can affect colloidal stability and are as follow (cf. Figure 2-5) [140]:

- Steric repulsion: it revolves around the coating of the surface of the nanoinclusion with an organic polymer that will adsorb on the surface of the particles. Such stabilisation relies on the reduction of the surface tension of the nanoparticles [139] and is largely dependent on the nature of the polymer used and its concentration [141]. Used in nanofluids, the organic surfactants negatively affect the thermal transport capability of the fluid/nanofiller [142].

- Electrostatic (charge) repulsion: For electrostatic stabilization, the surface charge will be developed at the surface of the nanoparticles and lead to the formation of a double layer that repulses other equally charged particles due to repulsive forces between two nanoparticles in the vicinity [143]. Such surfactant-free stabilisation has the advantage of not affecting the physical properties of the nanofluids as much as the steric approach.

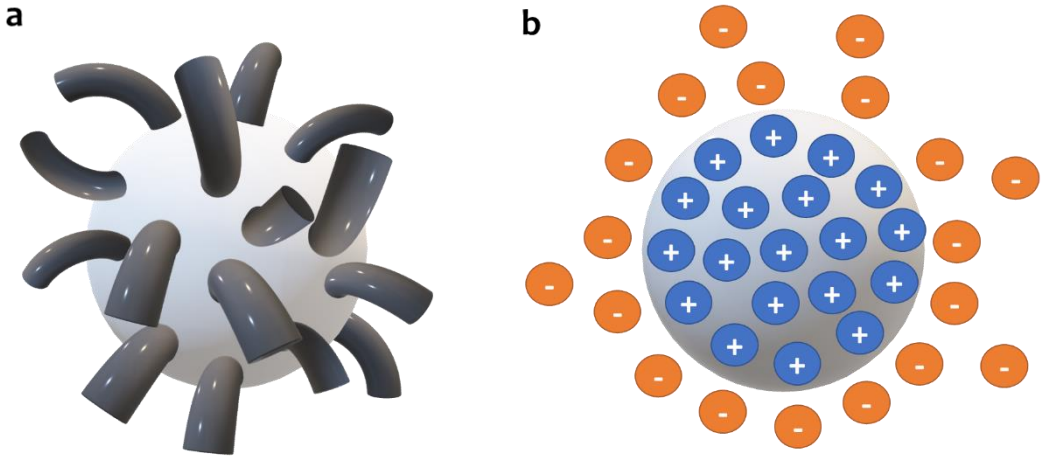

Figure 2-5: Type of nanofluids stabilization (a) steric stabilization (b) electrostatic stabilization. Reproduced from [140].

Carbon-based materials are at the centre of Ultra-High-Power Device (UHPD) thermal management strategies. In the different heat dissipation technologies, carbon-based materials can be integrated to further enhance the thermal capability of the thermal design. From heat sinks technologies to nanofluids to PCM materials, those classes of material, and more specifically graphene, have shown the potential to improve the overall thermal properties in many ways. In the next section, graphene and its properties are introduced to highlight its potential integration in the thermal management strategies and the electronics development roadmap.

2.2 Graphene: The Material of The 21st Century, or almost!

Nanostructured carbon materials have attracted a lot of attention with increasing interest for many applications. They combine a set of outstanding properties that makes them an excellent candidate to be part of the 4th industrial revolution we are taking part in. The big family of carbon materials comprises zero-, one-, two- and three-dimensional materials and 2D graphene are by far one of its most promising. A graphene is a metastable form of carbon with sp^2 hybridisation in a honeycomb lattice where every carbon atom is bonded to three other atoms. The fourth valence electron of the carbon atoms in forming the backbone of the 2D sheet is in the 2pz state and oriented perpendicular to the sheet to form the π band [144]. Most of the outstanding properties of graphene stem from the π band in the graphene structure. So, when it comes to physical properties, graphene becomes more of a 3D material [145]. The carbon-based material in question has made many controversies worth of the material of the 21st century. It has sparked interest and generated a large effort for the potential integration and replacement of many materials. Even more controversial in this, is its discovery. Graphene was first studied as early as 1947 but never thought stable enough in normal condition until it was isolated in 2004 using a method as simple as scotch tape. Graphene is 100 times stronger than steel; it is as flexible as an elastic polymer; it breaks as a ceramic; it has a high field emitter property that translates into superior thermal conductivity [146] and an electrical density 1,000,000 times higher than copper. It is also impermeable to gases, and less than 1 gram of it, would cover a surface as large as and a football field. However, such outstanding properties come to no use without proper compromises and delicate processing. As much as graphene can be elastic, it breaks as a ceramic[147]. It can be deformed in many ways, but its thermal conductivity will highly suffer from it [148]. It also carries electrons so

fast that it becomes difficult to use them in current computing technologies. As much as graphene can be attractive, its applications have still to go through careful tailoring.

2.2.1 Structures of graphene

Since its isolation, graphene has sparked a large number of studies and research efforts to investigate its properties and overcome the challenges of its integration. Graphene is a single layer sheet of carbon atoms. In general, graphene is a zero-band gap semi-conductor where single-layer graphene mimics a system of relativistic Dirac particles with zero rest mass. In monolayer graphene, the electron mobility can be as high as $1.5x10^4 cm^2/V.s$ at room temperature. The mono layer also exhibits outstanding properties with Young's modulus as high as 1TPa combined with a tensile strength of 130GPa that competes with the strongest materials for structural applications and membranes capable of withstanding high pressures [149]. The latter also shows thermal conductivity values that raised its potential use in thermal management applications. Moreover, the optical absorption of single-layer graphene can be as low as 2.3% over the visible spectrum that qualifies it for many applications as transparent material.

When the number of layers is increased, the graphene electronic properties are modified. For instance, in the two layers system, the region around the k shows a minimal anti-crossing overlap of 1.6meV toward the T point due to the interaction between B and B' atoms of carbon as a semi-metal, while displaying a crossing behaviour when moving away from the TK region in the Brillouin zone. The increase in the number of layers, gradually modifies further the regions around the Brillouin zone and effort is put into tuning the properties of the multilayer graphene to match the electronic requirement of the application (cf. Figure 2-6) [150].

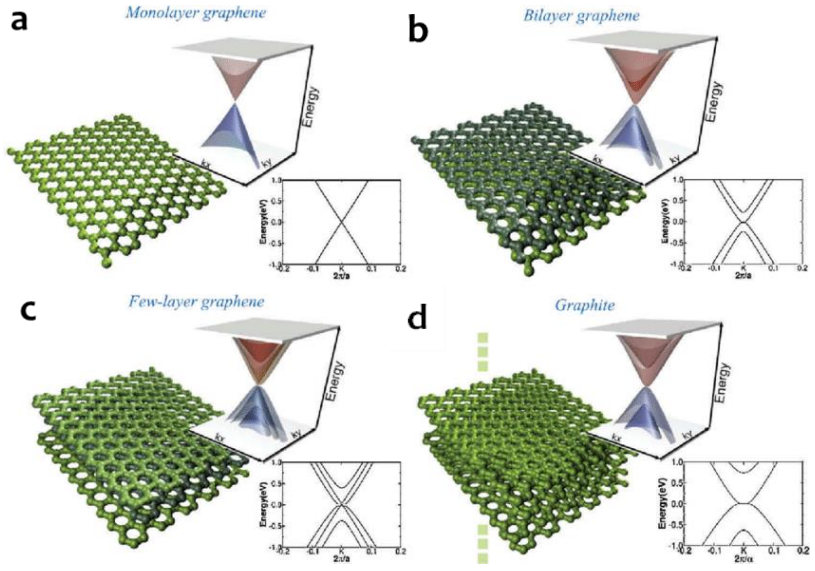

Figure 2-6: Low energy DFT 3D band structure and its projection on k_x component close to K point for (a) monolayer graphene, (b) bilayer graphene, (c) trilayer graphene and (d) bulk graphite. Adopted from [150].

Multilayer graphene can follow different stacking structures that affect its properties [151]. Graphene stacking can be identified in Bernal stacking as the thermodynamically stable form or Rhombohedral stacking that is metastable and is known to coexist in bulk graphite at volume fractions (up to 40%) that vary significantly with the production process. While the single-layer and bilayer graphene are considered semimetal, the few layers of graphene would be either semi-metallic or semi-conductor in the cases of Bernal or rhombohedral, respectively [152]. In Bernal stacking or commonly known as AB-stacking, half of the carbon atoms from the second layer coincide with the carbon atoms of the first layer, while the other half lies above the centre of the hexagonal lattice of the first layer. In a rhombohedral stacking commonly designated by AA-stacking, the two layers are aligned, and the carbon atoms overlap. Rarely do all the atoms match the positions of the carbon below with a 0-angle - stacking structure and layers can be shifted as an ABC stacking in rhombohedral structure. Additional

modification of the electronic properties of graphene can be achieved by adjusting the angle between the different layers. An angle of 0-30° can be found in twisted multilayer graphene as in AA' stacking, and a magical angle of 1.1° led to the discovery of unconventional superconductivity in graphene and paved the way for the birth of the Twistronics [153].

2.2.2 Graphene metal interaction

The application of graphene as in the majority of applications requires the need for a substrate. One important aspect of the interest developed for graphene is the graphene/metal interaction that plays a major role in the chemistry and physics of the graphene/metal interface and its properties. Substrate-induced effects are a critical aspect of graphene science. The arrangement of the substrate atoms with the carbon atoms strongly affects the bonding between the graphene and the metallic substrate and results in different interface separation and binding energy [152]. Four different structural arrangements of graphene/metallic substrate with a direct effect on the graphene properties to either form metal carbide or lattice mismatch (cf. Figure 2-7) [154][155]. Through the competition between carbon-carbon and carbon–metal interactions, the carbon-metal can be classified as [156]:

- Weak interaction in the case of silver, gold, copper, and platinum substrates, and is formed where the carbon atoms are located on the triangular hollow sites of the metallic substrate.
- Strong interaction in the case of ruthenium, platinum, rhodium, and iridium substrates and can occur as a result of (i) formation of carbides during the deposition (ii) small graphene/substrate separations where the substrate lattice and the graphene lattice match well,(iii) a substantial alteration of the graphene π-band, in particular, a shift to the higher binding energy of 1–3eV and opening of a bandgap; and (iv) large corrugation of the graphene layer with buckling of more than 1Å is observed.
- Very strong carbon metal interaction where the carbon atom intercalates the layer of the substrate in the case of palladium substrate.

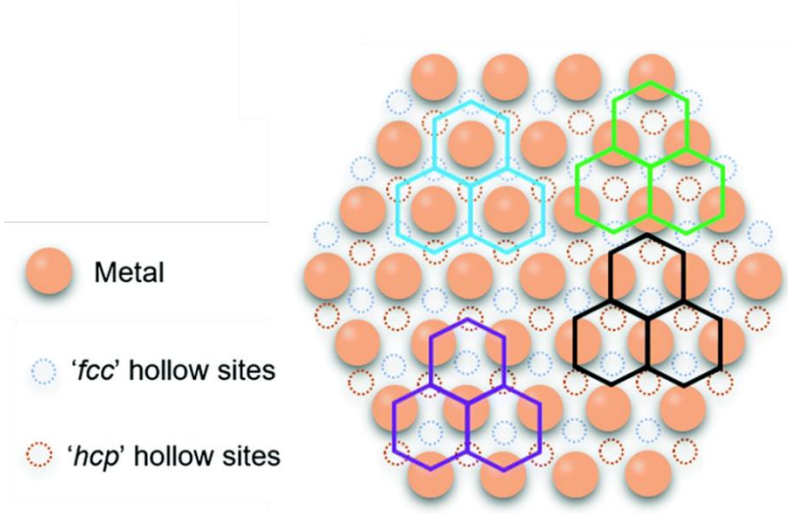

Figure 2-7: Four basic absorption models of carbon atoms on metallic surface forming graphene. Adopted form [156].

The presence of the metallic structure at the proximity of the graphene induced a doping effect on the graphene that was reported with graphene on silver and copper as n-type while p-type doping in the case of platinum was measured with the Dirac point 0.3eV above the Fermi level [157].

2.2.3 Thermal conductivity of graphene

Graphene is considered an excellent heat conductor. The thermal conductivity of single-layer graphene can reach up to 5300W/m.K [158]. Such outstanding values that can be 10 times as high as the thermal conductivity of highly conductive metals led to its potential integration in the thermal management strategies for UHPD [157]. Its high thermal conductivity is a combined effect of the long phonon mean free path as a result of its to the special 2D phonon band structure, and the large phonon group velocity as a result of the strong carbon-carbon bonds and the light carbon atoms [160]. However, many factors can influence the thermal conductivity of graphene. Graphene is highly sensitive to its production method that defines its quality, composition, and structural characteristics. While grain size of less than 5um already contributes to thermal conductivities of around 3000W/m.K [161], the grain boundaries might become a limitation in the thermal transport as grain boundaries scatter phonons and might dramatically reduce its thermal transport efficiency [160]. In the cross-plane direction, the situation is quite different. The heat transport in the vertical direction of the sheet is limited by weak interplane van der Walls interaction. with a mere 6W/m.K [163]. Other extrinsic factors might also affect the thermal transport in the graphene material. This includes the effect of interfacial interactions [164][165] atomic defects [166].

2.2.4 Synthesis of graphene

In general, top-down and bottom-up are the two main approaches to the production of nanomaterials (cf. Figure 2-8). In the top-down methods, the nanoparticles are generated through an initial macroscopic material that is transformed into small units of materials while involving one of or a combination of physical, mechanical, or chemical processes. Examples of top-down processes include high energy milling, ion implantation, lithography, laser ablation, and vapour condensation. The bottom-up method is about building the nanoparticles starting with a smaller atomic or molecular unit that is arranged into a nanoparticle. Examples of the bottom-up approach

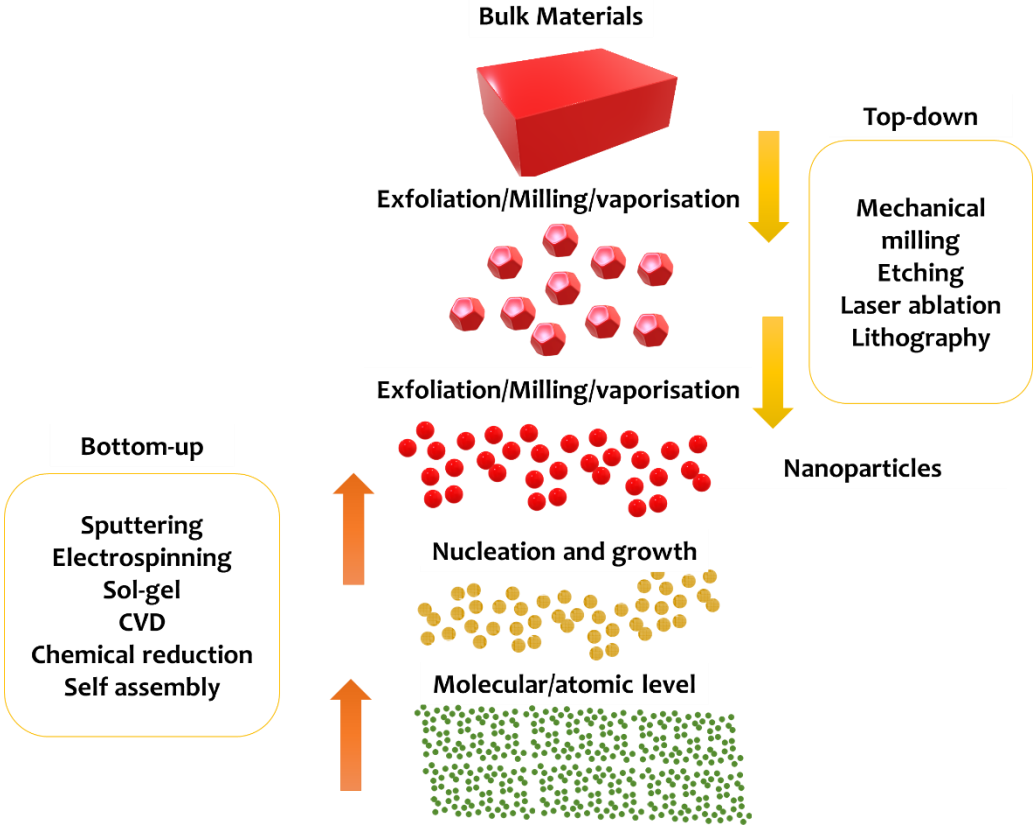

Figure 2-8: Different production methods used for the fabrication of NPs and based on bottom-up methods and top-down strategies.

include sputtering, sol-gel, precipitation, electrical deposition, cluster assembly/consolidation, self-assembly, self-alignment, chemical vapour deposition, atomic layer deposition, and anodizing.

In the case of graphene, both top-down and bottom-up strategies can be used based on mechanical, chemical, or physical processes. Currently, the most common industrial production way of the use of the exfoliation of graphite into graphene sheets synthesis involves the chemical oxidation of graphite to graphene oxide and is followed by its reduction by the removal of the oxygen functional groups at the surface of sheets. Mechanical exfoliation using ball milling and electrochemical exfoliations are also employed to produce large volumes of graphene sheets. However, in many cases, these top-down methods suffer from the low quality of graphene materials. To ensure high quality for the graphene sheets that tend to replicate the theoretical performances of graphene, more controllable methods such as Chemical Vapor Deposition (CVD) are employed.

CVD is commonly used in the thin-film deposition technique for the synthesize of carbon nanomaterials. The CVD method allows the production of a variety of carbon materials with the advantages of high yield at relatively low temperatures. The process also allows control over the structure and the morphology of the carbon materials with a good compromise with their quality. The CVD approach ensures repeatability and control on the dimensions and number of layers through a well-selected recipe and catalyst material. The production of carbon nanomaterials steps evolve around the dissociation of hydrocarbon molecules, but also the carbon saturation and precipitation in the catalyst material. The role of the catalyst is critical in mass production. Graphene is synthesized using CVD combining a carbon-source gas or through the surface separation of carbon, which is dissolved in the bulk of the catalyst. The CVD process for the synthesis of graphene has the advantage for potential large scale production that is combined with a more controllable approach for the growth of graphene. Two main growth mechanisms can be listed [167]:

- Precipitated growth: in the case of strong interactions carbon-metal such as the case of nickel. First, the carbon atoms dissolve into the catalyst at high temperatures. During the cooling step, the solubility of the substrate in carbon is decreased and the carbon atoms segregate at the surface in the form of multilayer graphene.
- Diffusive growth: in the case of weak interactions carbon-metal such as in the case of copper and silver, the decomposed carbon atoms stay at the surface and diffuse at a rate that dictates the nucleation and growth of monolayers graphene grains.

The Table 2-1 lists some of the methods used commonly to produce single or multilayers graphene:

Table 2-1: Production methods for single and multilayers graphene

Single-layer graphene	**Multi-layer graphene**
Reduction of single-layer graphene oxide	Reduction of multilayers graphene oxide
Chemical vapour deposition	Thermal exfoliation
Epitaxial growth	Aerosol pyrolysis
Micromechanical cleavage	Arc discharge
Dispersion in a polar solvent	

The focus on new technologies to support the manufacturing activities in the production of functional parts is one way towards establishing sustainable product life cycles. In industry 4.0, while the focus is highly given towards automated productions and connectivity, the development of green industries is by itself an automated societal demand for the future of living. In PM, such vision is put to sketch through the exploration of new technologies that might reduce further its impact on the production chains and the product life cycle of process. In the next section, the nanoscale concept is introduced as a potential new tool that can be implemented in PM activities to minimize the waste of natural resources and towards more energy-efficient production processes.

2.3 Nanoscale materials for low-temperature manufacturing: extra dimensions into building the building blocks

Nanoscale materials behave differently due to their geometries. The study of the thermodynamics properties of nanomaterials concluded on the non-negligible effect of the surface. Such an effect arises from the ratio of the number of surface atoms to the number of volume atoms as the dimension of the particle is constrained to the nanoscale. The concept of nanothermodynamics saw the light to provide explanations to the deviating behaviour of these tiny systems and describe their energies. The relative contribution of surface atoms, which is negligible in the case of bulk material, changes in the small system as the majority of the atoms are considered in the surface for a small nanoparticle most of the atoms are on the surface. This gives rise to atomic-scale properties such as a lower coordination number of surface atoms and other phenomena such as the melting transitions that occurs smoothly over a finite range of temperatures with lower latent heat and is reduced with dependence on the geometry of the particles and their composition. In this case, the surface tension is considered excess free energy and is available to drive the chemical or physical process on the surface such as the mass transport in reference to the sintering discussed below.

PM applies to the manufacturing approach of which materials in the form of powders are blended, compacted, and heated to consolidate them into high-density parts. The process is widely used and allows the limitation of the post-consolidation with a little amount of waste for applications where high precision tolerances are required. The elemental or alloy powder is blended with additives (e.g. binders and lubricants) before being compacted under the required pressures where the powder surface irregularities interlock in the form of cold welding and result in a high green density. The temperature is then increased to eliminate all traces of additives and generate diffusion processes at the surface and volume of the particles to fuse the consolidate the powder and eliminate the porosity. The processing temperatures in the case of PM vary between 0.5 and 0.8 of the melting point of the materials and allow already to form materials with less energy consumption. PM nowadays can produce functional parts with mechanical properties similar to bulk material through the full densification of the powder [168]. The process of sintering is governed by parameters related to the process such as sintering temperature, heating/cooling conditions, pressures, gas atmosphere, and also parameters that are related to the material including the composition of the materials the geometry of powders. Large choice of processes and methods were developed for the manufacturing of parts using in PM (cf. Figure 2-9). One particular example of a sintering process that combines energy efficiency with the advantages offered by PM technologies is Spark Plasma Sintering (SPS) that is described briefly here as part of this thesis work.

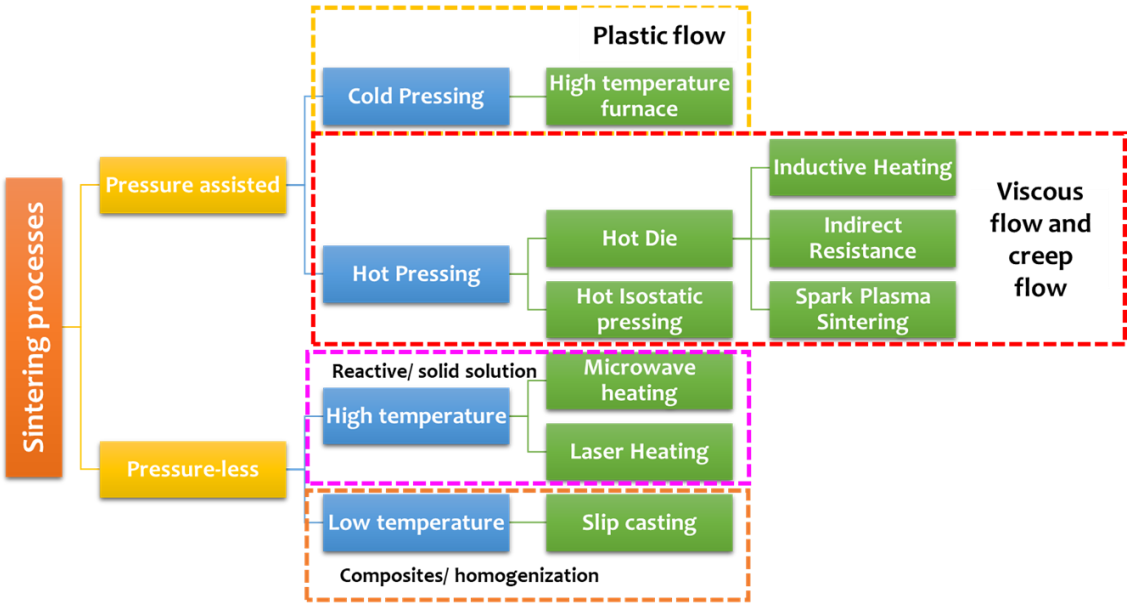

Figure 2-9: Sintering process based on different powder consolidation mechanisms.

Spark Plasma Sintering

Several sintering approaches have been developed through the years to sinter all kinds of materials. The non-conventional sintering process SPS have shown unique characteristic to become the sintering process of choice for hard-to-sinter materials such as the case of highly refractory [169], and nanocrystalline materials [170]. The SPS process is a mechanical and physical type of sintering process used in modern PM. It combines a uniaxial force and a pulsed electrical current that generates high temperature for the sintering of different materials (cf. Figure 2-10. In contrast to the conventional sintering method in PM, the SPS offers the possibility for rapid heating and allows the production of high-density parts in a shorter time compared to the case of conventional sintering technologies. Such a process offers the possibility to have good control over the sintering energy and the temperature and relies on the consolidation of powders using pressure-driven welding in which a pulsed direct electric current is forced through the powder. Commonly accepted theory for the sintering mechanism is based on the micro-spark/plasma concept where the intergranular arc results in a cascade of events and lead to the increase in the temperature through Joule heating. At the local contact points, the electrical resistance is developed and is directly linked to the geometry of the particles [171]. The same resistance is responsible for the self-heating development of the necks in-between the particles [172]. SPS is also known for its surface cleaning advantage that is attributed to diffusion mechanisms as a result of the high temperature and mechanical pressure [173]. Such effect is also claimed to originate from the electrical arc itself that occurs at the grain boundary between the particles [174][175]. The description of the mechanisms occurring during the SPS processes are summarized in four stages as the activation and refining of the powder combined with the formation of the sintering neck as a result of the are discharge that activates the surface of the particles, followed by the growth of the necks through the Joule heating and finally the pressure-driven plastic deformation densification [176], [177].

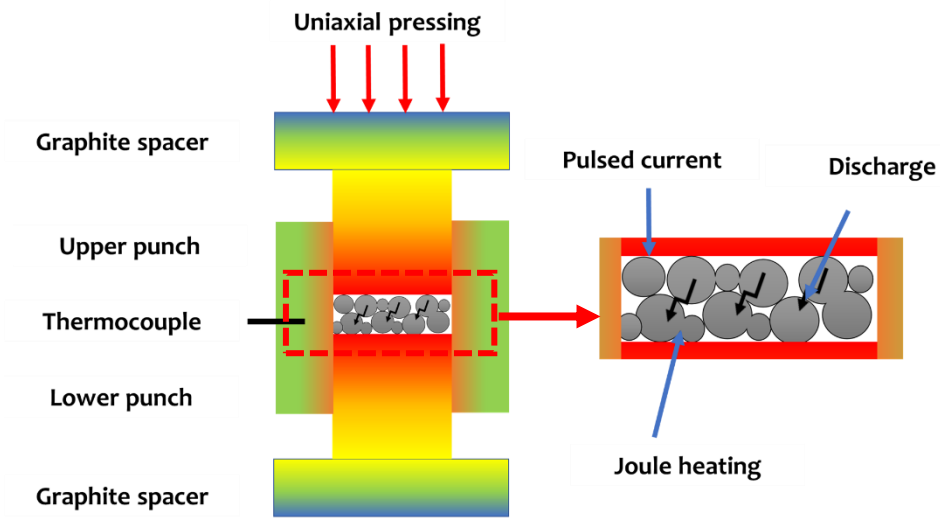

Figure 2-10: Schematic representation of the SPS equipment and the mechanisms of sintering within the powder.

2.3.1 The melting of nanoscale particles

The study of the melting behaviour of nanoparticles revealed a strong and complex dependence of their melting temperature and their dimensions. Early theoretical and experimental investigations on the melting of particles indicated a melting point depression occurs for almost all free nanoparticles. Such effect was linked to the geometries of the nanoparticles and there, no longer negligible, surface energy [178][179]. As the melting mode in the case of the small scale is a crucial element for the construction of a thermodynamic theory, different models have been proposed and include [180][181] (cf. Figure 2-11): (i) the homogeneous melting modal with an equilibrium between the entire solid and the melted particle; (ii) the liquid skin melting where the melting first occur on the surface; (iii) the liquid nucleation and growth melting with an unstable liquid skin that grows into the core of the particle.

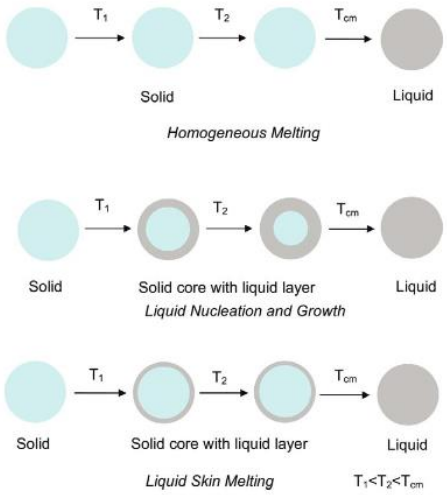

Figure 2-11: Different melting modes in the case of nanoparticles. Reproduced from [183].

In addition to the size of the particles, work on the melting of nanoparticles also reported on the importance of the surface curvature and interfaces. The melting temperature of a supported particle that has a curved surface was reported to be the same as that of a free spherical particle with the same effective surface curvature [182]. The studies of non-free nanostructure highlighted the effect of the interface epitaxial orientation and the anisotropy between supported and embedded [183] and strong orientation dependence of the surface melting [184]. The interface matrix-solid/liquid point to the importance of the orientation between the core and shell of the particles that contribute to the interfacial energy and decide on earlier/delay of the melting.

In the case of aggregates, the melting behaviour of the nanoscale particles can also be affected by the number and the size of the aggregate [179][185]. Clusters of nanoparticles form new bonds between the nanoparticles that result in reduced surface area, lower internal energy, and induce stable atomic configuration. The decrease in the surface and internal energy of the system induces a delay in the melting process of the nanomaterial and aggregated nanoparticles to show less pronounced melting depression. Stabilization methods, as mentioned in the case of the nanofluids, are employed to avoid the effect of agglomeration of the nanoparticles.

2.3.2 The sintering of nanoscale particles

Sintering is defined as the collective result of thermally activated atomic-level processes through diffusion, creep, plastic and viscous flow and evaporation [186]. It allows significant strengthening by metallurgical bonding which produces the growth of contacts between particles and their coalescence. The fundamental driving force for sintering is the surface area, curvature gradients and interface energies. The surface atoms are characterized by reduced coordination numbers and lead to additional energy, which might be lowered by forming additional surface bonds [187]. The process takes place via irreversible thermodynamics events to reduce the excess surface energy through mass transport. In contrast to conventional PM processes using microscopic powder, the sintering onset of nanopowder occurs at relatively low temperatures and can be as low as 0.2 to 0.3 in the melting temperature of the bulk material.

The process of sintering takes place through the mass transport to reduce the excess surface energy. Depending on the process employed and the materials used, different types of sintering can be distinguished based on the sintering materials and processes, and it includes [188]:

- Solid-state sintering: microstructural changes of the particles occur by diffusion of atoms in the solid-state. The compacted powder is usually heated and held for a sufficient time to reach the desired density depending on the volume of the part and the properties of the materials. Solid-states sintering can be applied for both homogenous and heterogeneous materials. In the former, the neck formation and growth are a function of the competing diffusion mechanisms summarised in Table 2-2. In the latter, alloys are formed at the contact point between particles (i.e., necks), and the further growth of the neck becomes directly depending on the nature of the alloy and the rate of the alloy formation [189].

- Viscous sintering: it applies to densification and deformation mechanisms in amorphous and glass material. In such material, the sintering occurs in the absence of grain boundaries diffusion mechanisms and grain growth.

- Liquid phase sintering: it refers to a sintering mechanism involving the presence of a small amount of liquid phase (typically less than 20 vol.%) through the addition of a metal or alloy that melts at the corresponding sintering temperatures. The high-diffusivity path for the transport of matter within the liquid phase helps to achieve densification at a much lower temperature than the required temperature for the matrix.

Table 2-2: transport mechanisms during solid-state sintering

	Material transport mechanism	*Material source*	*Material sink*
Non-densifying mechanisms: microstructural changes	1-Surface diffusion	Grain surface	Neck
	2-Lattice diffusion	Grain surface	Neck
	3-Gas phase transport	Grain surface	Neck
Densifying mechanisms: Displace material from grain boundary regions	4-Grain boundary diffusion	Grain boundary	Neck
	5-Lattice diffusion	Grain boundary	Neck
	6-Plastic flow	Bulk grain	Neck

2.3.3 Alloyed nanoparticles

The ability to alloy different elements into a homogeneous solid-solution structure is critical for continuous property tuning and materials development. The latter concept extends the possibility to mix different elements and results in a vast panoply of properties. The fundamental challenge of creating materials mixtures and alloys is rooted in the limited immiscibility of the materials as a result of their dissimilarities (i.e., different atomic sizes, electronegativity, crystalline structures, electronic structure, etc). In the bulk material, a wide range of equilibrium and non-equilibrium alloys and compositions have been developed, while experimental work on nano-alloys is considered rare. Many thermodynamic parameters such as Gibbs energy, the specific enthalpy and entropy are crystal size-dependant as the chemical potential is related to the number of atoms in the system [190]. In the case of graphene, a magical angle results in the apparition of superconductivity behaviour that does not exist otherwise. If the critical size of the nanoparticles to display a new set of properties can also be considered a magical number, then nanomaterial can possess another magical number where the compositions of the nanoparticles can result in

whole new set of properties that involve surface structures and electronic properties. Studies on the melting and solidification of nanoparticles revealed a modification in the solubility of chemical elements and a shift of the equilibrium curves at the phase diagram downwards towards low temperatures [191]–[193]. Due to the difficult task of analysing the chemical composition of multielement nanoparticles, many alloyed nanometric materials have been studied through the development of models to take into consideration the additional surface tension-dependant Gibbs free energy with additional segregation energy. The melting temperatures depression were found to nonlinearly decrease with increasing copper concentration in for Palladium–Copper systems and Palladium in both palladium–platinum and palladium–rhodium binary nanoparticles [194]. In the case of binary alloys, the structure of the particles varies depending on the nature of the interaction between the two materials' atoms. Different structures can be identified [195], and are closely related to [196]:

- Relative strengths between the two atoms and their structures
- Surface energies of bulk elements.
- Relative atomic sizes.
- Charge transfer.
- Strength of binding to substrates or surface ligands.
- Specific electronic/magnetic effects.

2.3.4 Production of alloyed and core-shell structured nanoparticles

Similarly to graphene, the production method for complex nanoparticles with different structures and compositions can be based on both bottom-up or top-down methods. These methods include physical, chemical, and mechanical approaches and have been reported to be valid for the production of complex shapes and compositions of the nanoparticle. In general, the processes of production of nanoparticles can be divided into three main categories: (i) Sol-gel and chemical wet methods for precipitation of oxides mainly from salt solutions; (ii) Flame and spray pyrolysis of both oxide and non-oxide powders, (iii) Physical vapour techniques for nanopowder. Among the large range of options for the production processes of nanoparticles, nonequilibrium physical processes are attracting increasing attention for the synthesis of advanced nanoparticles. More specifically, the physical method based on electrical discharges allows generating a variety of materials with large scale capability. Big European projects such as BUOANPARTe have proven the advantage of such a method with relative ease to increase the production of nanopowders. Below are details related to the production process.

Arc discharge method

Arc discharge method has been developed for a large variety of materials such as metallic nanoparticles [197], and carbon structures [198][199]. Through the adjustment of the compositions of the vapour in the plasma column, different structures and compositions can be obtained. The process is based on an electrical system similar to an RLC-circuit (cf. Figure 2-12.a), where the two electrodes separated by the dielectric correspond to a capacitor. When the high electrical power is applied in between the two electrodes and reaches a value high enough, the dielectric is no longer considered an insulator, and the capacitive spark occurs at a breakdown voltage. Such electrical breakdown is a result of the formation of 'streamers' of ions that propagates through electrons drift and diffusion between the electrode's gaps. A transition to spark takes place and the column becomes a conductive plasma connecting the two electrodes. The arc that forms contains high energy and velocity species that are accelerated in an avalanche kind of all physical matter-matter interaction to generate local high temperatures on the electrodes and erode it (cf. Figure 2-12.b) [200]. Several thousands of degrees are focused on the surface of the electrodes and induce the evaporation of the species from the surface of the electrodes. In the next step, condensation takes place as the plasma cools down and atoms come into contact through a diffusion-driven mechanism. The process of formation of the nanoparticles and carbon structures is described by the capillary theory of nucleation [201]. Under supersaturation conditions, a vapour phase mixture in the plasma column can

become thermodynamically unstable and result in the nucleation process [202]. This leads to the formation of nanoparticles via homogeneous and heterogeneous nucleation, growth, and coalescence of the particles.

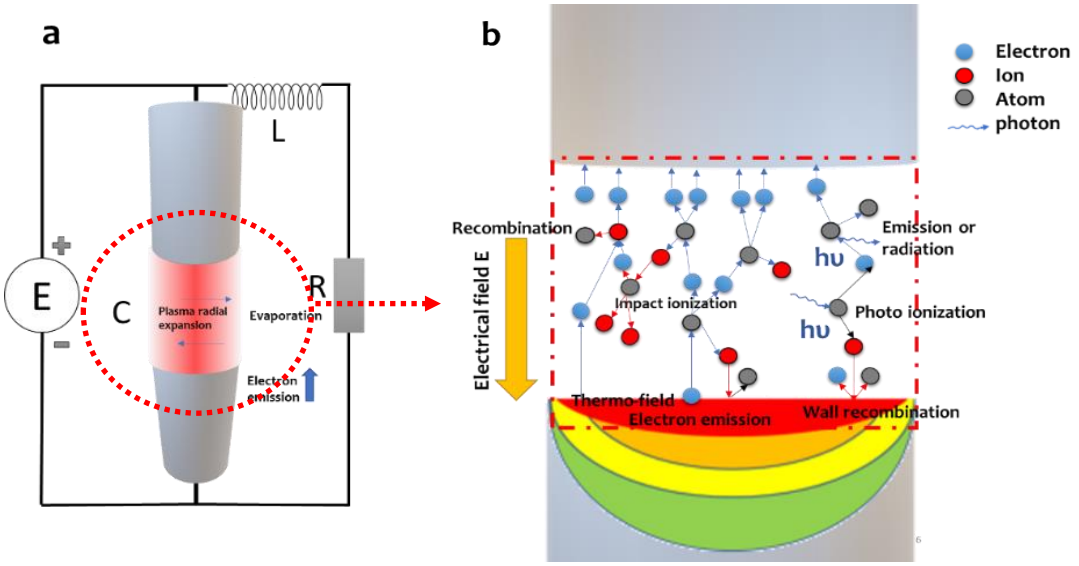

Figure 2-12: (a) Schematic of the arc discharge process and its equivalent electrical circuit with the two electrodes active as a capacitor, (b) cascade events during the spark discharge in the plasma area including ionization, electron attachment, radiation etc. Reproduced from [199].

In the case of core-shell structures of metal-carbon particles, the process of production is assimilated to the case of carbon nanotubes using the plasma method. In the case of nanotubes, a metal is used as a catalytic liquid alloy phase that adsorbs the vapour to its supersaturation and results in the nucleation of the carbon shell at the interface liquid-solid interface. During the plasma event in the arc discharge, such a mechanism can be observed when the electrode material is evaporated at a high temperature. The high concentration column is then quenched, and the metal catalyst forms particles rich in carbon. Upon cooling, the solubility of carbon decreases and the latter segregate at the surface of the catalyst. and the metal catalyst arc induces a diffusion process associated with a fast quenching of gas species. The more elaborated theory describes the formation of the carbon-based shell with, first the formation of the carbon layers then, the condensation of the metallic core [203]. As the temperature of the carbon condensation is higher, the carbon layer is formed first and then the liquid metal deposits on the surface of the solid carbon.

Different modifications of the arc discharge setup have been proposed including the gas atmosphere and submersion of the electrodes in liquid phase medium [204]. Such modifications allowed to produce a variety of structure and materials by adjusting the composition of the arc environment. In the case of carbon materials, the precise tuning of the gas within the chamber showed the possibility to produce different structure (cf. Figure 2-12).

Nanomaterials sparked a high interest for their potential to enhance industrial applications. At the centre of them, 2D materials around graphene promise large efficiency that combines a set of properties that might benefit many applications for thermal management. However, their integration is still lacking, and work is always needed to explore and exploit those promised properties. Through large option for the production of nanoparticles, we see possibilities for the development of large-scale production methods that provides control over all the dimensions of the nano realm properties. With an increased interest in tuning the properties of nanomaterials, the interest to develop knowledge about the possibility to explore the composition of the nanoparticles that comes as an additional tool to further use of those building blocks in many applications. In the next chapter, we will investigate the applications of nanomaterials in thermal management and low-temperature manufacturing. We will go through our effort to exploit the nanoscale effect of those materials and explore their integration to solve. We will demonstrate throughout this work their potential multifunctional role that can be further used to tackle other industrial challenges.

Chapter 3

3. Silver Nanoparticles for Low Temperature Sintering

The die attach materials play an important role in the microelectronic packaging as they connect the die and the device to the rest of the electronic components. In addition to offering a connection for the transmission of the electrical signal, the die attaches also act as a medium for the heat dissipation and must answer a set of physical and mechanic properties requirements. With the modification to limit the use of lead-based solder, lead-free solder alloys (SnAgCu) and metal-filled conductive adhesives have been commonly used as die-attach materials because of their low processing temperatures below 300°C. However, because of their low melting temperature and with the increase in the power densities of the integrated circuits, these dies attach materials became a serious limitation for the packaging sector and cannot be considered an alternative for the next generation of products.

As the die attaches are rarely enough to keep the temperature of the chip at acceptable working temperatures, heat sinks are employed and play an important role in dissipating the heat generated at the IC level to its environment. With the increase in the power density of the IC, the requirement for the development of new material capable of maximizing the heat dissipation from the system is highly critical. The effort along this line focuses on the combination of high performances materials with an efficient design, where the 3D structure of graphene-based foams can have a sharp edge. The high porosity heat sinks are being investigated to further enhance the thermal dissipation capabilities of the electronic system. However, the integration of this concept in the modern context of electronics and processing is still lacking.

In this section, we explore the nanoscale effect of silver nanoparticles (Ag NPs) to study their potential to solve two issues related to die-attach material and the integration of carbon-based microchannel heat sink. Initially, silver nanoparticles are used as a hybrid sintering aid to lower the sintering temperature of microscale copper used as a die-attach. Different sintering parameters are investigated and correlated to their physical properties. In the second part, the nanoscale effect of silver nanoparticles is exploited as a novel approach to integrate 3D graphene foam as a heat sink. The thermal properties of the heat sink are characterized and evaluated as a new heat sink for electronic packaging.

3.1 Silver Nanoparticles As a Sintering Aid for Copper

Among the few alternatives for high power devices die-attach materials, the sintering of silver stands as a promising approach that fulfils the criterion to replace current technologies. The reduction in the size of the silver into the nanometre scale and resulted in the decrease of its processing temperature sintering without applying any pressure. Due to its good electrical and thermal properties, silver is widely employed in microelectronic packages as die attach and connection lines to the different parts of the package. Silver was found to be better than currently used solders when it comes to thermal and electrical properties and was successfully integrated into printed electronics circuitry wirings [205], flexible thin-film and displays [206] and as die-attach joints [207]. While it offers a good alternative for high power electronics, its extremely high processing temperature is a bottleneck that hinders its full integration in electronic fabrication. As cited earlier in this thesis, exploring the nanoscale effect quickly became a potential candidate to lower the extreme processing condition of silver. The excess surface energy related to its decreased size can be the driving force to create good quality connections without needing to melt the material and at a lower temperature than the bulk silver.

The integration of silver in electronics processing also suffers from additional obstacles. Silver is a noble material that is out of reach to the large industrial volume need of the electronics sector. In the bulk format, silver is expensive, and in the nanoscale size, its price becomes even more expensive without going into the difficulty these days to produce large volumes of nanomaterials. In addition, silver is known to suffer from issues related to electromigration that are further worsened with the increase of the operating temperature and the current. A compromise is suggested by exploring hybrid approaches where nanoscale silver is used as a sintering aid. Comparatively to silver, copper is a cheaper solution compared to silver that can overcome the electromigration

failures encountered when using silver [208]–[210]. However, in addition to the ease of oxidation of copper, it has higher melting and sintering temperatures that affect the reliability of the overall package.

In this section, we explore a hybrid bimodal sized alternative combining the advantages of the silver nanoparticles with the microscale copper (Ag NPs/Cu). Different fractions of nanoparticles have been mixed into microscopic copper powder and the efficiency of the sintering was investigated while varying the pressure and the temperature of the sintering. Finally, the physical properties of sintered samples were evaluated by measuring the variation in the thermal and electrical conductivity.

3.1.1 Samples preparation

A hybrid bimodal powder composed of copper powder with a size of 10µm (Alfa Aesar, Thermo Fischer, Germany) was mixed with silver NPs with a particle size less than 50nm (Sigma-Aldrich AB, Sweden). The Ag NPs were stabilized in triethylene glycol monomethyl ether and different fractions of mixed microscopic powder with silver nanoparticles were including 0.5, 1 and 2wt.% of NPs. After mixing, powders were pressed under pressures of P_1 and P_2 corresponding to 4 and 8 MPa, respectively, and sintered on a hot plate under N_2 through a two-plateau heating profile. Heating to 220°C was followed by a hold for 10min, which corresponds to the degradation of the organic compound, then a second step heating to the sintering temperature of T_1, T_2 and T_3 equivalent to 250, 300 and 400°C, respectively. The additional sintering conditions include T_4= 500°C and pressure P_3= 100MPa were used to serve the comparison.

3.1.2 Microscopic observation of the hybrid powder

The quality of the mixing with the increase in the fraction of the Ag NPs is shown in Figure 3-1. The nanoparticles are seen covering the macroscopic copper powder already at 0.5wt.% fraction. With the increase of the fraction of the nanoparticles, more NPs are seen bridging the porosity between the macroscopic particles. Figure 3-2 compares the samples after sintering at different temperatures. At a relatively low temperature of 250°C (cf. figure 3-2.a), the sintered powder appears covered with a smooth and dim layer of materials. At a temperature of 300°C, the sintering of the Ag NPs in between the macroscopic Cu particles is observed with contrasted grains boundaries of NPs that indicates the non-completion of the sintering. With the further increase in the temperature up to 400°C, better sintering is achieved.

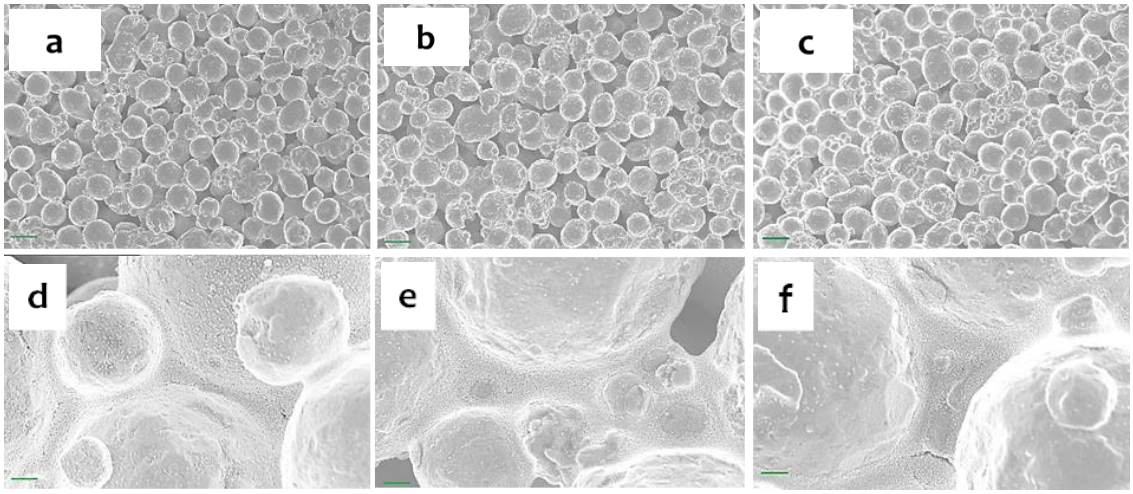

Figure 3-1: SEM images of the mixed powder with different fractions of NPs to the left and their corresponding high magnification observation to the right. (a-c) magnification 2k, (d-f) magnification 20k.

The increase in the fraction of NPs is seen providing better coverage and bridging the microscopic particles, and the increase in the temperature provides additional thermal energy for the sintering of the NPs. However, as can be seen in Figure 3-2, the increase in the fraction of the nanoparticles also results in the formation of large porosity that is difficult to eliminate. The presence of such microscopic voids in between the particles puts another constraint in the sintering process as it becomes difficult to close that porosity. As a result, those micropores will further weaken the structure by being the source of crack formation and propagation.

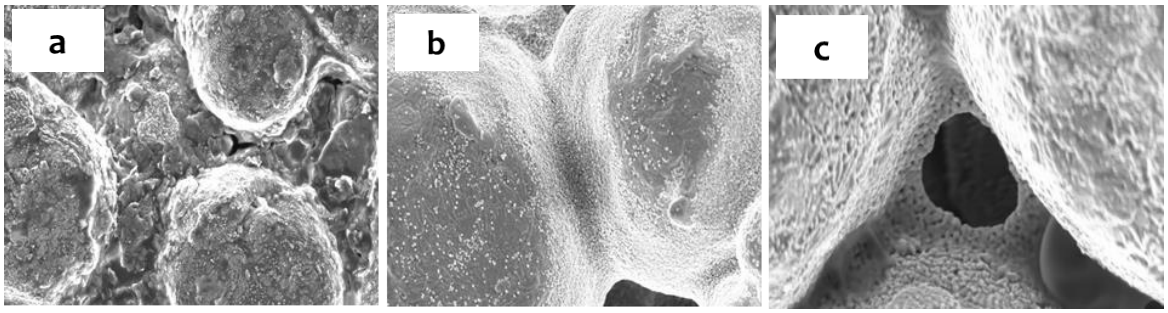

Figure 3-2: SEM images of 2% Ag NPs powder sintered at different temperatures: (a) 250° C; (b) 300°C; (c) 400°C. (a) magnification 10k, (b) magnification 20k, (c) magnification 40k.

Sample with 2wt.% Ag NPs was deposited on a copper disk and sintered at 300°C to verify the quality of the interface formed between copper and Cu-Ag NPs. The copper substrate was initially polished, and the sintering was performed under the same condition as the previous. The sintered powder with its substrate where later on cut and polished on the surface to observe the cross-section. It can be seen from Figure 3-3 that no interface can be distinguished between the sintered powder and its substrate. This indicates the possible good adhesion if the powder to the substrate. The discontinuity observed in the same figure is explained by the low density of the sintered powder due to the lack of pressure.

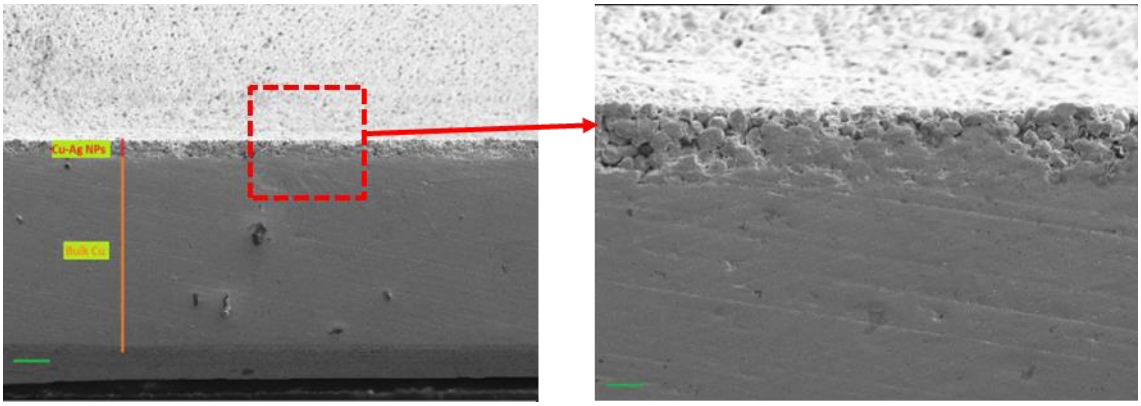

Figure 3-3: Sintered powder on a Cu bloc and cross section observed with SEM.

3.1.3 Density measurement

The different sintering parameters were correlated to the density of the samples. The measurements were done using Archimedes' principle by weighting the samples in air and water. Archimedes' principle has the advantage of measuring both surface and volume porosity but is rather restrained to material with higher density than water. The density measurements of the different samples under pressures 4 and 8MPa are shown in Figures 3-4.a and b, respectively. Using the same pressure, the value of the densities is seen increasing with the increase of temperatures. When pressed with 4 MPa and sintered at 250°C, the values of densities remain relatively low (i.e., between 55% and 65% of the bulk Cu) for the fractions of NPs between 0.5wt.% and 1wt.%. these low densities are explained by the poor quality of the sintering and the remaining of the organic phase. When the temperature was increased, the values of the density are seen correlating positively with the fraction of NPs and reach a maximum density of 91% for the hybrid bimodal powder sintered at 400°C. The same trend was observed when the pressure was increased to 8MPa. Relatively low densities were measured initially for the different samples

with values varying between 45% to 50% at 250°C but increased with the increase in the sintering temperature to reach density values as high as 92.5% for 2wt.% at 400°C.

Sintering is a thermodynamic mechanism where the pressure and the temperature are highly contributing to the densification of the powders. The increase of the temperature provides additional energy that drives the diffusion of the Ag and Cu species. The increase in the pressure has the effect of increasing the initial green density of the samples and compacting the powder where powders are brought to a larger contact area. To provide an additional comparison, the sintering of the hybrid bimodal powders was performed using an extra fraction of 5wt.% of Ag NPs and sintering parameters of 100MPa and 500°C. The results of the measured densities are shown in Figure 3-4.c. When sintering was processed at a temperature of 500°C, the pressure was kept at 8MPa, and when the pressure was increased to 100MPa, the sintering temperature was kept at 400°C. The results indicate that the sintering temperature as high as 500°C had a further positive effect on the quality of the samples. It induced more densification due to higher thermal energy and achieved a density of almost 95% of the density of bulk Cu. On the other hand and compared to the sintering under 4 and 8MPa, a higher pressure at 100MPa resulted in higher densities for the hybrid bimodal powder. Such increase is directly linked to the previously mentioned effect of pressure where the increase in the pressure results in a more compacted powder with a higher green density and large contact areas. In addition, with such high pressure, it has been demonstrated recently that the cold pressing might generate plastic deformations of the powder grains and translate into the creation of dislocations within the powder [211]. Such defects are additional stored energy that is later restored during the sintering to achieve higher densities. For the sintering temperature of 250°C, lower densities were achieved. It is believed that the compacted powder results in a more difficult condition to get rid of the organic phase.

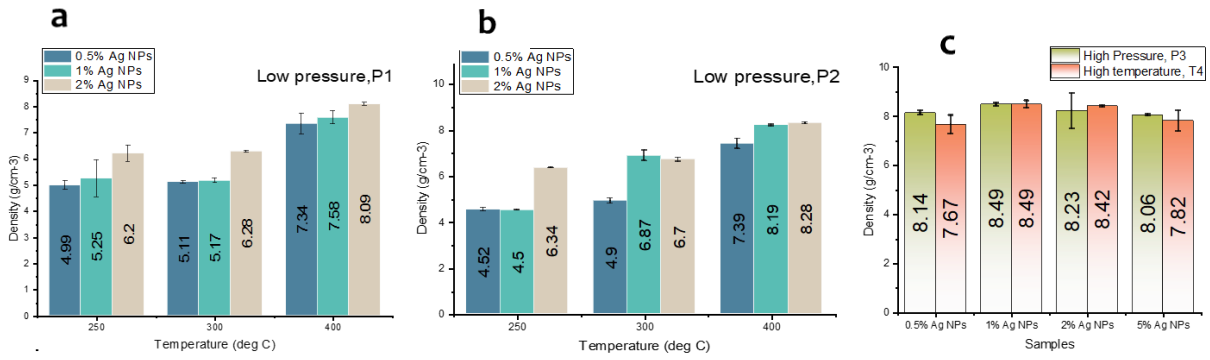

Figure 3-4: Density measurement of the sintered powders: (a) under 4MPa; (b) under 8MPa; (c) additional conditions 100MPa and 50°C.

3.1.4 Composition of the hybrid powder

A crystallography analysis was performed to investigate the chemistry of the obtained material and correlate it to the temperature and pressure on the sintering process. X-ray diffractograms of the sample containing 2wt.% of Ag NPs and sintered at temperatures between 250°C and 500°C are presented in Figure 3-5.a. The peaks of copper were compared to the reference sample composed of pure copper with peaks at values of two thetas at 43, 51 and 74°. In addition to the copper peaks, the sintered samples exhibited diffraction peaks at values of 36, 42 and 61° which were attributed to copper oxide. However, the intensity of the peaks was seen to gradually decrease with the increase in the sintering temperature. Such effect might be related to the efficiency of the reduction of the copper with the increase of the temperature but also to possible better densification where the silver around the copper serves as an oxidation barrier.

To investigate the additional effect of pressure, samples with 2wt.% Ag NPs were sintered at 300°C under the low pressure of 8MPa and high pressure of 100MPa. The results are shown in Figure 3-5.b. and show a shift in the peaks towards lower angles with a value shift between peaks observed for pressure of 100MPa. In the article we published (Paper A), this was explained as a change in the unit cell through a change in the crystal size or lattice strain. However, this effect can also be related to a doping effect where higher pressures contribute to higher diffusions rates or/and a possible Doppler effect in the measurement. The apparent increase in the intensity of the copper peaks can be observed accompanied by the narrowing of the peaks. Such effect can be attributed to the change in the grain size of the material where once again the dramatic increase in the pressure affects the sintering parameters.

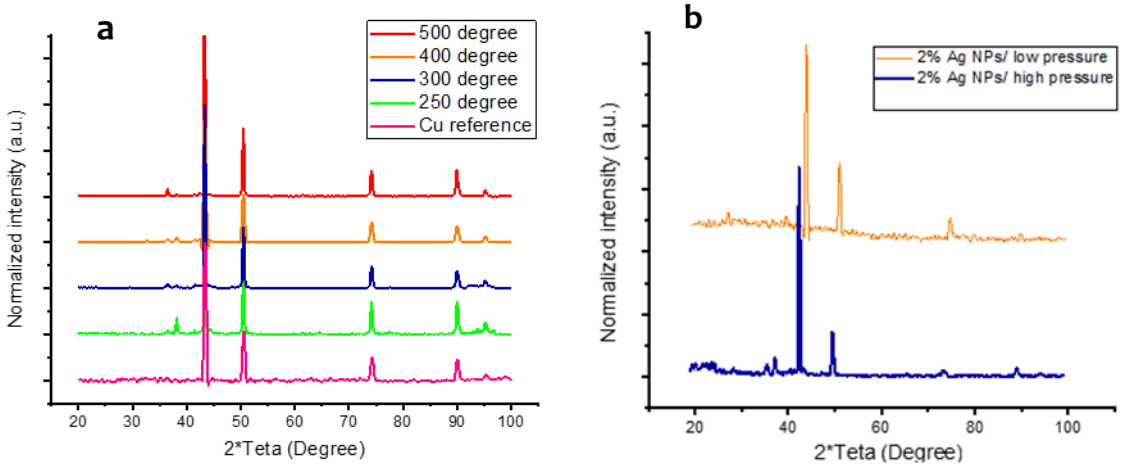

Figure 3-5: X-ray ray diffractograms of Cu-2%Ag NPs sintered at (a) different temperatures, (b) 300° C under low and high pressure.

3.1.5 Thermal and electrical properties of the hybrid bimodal powder

The sintered parameters of the hybrid Cu-Ag NPs powder were correlated with the physical properties of the samples. Samples with 1wt.% and 2wt.% Ag NPs showed a good compromise between density and fraction of the NPs used and were further investigated to review the potential of this approach in the electronic packaging. The thermal conductivity of the samples was measured when sintered at different temperatures. Figure 6 shows the results of the thermal conductivity of the sample with 1wt.% (cf. Figure 3-6.a) and 2wt.% NPs (cf. Figure 3-6.b). At 250°C, the thermal conductivity of the samples with 1wt.% and 2wt.% Ag NPs was the lowest with and did not vary a lot with the temperature. This result is explained by the presence of the non-evaporated organic that limits the sintering of the particles and hinders the metallic conduction. The increase of the sintering temperature to 300°C resulted in a relatively higher thermal conductivity for both fractions. It is assumed that this sintering temperature allows the evaporation of the organic phase and the sintering of the powder. However, such temperature still results in low densities and smaller grain sizes that negatively affect the heat transport efficiency. The increase in the sintering temperatures induces a positive effect on the thermal conductivity of the hybrid powder. At 400°C, both samples exhibited higher thermal conductivity and remain stable between 25°C and 100°C. This can be explained by the high-density value achieved at this temperature for the samples with 1wt.% and 2wt.% Ag NPs. The high density has as a consequence the elimination of the pores through the densification of the powder but also the increase in the grain sizes that correlates positively with the thermal conduction. For comparison, the thermal conductivity of the samples sintered at 500°C was measured in the sample containing 2wt.% Ag NPs. The results showed an even larger enhancement of the thermal conductivity that reached values of 276W/mK at 25°C. The further increase in the thermal conductivity of the samples is reflected through better sintering at the temperature of 500°C.

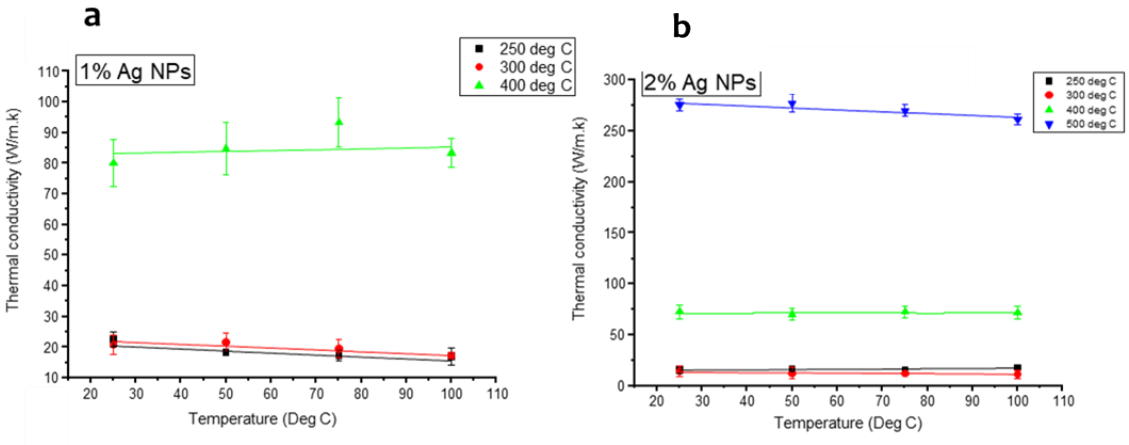

Figure 3-6: Thermal conductivity of (a) Cu with 1% Ag NPs, (b) Cu with 2% Ag NPs.

The electrical conductivity of the two samples was also evaluated through the measurement of the sheet resistance (cf. Figure 3-7). The electrical conductivity of the two samples increased with the increase of the sintering temperature. The electrical conductivity of the two samples increased tenfold between 250°C and 300°C, and between 300°C and 400°C to reach a value of 1.41×10^6 S/m.

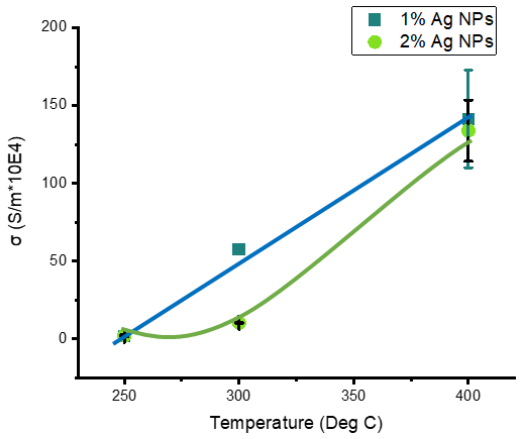

Figure 3-7: Electrical conductivity of the sample containing 1% and 2% Ag NPs when sintered at different temperatures.

The use of silver nanoparticles as a sintering aid shows promising results in terms of consolidation of the hybrid bimodal powder. The density of the sintered material is seen directly linked to the sintering parameters and the fraction of the NPs. The increase in the temperature and pressure of the sintering increased the densities of the hybrid bimodal powder and values as high as 95% of the bulk copper could be achieved at relatively low pressures and a fraction of the NPs. Such an approach also allowed to achieve thermal conductivity values at 75% that of copper. Due to the nanoscale effect, such kind of low-temperature processing is possible, and in the next section, this effect is exploited for the integration of high porosity carbon-based foam as an advanced solution for thermal management.

3.2 Silver Nanoparticles as Die Attach For Graphene Foam Heat Sink

Metallic foams are a kind of heat exchangers used as passive or active approaches for cooling electronic devices. Due to their simplicity, low cost, and high thermal performances, these solutions are becoming increasingly interesting. As explained in the second chapter, currently, microchannels heat sinks are offering an

advanced alternative to the earlier versions of heat sinks, by combining large surface areas, low densities, and high solid thermal conductivities. The open cell microchannels heat sink such as in the case of foams offer a real advantage for enhanced thermal design capabilities in the electronic package and work is ongoing to optimize their application and develop further their properties. In recent years, the development of production methods allowed the production of 3D graphene foams (GFs). The 3D structures consisting of ultrathin graphite offers thermal conductivity that can be as high as 10 times higher than the thermal conductivity of aluminium for only a fifth of its density [102], [103]. As heat sinks, open cells microchannels graphene foam was previously reported with effective thermal conductivities between 0.26 to 1.70W/mK [212]. Electroplated copper on a reticulated vitreous carbon foam improved the effective thermal conductivity of the foam to reach 100% enhancement at 5% porosity increase and up to 3500% enhancement at 52% in density [213] due to the increase of the solid conductive phase. However, with the potential of the high porosity, and low density for becoming a good alternative for the replacement of microchannels metallic foams, no solution is suggested to integrate graphene foams in the thermal management strategies.

To our knowledge, despite developed models and experimental effort to apply high porosity materials in electronics packaging, the use of high thermal conductivity, low density, graphene foams has not been shown in the literature with a real study case combining the intrinsic thermal properties of graphene in 3D, with improved mechanical and thermal properties of metallic coating and the presence of organic PCMs. Besides, even though many studies highlight the low density and surface area of the graphene foam, very little attention is given to investigating the contribution of the additional microporosity in the secondary microchannels.

In this section, we explore the open cell microchannel graphene foam as a potential heat dissipation solution for advanced thermal management. We investigate the possibility to integrate such low density, high porosity material in the electronic package and use the nanoscale effect of Ag NPs as a solution to attach the 3D structure on a substrate to mimic the package of a heat sink directly onto the electronic package. The thermal properties of the foams are evaluated as a passive solution for heat dissipation. To further enhance the thermal properties of the prepared composite, different fractions of paraffin were infiltrated into the porous media, and the temperatures profiles were recorded. Finally, a model was developed to study the importance of the secondary microchannels within the foam.

3.2.1 Characterisation of the Graphene foam as a heat sink

3.2.1.1 Sample preparation From 2D to 3D graphene

Various production methods of the 3D graphitic structure have been proposed and can be correlated to different properties and applications. The production of 3D graphene structures methods includes a foam-like template or aerogels/hydrogel and can be categorized into three primary strategies: direct synthesis of 3D graphene, assembly of graphene oxide sheets and template-assisted assembly. While the two latter methods result in modest structural and physical properties, the direct synthesis of the graphene foam via CVD is the most reliable.

As in the case of the fabrication of graphene, the CVD growth of the graphene foam relies on the saturation and precipitation of carbon atoms on the surface of the catalyst material. In the case of the foam, the catalyst material is a prefabricated 3D metal foam substrate. The porous foam in our case is nickel and was subjected to pyrolyzed carbon gas source in a tube furnace at temperatures of 1000°C. The graphene foam obtained was obtained with pore size between 100–200µm, 99.6%, with a density of 5 mg/cm^3 and 1.7mm height. The initial nickel foam with a bulk density of 0.95g/cm^3 and 95% porosity was coated with polymethyl methacrylate after the graphene growth. The metallic skeleton was etched using $FeCl_3$ solution, before being enclosed into an acetone vapour chamber.

The foam was attached to the backside of a thermoresistor using silver NPs. The dispersion of NPs was spread on the back of the heater using a spin coating to guarantee a thin homogenous layer application. The high porosity material 3D structure was then deposited onto the surface of the Ag NPs and sintered in a vacuum oven at 290°C. to strengthen the structure of the foam and investigate the effect of the solid fraction in the foam, additional silver nanoparticles were added and sintered under the same conditions. Figure 3-8 is a simplified schematic of the sample preparation.

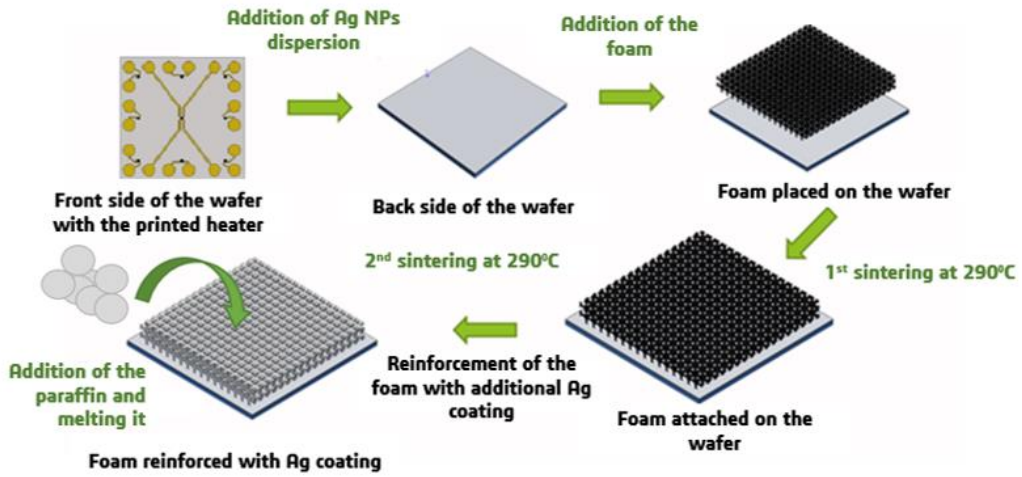

Figure 3-8: Schematic representation of the sample preparation of graphene foam/silver composite. A layer of Ag Nanoparticles is first coated on the back of the heater, the foam is then deposition and sintered. Additional Ag coating is added and sintered under the same conditions. The PCM is melted and infiltrated gradually into the porous structure.

3.2.1.2 Microscopic characterisation of the graphene foam heat sink

SEM observations of the 3D porous structures are presented in Figure 3-9. The use of Ag NPs on the surface of the die was found to successfully connect the 3D graphene structure and to offer good adhesion to its substrate. In addition, as presented in Figure 3-9.a. In addition to the stabilisation of Ag NPs, the ethylene glycol was found to affect the wetting of the surface between the graphene foam and its substrate. As presented in the figure, the graphene 3-9.b. The bottom branch of the foam opened at the contact of the back side of the wafer. While this effect was solely linked in our published article to the presence of the organic phase that stabilized the graphene material, it is worth noting that such effect can also be attributed to the densification of the metallic NPs at high temperature and its shrinkage upon cooling.

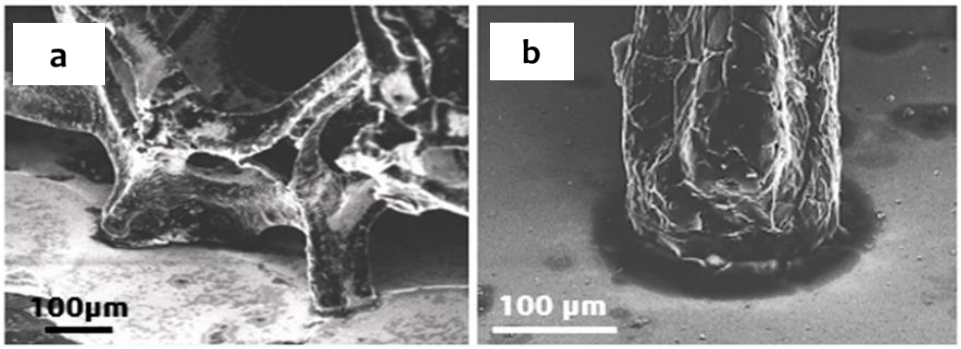

Figure 3-9: (a) SEM observation of the contact between the graphene struts and the substrate with multiple struts connected and (b) single column in contact with the substrate.

Although unexpected, this effect is highly suitable for the application as it allows to increase the contact area between the foam and the substrate. Hence, the surface adhesion between the graphene and the wafer is improved in addition to the increase of the surface area for heat dissipation. Due to the flexibility of the foam, no additional pressure was needed to connect the foam to its substate. Combined with good wetting, the graphene foam can be applied on surfaces with different roughness without sacrificing the interface contact between the foam the solid substrate. It is also worth mentioning that the flexibility of the foam allows its perfect matching with the surface

The further addition of the sintered silver nanoparticles to the foam as a coating can be observed in Figure 3-10.a The Ag NPs can be distinguished with bright colour on the surface of the foam. The added Ag NPs were absorbed to the internal porosity of the foam through capillary forces and were found to fill the concave surface of the graphene branches. The coating was found to cover the branches of the graphene with a thin layer observed covering part of the foam wall with a layer of less than 500nm around the struts (cf. Figure 3-10.b). After the addition of the metallic coating, the fraction of the porosity slightly decreased. The measurement of the density of the foam after coating using Archimedes' principle showed a decrease in the porosity to reach a value of 99.44%.

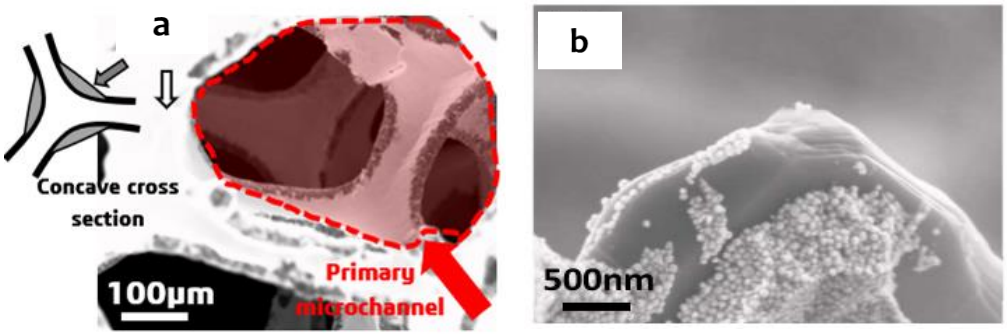

Figure 3-10: (a) graphene foam coated with Ag NPs, (b) Ag NPs deposited on graphene sheets.

3.2.1.3 Thermal characterisation

The thermal conductivity of the foam was compared before and after the addition of the coating to evaluate the investigate effect of the presence of the Ag coating. The thermal properties of the porous GF were measured using Dependence of Resistance on Temperature (DRT) Joule Heating method. In the DRT method [214], the suspended sample is heated by running the alternating current (AC) and DC through the GF and the temperature of the sample was measured by the dependence of the resistance on the temperature of the GF. In this case, the temperature coefficient of resistance of the sample was measured and the thermal conductivity of the samples was calculated through the measurement of the resistance variation of the foams as a function of the I_{DC} current [215].

The result of the DRT Joule heating for the thermal conductivity measurements of the porous structure of graphene before and after the addition of the silver coating is shown in Figures 3-11.a and 3-11.b, respectively. It was found that the addition of the metallic coating had a critical effect on the electrical behaviour of the foam. Before the addition of the silver coating, the variation of resistivity in the case of graphene foam followed a nonlinear inverse proportional resistance increase with the current (cf. Figure 3-12.a). A typical graphene electrical behaviour is explained by the negative temperature coefficient [216]. A resistance value of $1x10^{-3}\Omega.m$

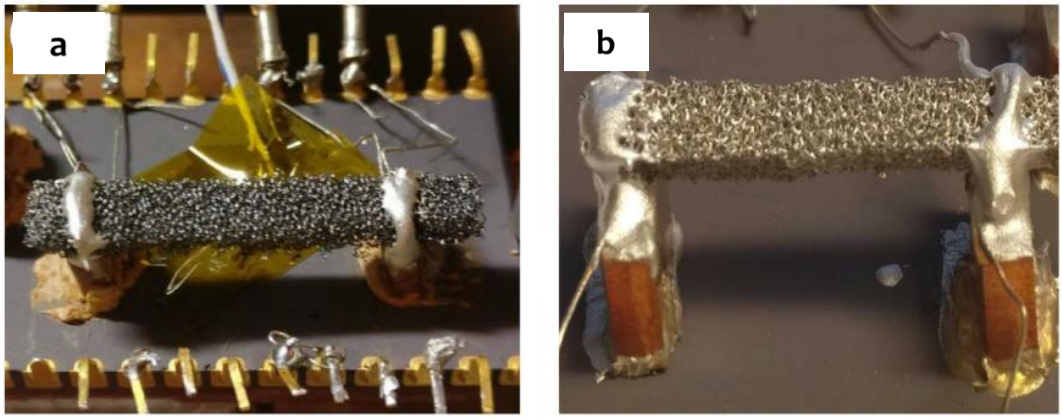

Figure 3-11: DRT setup and results of the measurement. (a) photograph of the graphene foam suspended between two copper blocks; (b) photograph of graphene foam coated with silver and suspended between two copper blocks.

was measured that is equivalent to the thermal conductivity of 1.3W/mK. After the addition of the silver coating (cf. Figure 3-12.b), the evolution of the resistivity was found to follow a metallic behaviour that is characterized by a positive temperature coefficient of resistance and a proportional increase in the resistance with temperature as an ohmic linear behaviour and a resistance of $1.35x10^{-5}\Omega m$. The thermal conductivity of the coated film was estimated in this case to 2W/mK. The values of thermal conductivities measured are following previously reported values of graphene foam effective thermal conductivities [212]. It is assumed that in the presence of the metallic phase, the valance electrons present in the conduction band contribute more to the electrical conduction with a weak interaction between silver and graphene (i.e., low carbon-carbon atomic distance 1.28Å that indicate a value atomic distance between carbon-silver [217]). The graphene foam is assumed to act as a scaffold for the metallic structure, and that the measured electrical resistivity is a result of the composite response where the graphene foam electrical property plays a negative role to degrade the properties of the electrical response of the sintered silver nanoparticles.

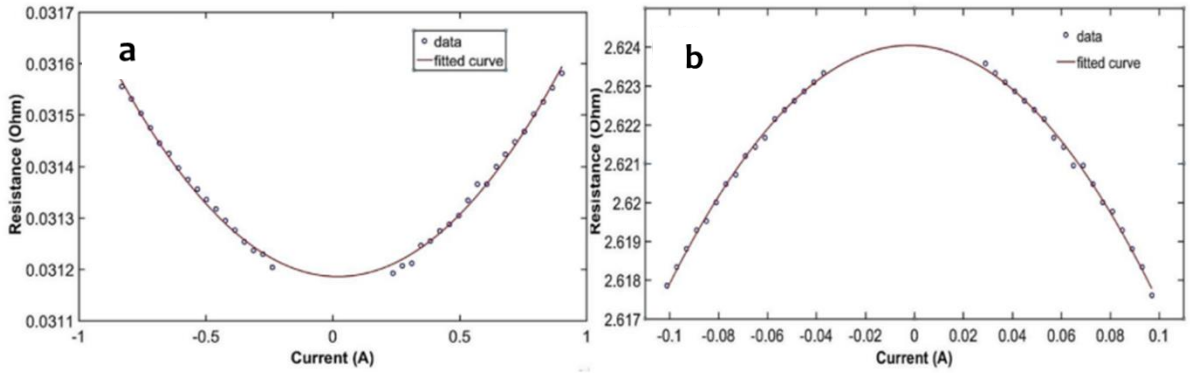

Figure 3-12: (a) resistance measurement at different current of the graphene foam, (b) resistance measurement at different current of the graphene foam coated with silver.

The parallel composite mode was used to evaluate the solid thermal conductivity of the porous GF, The value of thermal conductivity for the graphene foam was found to reach a value of 319W/mK, which compares well to the magnitude of solid thermal conductivities reported elsewhere. It is worth mentioning also that such value is 82% that of copper for the quarter of its density. The addition of the Ag coating resulted in a further enhancement of the thermal conductivity of the foam and an increase to up to 352W/mK. Such effect is directly linked to the solid phase conduction with the presence of silver that has high value thermal conductivity. Such an increase in the thermal conductivity of the foam with the silver coating is assumed to be due to the high thermal conductivity of silver and the increase in the carbon-based and metallic fraction to detriment of the porosity. The porosity level after the addition of the metallic coating decreased to 99.44%.

The heat dissipation properties of the foam as a heat sink were evaluated by monitoring the variation of the Tj at different power levels using the thermoresistor (cf. Figure 3-13) [218]. The profile of temperatures was recorded as a function of time and power. It was found that the value of the Tj correlated with the increase of the power from 0.24W to 1W. At power values of 0.24W, the Tj of the heater reached a steady-state value of 27°C, which increased further to reach the values of 33°C and 42°C for power levels of 0.35W and 0.64W, respectively. The maximum temperature of 55°C was recorded at a power level of 1W.

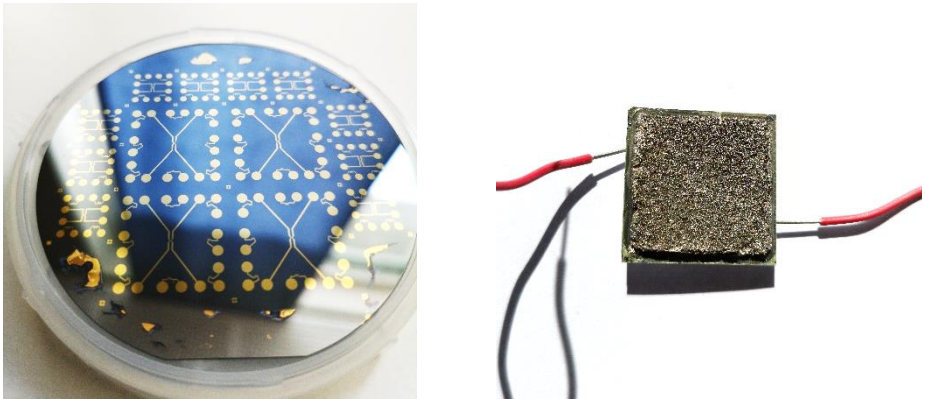

Figure 3-13:Photography images showing (a) the fabricated heaters on a 3" wafer and (b) the foam connected on the surface of the heater.

Furthermore, the temperature variation of the heater was recorded without the use of a heat sink and used as a reference to highlight the advantage of the GF-Ag heat sink. The values of the Tj in the case of no heater were compared to the values of Tj in the case of the nickel heat sink, GF (i.e., without coating), and GF-Ag. The results of the temperature variations are presented in Figure 3-14. It appears that the Tj in the case of the nickel foam were the highest compared to the other situations and for all power levels. While the temperatures at low powers (i.e.,0.24W and 0.35W) were comparable to the temperatures of the heater only, those of 0.64W and 1W were 4 degrees and 6 degrees higher, respectively. The explanation for the poor performance of the metallic nickel foam was attributed to the low quality of contact between the foam and the substrate. The rigid nickel structure can be difficult to accommodate the surface attach on top of the heater when no pressure and might result in limited surface contact. Such limitation hinders the heat dissipation of the metallic foam that acts more as a barrier that limits the contact with the ambient and results in worse thermal properties than in the case of no heater. In the case of the GF heat sink, the junction temperatures at the four power levels decreased by 1.5, 2, 6 and 12°C with

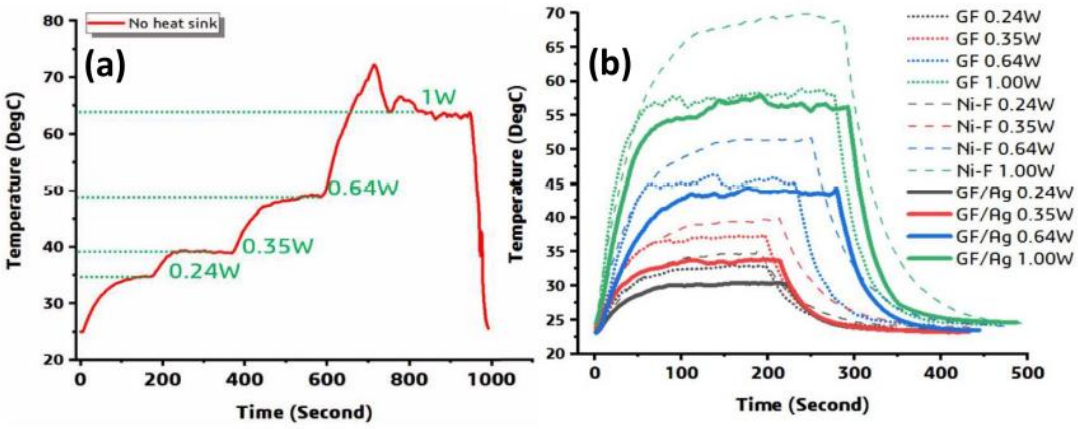

Figure 3-14: Temperature rise at different power level in the case of (a) no heat sink and (b) three heat sinks (i.e.,graphene foam (GF), nickel foam (Ni-F) and graphene foam coated with Ag (GF/Ag)).

the increased power levels compared to the case of no heater. Such results are explained by the good contact of the foam with its substate in addition to the superior thermal conductivity measured in the case of GF. Finally, the addition of the silver coating resulted in a further decrease of the Tj that corresponded to 4, 4.5, 7.5 and 13°C

differences. The additional improvement in the thermal behaviour of the porous composite can be explained by the presence of a high thermal conductivity metallic phase and the increase in the density of the solid phase to the detriment of the porosity. To verify the contribution of the natural convection in the heat dissipation of the integrated GF, the experiment was performed at an angle of 90°. The results of the temperature variation in the vertical direction showed similar values to the horizontal position of the heat sink (cf. Figure 3-15). This indicates the non-dependence of the heat sink performances on the orientation.

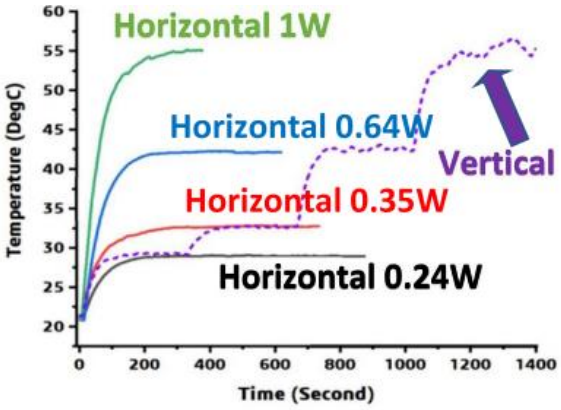

Figure 3-15: Measurement comparison of graphene foam coated with Ag at horizontal and vertical orientations.

3.2.1.4 Role of secondary microchannels in heat transfer

Despite the high interest in graphene foams and their application in thermal management and the role of the primary microchannels [219][220], there is no attention given to the secondary microchannels that are exclusively linked to the two-step production method of the GF (cf. Figure 3-16). The secondary porosity within the foam accounts for a non-negligible surface area and might be exploited for advanced application. The secondary micro-channels in the 3D foam studied herein correspond to the space occupied by the metallic catalyst used for the growth of the foam. After etching, the foam is mechanically strong enough to support itself, and the space occupied by the etched metal part is considered a secondary microchannel that differs from the primary microchannels in the outer surface of the struts.

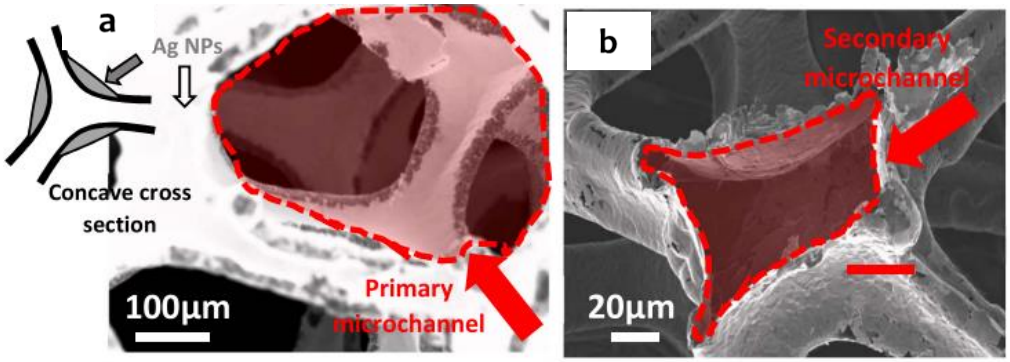

Figure 3-16: (a) Graphene foam coated with Ag NPs, (b) internal secondary microchannels within broken foam node.

To investigate the role of those secondary porosities in the heat transfer, a Computational Fluid Modelling (CFD) model was built using COMSOL Multiphysics v5.4. The case study of the model was related to the conjugated heat transfer in solid and fluid through the structure of the foam and the secondary microchannels. The radiative heat transfer and the temperature dependence of other properties were neglected. An air velocity of 0.1m/s was forced into the foam to depict the condition of natural convection experiment conditions [221],[222]. The structure of the graphene foam is complex, and it is delicate to reproduce to the last detail the nuances of the

3D structure. However, it is valid to simplify the representation to a model of interconnected fibres that allows to a fair degree to compute the properties and behaviour (cf. Figure 3-17) [223].

The CFD also allowed following the profile of temperature o the surface of the heater. The results are shown in Figure 3-18. It can be seen that high-temperature profiles are not restraint to the centre of the heater only. While the centre of the heater has the highest value of temperature, the density of power around the centre of the heater can be quite high. It indicates that good contact of the heat sink on the back of the chip is required to achieve good heat dissipation and maximise the efficiency of the thermal design. Figure 3-18.(a-c) show the results of velocity magnitudes, pressures, and convective heat fluxes along a vertical column of the foam. Insets of each parameter are shown within its respective figure. The velocity of the air flow is seen decreasing more within the secondary microchannels compared to air flow within the primary microchannels. A pressure build-up is observed within the inner volume of the cylindrical column as a result of the small diameters of the secondary microchannels. The convective heat flux follows the trend of the airflow velocities along the column, and a more significant decrease is observed within the column comparatively to the outer volume.

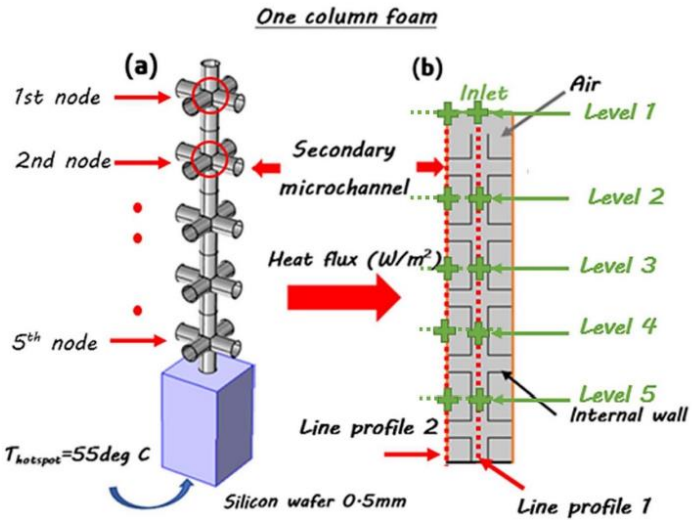

Figure 3-17: (a) 3D model of the one single column part of the foam with five nodes, (b) 2D representation of the single column foam with lines profiles and local levels indicated for the studied parameters.

Figure 3-18.d shows the variation of velocity magnitude and convective heat flux along with the lines profiles 1 and 2 positioned at the centre of the vertical strut and beginning of the horizontal struts, respectively. For the secondary microchannels (line profile 1), the convective heat flux is observed to gradually decrease after each node along the vertical strut. In the case of the primary microchannels (line profile 2), the same trend is observed with the convective heat flux that slowly decreases as the airflow along the line. Table 3-1 summarizes the values of the ratio between the airflow within the primary and the secondary microchannels at five different levels. The convective flux in the case of the secondary microchannels is still comparable to the convective flux within the primary microchannels. Such porosity is then expected to have a certain contribution to the heat transfer.

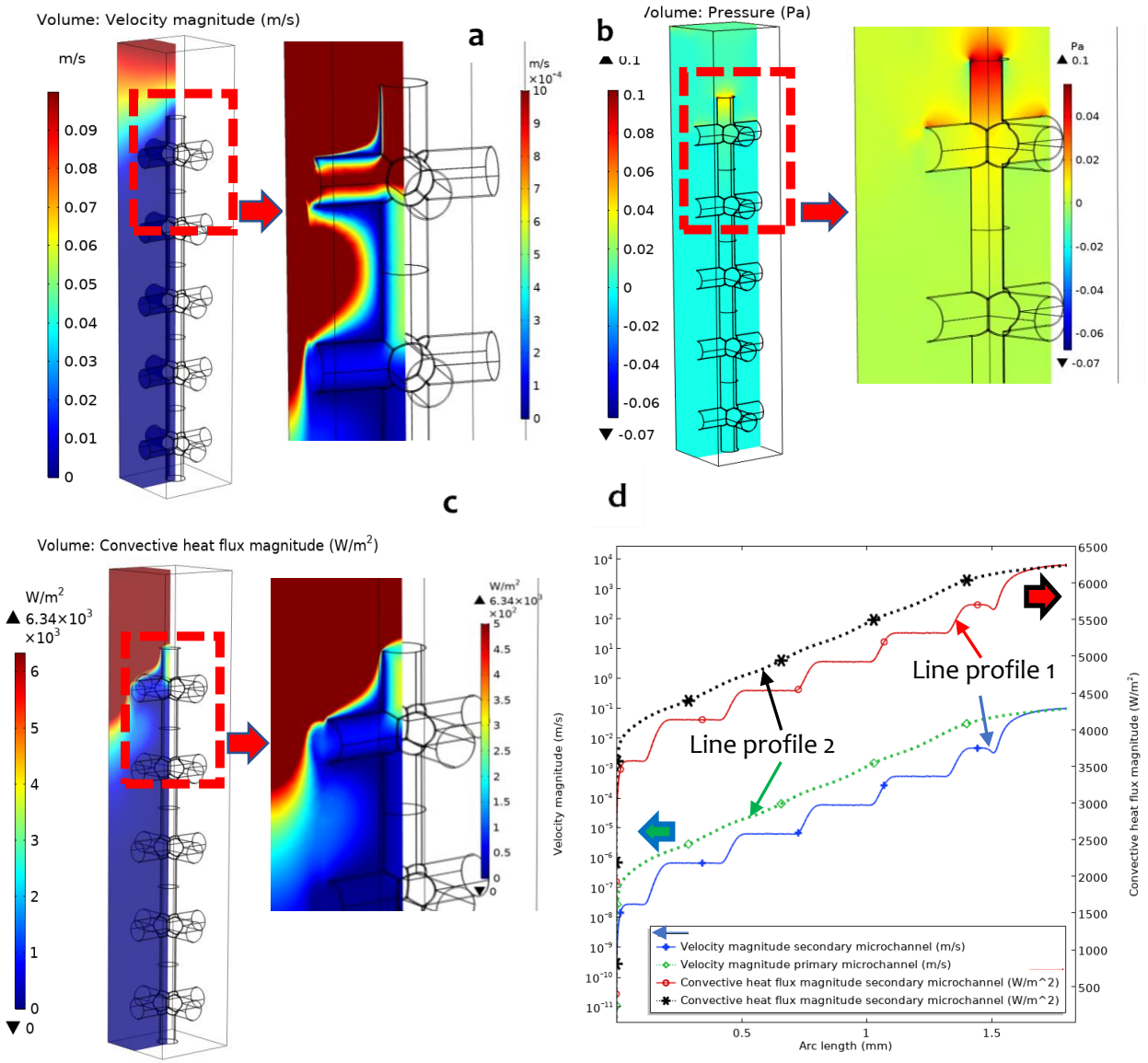

Figure 3-18: 3D profile showing the (a) velocity magnitude with an inset of the top of the foam with a maximum scale limited to x10⁻⁴ m/s, (b) pressure evolution along the vertical column with an inset of the top of the foam and a maximum scale limited to 0.1 Pa, (c) convective heat flux along the column with an inset of the top of the foam and a maximum scale limited to 5x10² W/m² (d) profiles of the air flow velocity and convective heat flux magnitudes along the primary and secondary microchannels in the vertical direction.

Table 3-1: Ratio values of velocity, pressure variation and convective heat flux magnitudes at five points along the foam column between the flow in the primary and secondary microchannels

	Velocity magnitude ratio	Pressure variation ratio	Convective heat flux ratio
Level 1	15,41	0,08	15,41
Level 2	10,61	0,20	10,61
Level 3	8,09	0,14	8,09
Level 4	6,50	0,12	6,50
Level 5	5,09	0,09	5,09

3.2.2 Graphene Foam as a Container for Phase Change Materials

Paraffin PCMs have the disadvantage of low thermal conductivity (i.e.,0.2W/mK) and diffusivity, which results in a long time for heat absorption and diffusion within the material. Such low performance induces a gradient in temperature and a possible hot spot that can have damaging effect the reliability of the electronic device. To improve the thermal conductivity and diffusivity of the paraffin specifically and PCM in general, metal foams have been used as an encapsulation structure where the PCMs are embedded. Such an approach has attracted large interest in recent years for its efficiency and high figure of merit compared to the use of nanofillers. The implementation of the microchannel heat sink to embed the PCMs results in the enhancement of their performances. Such enhancement is translated in the term of heat diffusion and melting. As mentioned earlier, the synergy between the thermal performance of PCM based metal foam heat sink is influenced by design parameters but also the intersecting properties of the materials involved. As shown in this work, the 3D structure of graphene foam showed good thermal properties with high thermal conductivity and performances when integrated into the electronic package. In what comes next, the low-density graphene foam is used as a container for the PCM, and the composite material is directly used in contact with a chip.

3.2.2.1 Sample preparation

Different amounts of paraffin were infiltrated within the GF-Ag. The PCM is commonly introduced into the heat sink in the liquid state. The PCM is deposited on top of the heat sink that is heated to a higher temperature than the melting point of the PCM. When the temperature of the heat sink increases to the level of the PCM melting point, the PCM melts and flows into the cavity of the heat sink. Similarly, in our work, the minimum amount of 0.1g of the PCM was deposited on the surface of the heat sink and the heater was turned on with a power of 1W. After the temperature increase, the liquid PCM started gradually to be absorbed into the 3D microchannel structure via capillary forces. Incremental amounts of 0.05g of PCM were then added at the end of each experiment where the temperature profile of the thermoresistor was recorded. The high porosity foam contained the melted PCM at different levels and up to a 0.4g of paraffin before it started to drip, which corresponds to a factor of 100 times the weight of the foam.

3.2.2.2 Thermal characterisation

Incremental amounts of paraffin were added to the graphene foam, and the evolution of the temperature of the heater was recorded in the case of GF-Ag. The results of the thermal behaviour of the graphene foam coated with sintered silver and infiltrated with paraffin are shown in Figure 3-19 (a-d). Higher amounts of PCM resulted in the improvement of the thermal conductivity of the GF-Ag/PCM system and lower Tj. No delay in the time to reach equilibrium was observed at 0.24W. This can be explained by the temperatures reached during the heating step with such low power being lower than the melting point of the PCM. When the power was increased further, the temperature of the heater increases to reach values higher than the melting temperature of the PCM. As a result, the paraffin melted, and the energy absorbed during the phase change from solid to liquid translated into the delay in the temperature increase of Tj. The incremental increase in the volume of PCM resulted in a gradual increase in the delay to reach temperature equilibrium. The highest time delay achieved was recorded in the case of 0.35W since the heat flux generated at this power resulted in a low melting rate.

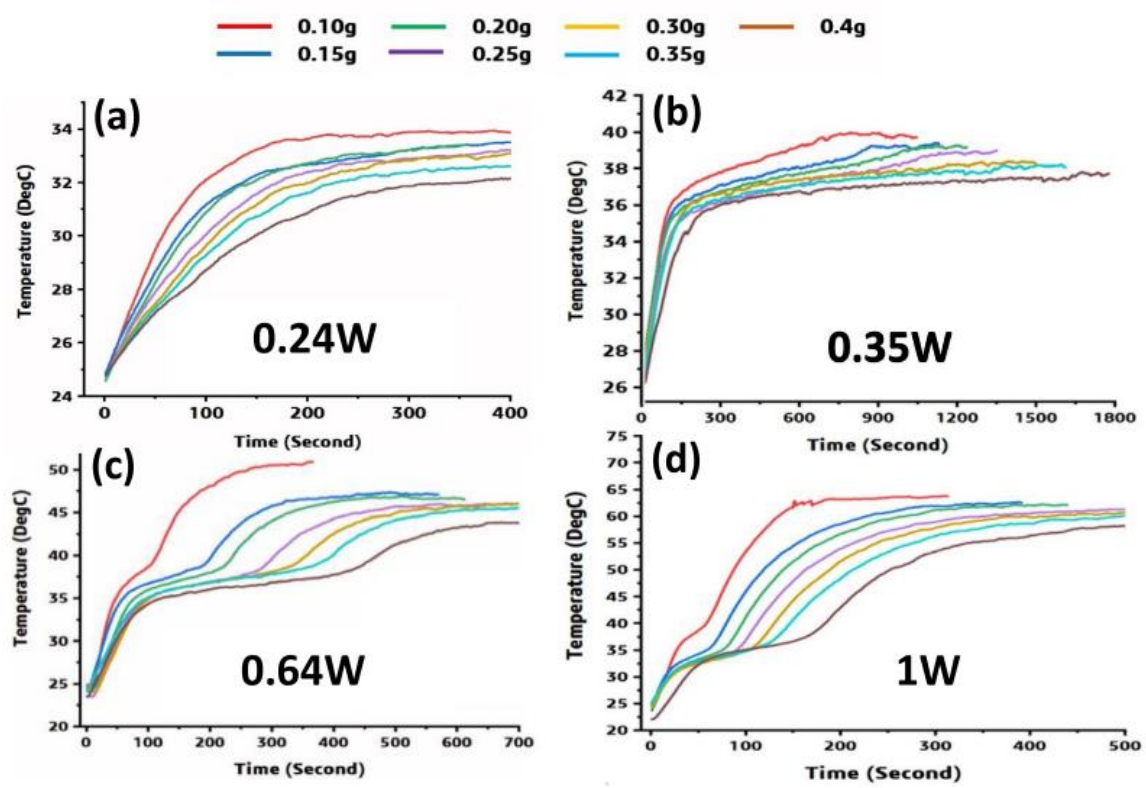

Figure 3-19: Transient temperature of graphene foam coated with Ag with different PCM load at: (a) 0.24W, (b) 0.35W, (c) 0.64W and (d) 1W.

3.3 Summary and discussion

In this chapter, the nanoscale effect of nanoparticles was explored as a potential approach for low-temperature manufacturing. In our effort, Ag NPs were used as a sintering aid in a hybrid bimodal macroscopic powder and as a die-attach for graphene foam. In the case of the hybrid bimodal powder where different fractions of Ag NPs were mixed into the microscopic copper powder, the use of silver nanoparticles as a sintering aid was found to offer promising results in terms of consolidation of the hybrid bimodal powder. The density of the sintered material is seen directly linked to the sintering parameters and the fraction of the NPs. At 250°C, low-density materials were obtained due to the low-quality sintering and the increase in the temperature and pressure of the sintering increased the densities of the hybrid bimodal powder and values as high as 95% of the bulk copper could be achieved at relatively low pressures and the fraction of the NPs. In addition, the presence of the silver coating on the copper micropowder was found to behave as a barrier to protect the copper against oxidation. Also, the metallic phases in the bimodal powder allowed achieving high thermal conductivity values when the sintering parameters were found ideal. Such an approach allowed to achieve a thermal conductivity as high as 276W/mK that is close to 75% that of copper. The application of the hybrid bimodal approach gives the possibility to take advantage of the low sintering temperature of the silver and combine the structural advantages of copper. As seen herein, silver also brings additional oxidation protection to copper.

In the second part, due to their low processing temperatures that arise from their surface energy, Ag NPs were also investigated as die-attach materials for novel high porosity, low-density graphene foam. While the approach aimed initially at developing a method to integrate the 3D foam as a new thermal management solution in the microelectronic package, these NPs were found to play an additional role in the reinforcement of the foam structure and contribute to the thermal transport. The die attaches and coating based on the sintering of Ag NPs allowed to reach high thermal dissipation properties at processing temperature lower than 300°C. The presence of the metallic coating on the foam enhanced its effective thermal conductivity by 54% and the solid thermal conductivity of such structure was estimated to be 376W/mK. Such value is superior to the thermal conductivity

of most metallic materials and can be expected to be a good alternative for applications where copper cannot be used.

It is worth mentioning that the use of the organic phase to disperse the Ag NPs had also an effect on the foam where the contact area between the foam is increased. The flexibility of the foam also had a positive effect as it removed the need for the use of pressure during the sintering. It allowed to maximize the number of vertical struts connected on the surface of the substrate and contributed to the increase of the heat dissipation properties of the foam. The high porosity foam was found to be used as a container for paraffin as a phase change material with a mass of paraffin being a hundred times larger than the one of the foam. The presence of the PCM in the foam resulted in the delay in the rate of heating. In this work, a CFD model was developed to investigate the possible contribution of the secondary microchannels in the foam. It was found that these microchannels had a non-negligeable effect on heat transfer. Even though the conduction mode is dominating the heat transfer process in such systems, we found that the secondary microchannels in the case of graphene foam can be further exploited in the heat dissipation approach. Figure 3-20 summarizes the time delays and the junctions temperatures corresponding to different power levels and weights of PCM. It was noted that the presence of the organic phase reduces the heat transfer via convection before melting and increases the conduction within the PCM. The thermal conductivity of the paraffin is known to be ten times higher than that of air and the addition of the different masses of paraffin resulted in a proportional improvement of the solid thermal conductivity. In addition, such an effect can also be linked to the high thermal conductivity of the solid phase of the foam where the conduction mode in such structure is considered dominating the heat transfer. The presence of graphene foam achieved an improvement of the effective thermal conductivity of the composite and the silver coating increased further its effective thermal conductivity by increasing the thickness and the density of the matrix. The thickening of the matrix dimension is assumed to increase the heat transfer efficiency and shortening the melting time of the PCM. With the small modification in the matrix density after the addition of the coating, the thermal energy storage capabilities were not sacrificed.

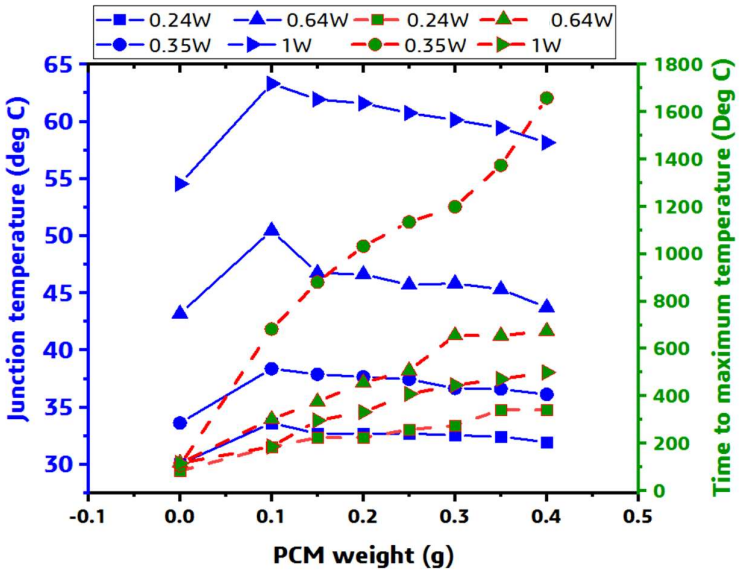

Figure 3-20: Summary of the junction temperatures (blue) and time to reach the maximum temperature (green/red) at different power levels and PCM loads.

Chapter 4

4. Graphene coating: new micro- and nano-scale additives for thermal management

Composite materials have for long been the material scientist's choice when it is about compromising materials properties and selection. Adding materials, by varying the composition and/or the structure, to the initial matrix has been covered by large industrial products and countless combination possibilities. Such an approach resulted in a composite material that combines the properties of the components or newer suitable properties. With their outstanding properties, carbon materials were explored as fillers for all sorts of matrixes. Carbon materials were found to be an excellent alternative as composite fillers leading to new potential industrial applications. More specifically, graphene stands out as a new composite material of choice. Stating the obvious by now, the 2D materials are being investigated for a large variety of applications where its integration in the industrial product portfolio is a priority. Graphene, as a 2D nanomaterial with high potential, is being investigated as a nanofiller in organic and metallic matrixes. Reports showed high potential in the improvement of the properties of the composite material through the reduction of the surface friction [224], an increase in the thermal [225] and the electrical conductivity [226]. Adding graphene as a reinforcing agent in a polymer matrix has improved the overall performance and properties of such composites, graphene reinforced polymer composites. Reports indicate the potential of graphene to play a major role provide a high degree of reinforcement of both mechanical and functional properties. already the vast potential of graphene reinforced metal matrix composites, including improved tensile strength, Young's modulus hardness, natural lubrication, and electrical and thermal conductivities [227]. On the other hand, advanced fluidic solutions have shown great potential in many applications [228].

In this chapter, graphene is investigated as a micro- and nano- coating for metallic particles. Its potential is investigated as filler for composite material in terms of thermal properties for heat transfer properties while exploring their possible additional multifunctional contribution into the properties of the graphene. We demonstrate the possibility to exploit CVD and arc discharge processes to produce graphene on micro- and nanoscopic copper particles. We investigate different processing parameters and correlate them with the properties of the carbon coating. In the case of microscopic copper particles, the CVD method was employed to produce the graphene-coated copper powder. The coated particles were mixed into a polymeric matrix as a Thermally Conductive Adhesive (TCA) and the variable thermal conductivity of the composite was investigated with the variation of the concentration of the filler. Additionally, the effect of the coating on the surface of the particles was studied as a potential oxidation protection layer. In the case of the copper nanoparticles, an arc discharge process was used to produce graphene-coated copper nanoparticles as fillers for nanofluids applications. Three kinds of Graphene coated Copper Nanoparticles (G-CuNPs) filler have been developed in this work and the properties of the resulting nanofluids were studied in terms of thermal conductivity as nanofluid heat transfer. Both functionalized and non-functionalized particles produced in this work were dispersed in water as a host fluid. The functionalization of the nanoparticles was explored in terms of oxidation of the coating and surface doping.

4.1 Graphene coating on microscopic copper powder

In electronics applications, copper offers many advantages that are closely related to its intrinsic properties. Such materials often combine high thermal and electrical properties that are comparable to the most attractive metallic materials for a fraction of their prices. From the electronics industrial perspective, copper helps to solve many issues. The microparticles of copper are for instance employed as homogenous fillers for TCA, where the thermal property of the organic matrix is largely enhanced through the use of the metallic phase. A good compromise is achieved between the physical, mechanical properties and cost. However, in the current state of the art, the use of copper as a filler comes with a certain constraint on the processing and the application. Copper be easily oxidized! And the resulting oxides can quickly hinder their contribution to the different properties solicitations and negatively affect its reliability. In microelectronics, the thermally stable oxides that form in the contact with the atmosphere of such oxidation can result in the loss of thermal/ electrical performances and difficulties in processing. Graphene, on the other hand, for the sake of repetition, combines extremely high

physical properties, chemical stability, and mechanical properties. The 2D material offers an excellent alternative for the oxide protection of metallic components.

The combination of the two materials is explored already to take the best of the two phases and proved to result in complementary of the composite material. Copper particles can be a scaffold for the good mechanical properties of the paste and the reduction of the agglomeration of the graphene while the graphene coating contributes to the electrical and thermal conductivity while insuring the protection of the metallic copper against oxidation. Many approaches have been observed to produce Graphene Coated Copper Particles (GCPs) [226]. Most of the techniques commonly used in the production of graphene coating/copper particles rely on the dispersion of graphene that is later deposited on the surface of the metallic phase. Such an approach can be relatively simple to apply but suffers from the tendency of graphene to form aggregates, where the nano dispersion effect is hindered. CVD technics, on the other hand, are based on the possibility to coat a carbon source on the surface of the copper particles and high-temperature processing that allow a better-quality coating and structure of the graphene layers around the spherical metallic substrate. The optimisation of the latter process depends on the development of recipes that allow fast processing and lower energy consumption. In contrast to the tube furnace technics, cold wall CVD allows a much shorter heating and cooling time that are critical for the production of such materials. In addition, the high capacity and efficiency of the cold wall furnaces have the potential to increase the industrial production of such materials.

In the following section, we demonstrate the potential of cold wall CVD to grow graphene coating on the surface of copper powders. Different growth parameters were observed, and the structure of the graphene is characterized to correlate it with the production process. In a second step, the coated particles are mixed with an organic phase as a TCA composite. The thermal properties of the adhesive material are measured in terms of the fraction of particles load and compared to commonly used silver-based TCA.

4.1.1 Production of graphene-coated copper particles

The production of the coating was explored using a cold wall chamber-based CVD method (cf. Figure 4-1), where sodium citrate coated copper particles with a dimension between 200nm-550nm (purity of 99.9%, from Aladdin Shanghai Biological Technology Co., Ltd) were used as a catalyst. Initially, the metallic particles were deposited into the chamber and heated to a temperature of 775°C at a rate of 200°C/min in the presence of a gas mixture of hydrogen and argon. The particles were annealed for 5 minutes under the same temperature before the introduction of CH_4 for the growth of the graphene at a varied flow rate between 8 and 10sccm. After growth, the particles were let to cool down before being taken out of the reactor.

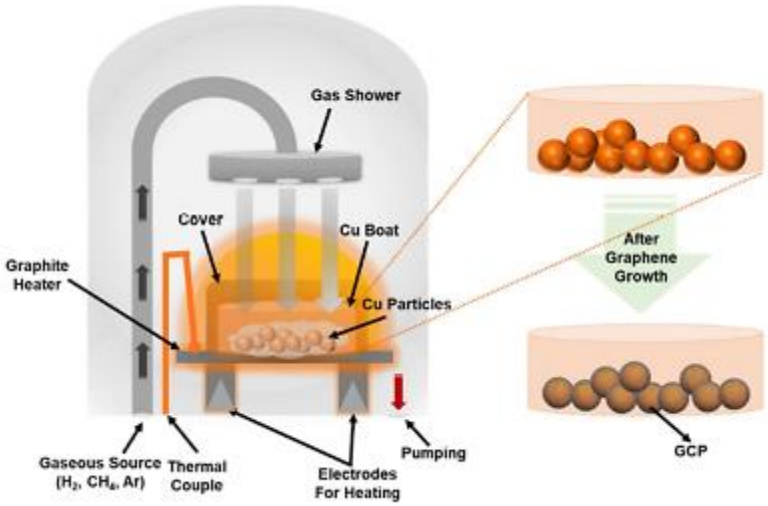

Figure 4-1: Schematic of the cold wall CVD used in the production of the GCPs.

For the fabrication of the TCA, a mixture of resin, diluent and coupling agent were prepared by shear mixing for 10 minutes. Different fractions of TCA were prepared by adding the corresponding amount of GCP additives and the curing agent to the previous mix followed by a second shear mixing and ultrasound steps for 20 and 5 minutes, respectively. Samples of 12,7mm in diameter and 2mm in thickness were prepared by curing the viscous mixture in an oven for 1h at a temperature of 150°C (cf. Figure 4-2).

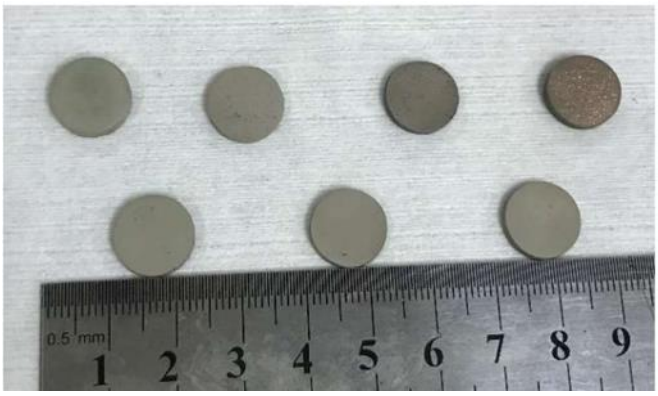

Figure 4-2: Photography image of the cured mixture in the form of palettes.

4.1.2.1 Microscopic investigation

Spherical shaped copper particles with a size variation between 200nm and 550nm can be seen in the SEM observation Figure 4-3. The particles are observed with white spots that were identified as sodium using EDX that are presented in the composition of the particles. After the graphene growth, the particles were found to maintain their original shape. The sodium citrate is believed to act as a separation layer that prevents the sintering of the particles microparticles at high temperature and prevent its deformation during the process that is important to the properties of the filler.

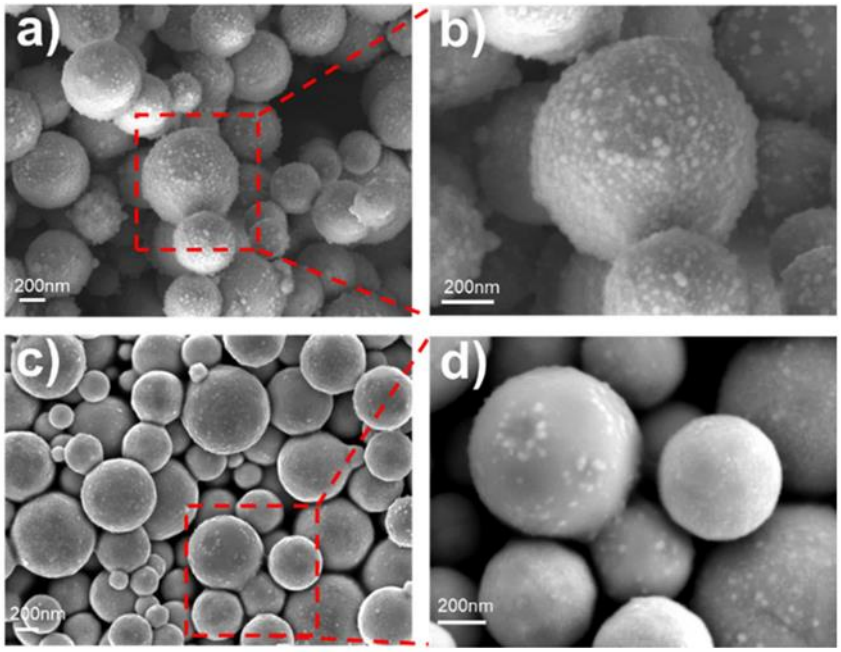

Figure 4-3: . Low-magnification and high-magnification SEM images of Cu particles before (a, b) and after (c, d) graphene growth.

The High Resolution Transmission Electron Microscopy (HR-TEM) was employed to investigate the structure of the coating around the copper particles. The observation in Figure 4.4 shows the presence of the graphitic structure with a thickness of 2nm at most and an interlayer of ~0.33nm that corresponds to the graphene interlayer. When the flow H_2/CH_4 ratio was varied, the structure of the coating was found to vary. In fact, with an increase in the ratio of H_2/CH_4 in the chamber, stacking of the graphene layer around the copper substrate was more regular than in the case of a lower ratio. HRTEM was carried out to characterize the number of layers of graphene. It can be seen that the number of graphene layers fabricated by the high H_2/CH_4 ratio is less than that of graphene layers fabricated by the low H_2/CH_4 ratio. Hydrogen not only played the role of both carrier gas and reducing reagent but also affected the speed of methane decomposition. Excessive hydrogen decreased methane decomposition and then decreased the graphene growth speed.

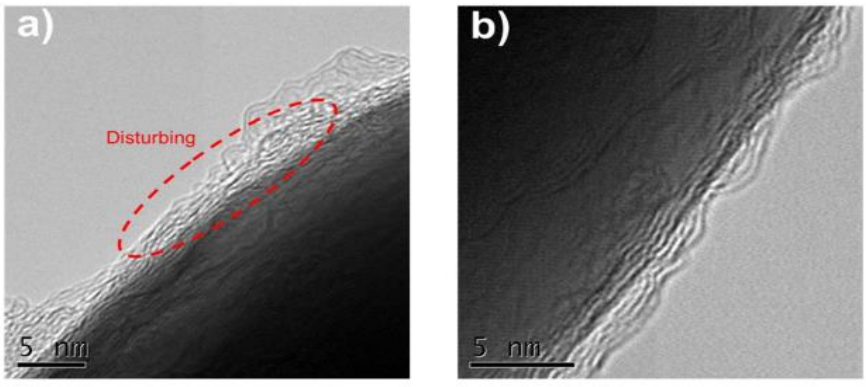

Figure 4-4: HRTEM observation of the graphene coating around the copper particles in the case of (a) low and (b) high ratio of H2/CH4

4.1.2.2 Structure and composition of the graphene coating

To investigate further the electronic structure of the coating and its quality, Raman spectroscopy was conducted on the coated powder with the variation of the H_2/CH_4 ratio during the production process. The results are shown in Figure 4-5 with the presence of D and G peaks at Raman shifts of 1360cm^{-1} and 1590cm^{-1}, respectively. The presence of the high-intensity D peak indicates the presence of defect induced peak and can be explained by the formation of distorted hexagonal sp^2 hybridized carbon atoms in graphene; strain-induced effects; and a finite flake size; the relative curvature of the of flakes around GCPs led to form stressed lattice structures within narrow domains. Most importantly, both analysed peaks show broad peaks ranging between 2300–3100cm^{-1}. Such peak represents a 2D peak is found larger than reported multilayers of graphene. The effect can be attributed to the nonplanar structure of graphene on Cu particles . The fitting of the 2D peak using Lorentz profiles confirmed the presence of D+G peaks overlapping the 2D peak. The presence of the D+G peak is generally attributed to the strained structure that might be explained in the case by the relative curvature of the multi-layer graphene.

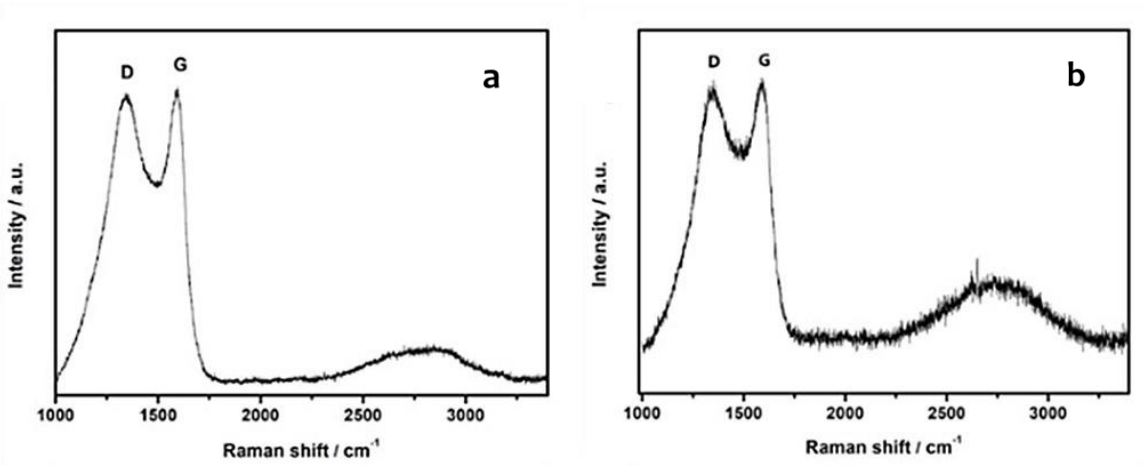

Figure 4-5: Raman spectra of GCPs synthesized by (a) low and (b) high H_2/CH_4 ratio.

4.1.2.3 Composition of the graphene-coated copper particles

The XPS analysis was run to investigate the composition of the copper particles before and after the thermal processing. The result of the analysis is presented in the Figure 4-6 and shows the comparison between the carbon peak of the pristine particles and the coated particles. In the case of the pristine particles, the presence of a peak at a binding energy of 288e.V was linked to the presence of the C=O bond and in the sodium citrate on the surface of the copper. Such peak was found to disappear after the growth as a result of the high-temperature treatment that induce the degradation of the sodium citrate and convert it into a carbon layer. It is also worth noting the presence of the two strong fingerprint narrow bands situated at around 284eV C-C/C=C bonds and indicating a significant sp^2 hybridization of graphene structure within GCPs.

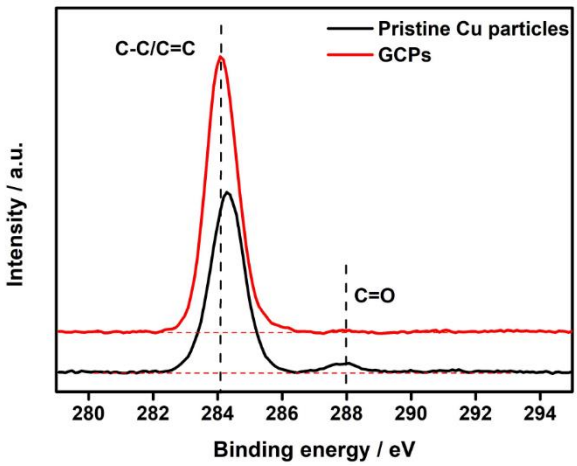

Figure 4-6: XPS spectra of C1s peak for pristine Cu particles and GCPs.

Figure 4-7 represent the elemental distributions of Cu(green), C(red) and O (light blue) within pristine Cu particles and GCPs, respectively. For pristine Cu EDX data, the exhibition of oxygen element illustrated the presence of sodium citrate and was reflected as white spots attached on the surface of the particles. Such spots were not visible after heat treatment, which indicate the conversion of the sodium citrate.

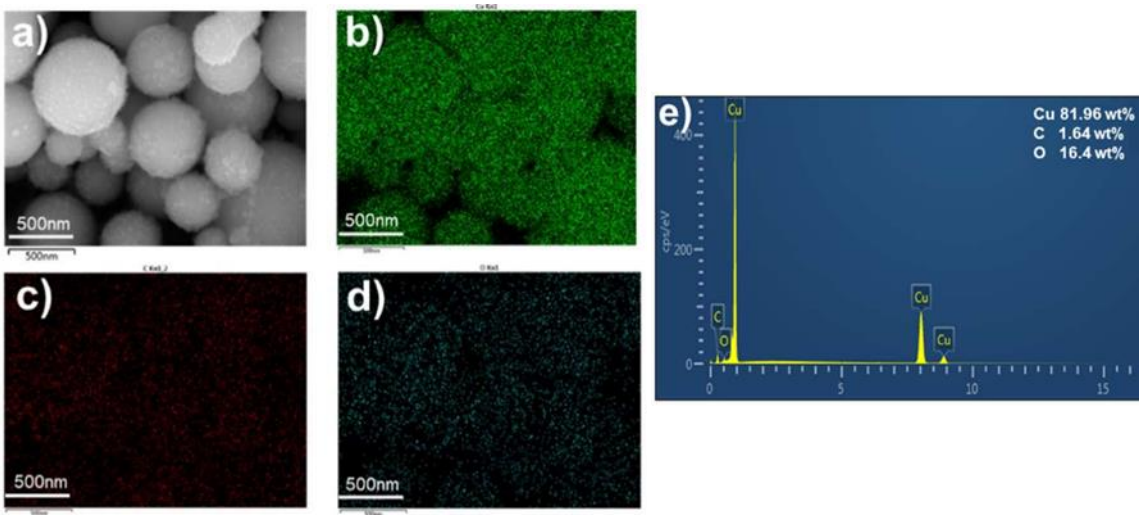

Figure 4-7: EDX profile of the copper powder after the growth showing (a) SEM of the powder, (b) copper map, (c) oxygen map, and (d) carbon map, (e) compostion diagram.

4.1.2.4 Thermal stability of the graphene-coated copper particles

The thermal stability of the GCPs was investigated at a temperature as high as 600°C and under an oxygen atmosphere to compare the degradation of pristine and coated copper particles. The results are shown in Figure 4-8. With the increase in the temperature, a slight weight loss took place and was attributed to the evaporation of the physisorbed water in the coated particles Compared to the pristine particles where the oxidation started at temperatures as low as 133°C, the coated particles showed an onset of oxidation at a temperature of 179°C. The weight of coated particles increased slowly at 179°C, rose rapidly at 253°C, and climbed moderately at 374°C. The TGA-DSC results indicate that the oxidation of GCPs by forming Cu_2O starting at about 179°C, and the combustion of graphene shells by a reaction from C to CO_2 started at 253°C. After that, Cu_2O was oxidized further to become CuO at 374°C. The shift in the oxidation temperature is assumed to be related to the presence of the coating that provides stability to particles.

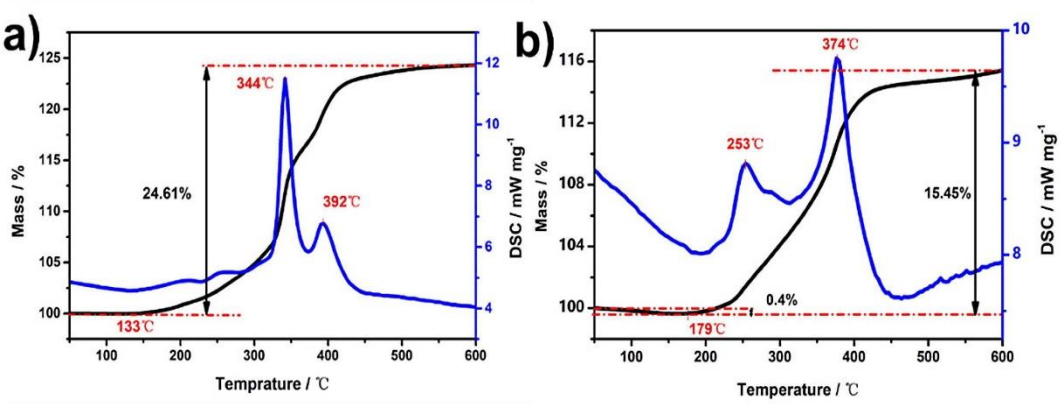

Figure 4-8: TGA-DSC curves of (a) pristine Cu particles and (b) GCPs.

The composition of the pristine and the coated copper particles were also verified using XRD. The two powders were submitted to a temperature of 150°C for 3 hours under an oxygen atmosphere. The results of the analysis are shown and compared in Figure 4-9. In addition to the copper peaks detected in the case of the coated copper particles at 43.4, 50.5 and 74.2°, the diffractogram of the pristine copper also showed a peak at a value of two thetas equal to 36.6° that is attributed to Cu_2O. The coating in the case of the GCPs acts as an oxidation protection layer. Such effect was confirmed in the long-term exposure of the GCPs to oxygen. The coated particle was left at room temperature in the air for 60 days. The diffractogram of the particles is shown in the figure and does not display any peak related to the oxides.

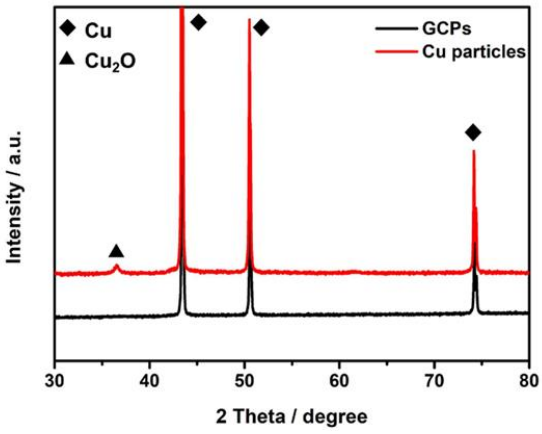

Figure 4-9: XRD patterns of pristine Cu particles and GCPs after annealing at 150 °C for 3 h.

4.1.3 Thermal properties of the graphene-coated copper particles as a thermally conductive adhesive

The thermal properties of the GCPs were evaluated as a filler for TCA. A fraction of 5wt.% of the silver NPs was replaced with GCPs and pristine copper particles and compared to the thermal conductivity of the standard 80wt.% silver-based TCA. The results of the thermal conductivity measurement are shown in Figure 4-10. In the case of GCPs, the thermal conductivity of the adhesive was found to be comparable to the values of the standard Ag-based TCA. In contrast, the thermal conductivity of the pristine copper-based TCA was around 6% lower. It is assumed that the difference in the thermal properties of the pristine copper is mainly related to the oxidation of the copper. The presence of the graphene coating around the copper particles is also assumed to contribute to the heat transfer and confers thermal stability to the encapsulated copper particles. In the second step, the thermal properties of the GCPs were evaluated with different fractions. While the fraction of the solid phase was kept constant and at a value of 85wt.%, different amounts of GCPs replaced the silver flakes. Figure 4-10.b shows the

result of the thermal conductivity measurement as the fraction of the GCPs increased from 10.wt% to 20wt.%, to 40wt.%. It can be seen that the thermal conductivity of GCP-based TCA improved significantly with the increasing proportion of GCPs to reach a value as high as 4.13W/m.K. Additionally, besides protecting Cu particles from oxidation, few-layer graphene dispersing uniformly in TCA provides low resistance for phonon path. This together with the superior thermal properties of graphene compared to Cu and Ag effectively improves the thermal conductivity.

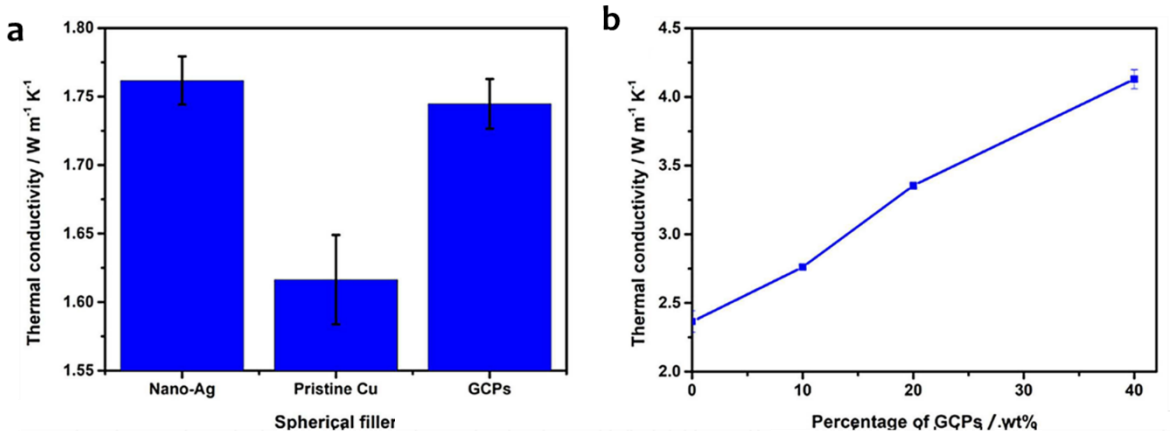

Figure 4-10: (a) The effect of different spherical particles on thermal conductivity in TCA, (b) The influence of weight distribution percentage of GCPs on thermal conductivity.

4.2 Graphene Coating On Copper Nanoparticles For Nanofluids

Advanced thermal management using fluidic technics have shown promising results in the cooling of electronics systems. The nanofluidic medium more specifically allows surpassing the limitations of physical properties of the host fluid by the integration of a nanoscale solid phase. Such dynamic composite material allows the enhancement of the thermal capability of the nanofluids through different complex mechanisms enumerated in chapter 2. The presence of these nanoscale particles in the fluid induces a large effect on the properties of the fluid including density, specific heat, viscosity, and the thermal conductivity that lies at the centre of the thermal transport improvement. With the present extremely good physical properties, the 2D material of graphene raised interest in its use in modern cooling solutions in electronics. The nanofiller solid thermal properties are among the best and its presence within the fluid can be expected to benefit highly from the phonon transport that takes place in the in-plane direction. Comparatively to other metallic nanoparticles, graphene materials present combined superior thermal conductivity, higher chemical stability [230], and lower erosion effect [231], [232]. In polar solvents, an increase in the thermal conductivity reached up to 48% as a result of a long-range ordering of the molecules along with the stable graphene sheets [233], [234]. However, it can never be mentioned enough, graphene is highly sensitive to its environment, and it was reported that the graphene sheet in-plane thermal transport was key for efficient heat dissipation. Such effect was closely related to the orientation of the graphene sheets to the heat flux with the maximum efficiency at angles parallel to the heat flux that allows the in-plan propagation to take place [235] (cf. Figure 1. a). In addition, sheet curvature was found to also play a major role in heat transfer efficiency. The effect of wrinkles was found to induce complex graphene/host fluid interface and an intrinsic change in the graphene sheet that acts as a modulator [236]. Wrinkles resulted in a decrease of up to 35 % of the thermal conductivity of sheet graphene [237]. In a realistic situation and without the use of any external force, graphene sheets move within the liquid and take random orientations with possible folding that reduces their contribution in the heat transfer process (cf. Figure 4-11).

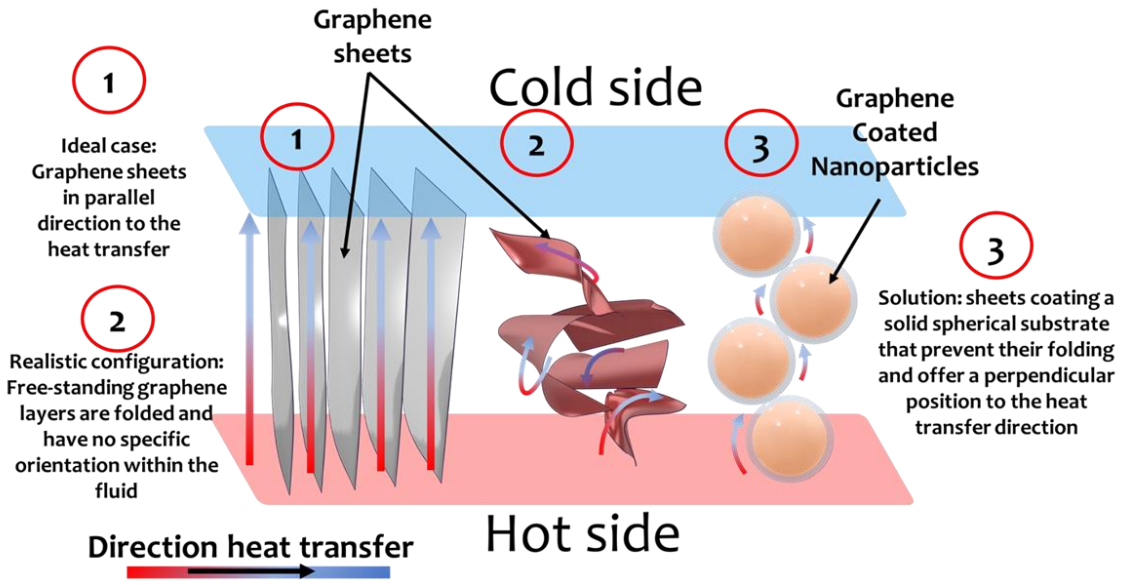

Figure 4-11: Schematic representation of the orientation of the graphene sheets in the host fluid.

In this section, we investigate the properties of graphene-coated copper nanoparticles. The products have been developed as nanofillers for thermal management applications. In an attempt to combine the size effect of low scale nanoparticles with the high surface the graphene has high physical, chemical, and mechanical properties.

4.2.1 Graphene coated nanoparticles

Due to the limited intrinsic thermal conductivity of the nanoparticles and their challenges with chemical stability and physical properties, effort into exploring new materials and their combinations led to hybrid solutions and encapsulated nanofillers for further enhancement of the properties the Heat Transfer Fluids (HTFs). Hybrid nanofluids composed of metallic and non-metallic nanoparticles such as Cu-Al_2O_3 [238], [239] and Ag-MgO [240] were studied. While the pure metallic nanofillers exhibit high thermal conductivity, the oxides particles show better stability. In addition, those hybrid mixtures often increase the thermal transport properties that can be related to the high aspect ratio, an increase in the thermal network, and the synergistic effect between the nanomaterials [241]. The combination of graphene and metal particles showed that the large surface area 2D sheet allows a low percolation threshold while the presence of the metallic particles contributes to the enhancement of the heat transfer [242], [243]. Carbon Nanotubes (CNTs)-Al_2O_3 [244], and hybrid sphere/CNTs NFs [245] have been formulated and showed that the combination of the CNTs and the NPs induced an improvement of 20 % in the thermal conductivity at 0.1% loading, in addition to the reduction in the thermal contact resistance of the CNTs with the presence of the second additive. Nano-encapsulated particles have also been explored as an advanced type of NFs. Cu and Ag were encapsulated in CNTs and showed better thermophysical properties than in the case of functionalized CNTs with good stability in both water and ethylene glycol (EG), and a thermal conductivity enhancement ratio close to 1.5 for Ag-CNTs in EG at 0.5 wt.% [246].

4.2.1.1 Production of graphene-coated nanoparticles

The mechanism of production of Graphene-Coated Copper Nanoparticles (G-CuNPs) can be similar to the case of carbon nanotubes using the plasma method. In the case of nanotubes, a metal is used as a catalytic liquid alloy phase that adsorbs the vapour to its supersaturation and results in the nucleation of the carbon shell at the interface liquid-solid interface. During the plasma event in the arc discharge, such a mechanism can be observed when the electrode material is evaporated at a high temperature. The high concentration column is then quenched, and the metal catalyst forms particles rich with carbon. Upon cooling, the solubility of carbon decreases and the latter segregate at the surface of the catalyst. and the metal catalyst arc induces a diffusion process associated with a fast quenching of gas species. As presented in Figure 4-12, by adjusting the composition of the arc discharge chamber, the carbon structure and composition can be varied.

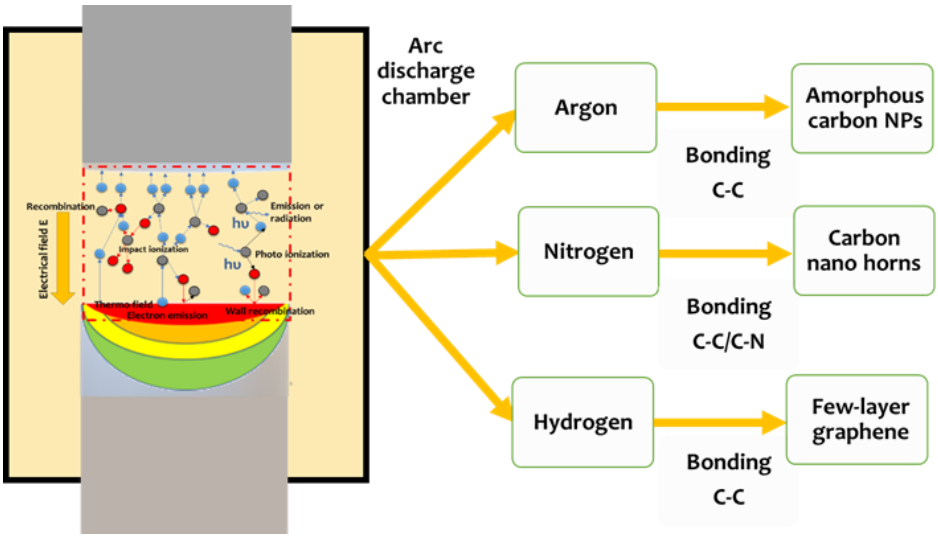

Figure 4-12: Production of different carbon structures by tuning the composition of the arc environment. Adopted from [204].

4.2.1.2 Morphology of the graphene-coated copper nanoparticles

The size distribution of the nanoparticles includes a large range of particles size starting from a few nanometres up to over 100nm. To observe the coating around the particles, a large particle of over 100nm was presented in

Figure 4-13. and appears with a core-shell structure where the metallic copper core is seen covered with a continuous coating. A higher resolution observation is also presented and shows the coating as a layered structure covering the NP facets. Due to the aggregation of the nanoparticles, smaller dimensions of particles were difficult to distinguish individually. The graphene-coated copper nanoparticles were found to exhibit a spheroidal to spherical morphology. All the observed particles showed a multilayer structured coating on their surface with a layer that reached 15 layers at most. The nanoparticles were analysed with SPM to reveal their surface topology. A scan resolution of 512x512um^2 was achieved for a surface of 1x1um^2. Data acquisition was then followed by an image processing procedure. First, a three-point flattening was applied to correct the tilt resulting from the tip-substrate interaction. A 2D surface mapping of the surface topography of the sample is shown in Figure 4-13.d. The image processing was followed later with data analysis by performing a particle analysis using Nanoscope analysis 1.5. The grains were marked using a height threshold of 0.1nm. The selected grains were allowed later to determine the size distribution of the NPs. Results showed a size distribution with an average size of 57.5nm and a maximum of 87,27nm.

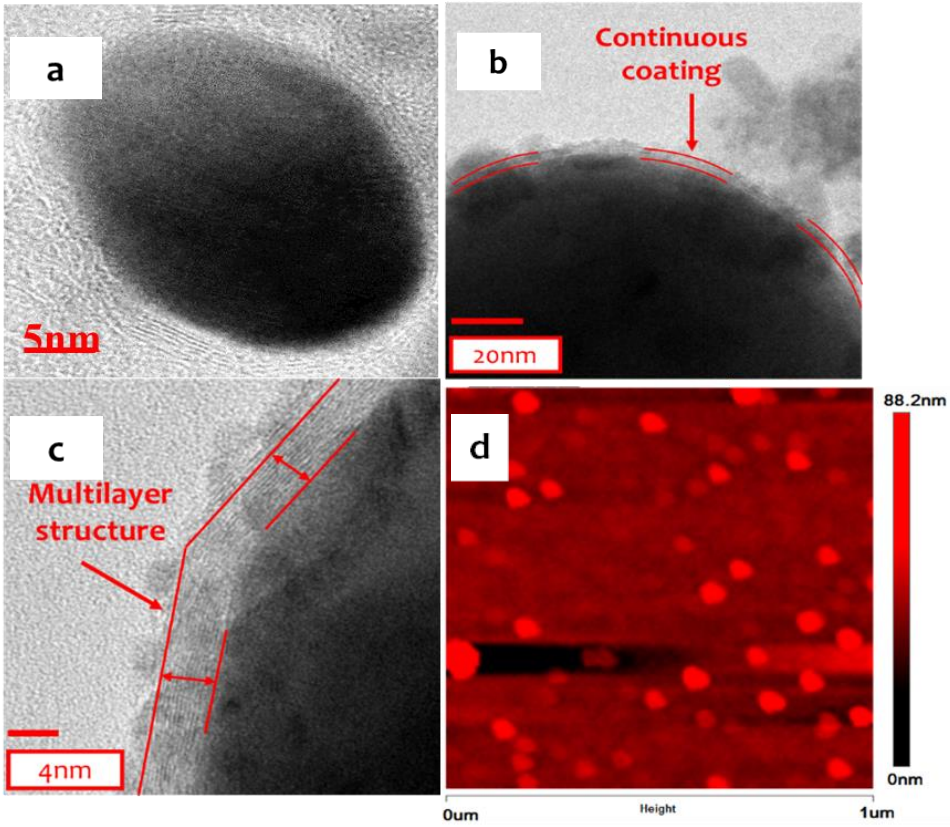

Figure 4-13: TEM observations of the G-CuNPs showing (a) a copper core coated with a multilayer graphitic structure (b) continuous coating around the particle, and (c) high resolution showing multilayer structure. (d) SPM height mapping of the coated NPs.

4.2.1.3 Structure and composition of the graphene-coated copper nanoparticles

To confirm the origin of the coating, the nanoparticles were centrifuged and dried at 80°C on a hot plate and then pressed into small platelet on carbon adhesive before being loaded into the XPS instrument. The collected signal was generated from a 10um spot and offers a good representation of the powders. The analysis of the chemical composition of the nanopowder is shown in Figure 4.14. The results of the XPS analysis confirm the nature of the graphitic coating that surrounds the copper core. An asymmetric carbon peak typical of graphene composition was observed cantered at 284.8eV (cf. Figure 4-14.a) and was deconvoluted into 7 component peaks.

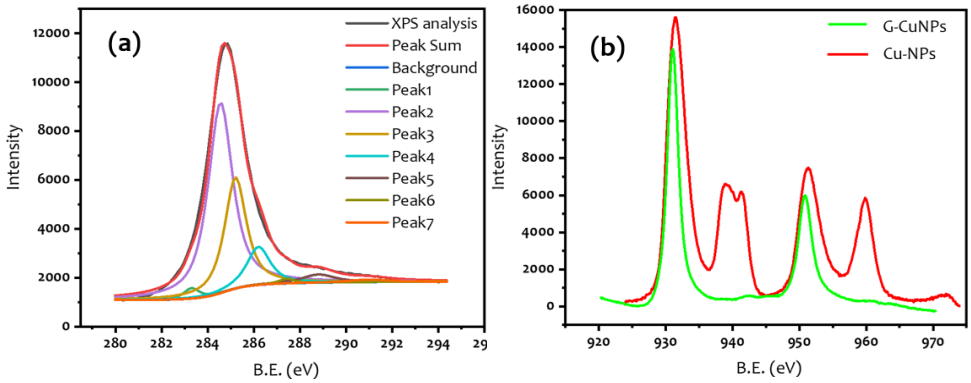

Figure 4-14: XPS analysis showing (a) the asymmetric carbon peak and (b) the copper peak comparison of G-CuNPs and CuNPs.

At relatively low binding energy, the peak at 283.3eV was assigned to the metal carbide presence resulting from the copper-carbon bond and indicating the probable diffusion of carbon into the copper matrix. The peak at 284.5eV was assigned to the main graphene compound as sp^2 bond, while the peak at 285.2eV was attributed to the graphitic defect sp^3 in the graphene lattice [247]. At higher energy bond, the peaks at 286.2, 287,3, 288.8 and 290.5eV are assumed to represent the C-O bond, the C=O bond, the O-C=O bond and the shake-up satellite peak π-π^* present in the coating, respectively [248], [249]. Table 4-1 summarizes the peaks ids and their respective binding energy for the deconvoluted carbon peak.

The coated and non-coated copper nanoparticles were analysed and compared to investigate the effect of oxidation protection of the graphene coating. The results are presented in figure 4-14.b. In the case of the G-CuNPs, no shake-up satellite peaks were detected in contrast to the non-coated NPs. The presence of the shake-satellites is a sign of the presence of oxides [250]. It can be assumed that the graphene coating around the copper NP offers an additional effect that is reported as oxidation protection that is in line with previous reports on graphene acting as an oxygen diffusion barrier [251]. It is worth noting that the possible deviation from the energy values for each bond reported here can be related to the combined effect of the dimensions of the nanoparticles, their surface curvatures, and the presence of the interaction between the coating and the substrate.

Table 4-1: XPS peak deconvolution of the carbon peak.

PEAKS POSITION (EV)	IDENTIFICATION
283.3	Copper carbides
284.5	sp^2 carbon, main lattice
285.2	sp^3 carbon, amorphous carbon/defects
286.2	C-O
287,3	C=O
288.8	O-C=O
290.5	π-π^*

Raman spectroscopy was used to describe the electronic structure of the coating. The results of the analysis of the G-CuNPs are shown in Figure 4-15. The detected peaks correspond to the D band (disordered mode) at 1318cm^{-1}, the G band (graphitic mode) at 1575cm^{-1} and the 2D band (D overtone disorder mode) at 2641cm^{-1},

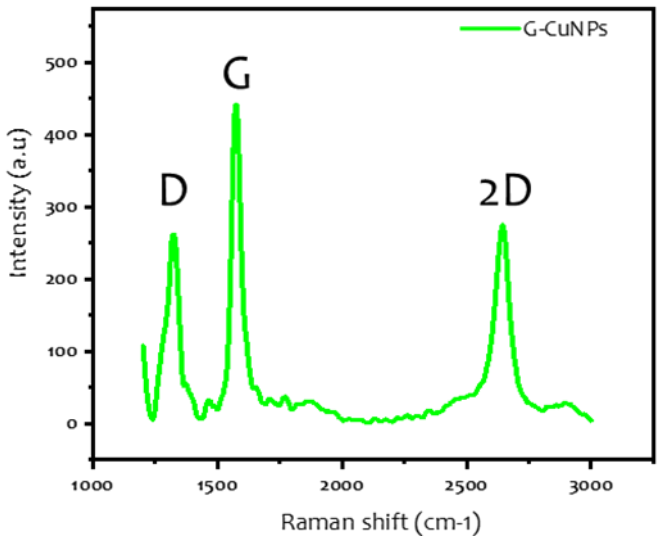

Figure 4-15: Raman analysis of G-CuNPs showing three different peaks indicating a disordered multilayer graphene structure.

respectively. While the ratio of the amplitudes of the 2D to the G bands confirms the presence of multi-layered graphene structure, the appearance of the D band indicates the presence of a disorder within the graphitic coating. As mentioned above in the case of the graphene-coated microscopic powder, the D peak is disorder-induced might originate from either small crystallite sizes, missing atoms, a high number of edges, lattice distortion, adsorbed molecules or the influence of the substrate and their combination, which directly affect the electron mobility in the structure [252]. Such results might also confirm the reasons for the reported shift in the XPS measurements.

4.2.1.4 Thermal stability of the graphene coating

The analysis of the TGA for the G-CuNPs powder and a mixture of nanopowder and microscopic copper powder were run under different gas atmospheres. The results are shown in Figure 4-15. Under nitrogen gas, the microscopic copper powder does not show any distinguishable weight loss until it reaches a temperature of 700°C

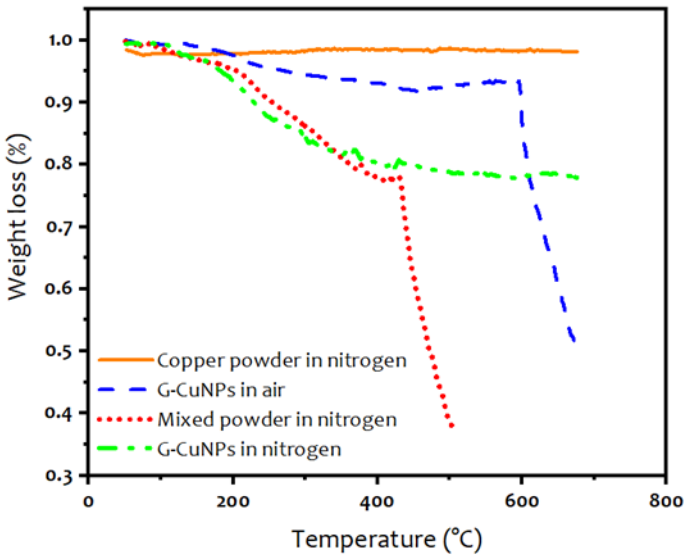

Figure 4-16: TGA analysis of G-CuNPS and mixed G-CuNPs with micro copper powder under air and nitrogen.

In contrast, the G-CuNPs in the nitrogen atmosphere displays a continuous weight loss in two steps. The first weight loss at around 100°C and is presumably linked to the evaporation of the adsorbed water followed by a slow 25% mass loss linked to the decomposition of the oxygen-containing functional groups [253]. Similar behaviour to the analysis of G-CuNPs under nitrogen is observed in the case of air atmosphere, with the water evaporation and the initial reduction of the oxygen group before a short stabilization at around 400°C. The G-CuNPs powder displays a further and fast weight loss starting at 430°C. The large weight loss is assumed to be related to the degradation of the graphitic structure through the oxidation of the carbon [254]. Due to the limitation on the setup, the analysis under air atmosphere was stopped at 500°C which corresponds to 65% mass loss, and before the complete degradation of the multilayer, graphene coating was reached. A mixture of 30 wt.% G-CuNPs and 70 wt.% of microscopic powder was prepared and was analysed under a nitrogen atmosphere. The profile of the weight loss is seen with the initial continuous degradation of carbon and the evaporation of the water before reaching a plateau at around 450°C and 7% mass loss. The increase of the temperature above 450°C does not affect the degradation of the powder until a temperature of 600°C. A fast weight loss takes place similar to the case of the previous case of the carbon combustion in the case of G-CuNPs under air atmosphere. This weight loss is attributed to the reduction of the copper oxides that originates from the microscopic powder. The copper oxides on the surface of the copper powder are stable in the presence of the graphitic structure and it is assumed that a reduction of those oxides starts at high temperature (i.e., above 600°C), where the carbon can adsorb into the surface of copper oxide and contributes to the reduction of surface oxides [255].

The DSC analysis of the G-CuNPs is presented in Figure 4-17. The powder was subjected to three cycles of heating up to a temperature of 500°C under argon gas. During the first cycle, an endothermic peak was observed at a temperature of 155°C. The second and third cycles of the DSC show no obvious peak at the same range of temperatures. The large endothermic peak at 155°C can be explained by the possible melting of the low size particles of copper and is related to the size effect of the particles. As discussed in chapter one, despite the presence of a high melting point shell around the metallic core, a melting depression can still occur when the condition on the interface between the graphene coating and the metallic core allows it. The melting of the NPs at low temperatures is also in line with the previously reported results of the oxidation-free metallic NPs [256]. The multilayer graphene coating preserves the metallic structure of the copper core that allows an early melting at low

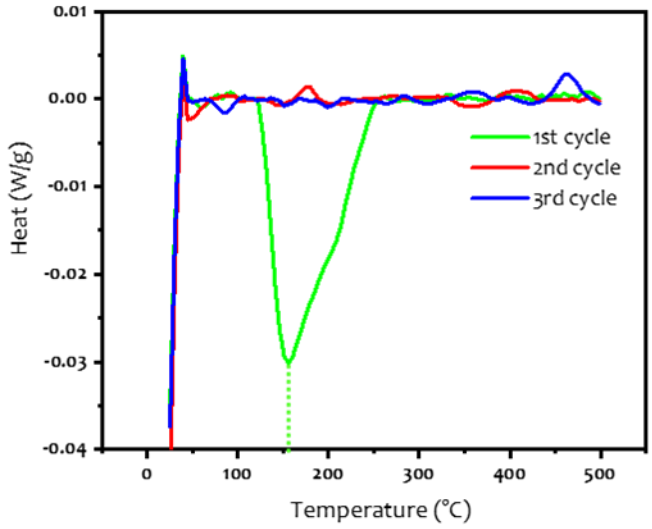

Figure 4-17: DSC analysis of the G-CuNPs of a powder heated for three cycles.

temperature. The explanation for the disappearance of the endothermic peak in the second and third cycles can be linked to a possible change in the size of the particles after the first melting. During the first cycle, it is possible that the multilayers graphene structure collapses and leads to the leakage of the liquid phase of the metallic copper outside the graphitic shell. This results in the coalescence of the metastable phase that solidifies in larger sizes.

4.2.1.5 Local mechanical properties of the graphene-coated copper nanoparticles

To understand the potential effect of the multilayer graphene coating on the metallic core, qualitative and quantitative SPM measurements were realized using peak force quantitative Nanomechanics (QNM) modes. The results are shown in Figure 4.18. The energy dissipation mapping of the G-CuNPs is compared to CuNPs (cf. Figure 4.18.a and b). The colour scale is presented only for quantitative comparison and no values can be directly exploited. In the case of the G-CuNPs, a contrast between the core of the particles and their surfaces is visible. The surface of the particle can be distinguished with a light brown colour, while the centre of the particle that corresponds to the core is shown with a dark colour. Such effect is directly linked to the presence of the coating on the surface of the NPs that present a different mechanical behaviour. The G-CuNPs presented in this work and produced through the process of arc discharge, showed a structure that fits well around the shape of the NPs. In the case of the two-steps graphene coating process on the surface of NPs [257], thermal annealing is usually required to generate compressive stress around the particles. Such step modify the rippling of the graphene sheet around its substrate and affect the structure of the graphene. In the case of the non-coated NPs, the energy dissipation mapping shows a well-defined dark region with no contrast between the core and the surface of the particle indicating the same mechanical properties all over the area of the NP. Such results indicate an additional effect of the coating around the particles. The presence of the multi-layer graphene coating offers a different mechanical behaviour to the surface of the particles that can be utilised in lubrication applications. The sliding between the graphene layers has been reported to efficiently reduce surface friction and wear [258]. In the case of spherical particles, the curvature of the surface can be exploited to further reduce the friction.

QNM measurements were made to investigate and compare further the mechanical properties of the coated NPs and the non-coated NPs. Figure 4-18.c shows a comparison of the approach-withdraw curves in three different positions identified as P_1, P_2 and P_3 with an inset of the contact region between the tip and the NPs. The point P_1 is located on the edge of the G-CuNP, and the points P_2 and P_3 are centred on the G-CuNP and CuNP, respectively. While the peak force in the case of P_1 and P_2 show almost identical profiles, a slight difference in the deformation value is noticed. Despite the ductility of the graphitic coating, the deformation in the case of P_1 is lower compared to the case of P_2 and might be related to the shape factor of the small coated spherical particle. The spherical shape of the NP makes it harder for the SPM tip to make a similar approach on the centre and edge of the spherical particle. However, due to the ductility of the coating, it is still possible to detect a difference in the mechanical response of the G-CuNPs surface compared to the Cu-NP. While the mechanical deformation of the graphene is reported highest when the sheet is suspended as a membrane [259], the result reported here still shows a possible advantage in using such structured coated particles for friction reduction and increase powder flow. Finally, compared to the Cu-NPs, higher dissipation energy in the case of the G-CuNPs can be deduced from the force-displacement curve. Such remark might be directly linked to the deformation of the coating and the 3D electronic cloud that steams from the surface of the coating.

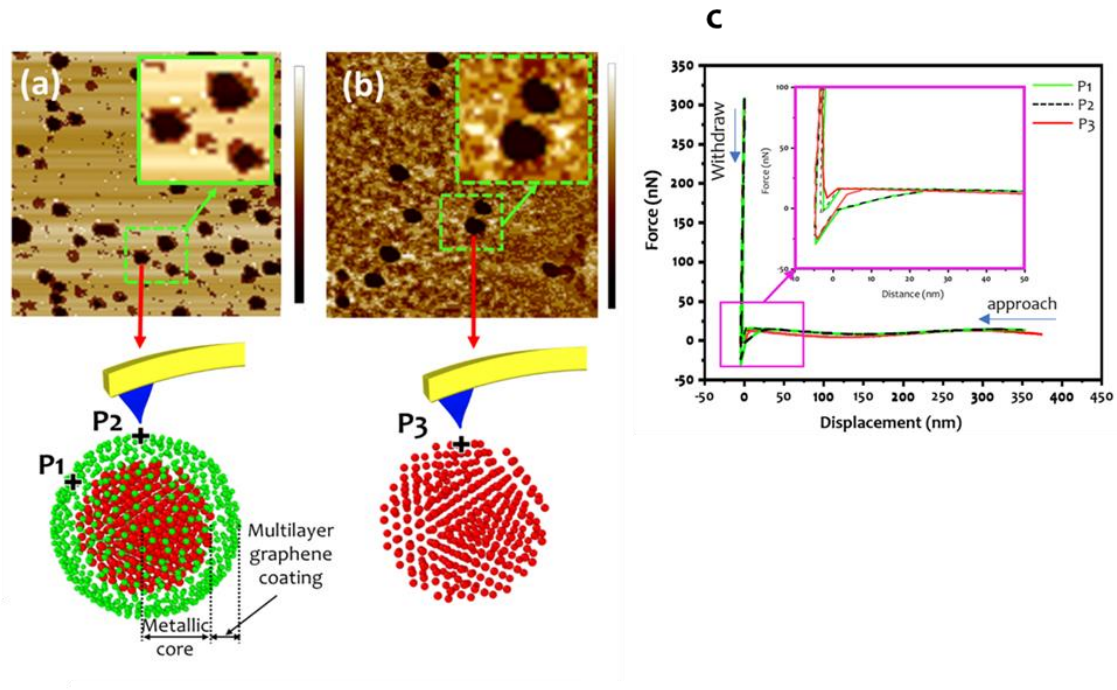

Figure 4-18: SPM qualitative dissipation energy in tapping mode of (a) G-CuNPs and (b) Cu-NPs. (c) Force-distance curve of peak force measurement comparing G-CuNPs and Cu-NPs in P1, P2, and P3.

4.2.2. Functionalization of graphene-coated copper nanoparticles

Carbon nanomaterials require further effort in developing practical solutions that lead to further improvement of the thermal capabilities of the HTFs. Due to the Van der Waals interactions and cohesive forces between the carbon atoms, their low stability makes it challenging to obtain homogenous dispersion for a long time [260], [261]. Such limitation led to the development of stabilization approaches based on the surface modification of graphene. The modification of the electronic properties of graphene sheets can be produced through chemical functionalisation of the sheet or a chemical doping. Commonly used, oxygen groups fixation on graphene sheets resulted in an increase of the thermal conductivity up to 77% in paraffin [262], and 61% in the case of ethylene glycol [263] at 5vol.% concentration. In water, the thermal conductivity improvement was reported up to 30% at 0.02wt.% and a temperature of 70ºC [264]. The integration of dopant atoms within the carbon lattice has led to the possibility to tailor the electronic bandgap of graphene sheets [265]. Nitrogen atoms were introduced within the graphene structure and resulted in the modification of the electrical properties of the graphene through the doping effect leading to higher capacitance values [266]. The use of nitrogen-doped graphene (NG) as an additive for water-based fluids was reported to affect the electrical double layer around the particles [267]. The thermal performances of the NG sheets were also evaluated, and the results showed improvement of the thermal performances up to a 37% increase in the thermal conductivity at a concentration of 0.06wt.% at 40ºC [268].

However, due to the short stability of the graphene in water, such nanofluidic systems required additional effort to optimize their properties further. In this work, we explore the possibility to introduce the concept of surface modification and doping to the G-CuNPs nanofillers. Graphene oxide coated copper nanoparticles (GO-CuNPs) and atomic covalent functionalization of graphene as nitrogen-doped graphene-coated copper nanoparticles (NG-CuNPs) are investigated as nanofillers for water-based solutions. The correlation between the thermal conductivity of the NFs with the concentration of two types of nanofillers and the temperature is investigated.

4.2.2.1 Surface modification using oxygen groups on the graphene coating

The production of graphene oxide coated copper nanoparticles nanofluids Graphene-coated NPs were using a two-step method. G-CuNPs were first produced using the arc discharge method. In a second step, The initial G-

CuNPs were oxidized in a mixture of sulfuric acid (H_2SO_4, 98 wt.%, from BASF) and nitrile acid (HNO_3, 70%, from MERK) in a 3:1 volume ratio [269]. The dispersion was stirred at 60°C overnight. The strong acidic solution reacts with the graphene materials and induces its oxidation. Concentrations of 0.01, 0.02, 0.05 and 0.10wt.% of graphene-coated copper nanoparticles were prepared. The nanoparticles were dispersed to their respective concentrations into DI water and sonicated for 10min before each measurement. The solutions were later diluted further for analysis in TEM, SPM.

a) Morphology of the Graphene oxide coated copper nanoparticles

The TEM analysis was carried out to investigate the morphology and the presence of the coating on the GO-CuNPs. The GO-CuNPs was observed with core-shell structures with a contrasting thin coating around the NPs (cf. Figure 4-19.a). Such coating is seen as a non-structured semi-transparent layer covering the solid core, which can be explained by the modification of the original carbon coating through the chemical fixation of the oxygen groups. The functional groups lead to the destruction of the graphitic layering and result in instability of the sheets under a high energy beam [270]. It is also worth mentioning that the GO-CuNP also shows a relative detachment of the coating from its core, which can be related to the fracture of the shell structure and its possible exfoliation from the core of the NP.

The size of the GO-coated copper nanoparticles was mapped with SPM and are presented in Figure 4-19.b. The average size of the GO-CuNPs were found to be 14.7nm and the density of the GO-CuNPs was found to be 8.06g/cm^3. This value of density might be indicating a thin coating of the copper particles. The SEM observation in Figure 4-19.c shows a large graphene oxide coated copper particle with a contrasting surface. The difference in the contrast indicates a difference in the thickness of the coating and can be explained by the exfoliation of the graphene sheets as a result of the penetration of the acid through the coating. The latter exfoliation can induce the detachment of the layers from the surface of the coating and reduce the thickness of the coating. Such observation can also be valid for smaller particles and indicates that the coating size can be affected by the oxidation process.

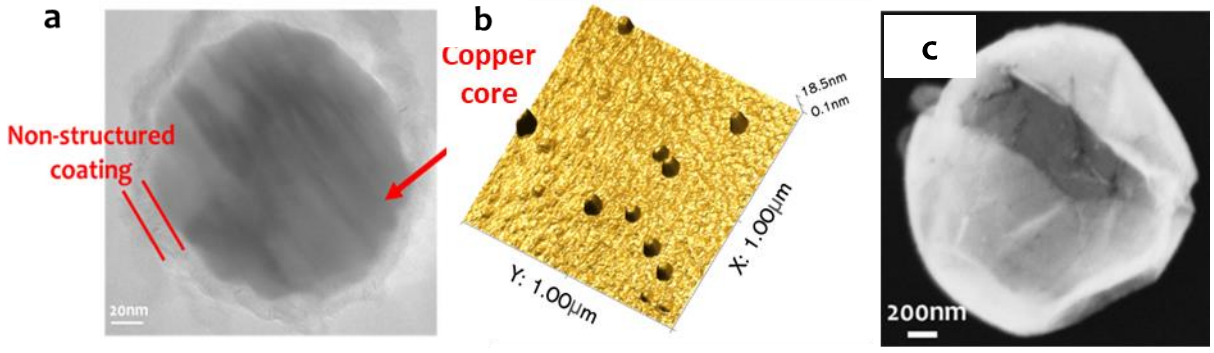

Figure 4-19: Morphology investigation of the NPs showing: (a) TEM image of GO-CuNPs with the destroyed coating, (b) SPM height map of the GO-CuNPs, (c) SEM observation of the exfoliated graphene coating around the copper core.

b) Structure and composition of the graphene oxide coating

The FTIR analysis was performed to identify the functional groups in the case of the GO coating. The result of the analysis is presented in Figure 4-20. In the case of GO coating, a broad and strong peak at 3287cm^{-1} is attributed to the presence of the O-H bond. Single bond C-O is also visible at wavenumbers of 2887cm^{-1} and 2985cm^{-1}. Carboxyl groups (O=C-OH) presence could be identified by the peaks C–OH, C=O and C-O vibrations at high and low wavenumbers of the hydroxyl group at 3287cm^{-1}, the ketonic group at 1637cm^{-1} and the monoxide group at 1064cm^{-1}, respectively. In the planar direction, the peaks at 1451 cm^{-1} can be attributed to the C=C bond.

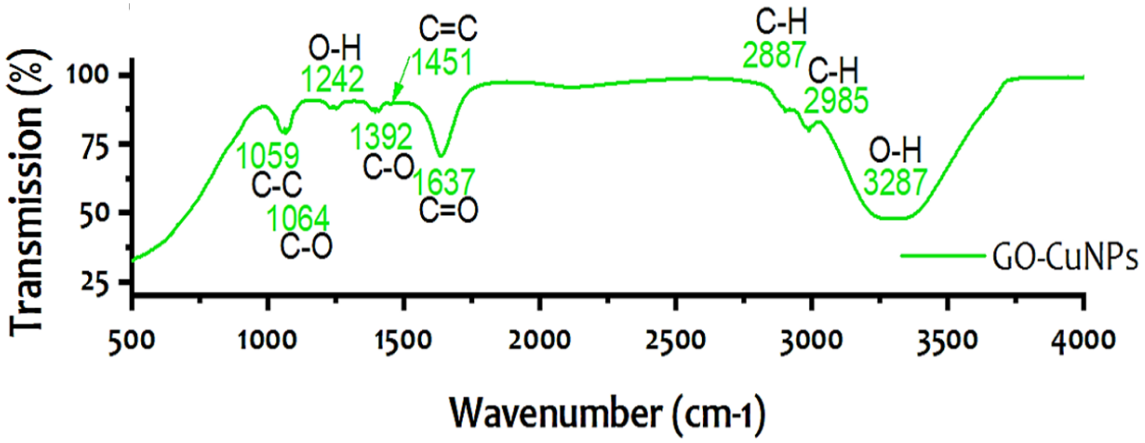

Figure 4-20: FTIR analysis comparing the functional groups present in the GO-CuNPs.

XPS analysis results for the GO-CuNPs are presented in Figure 4-21. In the case of the GO coating, the graphitic carbon atom is centred at 284.0eV (cf. Figure 4-21.a) and is deconvoluted primarily into the sp_2 and sp_3 peaks as Peak2 and Peak3, respectively. Other peaks that can be noticed are labelled as peaks 4-6 and are attributed to the C=C, C-O and C=O bonds, respectively [271]. Weak peaks detected at 283.06eV in the case of GO-CuNPs is assigned to the metal-carbide bond involving copper atoms from the core of the NP. The values of the deconvoluted peaks are summarized in Table 4-2.

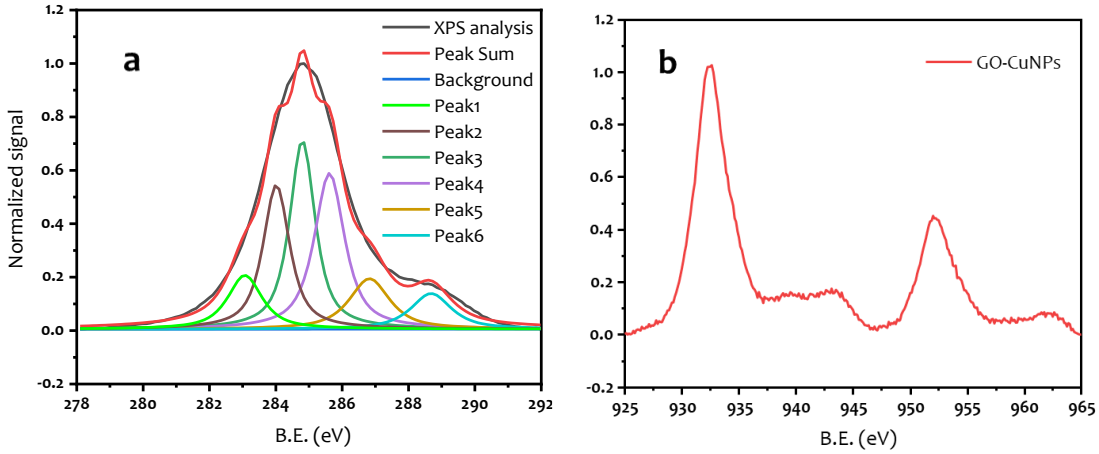

Figure 4-21: XPS analysis showing (a) carbon peak, (b) copper peak in the case of GO-CuNPs.

The XPS analysis result of the copper 2p peak is shown in Figure 4-21.b. In the case of the GO-CuNPs, the copper peak is observed with a broad main peak at around 932eV which corresponds to the $Cu_2P_{3/2}$. The strong shakeups satellites at higher binding energy confirm the nature of the copper core as Cu (II) and indicate the oxidation of the metallic copper core. In this case, it is possible to consider the destruction of the multi-layered graphene coating through its potential fracture and defects formation because of the oxidation of the metallic core. However, the correlation between the XPS results of density measurement reported in this work might indicate that the particle's core is not completely oxidized since the value of the density of the solid phase (i.e., 8.01g/cm^3) is in-between the values of densities of copper and copper oxides. In the bulk material, the Cu_2O that form as a result of the oxidation of copper acts as a diffusion barrier against further propagation of the oxides and such an effect might be occurring at the nanoscale level.

Table 4-2: Details of the deconvoluted XPS peaks in the case of GO-CuNPs

		Peak1	Peak2	Peak3	Peak4	Peak5	Peak6
Carbon Peak	Position (e.V)	283.06	284.07	284.78	285.60	286.80	288.60
	FWHM	1.29	0.93	0.94	1.09	1.35	1.50

4.2.2.2 Nitrogen doping of the graphene coating

Doping graphene with heteroatoms modifies the electrostatic properties of the 2D materials. The integration of the foreign atoms such in the case of nitrogen creates a bandgap in the electronic structure of the graphene and acts as p-type doping. Compared to the fixation of oxygen groups on the surface of graphene, the modification of the surface composition with heteroatoms prevent the degradation the physical and mechanical properties of the graphene and might be even better [272]. Nitrogen-doped graphene-coated copper nanoparticles (NG-CuNPs) have been produced in this work using arc discharge method by saturation of the chamber atmosphere with carbon and nitrogen as a one-step production method.

a) Morphology of the Graphene oxide coated copper nanoparticles

The presence and the morphology of the NG-CuNPs were observed using TEM. Figure 4-22.a show the NG-CuNP with a multilayer coating on the surface of the particle. In contrast to the GO-CuNP, the Nitrogen-doped coating appears with an ordered graphitic structure that surrounds the particle. Using SPM analysis (cf. Figure 4-22), the average size of the particles was found to be slightly higher than in the case of the GO coated NPs and with a value of 17.7nm. The density of the NG-CuNPs was also measured and found to be as low as 5.01g/ cm^3. Such differences in the values of the densities can be directly linked to the nature of the materials in each nanofiller but also the complex physicochemical phenomena taking place during the production processes. In the nitrogen coating, such low density might indicate a larger thickness coating around the particles or the presence of graphitic structures other than that of the coated particle.

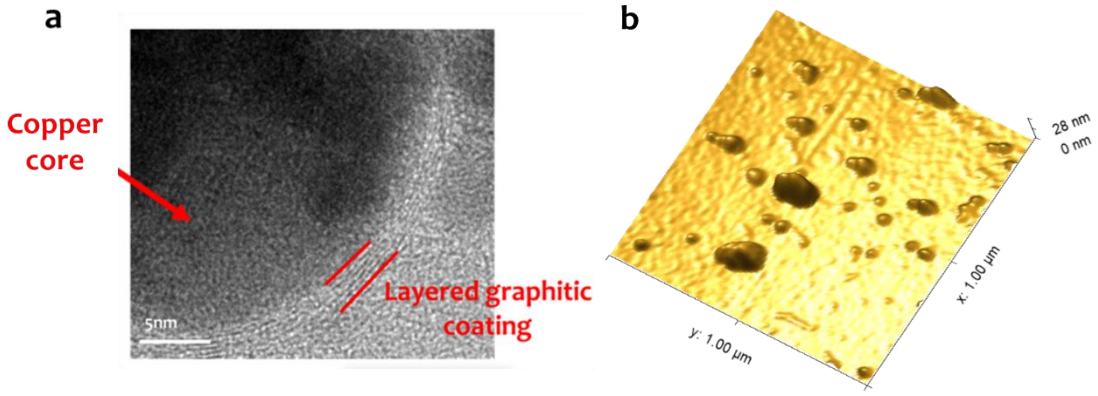

Figure 4-22: Morphology investigation of the NPs showing: (a) TEM image of GO-CuNPs with the destroyed coating, (b) SPM height map of the NG-CuNPs.

b) Structure and composition of the nitrogen-doped graphene coating

Similarly to the case of GO coating, FTIR analysis was performed to identify the functional groups in the case of the NG coating. The results of the analysis are presented in Figure 4-23. The FTIR result in the case of the NG-CuNPs shows the presence of peaks related to nitrogen bonds. In addition to carbon peaks including C-H, C=O, C-O and C-C, broad and medium intensity peak is formed at high wavenumbers. This peak has a higher probability to be associated with N-H stretching vibrations at 3329cm^{-1} that replaces the O-H vibrations. The C–N stretching in benzenoid rings is identified at a peak value of 1385cm^{-1}. Similarly, a peak at 1655cm^{-1} could be related to the C=N bond.

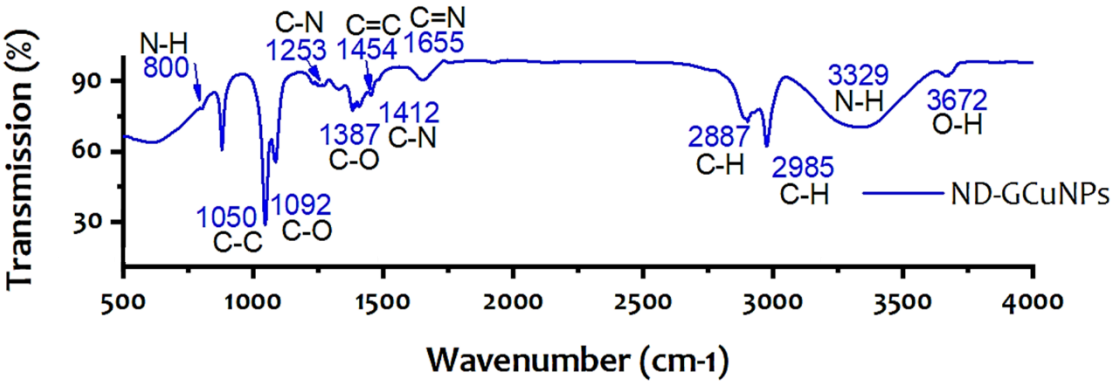

Figure 4-23: FTIR analysis comparing the functional groups present in the NG-CuNPs.

XPS analysis was also conducted to determine the composition of the coating and the results are shown in figure 4-24. A weak peak detected at 282.7eV (peak1) in the case of NG-CuNPs is assigned to the metal-carbide bond indicating the presence of carbon in the metallic core. In the latter coating, additional peaks could be distinguished and are attributed to the lattice sp^2 and sp^3 and labelled as Peak2 and Peak3, respectively. Other peaks labelled Peak5 and Peak6 were assigned to C-N [273], [274] and O=C-N bonds [275], respectively. The XPS analysis of the NG-CuNPs also revealed the presence of a nitrogen peak (cf. Figure 4-24.b). The deconvolution of the main nitrogen peak reveals the presence of a peak around 398.3eV (Peak1) that is attributed to pyridinic nitrogen atoms that are bonded to two carbon atoms and next to a vacancy. The binding energy peak at 400.1eV (Peak2) is related to nitrogen in a five-membered ring, while peaks at 401.3eV (Peak3) can be assigned to the substitutional case [276]. The last peak at 404eV (Peak4) has typically been assigned to N_2 molecules trapped inside the graphene layers [277]. The analyses of the copper peak showed less pronounced evidence of

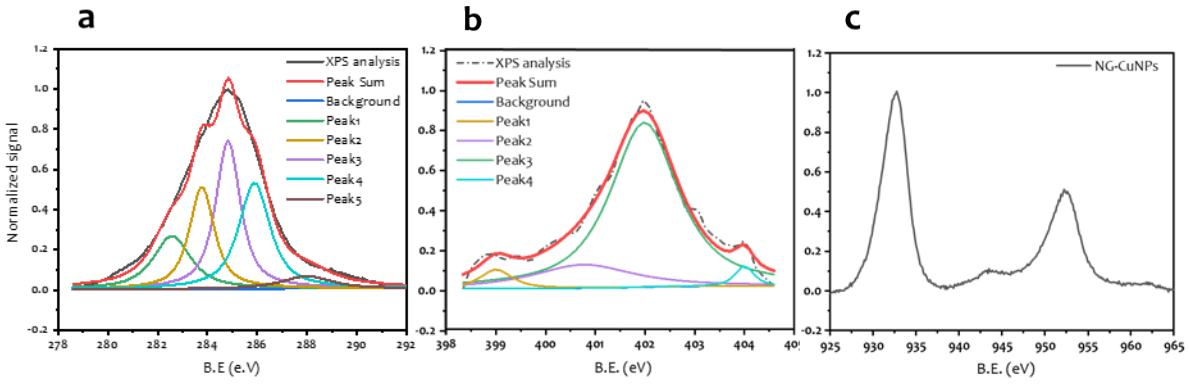

Figure 4-24: XPS investigation of the composition of the two coatings showing: (a) carbon peak of the NG-CuNPs, (b) XPS nitrogen peak of the NG-CuNPs and (c) XPS copper peak of the NG-CuNPs.

oxidation of the metallic core (cf. Figure 4-24.c). The values of the deconvoluted peaks are summarized in Table 4-3.

Table 4-3: Details of the deconvoluted XPS peaks in the case of NG-CuNPs,

		Peak1	Peak2	Peak3	Peak4	Peak5
Carbon	Position (e.V)	282.70	283.90	284.80	285.90	288.02
Peak	FWHM	1.55	1.09	1.14	1.48	1.97
Nitrogen	Position (e.V)	399.00	400.77	401.97	403.90	/
Peak	FWHM	0.73	2.61	1.60	0.51	/

4.2.3 Thermal properties of nanofluids with graphene-coated nanofillers

4.2.3.1 Thermal properties of the graphene-coated copper nanoparticles nanofluids

The results of the thermal conductivity measurement are presented in Figure 4-25. At 25°C, the thermal conductivities measured were found to correspond to the thermal conductivity of water and minor deviations were recorded for samples with 0.1wt.% and 0.05wt.%, However, an increase is seen at a higher temperature where the thermal conductivities of the NFs samples increased with the increase of the concentration. At 30°C, the thermal conductivity increased between 3% and 9% when the concentration NPs increased up to 1wt.%. At 35°C, the increase varied between 2% and reached an 11% increase at 0.1wt.% At 40°C, the results showed almost the same improvement with a maximum of 15% increase in the thermal conductivity of 0.05wt.% NF. The thermal conductivities at 45°C reached value with a 17% increase.

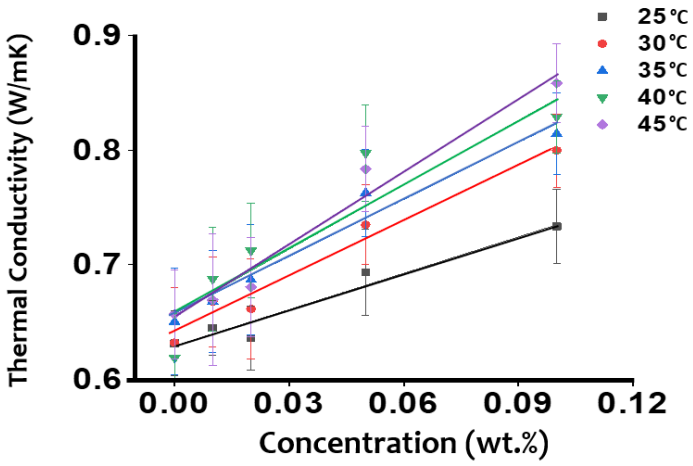

Figure 4-25: Thermal conductivity measurements of the different concentration of NFs at temperature between 25 and 45°C.

The viscosity of the nanofluids plays a major role in their thermal conductivity that can positively contribute to, or hinder, the heat transfer. As a Newtonian fluid, the viscosity of water does not change with the shear rate. However, the addition of NPs to the fluids might strongly affect the base fluid rheology. Figure 4-26 shows the results of the measurement of the viscosity of water and the other nanofluids. The results confirm the nature of the Newtonian behaviour of water where its viscosity remains relatively unchanged with the applied shear rates. For the NFs, it can be seen that the increase in concentration results in an increase in the viscosity of the fluid in all the samples. In the case of 0.1wt% and 0.05wt.% NFs, the values of the measured viscosities displayed a different behaviour with an increase in viscosity at low shear rates. The latter behaviour was found to be rather a consequence of aggregation of the NPs that occurs faster in the case of high concentration since the particles are more easily attracted to each other.

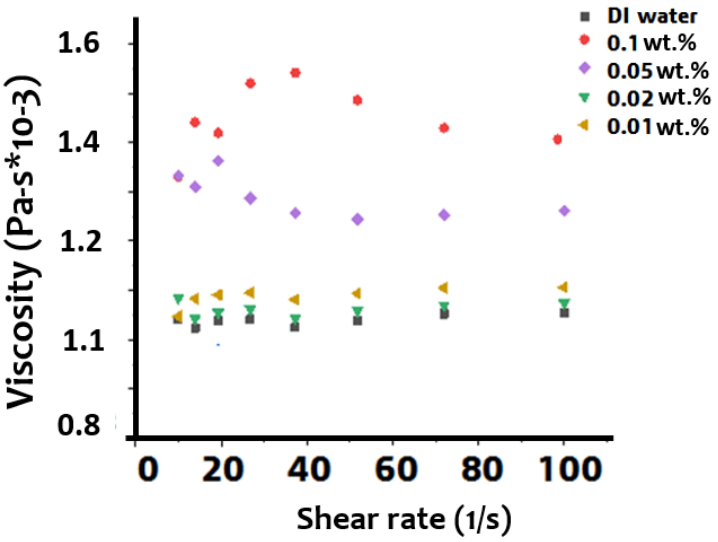

Figure 4-26: : Dynamic viscosity measurements of DI water and different concentrations of NFs.

4.2.3.2 Thermal properties of the graphene oxide coated copper nanoparticles nanofluids

Graphene oxides nanoparticles were also dispersed in fluids and the resulted nanofluids were found to exhibit better stability due to the surface functionalization with oxygen groups. It was reported that the functionalized graphene reached an increase of 61% at 5vol% when dispersed in ethylene glycol. In water, an increase of 181% in the heat transfer coefficient of the base fluid was recorded at a concentration as low as 0.2vol.% [278]. The thermal conductivities of the GO-CuNPs NF is presented in Figure 4-27. The general trend of the enhancement in the thermal conductivity of the GO-CuNPs NFs is visible with the increase in the fraction of the nanofillers and the temperature between 20ºC and 50ºC. At 20ºC, the thermal conductivity of the fluids varies from 0.58W/mK (4.0% enhancement) and 0.74W/mK (30.6% enhancement) with the increase of the GO-CuNPs fraction from 0.1wt.% to 10wt.%. Such enhancement can be linked to the increase in the fraction of the solid phase that has higher thermal conductivity than the base fluid and contributes to the heat transfer.

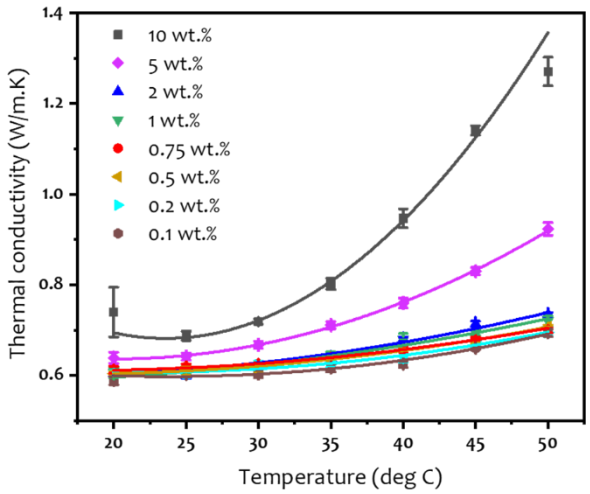

Figure 4-27: Thermal conductivity measurement in the case of GO-CuNPs in function of the fraction of the fillers and the temperature.

The increase in the temperature appears to affect positively the values of the thermal conductivity of the GO-CuNPs NF. The increase in the temperature is followed by an increase in the thermal conductivity that reaches a maximum value of 1.27W/mK (103.4% enhancement) at 50ºC and 10wt.% loadings. Such an effect can be explained by the increase in the Brownian motion of the particles and enhanced convection at a higher temperature. With higher fractions of solids in the fluid, the combined effect of larger solid phase and higher particles movement due to the Brownian motion is assumed to lead to longer thermal transport paths. The result is in line with previously reported works for low concentration of the added NPs up to a concentration of 0.5wt.% but contradicts the saturation in the thermal conductivity improvement with a critical concentration of the graphene oxide due to the formation of larger aggregates of the graphene oxide sheets that limits the movement of the solid phase within the fluid [279]. Figure 4-28 shows a schematic representation of that describes the increase in the fraction of the GO-CuNPs.

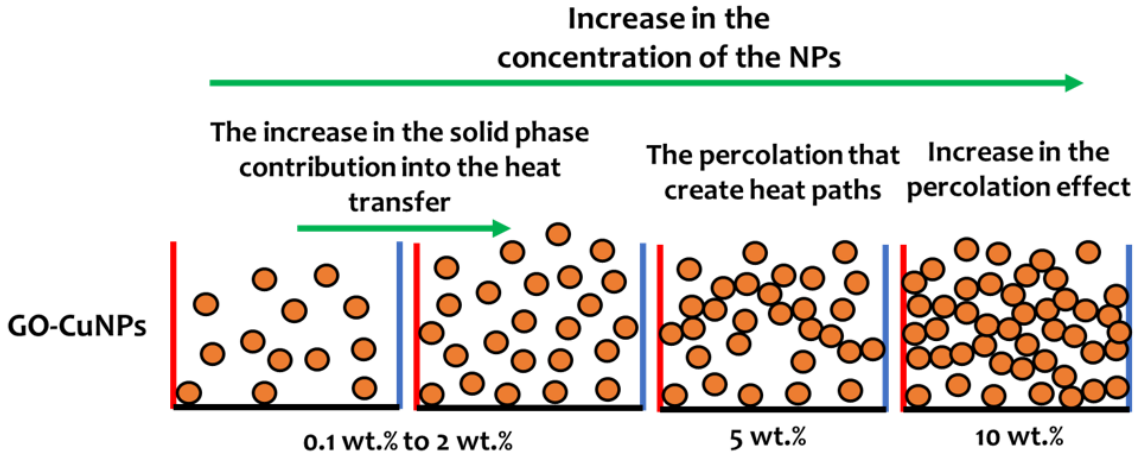

Figure 4-28: Schematic representation of the effect of the increase in the fractions of the nanofiller in the case of the GO-CuNPs.

4.2.3.3 Thermal properties of nitrogen-doped graphene-coated copper nanoparticles nanofluids

In the case of NG-CuNPs (cf. Figure 4-29), the variation of the thermal conductivity of the NF presents different profiles with the increase of the fraction of the nanofillers and the temperature of the fluid. A relative increase of the thermal conductivity of the NF compared to the water is visible for all the samples with different loadings and at different temperatures. At a low concentration of 0.1wt.%, the presence of NPs has a minor impact on the increase of the thermal conductivity with a value of 0.57W/mK (1.45% enhancement) at 20ºC but increases noticeably with the increase of the temperature to reach a value of 0.74 W/mK (19.05% enhancement) at 50ºC. At NPs loadings between 0.2wt.% and 1wt.%, the increase in the fraction of the NPs and the temperature induces an increase in the thermal conductivity of the fluid. While the thermal conductivity values at concentrations of 0.2, 0.5, and 0.75wt.% converge towards a value of 1.1W/mK at the highest temperature, the nanofluids with 1wt.% loading show a lower value that is close to 1W/mK (53.68 % enhancement). The explanation of the enhancement in the thermal conductivity of the NFs with concentrations up to 0.75wt.% is the presence of a higher amount of solid phase with a higher thermal conductivity than the base fluid. The increase in the temperature has also a positive effect on the thermal conductivity of the latter concentrations with an increase in the Brownian motion of the particles. At 1wt.% NPs loading, the thermal conductivity enhancement at low temperatures matches the predicted effect of the increase of thermal conductivity with a higher fraction of the NPs. However, the higher temperature during the measurement is equivalent to a longer time to reach the setpoint for the measurement and the limited stability of the NPs in water can explain the decrease of thermal conductivity at a temperature of 50ºC.

The stability of the doped graphene sheet is limited, and the aggregation of the NPs results in a lower surface area that reduces the contribution of the NPs in the heat transfer to result in less enhancement.

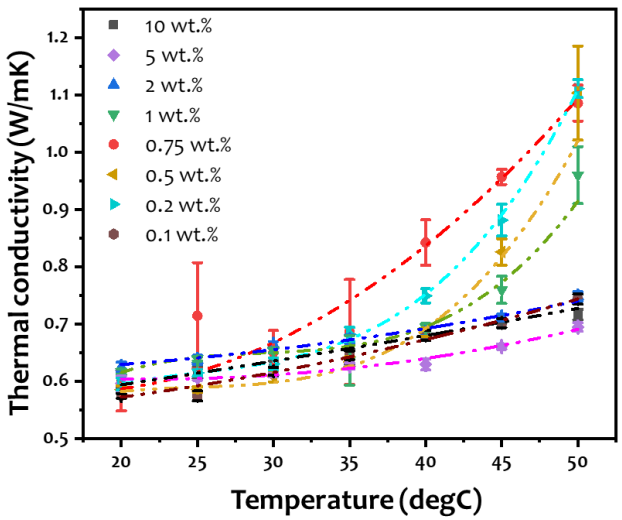

Figure 4-29: Thermal conductivity measurement in the case of NG-CuNPs in function of the fraction of the fillers and the temperature.

The same situation is encountered with the further increase in the fraction of the NG-CuNPs that results in a faster aggregation that limits the increase in the thermal conductivity of the NF. By increasing the amount of the NPs in the liquid, the NG-CuNP with low stability makes faster contact with other particles and form bigger aggregates that limit their contribution to the heat transfer. Such a situation can be observed in the case of 2wt.% NPs loading with a thermal conductivity that varies between 0.62W/mK (10.34% enhancement) and 0.74W/mK (19.78% enhancement) and is more pronounced in the case of 5wt.% loadings with a thermal conductivity that varies between 0.59W/mK (5.33% enhancement) and 0.69W/mK (11.23% enhancement) throughout the range of measurement temperatures. Finally, at a concentration of NPs as high as 10wt.%, the thermal conductivity of the corresponding NF shows a thermal conductivity that varies between 0.59W/mK (5.43% enhancement) and 0.71W/mK (14.66% enhancement) when the temperature is varied between 20ºC and 50ºC. The relative enhancement in the thermal conductivity compared to the previous NPs loading (i.e., 5wt.%) is assumed to be linked to the increase in the solid phase that aggregated as a thicker layer at the bottom of the fluid without a possible contribution of the individual particles through their mass transport and Brownian motion. Figure 4-30 shows a schematic representation of that describes the increase in the fraction of the NG-CuNPs.

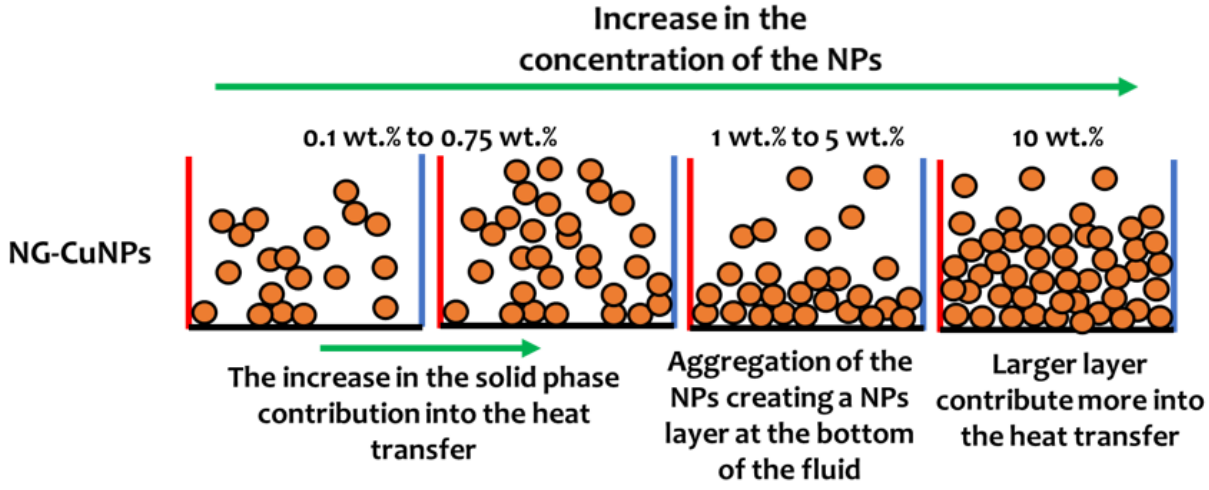

Figure 4-30: Schematic representation of the effect of the increase in the fractions of the nanofiller in the case of the NG-CuNPs.

4.3 Summary and discussion

In summary, we developed a novel, efficient and facile process to fabricate GCPs without agglomeration through an improved CVD process. A cold wall CVD method was firstly introduced in this work for fabricating few-layer graphene directly on spherical Cu particles by using a gaseous carbon source. By adjusting the gaseous flow rate, the deposited graphene layer on Cu particles can be optimized, and the outcome GCPs and the outcome GCPs achieved good encapsulation of the particles. The cold wall CVD process offers the advantage of reducing the procedural temperature, as well as shortening processing time. GCPs processed by cold wall CVD possess excellent oxidative stability up to 179°C, which resolves the critical problem of easy oxidation of fine Cu nanoparticles and opens up a wider application prospect. In addition, the superb thermal conductive property of processed GCPs allows for practical uses such as TCA. The measurements support the possibility of replacing nano-Ag and flake Ag with GCPs in TCA. In conclusion, owing to their unique physical features, GCPs are a strong candidate as functional filler materials for TCAs and conductive inks.

Graphene coated copper nanoparticles are investigated here as potential multifunctional nanofiller used as a sintering aid in the metallic based paste. The results of the TEM observations revealed a continuous graphitic coating surrounding the spherical particles. The composition of the coating was verified and the presence of the multilayer structure on the surface of the particles was found to provide oxidation protection for the metallic core of the particle. Raman microscopy confirmed the multilayer graphitic layering with the presence of a disordered structure that affects its electronic configuration. The TGA analysis of the powder was realized under different atmospheres. The results showed the reducing effect of the G-CuNPs in the presence of copper powder that might be used as a self-reduction component without an extra reducing agent. In addition, due to the metallic nature and the size of the particles, DSC analysis showed a melting depression of the nanopowder at temperatures as low as 155°C. Finally, the multilayer graphene coating around the copper particles was found to provide an additional effect on the mechanical properties of the particles that offer ductility and a possible friction reduction pre-and post-processing.

This work aimed at investigating the effect of graphene-coated NPs in water on the thermal and rheological properties of the base fluid. Results from the TEM confirmed the presence of several layers of coating surrounding the NPs, while SPM analysis showed a size distribution in the nanometre scale. Furthermore, the elemental analysis of the surface of the NPs confirmed the presence of the graphitic sp_2 bonded structure centred around 284.8eV. The presence of graphene-coated NPs within the liquid was later on found to have a positive effect on the thermal conductivity of the NF with an increase of up to 17% at 45°C with a concentration of 0.1wt.%. Finally, the rheological behaviour of the NFs was evaluated. The measurement of the dynamic viscosities showed a Newtonian behaviour of the NFs with an increased viscosity as the concentration of the NPs in the fluid increased. The low contribution of the NPs to thermal transfer and the deviation from the Newtonian behaviour at low shear rates is explained at this step by the weak surface charges. As a consequence, the NPs were prompt to segregation.

New types of nanofillers composed of graphene oxide and nitrogen-doped graphene coatings of copper nanoparticles have been developed in this work. The characterization of the coating showed the presence of a continuous and graphitic-like structure coating around the copper core. The fixation of the oxygen group around the graphitic coating and the presence of nitrogen in the carbon structure was confirmed using FTIR and XPS analysis. The evolution of the thermal conductivity of the dispersed nanoparticles in water was found to rely on the temperature and the fraction of the solid phase. An increase in the thermal conductivities with the increase of the solid phase fraction in the fluid and the temperature is reported for all the prepared samples with varied enhancements that depend on the level of stability and a probable effect on the viscosity of each type of NF. At a concentration of 0.5wt.% and a temperature of 50ºC, the thermal conductivity of the NG-CuNPs nanofluid reached its maximum value increase of 76%, compared to a 13% increase in the case of GO-CuNPs. While an increase in the fractions of NG-CuNPs did not provide any additional improvement due to their relatively low stability, further

increase in the fraction of GO-CuNPs achieved a maximum of 103% enhancement in the thermal conductivity at a temperature of 50ºC and a fraction of 10wt.%.

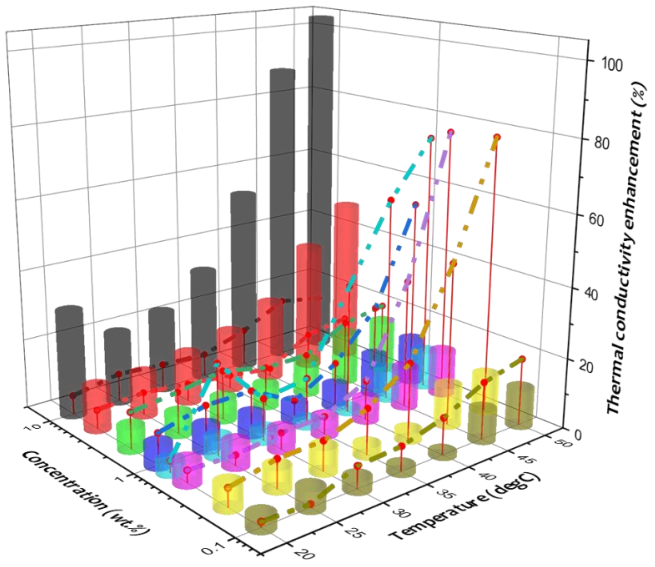

Figure 4-31: The enhancement in the thermal conductivity showing the combined effect of type of the nanofillers (GO-CuNPs/columns and NG-CuNPs/dashed lines), and their concentrations at different temperatures.

The Figure 4-31 compares the combined effect of the type of the particles, their concentration, and their thermal conductivity at different temperatures. The thermal conductivity enhancement in the case of GO-CuNPs is shown with cylindrical columns, while the effect of the NG-CuNPs can be seen with red dots connected with dashed lines. All the samples show a relative enhancement in the thermal conductivity of the fluid. At 0.1wt.% concentration, minor increases in the thermal conductivity are observed for the two types of nanofillers. While the initial values of the thermal conductivity in the case of GO-CuNPs NF appear higher, the increase in the temperature induces a larger effect on the thermal conductivity of the fluids in the case of the NG-CuNPs. Despite the destroyed structure of the coating, the thermal conductivity of GO-CuNPs in water seems to be higher than that of the NG-CuNPs at 20ºC and can be explained by a lower thermal resistance at the interface of the GO-CuNPs and a potential large layering effect around the particles. With the increase in the temperature, the thermal conductivity of the NG-CuNPs excess the values of the thermal conductivity of the GO-CuNPs. The latter can be explained by possible lower viscosity values that allow the NG-CuNPs to move more freely. In contrast to the NG-CuNPs that were observed to retain the structural and electronic properties of multilayer graphene, the GO-CuNPs showed a destroyed coating with a possible exfoliation of the graphene sheets that deforms the shape of the particle and might create a resistance to the flow of the fluid. In this case, the increase in the temperature has the effect of creating a faster movement of particles in the NG-CuNPs dispersion and allowing them to contribute better to the enhancement of the thermal conductivity. While the graphene oxide coating might benefit from its stability at relatively low temperature, it is the effect of temperature that allows the increase in the Brownian motion and the local mass transport of the NG-CuNPs to show higher thermal properties. A similar effect is reported with concentrations up to 0.75wt.% of NG-CuNPs with thermal conductivity enhancements that reach 78% compared to only 13% enhancement in the case GO-CuNPs. The presence of higher amounts of NG-CuNPs within the fluid results in longer thermal paths and more efficient heat transfer. However, such an advantage in the heat transfer offered by the doped coating is observed to slowly fade away. While the enhancement in the thermal conductivity is still highest in the case of the NG-CuNPs at high temperatures, the maximum enhancement drops to 50% at a concentration of 1wt.% at 50ºC, and further addition of NPs (i.e., 2wt.%) induces lower thermal conductivity enhancement. As mentioned earlier, this behaviour can be explained by the instability of NG-CuNPs that worsen with a higher fraction of NPs and results in faster aggregation and formation of large particles that reduced the efficiency of the NG-CuNPs in the thermal transport. Despite higher stability in the base fluid, the

low thermal conductivity of the GO-CuNPs and probable higher viscosities hinder their contribution to heat transfer at low NPs loadings. At high concentrations, with the increase in the fraction of GO-CuNPs in water, the thermal conductivity enhancement is seen to improve further. The increase in the temperature has also a positive effect with this type of nanofillers. The enhancement in the thermal conductivity of the GO-CuNPs NF increases due to the local convection and Brownian motion. At a concentration higher than 2wt.%, the GO-CuNPs is assumed to reach a percolation threshold and a major improvement in the thermal conductivity takes place. It is worth mentioning that the size of these NPs is quite small and therefore a percolation threshold can be expected at lower concentrations. While the contribution NG-CuNPs is reduced to the effect of a layer of aggregates formed at the bottom of the solution, the thermal conductivity of the stable GO-CuNPs combines a conjugated mode of heat transfer that is further enhanced with the increase of the temperature and reaches the enhancement of its maximum value (i.e., 103%) at 10wt.% and 50ºC.

Chapter 5

5. Alloyed based Nanoparticles and the Effect of Nanoscale Composition: Connecting The Top-Down To The Bottom-Up

Powder metallurgy (PM) is a process where solid powders are compacted into a shape and then consolidated at high temperatures to achieve densification. The process allows cutting the cost of the processing steps by limiting the number of steps and time required for the production of functional parts. It also helps to limit the use of energy during production and comes with high efficiency on the use of materials. In addition, PM has been well-known to produce functional parts that do not scale considerably in terms of cost/energy in the process with complex geometry. Such multiple advantages attracted many applications where the functional other production methods might not be attractive. Nowadays, a particular focus is given to the integration of PM in the production gears. Such functional parts are highly complicated to produce and might benefit from the near-net-shape PM processes offer. However, such a component requires a considerable effort to ensure their reliability, which the conventional press and sinter technologies in PM might come short of. The limit on the density of conventional PM often results in poor mechanical properties that do not promote their use in parts that requires good mechanical properties.

The ability to alloy different elements into a solid-solution structure is critical for continuous property tuning and materials development. The variation of the composition of the material extends greatly the possibility to develop a vast panoply of properties and target large applications. Combined with the size-dependent properties, the addition of alloying elements into the matrix of the nanoparticles opens up an extra dimension to tune the behaviour of materials. In the current manufacturing context, the integration of such low dimension materials is starting to see an increasing pace due to the multiple benefits those materials might bring. The nanometre-scale particles features a high driving force and enhanced sintering kinetics that can be highly valuable in conventional and non-conventional processing technics. On the other hand, a significant increase in the possibility to process materials and functional parts has been achieved through non-conventional, non-equilibrium conditions, process. The Spark Plasma Sintering (SPS) method explored in the current chapter is one of them. The process offers new opportunities to produce material using advantageous PM processing while adding further energy-saving concepts and properties. If such advantages are combined with production methods that allow the flexibility to explore chemical variation within the nanopowders, large benefits can be achieved in terms of production efficiency and properties of the final parts.

In this chapter, we explore the possibility to bridge the production of nanomaterials to their processing into the microscopic part using energy-efficient state of the art technologies. The mechanism of arc discharge is explored herein as a top-down approach to produce multi-element based alloyed nanopowder, and as a bottom-up process to consolidate the powder in an iron-based hybrid bimodal composite. Arc discharge method is used for the production of Low Carbon Steel (LCS) based nanopowder that is characterized in terms of morphology and composition. Such powder is also compared to a Cast Iron (CI) alloy based nanopowder in terms of densification properties at high temperatures. In an additional effort, the nanopowders are mixed to a microscopic powder and consolidated at high temperatures using the non-conventional SPS process. A correlation between the sintering parameters and the properties of the different powders is introduced.

5.1 Production of alloyed based iron nanoparticles

In this work, the alloy-based iron nanoparticles were produced using the submerged arc discharge method where cast iron electrodes were eroded under current values of 20A. In addition to the LCS, CI electrodes were also employed for the production of LCS alloy based nanopowder that was compared to the CI alloy based nanopowder. The nanopowders were filtered and rinsed with ethanol. For the bimodal approach, the nanopowders were sonicated in two steps. The nanopowder dispersed in ethanol were sonicated with a power of 2W for two minutes before the microscopic powder were added with the right fractions. Before sintering, the bimodal powders were prepared by mixing powders and exposed to a magnetic field using a magnetic plate. In the second step, the mixed powder was sonicated with a power of 1W for 30 seconds. After mixing, the powders were dried on a hot

plate in an open atmosphere at a temperature of 60°C. The powders were then compacted with a pressure of 20MPa using a graphite mould and transferred to the SPS equipment for sintering. While the focus in this work was put on fractions of nanoparticles of 5wt.%, a fraction of 25wt.% was also used to investigate the effect of the increase in the fraction of the nanoparticles in the sintering. The temperature of the sintering was varied between 600°C and 900°C with a pressure of 40MPa during the sintering process. An additional pressure of 80MPa was

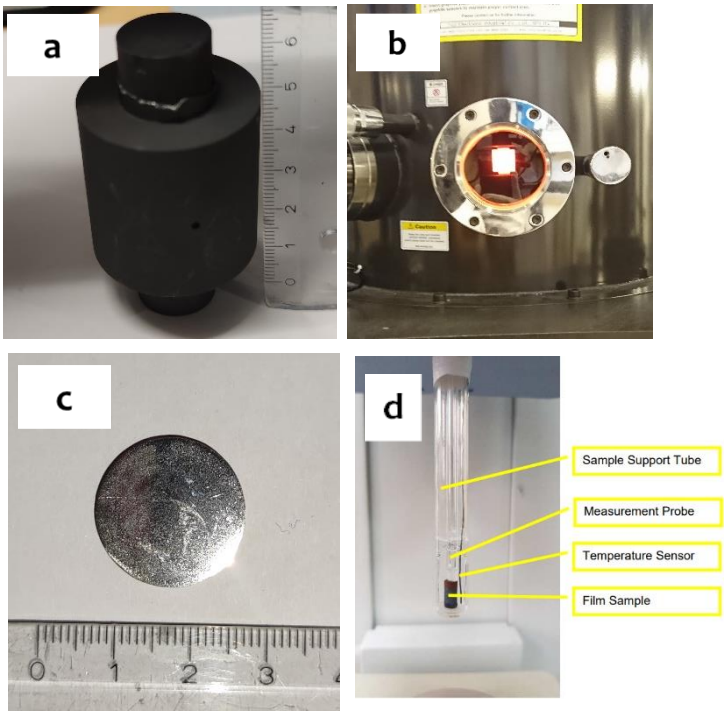

Figure 5-1: Photography images showing the powder being pressed in between the upper and lower punches, (b) the graphite mould radiating heat during the SPS process, (c) the sintered sample, (d) cylindrical sample prepared for dilatometry.

also observed to compare the effect of pressure on the sintering of the bimodal powder. Figure 5-1 shows photography images of the sample and the SPS setup. The composition of the initial materials used in this work is shown in table 5-1.

Table 5-1: compositions of the different materials used in this study.

Raw materials	%C	%Cr	%Si	%Mn	% S	% O
Grey CI-electrodes. SS 0125	3.31 - 3.46	No data	2.56 - 2.67	0.58– 0.66	0.064– 0.094	No data
LCS-electrodes	0.17 – 0.22	1 – 1.3	max 0.4	1.1 – 1.4	max 0.035	No data
Microscopic powder, LCS. ABC 100.29	0.0023	No data	No data	No data	0.0049	0.0610

5.2 Characterisation of the nanopowders

The morphology and composition of the two powders were investigated using electron microscopy and chemical spectroscopy. A dilatometry study was made on mono dispersions of the two powders to compare their

densification process with a temperature up to 900°C. The samples were prepared by pressing cylindrical samples to achieve dimensions of 10x5mm^2. For the SPS process, the powders were mixed in the correct fractions using a wet route and dried. After drying, the two bimodal powders were compacted with a pressure of 20MPa using a graphite mould and sintered using the SPS technique at temperatures of 600, 700, 800, and 900°C. All powders were sintered under vacuum conditions.

Electron microscopy and EDX analysis were employed to analyse the composition of the sintered material at a temperature of 900°C. Hardness measurements were performed to compare the hardness of the microscopic powder and the NPs regions using the Vickers hardness method with a set of 5 measurements. Finally, the local composition of SPS sintered NPs region nanopowder region were analysed using Atom Probe Tomography (APT) by preparing sharp needle-like samples.

Unless clearly stated, the bimodal powder composed of microscopic powder and CI-NPs had 5wt.% NPs and sintered at 900°C using a heating rate of 100°C/min and under 40MPa of pressure. The temperature is held constant for 5 minutes before the sintering is stopped. In all cases, after sintering, the samples were left to cool down without external or forced cooling in a vacuum. In the following sections, the words microscopic powder and microparticles refer to the low carbon steel ABC 100.29.

5.2.1 Morphology characterisation

The morphology of the alloyed NPs in this work through arc discharge are presented in figure 5-2. It can be seen that the produced LCS particles are in the nanoscale range and have a spherical shape. Small dark spots were observed on the surface of the NP (cf. Figure 5-2.b). Additional TEM observations were also used to identify the structure of individual particles with a high resolution. The TEM observations are presented in Figure 5-2.c and d, and indicate the presence of a core-shell structure with a thin low-density layer surrounding the core of the NPs. An interlayer distance of 2.7Å could be measured from the core of the particle and corresponds to the iron atomic interlayer. Such a result was later confirmed by the development of an XPS model that estimated the thickness of the oxide layer in the present powder to a range of a few nanometres [280].

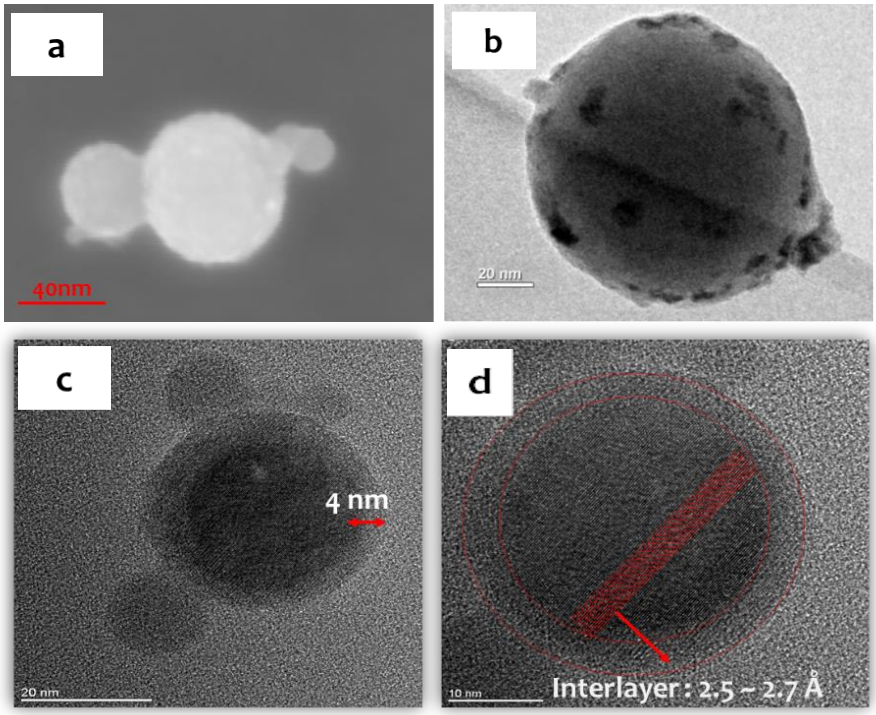

Figure 5-2: electron microscopy images showing (a) SEM, (b) TEM observations of the LCS NPs, (c) High resolution TEM observation showing a core shell structure on the NPs, and (d) a higher magnification that allow to distinguish the interplanar distance in the iron atom.

The Scanning Mobility Particle Size (SMPS) aerosol technics was employed to quantify the size distribution of the NPs, and the results are shown in Figure 5-3.a. The average size of the LCS-NPs was found at 53nm. Due to the limitation from the used method, SPM was used to verify the presence of smaller particle. The results are shown in Figure 5-3.b.

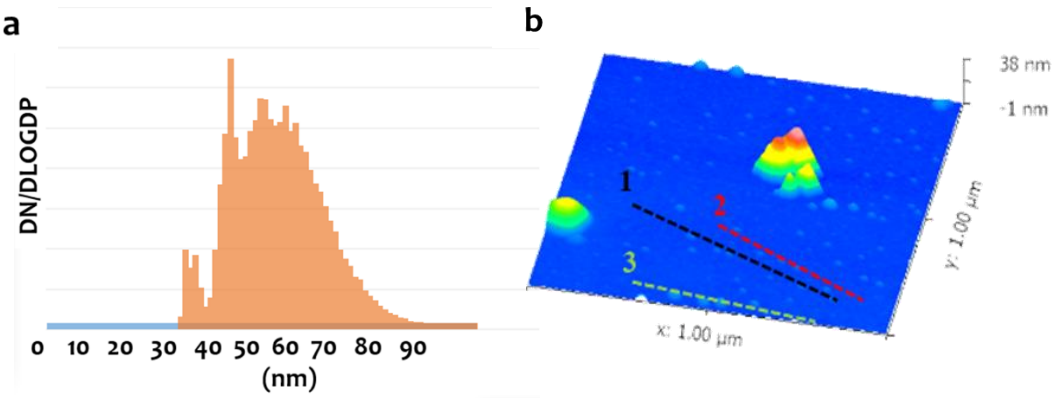

Figure 5-3: Size distribution of the produce LCS-NPs using (a) SMPS and (b) SPM technics.

A wet mixing route was developed in this work to ensure a suitable distribution of the NPs around large particles in a bimodal size powder. The results of the two-step magnetic method are shown in figure Using a two-steps magnetic approach, the result of the mixing is presented in Figures 5-4. It can be seen that a relatively good mixing was achieved where the nanoparticles can be seen covering the large microparticles. More importantly, the NPs are seen with a bridging effect between the microparticles with a high number of NPs. During the sintering, the NPs in the bimodal powder is supposed to become a source of matter and provide mass transport for the diffusion process to connect the microscopic particles.

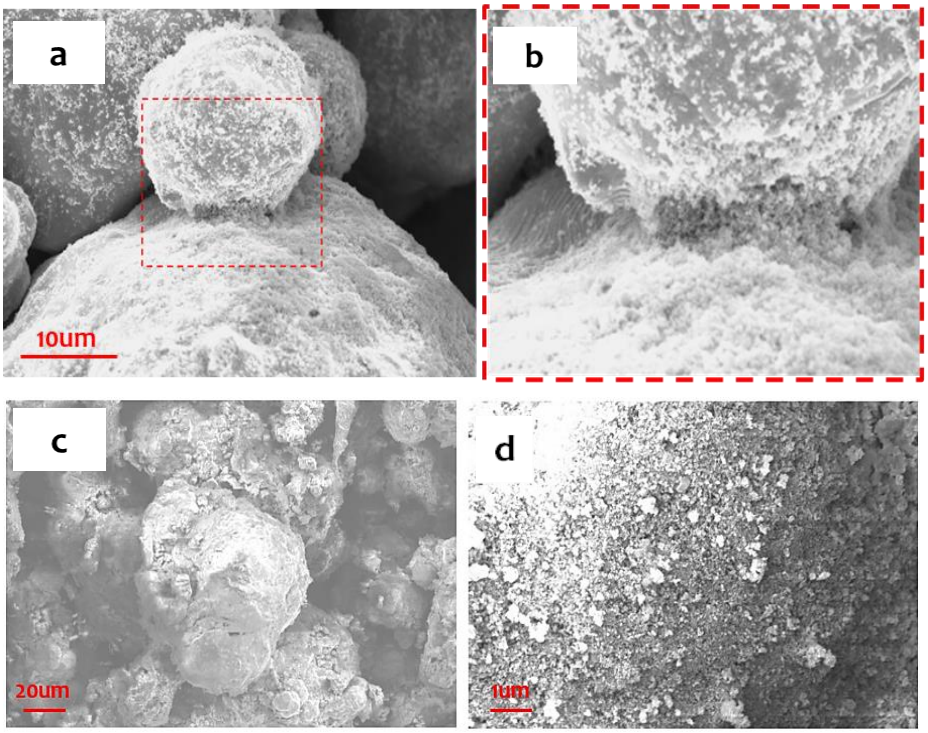

Figure 5-4: Two-step method used to disperse the NPs around microscopic powder. (a) and (b) low and high magnification SEM observations of mixed powder 5wt.% of NPs, (c) and (d) low and high magnification SEM observations of mixed powder 25wt.% of NPs.

5.2.2 Composition of the Nanopowders

The composition of the LCS-NPs was first investigated using XPS analysis. The powder composition is seen in Figures 5-5. The analysis was combined with a sputtering step to analyse the depth component of the powder and not be a restraint to only the surface of the pressed powder. Six different peaks have been analysed including iron, carbon, chromium, silicon, manganese in addition to oxygen which corresponds to the composition of the initial bulk LCS rods, and the observations made so far. The peaks correspond to the composition of the base alloy used for the fabrication of the LCS-NPs. The iron peak is observed with the Fe2p at a value of 710eV. Such a peak indicates the presence of the Fe_2O_3. Interestingly, after sputtering, a small peak gradually starts to appear as a shoulder on to the initial iron oxide peak reported here and corresponds to the metallic iron compound. Such a result might be explained by the presence of a core/shell structure with a layer of oxides surrounding the nanoparticles. If we consider all the nanoparticles to be oxidized on their surface as in the core-shell reported above, it is reasonable to expect no metallic atoms from the surface of the particles. As the sputtering goes on, the surface of the first layer of nanoparticles is slowly cleaned from the oxide shell that reveals the core of the particle as pure metallic. The peak detection of chromium was difficult to distinguish but its presence was confirmed.

Except for the carbon, the other detected peaks remained unchanged throughout sputtering. This can suggest that the presence of these elements depend on the shell/core structure and might indicate more of a homogenous distribution all around the particles. In the case of carbon, a clear peak is initially observed and abruptly disappear after the first sputtering step. While some carbon can still be detected in the different sputtered layers, its amount is much lower. The first peak detected at 284.8eV, in this case, might be attributed to the adventitious carbon deposited from the atmosphere onto the surface of the sample. After sputtering the carbon peaks are seen with lower intensities. It is difficult to assess whether those peaks come from the composition of the powder or relate to external structure features such as contamination of the dark spot observed on the surface of the particles.

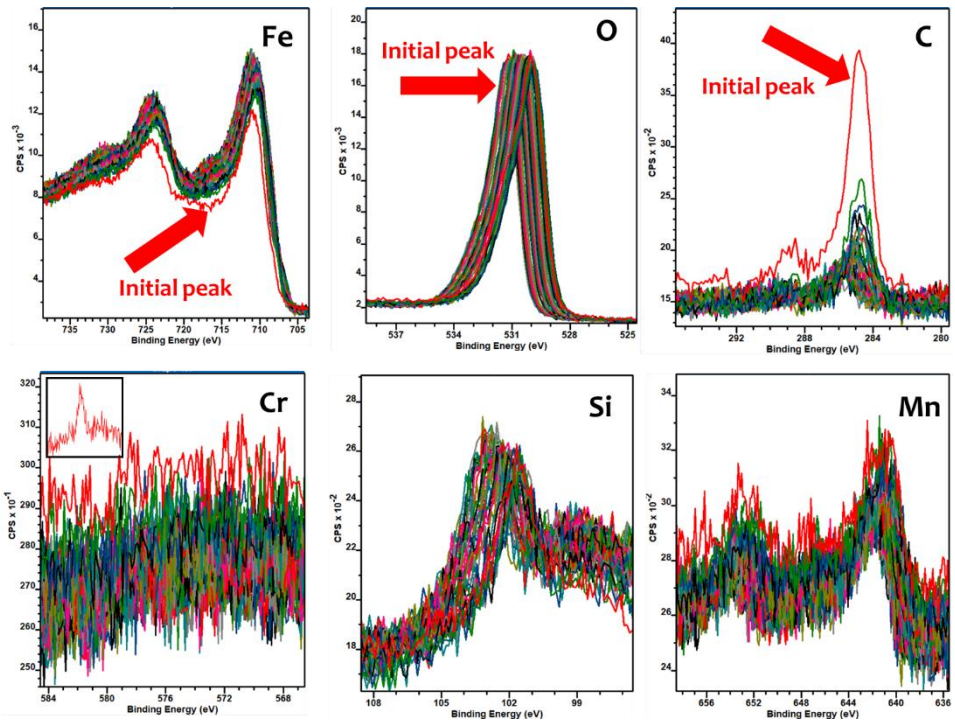

Figure 5-5: XPS results showing the surface composition of the nanopowder. Sputtering was realised during the analysis to obtain the depth profile.

In a second step, the same sample was in-situ heat-treated at a high temperature in a furnace connected to the XPS equipment. The powder was exposed to 870°C under argon and then transferred to the XPS chamber without exposing it to the air. Here also, the powder was sputtered to obtain a depth profile of the composition. The result is shown in Figures 5-6. The iron peak is seen initially with a Fe_2O_3 oxide peak and gradually shows a shoulder that appears when the sputtering takes place. Similarly to the non-treated powder, such a result might be explained

by the presence of a core/shell structure with a layer of oxides surrounding the nanoparticles. In the case of carbon, the same observation is made and show an initial peak that is attributed to the adventitious carbon before the sputtering. The same carbon peak was observed with much lower intensities after the sputtering started. It is worth mentioning that a shift in the peak of the binding energy between the carbon peaks before- and after- sputtering takes place. The peaks of carbon flatten and shift towards the low energy level where carbon-carbon and metal carbides peaks are identified. It is also to be noted mentioning that the chromium peak after thermal reduction was more obvious and kept relatively unchanged throughout the analysis. It is difficult to determine whether such a result occurs as a result of a chemical reordering or other mechanisms related to the analysis or the effect of the high temperatures.

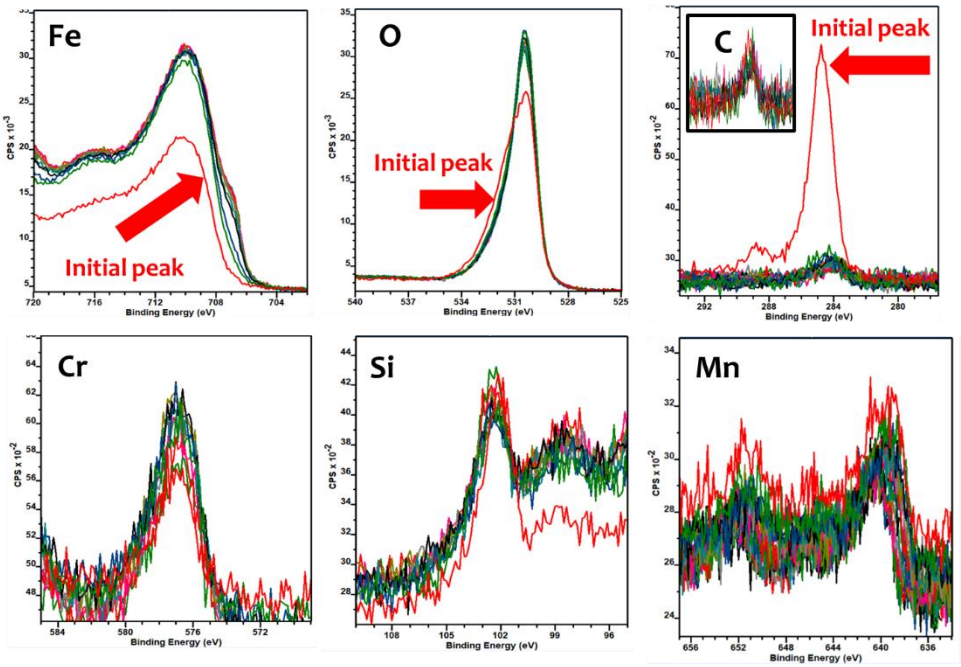

Figure 5-6: XPS results showing the surface composition of the nanopowder after heat treatment. Sputtering was realised during the analysis to obtain the depth profile.

The composition of the LCS-NPs were confirmed further using EDX analysis. Initially, EDX analyses were used on the LCS nanopowder and the results are presented in Figure 5-7. The composition of the powder can be seen with a homogenous distribution of the different elements with no apparent gradient. In the case of carbon, a very low signal is detected, and it is assumed that the result cannot be describing the real situation as carbon has an atomic mass and is difficult to detect.

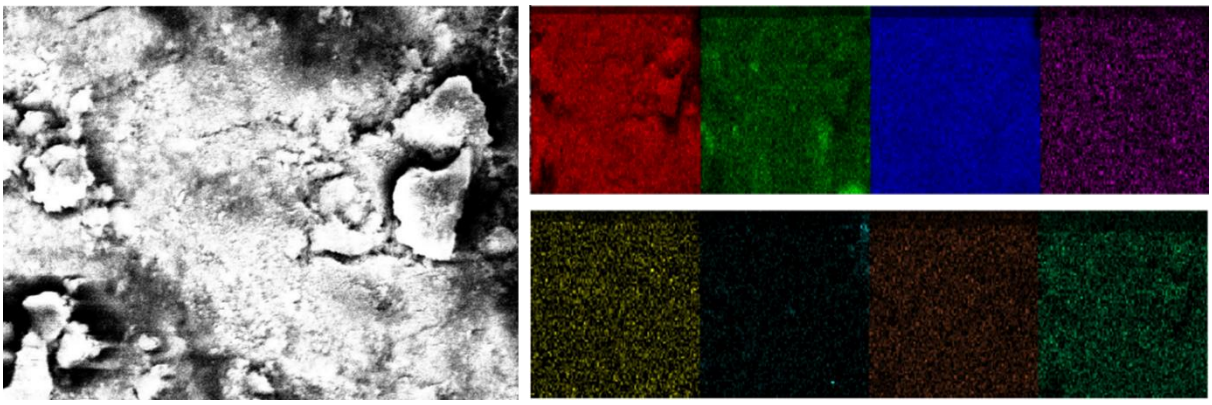

Figure 5-7: EDX analysis performed on the surface of LCS nanopowder and showing different elements.

The XRD analysis was run to identify the structure of the nanopowder. The diffractogram corresponding to the nanopowder is presented in Figures 5-8. Two structures can be distinguished. First, the iron structure can be distinguished with peaks at 44, 65 and 82°. The other structure concerns iron oxides and is identified at values of two thetas of 35 and 56°. Such result is in line with the previous results where oxygen is detected across the sample and the presence of core/shell structure where the oxides occupy the surface of the nanoparticles

XPS analyses of LCS nanopowder were also run for comparison. The analysis was made on two different spots and the results are shown in Figures 5-8. The presence of an iron peak is confirmed and found centred at 710eV. The later peak indicates the presence of the oxides with the existence of an oxygen peak in the two spots. The carbon is also detected at a binding energy of 284.8eV. In addition to the aforementioned element, the presence of silicon is reported with peaks centred at around 100eV. No other alloying elements such as chromium or manganese were detected.

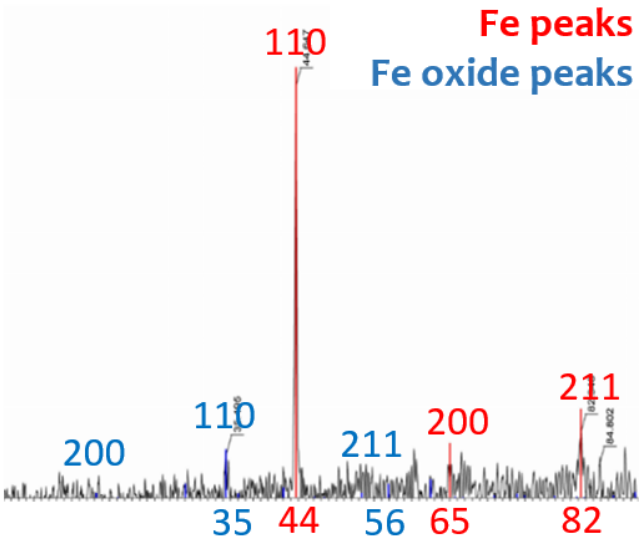

Figure 5-8: XRD analysis showing the structure of the LCS nanopowder and confirming the presence of both iron oxide and metallic iron.

The investigation of the composition of the CI-NPs was carried out by combining XPS analysis and EDX. Figure 5-9.a shows the results of the measurements. The XPS analysis was performed on two different spots showed in red and blue. The results indicted the same trend in both spots and confirm initially the presence of an iron peak cantered at 710eV. Such peak corresponds to the iron oxide as the oxygen peak can confirm. Despite the lack of high-resolution observation, such composition might indicate the same situation as the case of the LCS-NPs with its core/structure. Carbon peak was also detected in the analysis together with the presence of the silicon. No other alloying element were detected. The TEM-EDX analysis was used confirm the result of the XPS analysis. The results are shown in Figure 5-9.b and shows multiple peaks that were attributed to the iron, oxygen, and silicon peaks. Due to its low atomic weight, carbon was not successfully detected. Despite the lack of high resolution TEM observation, it is possible that the structure of the CI-NPs can be similar to the case of the LCS-NPS with the core/shell structure.

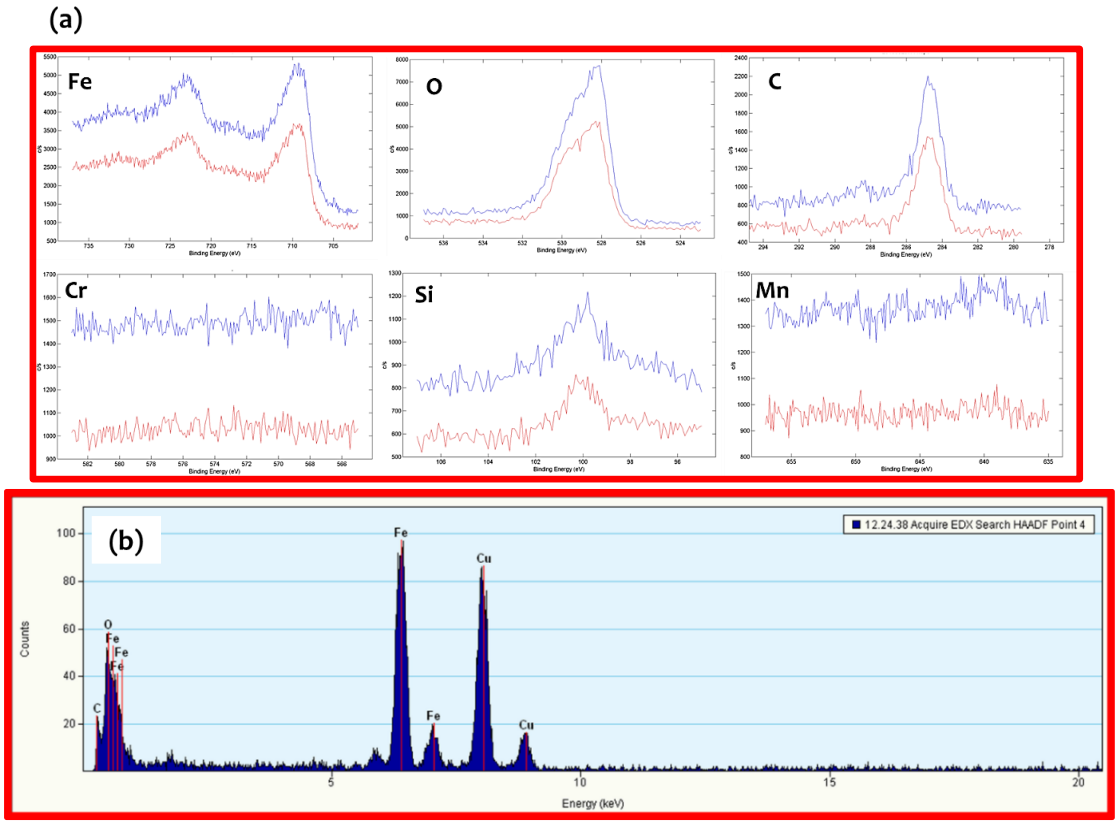

Figure 5-9: (a) XPS results showing the composition of the CI nanopowder and confirmed with (b) EDX analysis. The nanopowder is mostly composed of iron and carbon.

5.2.3 Dilatometry analysis

Dilatometry analysis was used to investigate the densification process of the LCS-NPs. The results of the analysis were later compared to the densification process in the case of CI-NPs. The results are shown in the Figure 5-10. In the case of the CI-NPs, it can be seen that a shrinkage starts occurring at temperatures as low as 150°C. The dimensions of the sample keep decreasing as a result of the decrease in the porosity level within the sample until the maximum temperature of 900°C is reached. Previous work on the densification of plasma discharge-produced iron nanopowder with an oxide layer on the surface reported a sintering mechanism starting at 270ºC in the under argon/H_2 atmosphere [281].

In the case of dilatometry analysis of the produced alloyed nanoparticle, no reducing agent was used during the dilatometry analysis performed under argon atmosphere. Different behaviour is observed in the case of the LCS-NPs. The profile of the dilatometry analysis of the LCS-NPs shows densification that starts at a temperature of 800°C. When the temperature increases to a value of 800°C, the LCS-NPs is seen with an abrupt change in the dimension of the samples. This effect is linked to a late densification process which starts at high temperature. The differences in the behaviour between the two kinds of particles can be related to the presence of the oxides around the nanoparticles and the composition of each powder. The oxides around the nanoparticles, if not reduced, act as a diffusion barrier that inhibits the mass transfer between the particles and therefore, their densification. In the case of the CI-NPs, the high presence of carbon from the base initial based material that is found in the nanopowder might play a role to eliminates such oxides. This reduction mechanism is very common in the reality of the metallurgical activities of iron [282] and was reported in the author publication (Paper D), where carbon is

used as a reducing agent. In the case of the LCS-NPs, the earlier XPS analysis shows no obvious change in the fraction of the carbon after the heat treatment except the difference between the first layer of carbon that was attributed to the adventitious carbon. It is not until a high temperature of 800°C is reached that the particles start densifying. This temperature might correspond to the moment the iron oxide is no more stable, and the high energy absorbed by the NPs at that temperature can be expected to result in a fast mass transport kinetic and rapid sintering of the powder. How much effect takes place and through what structure is outside the scope of this thesis. However, a report on the reduction of iron nanoparticles without the use of additional carbon or hydrogen showed that such reduction can happen at temperatures as low as 440°C and up over 700°C and is directly linked to the nature of substrate where oxygen from the iron oxide is transferred to [283].

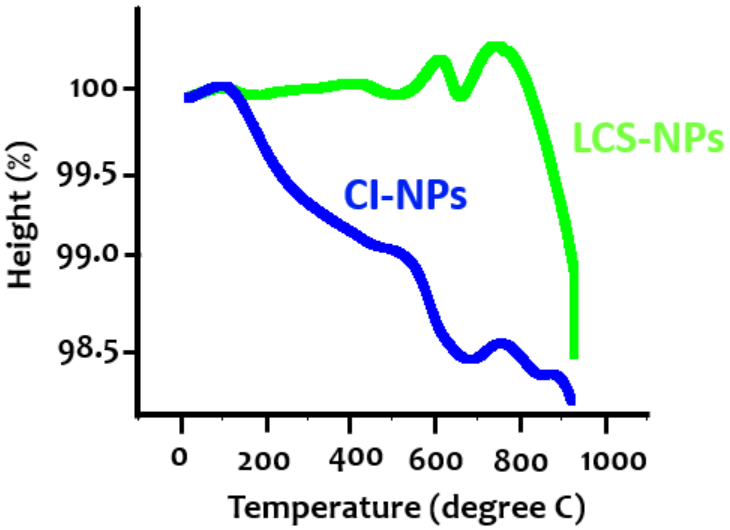

Figure 5-10: Dilatometry analysis comparing the densification of LCS-NPs and CI-NPs.

5.3 Spark Plasma Sintering Parameters

5.3.1 Process parameter

To investigate the effect of the powder and its potential use of low carbon steel-based nanoscale powder in the sintering of microscopic powders, monomodal sized microscopic powder and a bimodal sized mixture of LCS-NPs and microparticles were sintered using the SPS technique using different sintering parameters were explored.

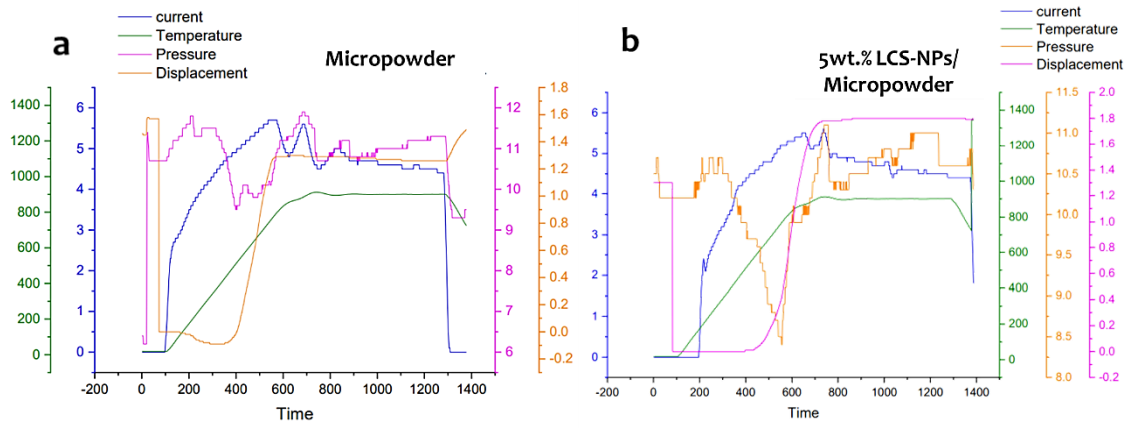

Figure 5-11: SPS process parameters showing the variation of the current, the temperature, the pressure, and the displacement during the process.

The SPS parameters in terms of variation of the current, the temperature, the pressure and the displacement are compared in Figures 5-11. The results indicate a possible involvement of the nanopowder in the sintering mechanisms that can be observed from the variation of the sintering parameters The current in the case of the monomodal microscopic powder presents the same trend as in the case of the mixed powders. Initially, the current increase continuously during the heating up step as a way to increase the temperature of the powder with all the mechanisms discussed above. Then the current was kept constant for the next 5 minutes to maintain a temperature plateau.

The temperature in the case of the two sintered powders following the increase in the current to reach the maximum sintering temperature. However, the difference in the sintering is seen in the case of the pressure where the profile of the pressure of the bimodal powder decreases quickly compared to the monosized one. When the temperature increase during the sintering, a competition between the dilatation of the metallic powders and their shrinkage occurs. When all the porosity is closed, only the expansion of the powder remains and is expected to increase the pressure. As the bimodal powder contains a fraction of nanopowders that form the joints between the particles, the decrease in the pressure is directly related to the melting of the nanoscale powder. Such event is expected as a result of the early sintering that starts [284] and results in a decrease in the pressure. Once the solid microscopic powder comes into contact, and the dilatation of the iron begins, the samples expand and an increase in the pressure is seen increasing again. In terms of densification, when the temperature increase, the energy absorbed by the powder is used to consolidate the particles. During the consolidation process, the density of the samples increases to detriment of the porosity that is eliminated through the melting of the materials between the particles and the mass transport. Compared to the mono-sized powder, the mixed microscopic powder with CI-NPs shows a higher shrinkage with a larger displacement of the dies. This can be explained by the presence of the nanopowder at the interface between the large powder, which might result in the softening of larger areas and further shrinkage of the bimodal powder.

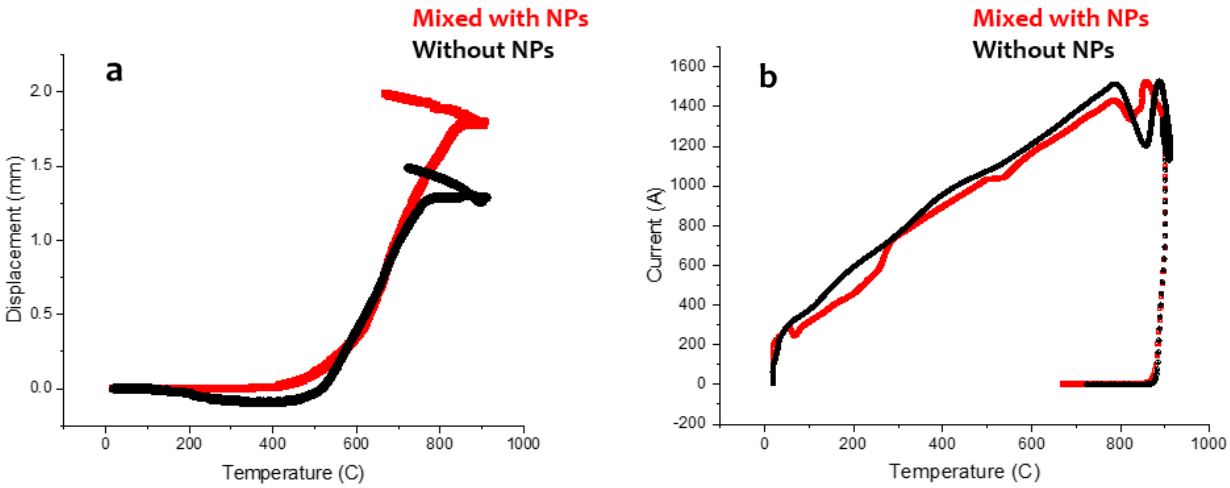

Figure 5-12: Comparison between the process parameters and the increase of the temperature in the case of the two powders. The variation of (a) the displacement and (b) the current in function of the temperature is presented.

Figure 5-12.a shows a comparison between the mono and the bimodal powder correlating the displacement of the dies to the temperature. It can be seen that the mono-sized powder shows initially a negative displacement with the increase of the temperature. Such an event is linked to the expansion of the powder that slowly increases in volume before the sintering kinetics increases at high temperatures. At a temperature close to 500°C, an increase in the displacement is noted where the upper die continues to move in the direction of the compacted sample until the temperature reaches the maximum of 900°C. The constant temperature does not seem to result in any additional variation in the dimension of the sample. In the case of the mixed powder, no negative displacement is noticed at the beginning of the sintering. This can be explained by either the early sintering/melting of the nanoscale CI particles or/and by the mechanical deformation of the nanopowder as a consequence of the expansion of the large particles. In the latter case, the expansion of the microscopic powder results in mechanical stress where the small particles are pressed together and compacted. Taking into consideration the fact that a major decrease in the value of the pressure occurs already at that temperature, it is more likely that an early

sintering/melting of the nanopowder is the reason for such a difference. Above 400°C, the displacement curve of the mixed powder increases rapidly with the increase of the temperature. At these levels of temperatures and currents, it can be assumed that the sintering/melting between the particles starts occurring through the current discharges and the Joule heating and leads to higher densification with the melted nanopowder. The value of the final displacement in the case of the bimodal powder reaches the value of 1.6mm, which is equivalent to 30% higher than the case of the mono-sized powder. Knowing that the measured densities for the two types of samples showed a density of 93% and 96% of the density of iron in the case of the micropowder and the mixed powder, respectively, such result shows a potential advantage of using nanopowders combined with the large powders, where the latter powder can benefit for additional densification of the material.

In terms of energy, the variation of the current is plotted against the variation in temperature in figure 5-12.b. A linear correlation can be observed between the variation of the current and the increase in the temperature in both mono- and bimodal-sized powders. However, the introduction of nanopowder as a sintering aid in the case of the bimodal powder results in less power consumption to increase the temperature of the sample. Such effect stems from the effect of the size of the particles on the process of SPS. The decrease of the size of the particles results in the decrease of the local contact between the particles, which in return results in a high resistance for the current to flow through scaling with the particle size by 1/(diameter of the particle)^2 [285]. As a consequence of the nano-sized, more contact points are established with low contact areas and induce a higher heating rate. While the difference in the currents does not seem huge, such difference is still in the range of 50A and can be a synonym of a relative gain in energy consumption.

5.3.2 Density measurement

Bimodal sized powder-based mixtures of 5wt.% NPs of LCS and CI have been sintering at different temperatures using SPS. The density measurement of the two kinds of bimodal powders is presented in Figures 5-13. The result indicates a correlation between the density of the samples and sintering temperatures. At a temperature of 600°C, the value of the density of the bimodal CI-NPs/Microscopic powder reached a value of 6,72g/cm^3 which is as low as 85% of the density of iron. With the increase of temperature, the value of the density quickly jumps to 95% of the density of iron at a value of 7.47g/cm^3 at 700°C. The further increase in the temperature resulted in a further increase in the density that reached a value of 96% the density of iron at 800°C and 900°C. In the case of LCS-NPs/microscopic iron powder, the density of the samples varied in the same trend. At a low temperature of 600°C, the measured density was 6.52g/cm^3 which corresponds to 83% of the density of iron. The increase in the temperature of sintering had a positive effect on the density where the density of the samples climbed to 6.95g/cm^3 and reached values of 7.38g/cm^3 and 7.5g/cm^3, at temperatures corresponding to 700, 800 and 900°C, respectively.

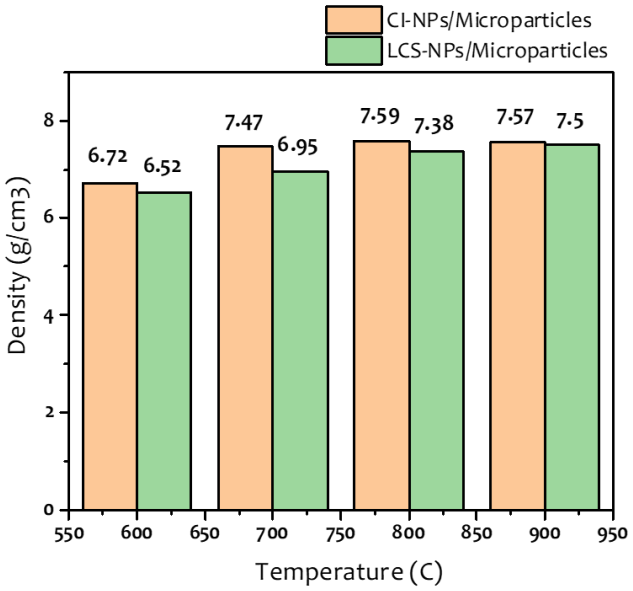

Figure 5-13: Comparison between LCS-NPs and CI-NPs densification effect at different temperatures.

To further explore the effect on the nanopowder in the sintering process, the temperatures of sintering was fixed to 600°C, while the sintering pressure, the fraction of NPs and the holding time were changed. The results are shown in Figure 5-14. When the fraction of the nanoparticles was increased to five-fold the initial value, while maintaining the pressure and the temperature at reference values of 40MPa and 600°C, respectively. The result of the measurement of the density of the samples revealed a small enhancement in the values of densities. The increase in the density values of the powders is explained by the possible contribution of the additional powder in filling the gap between the microscopic particles.

At a pressure of 80MPa, the density of the samples were increased to a value of 6.75g/cm^3 in the case of CI-NPs/microscopic powder and 6.52g/cm^3 for the LCS-NPs/microscopic powder. Such increase can be related to the pressure that continuously brings the powder into contact and contributes to enhancing the contact surfaces closing the pores. The increase in the pressure during sintering is an efficient way to improve the mechanical properties of the sintered powders as a process parameter of the sintering. As more powders come weld and establish large connection areas, the pores are closed, and the density of the samples is improved further.

The holding time was also changed to investigate its effect. When the holding time was increased to 1h while the pressure was kept at 40MPa, the density of the samples varied slightly. The SPS method is a fast-sintering process that involves local evaporation and melting the neck area. Such a mechanism is supported by the application of a pressure that continuously bring the powder into contact. Most of the densification in the case of SPS occurs during the initial step of the sintering where the necks are formed and grown. The increase in the holding time at high temperatures is not expected to result in any major effect on the densification of the powders.

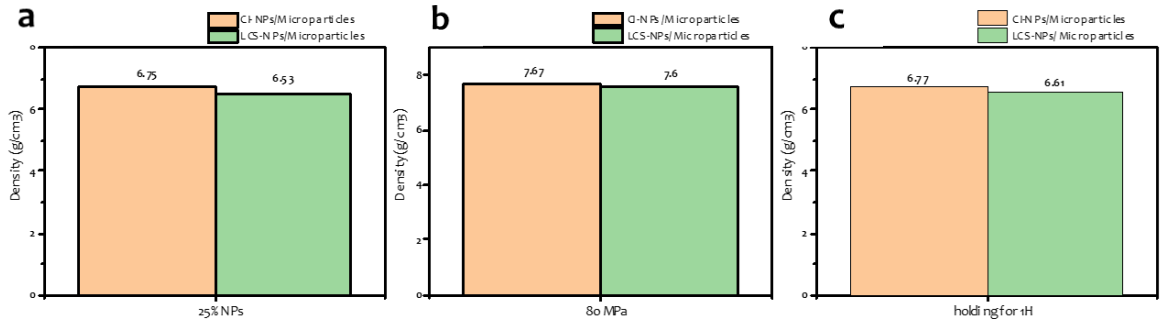

Figure 5-14: Comparison between LCS-NPs and CI-NPs densification effect at (a) a fraction of 25wt.%, (b) a pressure of 80MPa, and a holding for 1h at 600°C.

5.3.3 Microstructural and composition investigation

The sintering efficiency of the bimodal sized iron alloyed NPs was also investigated in terms of microstructure and composition. Figure 5-15 shows the SEM observation of the two kinds of powder compared herein. In the case of the micropowder, no contrast was observed between the sintered large particles. However, in the case of the bimodal LCS-NPs/microscopic powder, a clear distinction could be made. In the latter case, the microstructure of the bimodal powder shows contrasted bright regions that represent the initial micro powder alternated by small dark areas that represent the sintered nanopowder. Within the dark regions, small islands of bright solid particles could be observed. Such islands appear with the same contrast as the large micropowder and can be identified as isolated material from the initial microscopic powder. Whether the arc discharge, in this case, occurs or not remains an open question. However, the presence of that debris, if found indeed originating from the microscopic powder, can indicate the occurrence of the discharge between the particles.

The interface between the sintered nanopowder and the microscopic powders is presented in figures 5-15.e and f. The interface is seen with a continuous presence of material that indicates a certain degree of synergy between the two types of materials. It is also worth mentioning that large porosity was observed in the case of the microscopic powder. Less frequent and smaller size pores were observed in the case of the bimodal mixture.

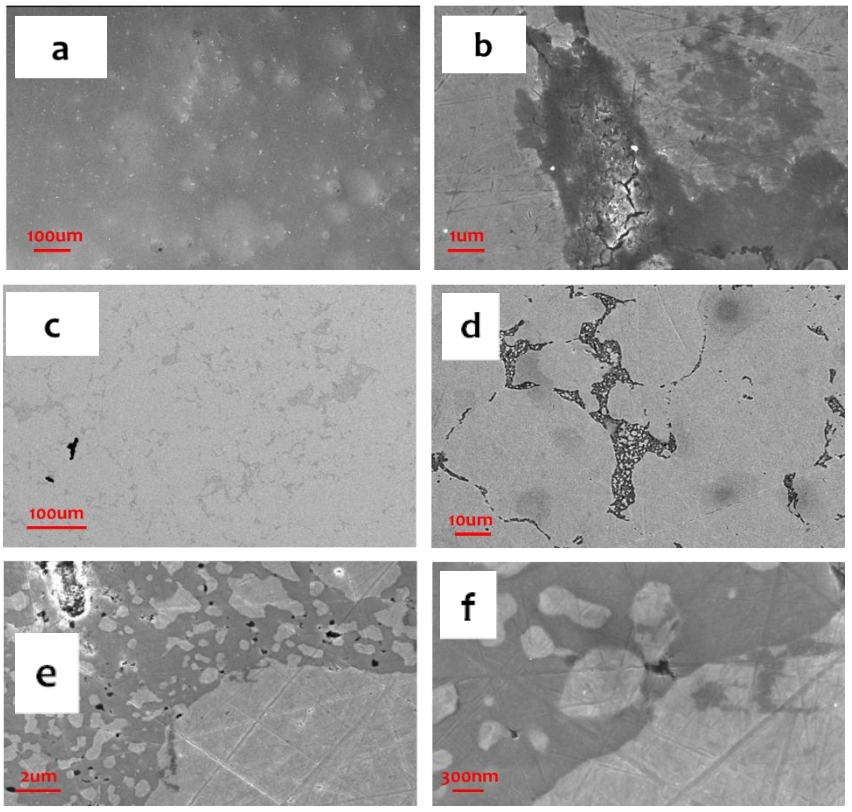

Figure 5-15: SEM observation showing the surface of the sintered sample in the case of (a) micropowder only with low magnification, (b)) micropowder only with higher magnification and the presence of large pores, (c) the bimodal powder with low magnification, (d) the bimodal powder with higher magnification, (e) the interface between the micro- and nano-sized particles with low magnification, (f) the interface between the micro- and nano-sized particles with high magnification.

To further investigate the quality of sintering, large micrography of the samples were taken in the longitudinal- and cross-section directions. The results are presented in Figures 5-16 as a panorama of images comparing the sintered micropowder to the bimodal one. The cross-section of the mixed powder is also shown for reference. In the case of the monosized powder, the top view shows the presence of large porosity on the left side of the sample and the presence of porosity all along the surface of the samples. The situation is different in the case of the mixed powder where no large porosity could be observed. The gap between the particles is rather filled with the sintered nanopowder. No concentration gap is seen along the top surface of the sample. The presented cross-section of the latter sample shows the same observation. Along the vertical direction of the sample, no anisotropy is observed, and no large pores can be reported. These results indicate a benefit of using the bimodal approach the initial nanosized matter can fill the gap in between the large particles.

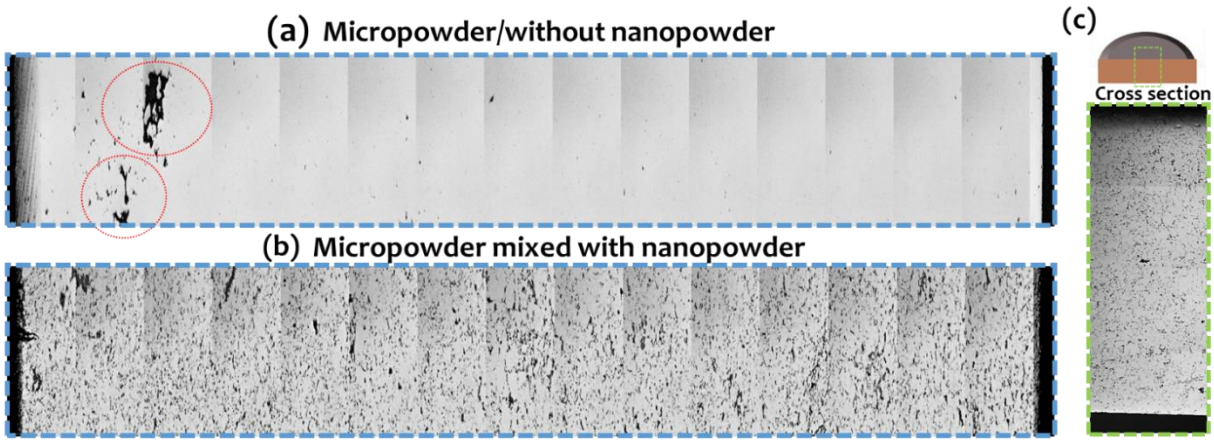

Figure 5-17: SEM panoramas pictures showing the surface of the sintered (a) Microscopic powder, (b) mixed powder and (c) the cross-section of the bimodal sample.

The surface of the two types of samples was polished and etched using 5% Nital to reveal the microstructure of the samples. Initially, the microscopic powder was only pressed and prepared for microscopy. The results of the observations are shown in Figures 5-17. The polished powder shows a flat surface where no contrast can be observed. After 5 seconds of etching, the microstructure started to show contrasting features with no well-defined internal boundaries. Further etching did not help improve the observation of the microstructure.

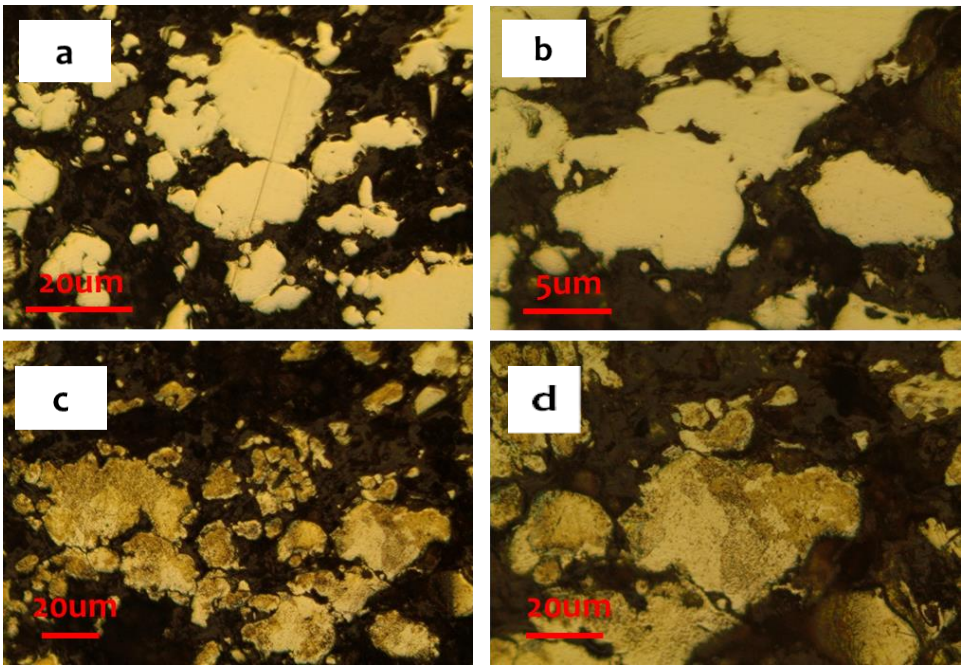

Figure 5-16: microscopy observations of the pressed microscopic powder with (a) and (b) as different magnification of the pre-etching powder (c) and (d) as different magnification of the post-etching powder.

The surface of the sample was etched with 5% Nital for 2 seconds and 5 seconds to enhance the contrast between the different phases. The result of the etching is shown in Figures 5-18. Before etching, the surface of the sample is seen with a solid phase that contained dark spots representing microporosity. After etching for 2 seconds, the microstructure of the samples is seen with a contrast that is further distinguished through the overexposure of the surface to the Nital 5% for 5 seconds. After sintering the reference microscopic powder to a temperature of 900°C, the microstructure of the samples presents different features that include regions of needle-like morphologies. Such morphology is different from the pre-sintered powder microstructure and is might be a result of a melted-solidified structures. A bright phase with needle-like shape can be seen in the matrix of dark phase.

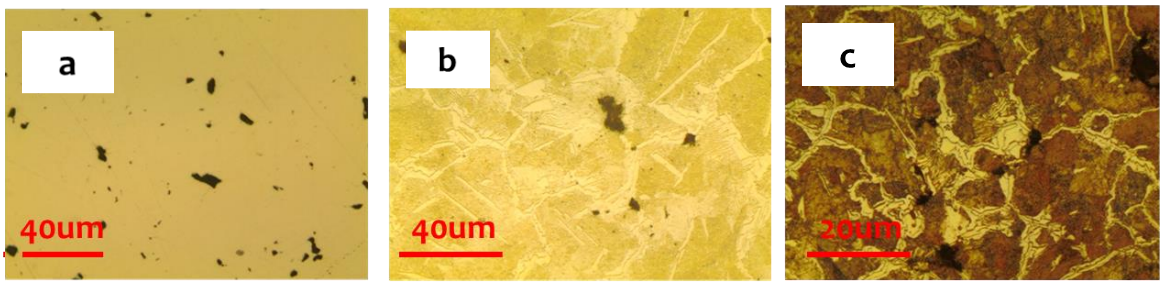

Figure 5-18: microscopy observation of the sintered microscopic powder at 900°C showing the surface of the sample (a) before etching, (b) after 2 seconds etching, and (c) after 5 seconds etching

To compare this further, the microstructure of the mixed nanoparticles and microscopic particles was observed after sintering under the same previous conditions. The result of the metallography observation is presented in Figures 5-19. After etching with 5% Nital solution for up to 5 seconds, the initial microscopic powder can be seen only showing clear grain boundaries that were not initially visible in neither the pre-sintering nor the post-sintering powder. The dark regions corresponding to the initial NPs are not affected by the etching. The dark regions corresponding to the initial NPs are not affected by the etching. The presence of grains boundaries can be seen in Figure 5-19.c. Such grains boundaries were not visible in the original micropowder.

To explain such difference in the microstructure. Different factors should be compiled and taken into consideration. First, the microstructure of the monosized powder showed an indication of melting/solidification with a needle-like light features not observed in the mixed or in the initial powder. While the temperature underestimation during the process of SPS can occur due to the large macroscopic difference in the temperature distribution [285], both experiments (i.e., sintering of monomodal and the bimodal sized powders) were realized using the same procedure. It is also worth mentioning that during the sintering of the monosized particles, there was no noticeable drop in the pressure that can indicate the rise in the temperature to the point where the sample melts (cf. Figure 8). The macroscopic observation of the sample also did not reveal the deformation of the sample or a dramatic change in the dimension of the sample. Finally, the measured density in the case of the mono sized powder was still lower than in the case of the powder with NPs. In this case, the difference in the microstructures between the monosized large powder and the bimodal powder cannot be explained by the melting of the whole sample.

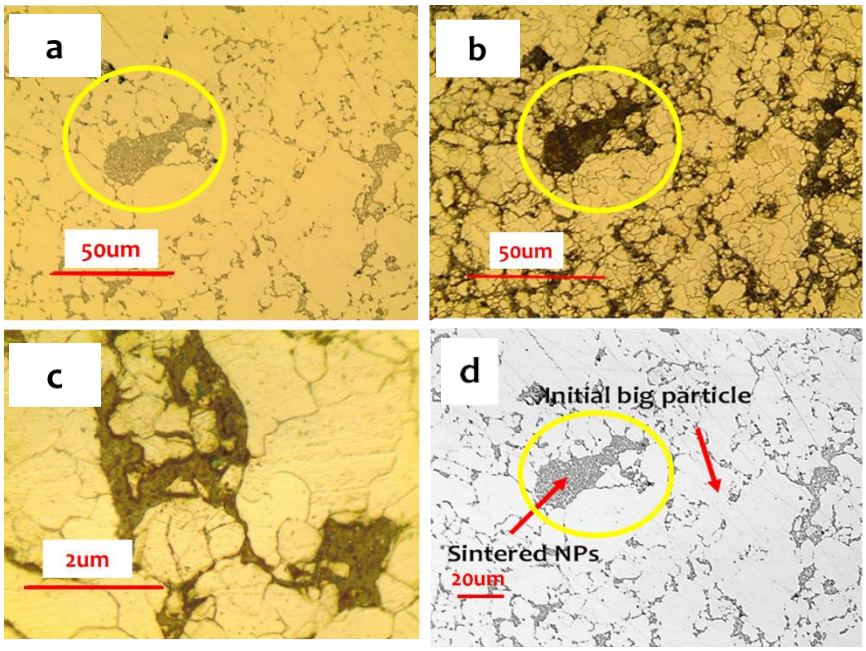

Figure 5-19: Microscopy observations showing the microstructure of the sintered sample as (a) pre-etching, (b) after etching, (c) higher magnification of the etched sample (d) SEM observation of the corresponding area.

Such difference in the microstructure can be explained by explained by the partial melting of the particles that was reported in the case of SPS [286] and /or an overheating that is followed by a quick cooling down. The partial melting can occur gradually and locally on the surface of the grains without an effect on the overall sample. The variation in the measured temperature and pressure would not be affected while the liquid layer of the partially melted particle would slowly contribute to the shrinkage and densification of the sample.

As the two type of samples (i.e., sintering of monomodal and the bimodal sized powders) were processed under the same conditions, it can be suggested that the presence of the nanopowder at the inter-granular gap between the particles can play a role in the sintering process. The presence of the needle-like bright structure that can be attributed to the ferrite structure, can be compared to the microstructure of an overheated sample that is rapidly cooled down to results in the sharp ferrite structure. A possible effect from the presence of the nanopowder is to affect the heat dissipation and the cooling of the powder. In this case, the role of the nanopowder at the intergranular gaps between the microscopic powder results indirectly in a difference in the microstructural property of the sintered material by slowing down the cooling of the powder. The presence of the grain boundaries in the sintered bimodal powder can support this hypothesis. In contrast to the non-sintered powder and the sintered monosized powder, large grain boundaries could be seen in the sintered sample and might indicate a slow cooling that results the coalescence of the grains of the powder.

EDX analysis of the two kinds of powder (i.e., only microscopic powder and bimodal powder), was employed after SPS took place at 900°C using the previously mentioned conditions of pressure and heating rate. The results are shown in Figure 5-20. In the case of the microscopic powder only, no clear difference in the composition of the powder could be seen. The presence of iron and oxygen could be seen all around the analysed area. The situation seemed to quite differ in the case of the bimodal powder. A contrasted composition between the iron and the oxygen could be seen when comparing the initial microscopic powders to the CI-NPs areas (i.e., dark areas in the SEM image). The latter areas is seen as an oxygen-rich zones where the amount of oxygen surpasses the amount of oxygen in microscopic powder. This can be linked to the initial composition of powder but also to the

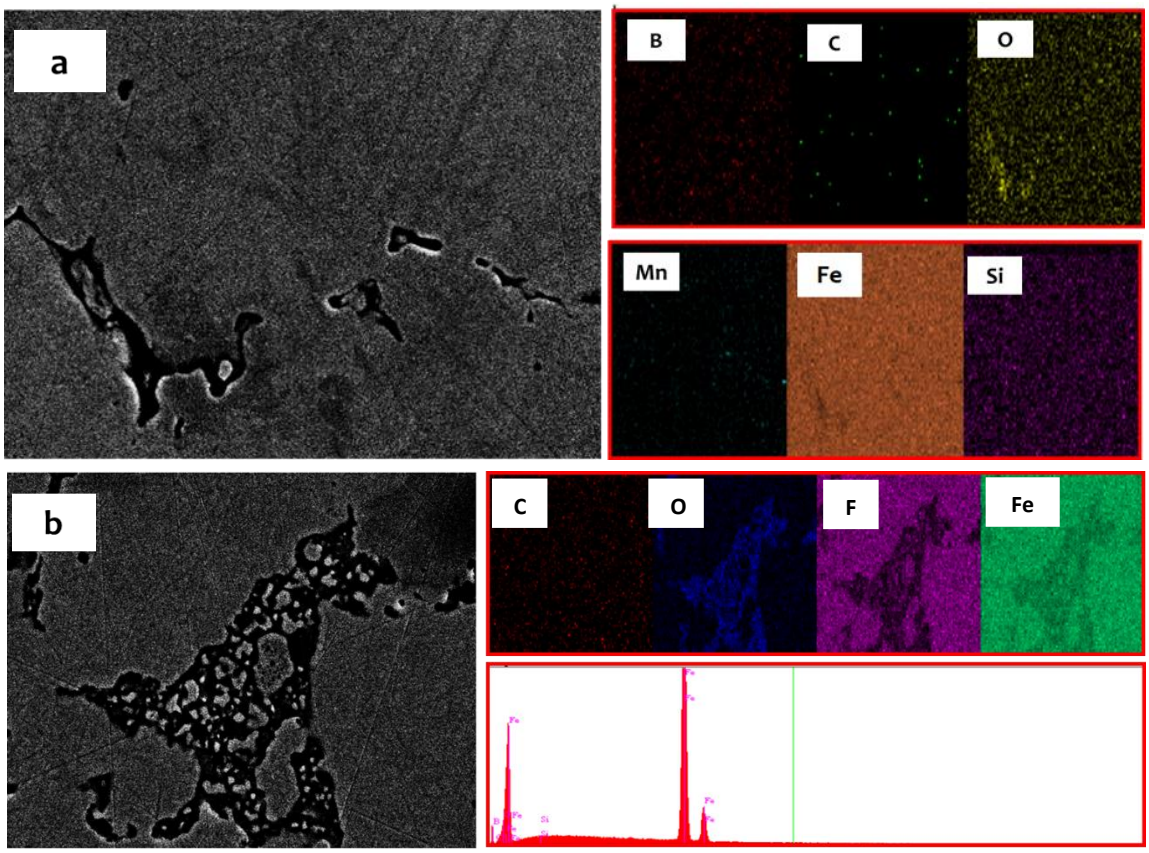

Figure 5-20: EDX analysis showing the composition of the sintered sample in the case of (a) microscopic powder, (b) bimodal powder, and their corresponding elements mapping.

fact that these NPs areas have potentially melted under the effect of the discharge and temperature, as a result of the complex mechanism occurring at the interfaces two kinds of materials. In this case, the presence of the oxygen in between the large particles can indicate the presence of iron oxides phases. In term of heat transfer, the thermal conductivity of the iron oxides can be one order of magnitude lower than that of the pure iron particles [287]. In this case, the presence of such phase acts as a barrier to the cooling of the powder. This fact support the earlier mentioned hypothesis where the presence of the nanopowder indirectly affect the sintering process as well.

The XRD analysis was also used to identify the structure of the bimodal LCS-NPs/microscopic powder to identify any potential effect on the crystal structure of the sintered powder. The result of the analysis is compared to the case of the CI-NPs/ microscope powder. The results are presented in Figures 5-21. The diffractogram in the case of the sintered powder containing CI-NPs is seen overlapping the case where the microscopic powder was mixed with LCS-NPs. Such a result indicates that no obvious effect on the crystal structure of the composite powder can be seen. The amount of nanopowder is low and mainly constrained to the grains boundaries where the sintering occurs between the particles.

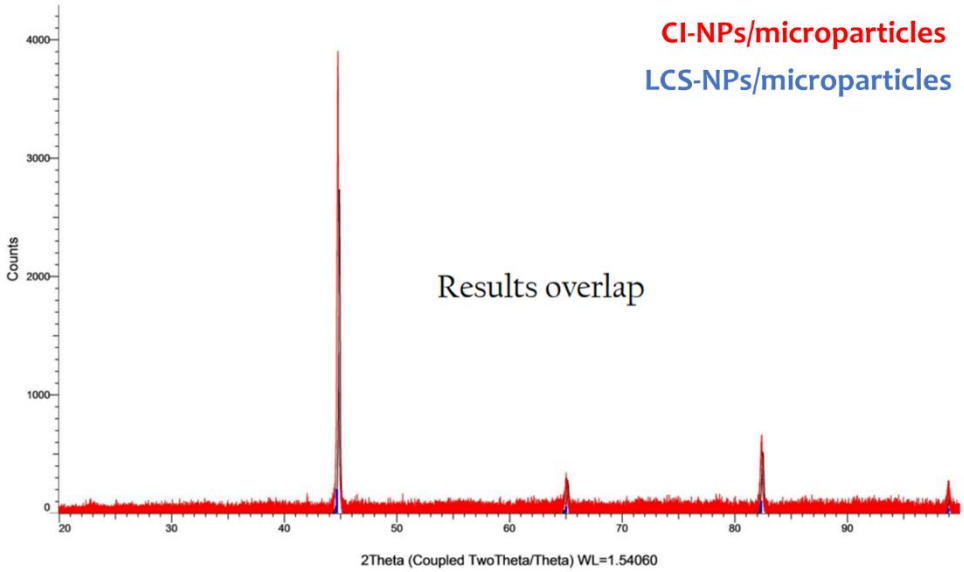

Figure 5-21: XRD results showing a comparison in the crystal structures of the bimodal powders composed of CI and LCS NPs.

To investigate the local chemical composition of the nanopowder regions after sintering, APT analysis was conducted to reveal the atomic-scale 3D chemical composition. Before the analysis, sharp tips at the area of interest around the interface sintered NPs/microparticle were prepared using a sequence of e-beam deposition and ion beam etching. Figure 5-22 shows the different steps for preparing the sample. The area of interest here was selected around the interface LCS-NPS/micropowder of sample sintered at 900°C using the SPS process. The area of interest was first covered with platinum. Then, a Toblerone-like wedge was prepared by a set of etchings on both sides of the sample and transferred for annular milling to produce sharp tips. An example of the APT tip that was analysed in this work is shown in figure 5-22.e with medium curvature of 200nm thickness at a distance of 500nm from the end of the tip.

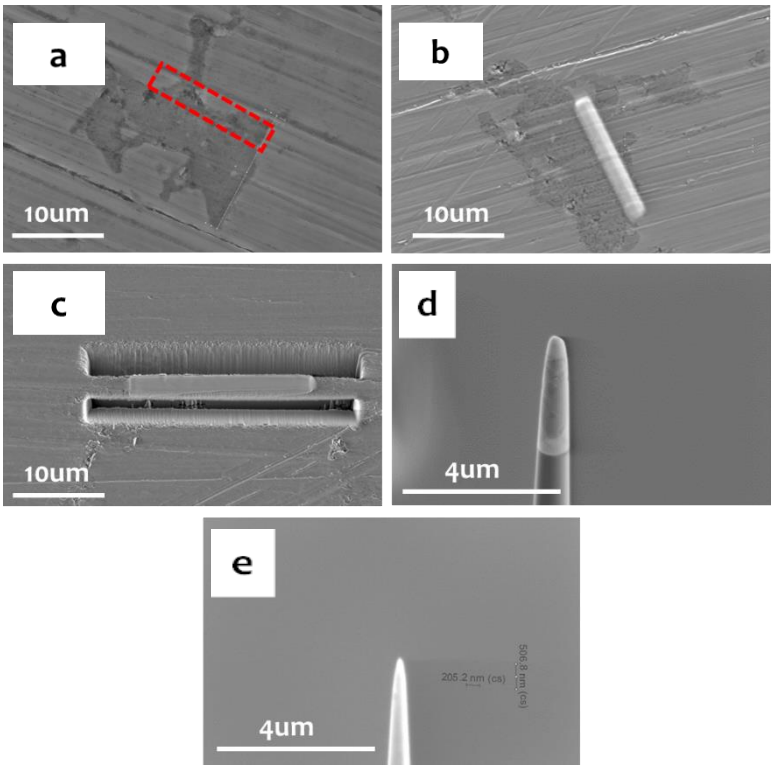

Figure 5-22: Sequence of production of the APT tip at the interface NPs/micropowder showing (a) the area of interest, (b) the platinum deposition seen with side view,(c) the preparation of the wedge seen with side view, (d) large tip of the sample, and (e) the final step with a sharp tip.

The results of the analysed sample using the laser-pulsed APT technic is shown in Figure 5-23. The distribution of the carbon and iron atoms are shown in the 3D representation of the tip, combining the atomic identification of the element and in position in the sample. From the obtained results, the distribution of the iron can be seen forming the matrix of the tip with high concentration regions in purple that represent the segregation of carbon atoms. Such configuration of a region rich in carbon atoms might indicate the presence of carbides. No other alloying elements have been detected in the analysis. The reason why the alloying element that was confirmed earlier in the prior analysis does not show here in the APT analysis is not clear. For this reason, the carbon-rich areas identified in the APT analysis can be attributed to the iron carbides. The mechanism of formation of these phases in a low carbon-based material is also an open question. The possible presence of carbon in the form of graphitic nanostructured has been reported by early work on arc discharge. However, whether these nanostructured can be source carbides formation is challenging to answer with these initial results.

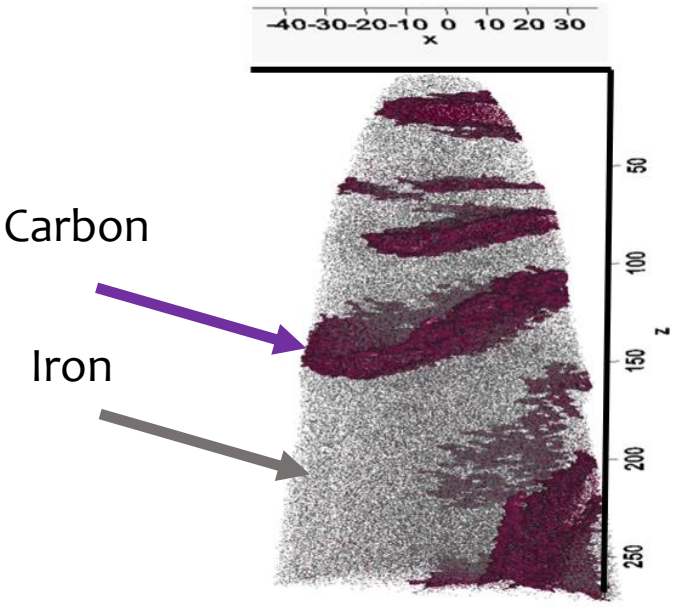

Figure 5-23: 3D representation of the iron-carbon atoms within the tip.

5.3.4 Mechanical properties of the sintered powder

The mechanical properties of the bimodal powder were investigated in terms of microhardness and the results were compared to the mono-sized microscopic powder. The hardness measurements were performed following Vickers's method where a pyramidal shaped tip penetrate the surface of the samples. The resulting dimension of the indent on the surface of the sample helped to determine the hardness of the material. Table 5-2 summarises the values of the hardness for the sintered microscopic and the bimodal powders.

Table 5-2: The results of the Vickers' hardness measurements.

	Sintered microscopic powder	***Sintered sample of microscopic powder + 5% NPs***
Hardness measurement (MPa)	***79.82***	***40,45***

In terms of hardness measurement, in other published reports on the SPS processing of bimodal particles, the hardness of the samples was higher in the presence of the nanoparticles in the initial mixture. It can be assumed that such an effect is mainly linked to the nanostructured phase with a high fraction in the initial nanostructured phase [288][289]. In this case, it is expected that the mechanical properties of the processed material follow the Hall-Petch effect and result in an advantageous compromise between the strength and ductility of the reference material. In the present study and with the low fraction of the NPs, the microhardness measured shows the contrary effect and reflects only on the micropowder properties and not the overall microstructure that is expected to be a mixture between nano- and micro- grains. The high hardness value obtained in the case of the micropowder is linked to the fine microstructure obtained upon cooling. Nevertheless, the contribution of the NPs is still accounted for through an indirect effect where the sintering mechanism might directly and indirectly affect the kinetics of the sintering and the reported microstructures.

5.4 Summary and discussion

The work undertaken herein had the objective to investigate the possibility to produce and process alloy based nanopowders and investigate its potential use as a sintering aid. Combining the size effect with the composition of the nanoparticles, this work focused on the fabrication of cast iron alloy based nanopowder using a technic of arc discharge and combining this nanopowder in a bimodal sized approach with large iron powder that was later sintered using the SPS technic. The morphology of the product powder was investigated and was found to present a large size distribution within the nanoscale range. The powder also displayed a core-shell structure where the oxide layer was covering the layer of the iron core. The composition of the LCS-NPs was investigated combining as set microscopy and spectroscopy analysis. The different results confirmed the presence of the oxide layers and the appearance of the metal compound of iron as the powder was sputtered. The composition analyses also confirm the presence of alloy elements that were part of the initial bulk electrode used for the production of the LCS-NPs. The densification behaviour of the CI-NPs nanopowder was then compared to the case of CI-NPs. It was found that in the case of the LCS-NPs, early densification occurs that was attributed to the possible difference in the chemical compositions of the nanopowders. It is assumed that the carbon present in the case of the CI-NPs is a source of self-reduction that occurs at low temperatures. In contrast, the densification of the LCS showed a late activation that was explained by the non-reduced oxide layers. At high temperatures, it is suggested that the oxygen bonded to the iron atoms is less stable and might be converted to other components. While not having a precise theory to back such a hypothesis, the LCS-NPs sample showed fast densification that was assumed inhibited by the oxide layer.

The densification of the LCS-NPs was also studied when the nanopowder was mixed to microscopic powder and sintered with SPS. The result of the sintering process was correlated with the sintering parameters and compared to both a bimodal mixture of CI-NPs/micropowder and microscopic powder samples. It was found that the densification of the samples correlated positively with the increase of the sintering temperature and the pressure. As SPS is a thermomechanical process where the consolidation of the powder depends on the temperature and the pressure applied, it is understood that the temperature provides thermal energy for the mass transfer of material during the sintering, while the pressure increase further the plastic deformation that helps to close the porosity. It is also worth noting that the LCS-NPs achieved higher densities than in the case of the nanopowders when the temperature and the pressure were varied. Such effect was attributed to the difference in the composition and the nanopowder that can contribute to the sintering mechanisms. When the fraction of NPS was increased further, the density of the LCS-NPs increased further when compared to lower fractions of NPs. This was explained by the increase of the contact area that results in an increased softening during the sintering and better densification.

Later on, the densification of the LCS-NPs was compared to the density of only sintered microscopic powder. It was found that the density of the sintered bimodal CS-NPs/microscopic powder was higher than that of the sintered microscopic powder. This was attributed to the presence of the nanoparticles at the interface of the microscopic powder, which allows further plastic deformation through the melted of the nanoscale powder. It is also worth noting at this point that the presence of the nanopowder phase at the boundaries of the microscopic powder resulted in a higher increase of the temperature with a lower value of current. This was directly linked to the nanosized effect of the contact area with the particles. The values of the densities seem reasonably promising in the field of gear production (above 95%). However, the difference in the microstructure was found here to affect the mechanical property of the sample and was indirectly linked to the presence of the nanopowder that affects the sintering process and parameters. In addition, although, the current variation might not seem tremendous, with a difference in the value of 50A, this approach can help further to decrease the energy consumption for a more efficient process

In this work, the presence of the nanopowder was found to potentially affect the SPS process. In fact, due to different kinetics and contact morphology, it is suggested that the NPS induce a combination of two mechanisms. When compared to the microscopic powder, the bimodal nanopowder showed a different microstructure that was

explained by the early activation of the nanoscale particle that melt. Upon melting, it is suggested that the latter phase welds directly to the microparticles and cover the large powders. However, microscopy observations revealed the presence of small island-like regions within the melted nanoparticles and were attributed to the initial large particles. These small regions are considered as melting debris that separates from the large particles during a spark event. Whether the arc discharge, in this case, occurs or not remains an open question, however, the presence of that debris, if found indeed originating from the microscopic powder, can indicate the occurrence of the discharge between the particles. Therefore, the sintering mechanism in such an approach may be a combination of melting of the nanoscale particles and arching which might occur at different regions within the powder.

The analysis of the local composition of the melted nanoparticles regions reveal the formation of carbides. Such phases are not expected if we take into consideration the carbon content present in the mixed powder. It was suggested that such carbon might originate from the graphitic nanostructure as a by-product of the arc discharge process used for the production of the nanopowders.

Chapter 6

6. Final Notes: Small, Comes With Multifunction, and Is The Next Big!

Throughout this thesis, we explored the nano realm to develop materials, characterisation technics and processes where we aimed at taking advantage of the advanced properties of the nanoscale materials in the modern context of manufacturing. The different results of the bridging between the two worlds are summarized in the following sections with the important results that makes the small world a necessity to solve multiple issues in the reality of today's needs and tomorrow's challenges.

6.1 Conclusion

In this work, silver nanoparticles were used in a hybrid bimodal sized approach with microscopic copper powder as a sintering aid. The powder was sintered using different parameters and the results were correlated with the density and the thermal properties of the sintered powder. We reported on a positive correlation between the density of the samples and the sintering parameters. As sintering involves thermal energy and mass transport, the increase in the temperature and pressure enhanced the densification of the powders. The thermal properties in the case of the hybrid bimodal Ag NPs/Cu were directly linked to the density of the materials and the sintering parameters. The presence of the silver around the copper was found to have an additional effect and acted as oxidation resistance. A value of the thermal conductivity as high as 276W/mK (which is close to 75% that of copper) was achieved. Despite the poor values of the electrical conductivity, we show herein the potential of using Ag NPs for low temperature sintering as a result of the size effect but also it is a contribution to the coating of the copper particles with an oxidation barrier that is expected to contribute into the heat transfer.

We also report on a new way of integrating the high porosity graphene foam in the heat management strategy. Initially, the thermal properties of the graphene foam were evaluated, and the effective thermal conductivity of the foam was found to compete with most metallic materials with a value as high as 319W/mK. In our approach, the low-temperature sintering Ag NPs has been exploited to both coat the foam with an additional layer of the coating and to attach the graphene foam on a thermoresistor that replicate the effect of a chip hot spot. The addition of the Ag NPs as a coating was reported to increase further the thermal conductivity of the foam while at the same time provide more strength to the foam. The thermal conductivity of the foam was then investigated and compared to nickel and non-coated foam. We found that the approach of graphene foam/Ag NPs presented in this work possessed better contact with the substrate as a result of the flexibility of the foam. The foam was then introduced as a container for paraffin that acts as a phase change material. We reported on the excellent ratio between the density of the material and its capacity to host PCM that successfully act to delay the temperature of the chip. Finally, for the first time in the work around the development of graphene foams, we highlighted the potential benefit of exploiting what we introduced as secondary microchannels. This additional porosity was found to have a non-negligeable effect on the heat dissipation capability of the foam, that can be used in more advanced concepts.

With the potential of graphene and the large interest in integrating the 2D material in heat management, we reported on a new simple way to produce graphene-coated micropowder as a filler in the case of thermally conductive adhesive. Using chemical vapour deposition, we investigated different production parameters and reported on the effect of the gas on the quality of the coating. The thermal stability of the coating was also studied herein, and we highlighted the potential benefit of using graphene as a coating around metallic particles. Such coating also plays a role of an oxidation barrier that prevents the degradation of the copper at high temperatures. More importantly, the thermal properties of the coated copper microscopic particles were evaluated in the thermally conductive adhesive.

Core/shell structured graphene-coated copper nanoparticles were successfully produced using an in-house immersed arc discharge approach. These nanoparticles were investigated in terms of structure, composition and morphology and were for the first time used as nano additives for water-based nanofluids. The temperature stability of the graphene-coated nanoparticles was evaluated, and we reported on the potential extra benefit of using this kind of particles. The carbon present around the nanoparticles can be used as the source of carbon for

the reduction of oxides in hybrid applications with no need to use extra reducing agents. While such properties might not be valuable in the nanofluid application, such an effect can be exploited when those particles are used in the formulation of pastes or the sintering of functional parts. Also, differential scanning calorimetry analysis showed the presence of an endothermic peak that can be a sign of the melting depression that is preserved by the coating. Such effect can directly be combined with the previous effect to sinter material at low temperatures. While this might not be the primary use of nanofiller in the nanofluids, we already see some reports taking advantage of the presence of phase change material in the fluid [290][291][292]. With such effect, the coated particle can contribute to the heat transfer while offering an extra protection effect to delay the surge in power in case of a special event to protect the electronic device. The thermal capability of this kind of nanofiller was evaluated in water by measuring the variation of the thermal conductivity. We reported on the increase of the thermal conductivity of the nanofluid with the increase of both temperature and fraction of the solid phase of the coated nanoparticles. Despite the low stability of the graphene-coated nanoparticles, we attributed such effect to the presence of the solid phase in the fluids with high thermal conductivity.

The surface modifications were introduced on such graphene coated nanoparticles to further increase their stability in water. Both chemical bonding and electrostatic functionalisation were explored. Graphene oxides coated copper nanoparticles and nitrogen-doped graphene-coated copper nanoparticles were successfully produced using arc discharge methods and the nanoparticles were characterized to confirm the presence of the oxygen functional groups and the nitrogen in the coating. The thermal conductivity of the two kinds of fillers was evaluated in water and term of the fraction of the nanofiller in the fluid and the temperature. We report on the competition between the 'intrinsic' thermal conductivity of the solid phases and their stability in the fluid, where nitrogen-doped coated nanoparticles might have the advantage at low concentrations of the fillers, but the oxidise coated nanoparticles quickly surpasses the thermal properties of the doped nanoparticles with a continuous increase in the thermal conductivity to reach a maximum of 103% enhancement.

The combination of the size effect with the composition effect of nanoparticles is explored in this work. For the first time, cast iron- and low carbon steel-based alloy nanopowder were produced using the arc discharge method and combined to spark plasma sintering. The produced nanopowder was characterized and the presence of alloying element was confirmed. The densification behaviour of the two powders was compared to the densification of a microscopic iron powder. We report on the advantage of using nanopowders as a sintering aid in the non-conventional spark plasma sintering. Such advantage appears in the form of enhanced densification with the decrease of energy consumption during the process. In addition, we also reported on an additional effect that rises from the presence of the nanopowders. Such nanoscale material can be used to tune the chemical composition of the inter-granular structure and result in the diversification of the properties of the powder. In addition, it was found that the presence of those tiny nanoparticles at the grains of the microparticles affect directly and indirectly the process of spark plasma sintering. The theory to explain the involvement of nanoparticles in the sintering process is still unclear. Herein, we proposed that the essence of the process occurs at the NPs region and continues further through the densification of the powder through the consolidation of the nanopowder/micropowder interface. Such effect was found to affect the sintering parameters and the microstructural aspect for the sintering samples. The bimodal sized approach showed good potential to explore further and develop an understanding of the different mechanisms involved.

At the beginning of this thesis, we asked three fundamental questions that are related to the integration of nanomaterials in heat management in electronics and low-temperature sintering. These questions are written here again for the sake of not going back to the first pages:

- Can nanoscale materials be integrated further into the heat dissipation of modern electronics?
- How can graphene-based materials benefit from new structures of fillers and is it possible to use modern production solutions to manufacture even more advanced graphene fillers?
- How can non-conventional manufacturing processes benefit from the use of nanoscale materials and their?

To answer these questions, we conducted a set of experiments and explored new approaches where we show the potential of using nanomaterials in modern processing and manufacturing. To the question on whether the

nanoscale can be further implemented in the heat dissipation strategies, we answer yes, and in many ways! The nanoscale effect that originates from the high surface energy of the particles can be used in modern electronics in the fabrication of components and interconnections but also to integrate other heat transfer solutions that bring further enhancement into the thermal capability of the electronic package. To the question on how new structured graphene-based powders can further be used in the service of advanced heat dissipation solutions, we answer that the supported graphene on the spherical substrate allows an optimal orientation to the heat transfer and might result in a continuous increase in the thermal conductivity of Thermally Conductive Adhesive and water-based nanofluids, but that will depend largely on the right condition on the structure and stability of the core/shell spherical particles. To the question of how modern sintering technics can exploit the nanoscale materials, we answer that the key is to dare to explore the variation of the chemical composition of the nanoparticles to take full control of the potential of the nanoscale material in the future of electronics and beyond.

6.2 Future insight

Where there is life, there is progress, and the twenty-first century is not going to be the exception. A wave of technologies and innovations see the light and give rise to new waves of technologies in their turn. Each product and concept come with a modern solution to solve an issue, which, again in its turns, bring a set of more complex and modern issues. In the reality of today's world, we see sustainability as a hot topic where humankind looks to its surroundings and understands, 'finally!' the young generation would claim, it is not about him/her. The concept of equality moved from an intra-generational issue to an inter-generational ethical topic, where finite resources should be exploited wisely.

In the journey into the modern era, a set of concepts, technologies and materials accompanied life and makes it more possible. From the stone age to the bronze age, to the iron age, and the silicon age, each era had a material that transformed the technological concepts and the social-economical aspects around the brief story of us. Today, we see the emergence of new driving forces where the necessity to develop new materials and technologies is a quantum leap for the next era. The nanoscale material graphene is thought to be up to the task, or almost! Leading the world towards smarter, faster, lighter, stronger, and more connected technologies. Seventeen years after its isolation, we have heard a lot. Graphene promises a lot and has the potential to outperform a large number of materials but, with a note of pessimism, graphene cannot be everywhere and do everything. Such an era that comes after the silicon age may not be about a material specifically but, with a note of optimism, perhaps be more of a class of materials. In such a class of materials, tiny structures such as graphene, other 2D structures and nanoscale materials can all be part to lead the transformation of the big world. Perhaps, at this moment we have learned that secret is not in a specific material, but more in the ability to understand the properties of the materials at their smallest scale to make them the best for what they are used for. From bottom-up methods to molecular-scale modelling and alloy design, there are big promises in tuning the properties of building blocks to build functional parts. Along the way, we need to understand that nanoscale materials and technologies are a revolution in themselves that requires redefining concepts and building a new way of thinking. Such field also requires the investment in new production and processing strategies where the question around sustainability and the safety of everyone is at the 'core' of its development, for the sake of the one who wrote this thesis, the ones who read it all the way through, those who gave up somewhere above, those who would never hear of it, and all those who will come after us. Nanoscale materials and technologies are perhaps not about reinventing the wheel, but maybe about the possibility to make it lighter, stronger, and better… or maybe removing the need for one! Like many things in this world, the best comes to exist when bridges are built, borders are crashed, and disciplines are connected.

The work presented in this thesis explores multiple aspects of the nano realm. From the production of nanoparticles to their processing, we bridged the potential of these materials to solve multiple issues at the same time. We developed hypothesises to explain and support our findings. However, with the potential that arises from these materials comes large complexity in understanding them. Additional effort is required to develop a deeper understanding of the different mechanisms that control the nano realm and its integration into the big world of industrial processing. From the issue of stability of nanoparticles in their host fluids to their multielement effect in the sintering, more tools and effort are needed to make the nanoscale materials inevitable options for advanced manufacturing and processing. Throughout this work, we saw that the two industrial applications of the material in electronics or for low-temperature sintering are not that different. Both industries, at the end of the day, care about more performant materials that can be processed at low temperatures and ensure high reliability and

favourable properties. The never-ending role of the material scientist goes in line with the never-ending trend of progress, understanding the potential of materials and putting them at the service of life.

Acknowledgement

This thesis comes to an end with the acknowledgement for those who made it possible. It has been a challenge in many aspects and a lot about creating dots here and there. These dots were bridged with deadlines, pressures, unknowns, doubts, frustrations, hesitations, failures, late nights, and early mornings. But it was also bridged with growth, opportunities, some success and most importantly people!

A word of gratitude goes to my supervisor, Professor Johan Liu, for the opportunity to drive this work and explore different aspects and new ideas. We did not make it to Nature! But we reported on new findings that we hope could rise interests and further effort to either confirm or reject our hypothesises. The science, and the reality behind the physics of materials at that small scale is bigger than what we can fully grasp at the moment.

A word of gratitude goes to Dr Lilei Ye, who, for large part of this work, was available to follow closely my progress, to correct my shoots and short-circuit my failures. I appreciated your availability as much as I appreciated our exchanges and positive discussions.

A word of recognition goes to Dr Torbjörn Nilsson, who kept a close eye on my work and put a throughout effort to challenge my reasoning. I believe by now, I learned that properties should never be described by 'high'. I always looked forwards to receiving your feedbacks.

A word of thanks goes to Dr Yifeng Fu, for the effort to accompany me to the end of this thesis. It has been a learning curve where having solid support played a critical role.

A word of respect goes to my colleagues, collaborators and those people who played a positive part in my days. This also includes everyone at Chalmers University whose tasks help to keep moving forwards.

Finally, a word of love goes to my people. Those who were my public in this process and were available to hear my complaints, support my failures, and cheer for my progress. I cherish every moment of your presence and I value the time of having you around.

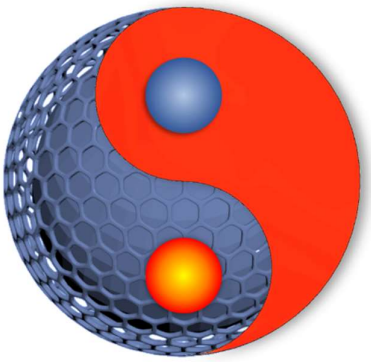

Hafid

References

[1] G. Moore, “Cramming more components onto integrated circuits,” *Electronics*, vol. 38, no. 8, 1965.

[2] C. A. MacK, “Fifty years of Moore’s law,” *IEEE Transactions on Semiconductor Manufacturing*, vol. 24, no. 2, pp. 202–207, May 2011, doi: 10.1109/TSM.2010.2096437.

[3] M. Lundstrom, “Moore’s Law Forever?” *Science*, vol. 299, no. 5604, pp. 210–211, Jan. 2003, doi: 10.1126/SCIENCE.1079567.

[4] ArunkumarAkhil *et al.*, “MCM-GPU: Multi-Chip-Module GPUs for Continued Performance Scalability,” *ACM SIGARCH Computer Architecture News*, vol. 45, no. 2, pp. 320–332, Jun. 2017, doi: 10.1145/3140659.3080231.

[5] W. Wolf, A. A. Jerraya, and G. Martin, “Multiprocessor system-on-chip (MPSoC) technology,” *IEEE Transactions on Computer-Aided Design of Integrated Circuits and Systems*, vol. 27, no. 10, pp. 1701–1713, Oct. 2008, doi: 10.1109/TCAD.2008.923415.

[6] S. M. Sohel Murshed and C. A. Nieto de Castro, “A critical review of traditional and emerging techniques and fluids for electronics cooling,” *Renewable and Sustainable Energy Reviews*, vol. 78. Elsevier Ltd, pp. 821–833, Oct. 01, 2017. doi: 10.1016/j.rser.2017.04.112.

[7] M. Treu *et al.*, “The role of silicon, silicon carbide and gallium nitride in power electronics,” *Technical Digest - International Electron Devices Meeting, IEDM*, 2012, doi: 10.1109/IEDM.2012.6478995.

[8] I. Khan, K. Saeed, and I. Khan, “Nanoparticles: Properties, applications and toxicities,” *Arabian Journal of Chemistry*, vol. 12, no. 7. Elsevier B.V., pp. 908–931, Nov. 01, 2019. doi: 10.1016/j.arabjc.2017.05.011.

[9] D. Astruc, “Introduction: Nanoparticles in Catalysis,” *Chemical Reviews*, vol. 120, no. 2. American Chemical Society, pp. 461–463, Jan. 22, 2020. doi: 10.1021/acs.chemrev.8b00696.

[10] S. Kiranmayee Manchili, “Role of nanopowder as sintering aid in the densification of water atomized ferrous powder,” Gothenburg, 2018.

[11] M. Green, L. Tian, P. Xiang, J. Murowchick, X. Tan, and X. Chen, “FeP nanoparticles: A new material for microwave absorption,” *Materials Chemistry Frontiers*, vol. 2, no. 6, pp. 1119–1125, May 2018, doi: 10.1039/C8QM00003D.

[12] T. Thu Trang Mai, P. Thu Ha, H. Nam Pham, and al -, “Magnetic fluid based on Fe3 O4 nanoparticles: Preparation and hyperthermia application,” *J. Phys.: Conf. Ser*, vol. 187, p. 12069, 2009, doi: 10.1088/1742-6596/187/1/012069.

[13] K. Rajan, I. Roppolo, A. Chiappone, S. Bocchini, D. Perrone, and A. Chiolerio, “Silver nanoparticle ink technology: State of the art,” *Nanotechnology, Science and Applications*, vol. 9. Dove Medical Press Ltd, p. 1, Jan. 11, 2016. doi: 10.2147/NSA.S68080.

[14] C. Kleinstreuer and Y. Feng, “me,” *Nanoscale Research Letters*, vol. 6, no. 1. Springer New York LLC, p. 229, Dec. 16, 2011. doi: 10.1186/1556-276X-6-229.

[15] F. Gao and Z. Gu, “Melting temperature of metallic nanoparticles,” in *Handbook of Nanoparticles*, Springer International Publishing, 2015, pp. 661–690. doi: 10.1007/978-3-319-15338-4_6.

[16] M. J. Coutts, M. B. Cortie, M. J. Ford, and A. M. McDonagh, “Rapid and controllable sintering of gold nanoparticle inks at room temperature using a chemical agent,” *Journal of Physical Chemistry C*, vol. 113, no. 4, pp. 1325–1328, Jan. 2009, doi: 10.1021/jp808927t.

[17] G. Vandevenne *et al.*, “A study on the thermal sintering process of silver nanoparticle inkjet inks to achieve smooth and highly conducting silver layers,” *physica status solidi (a)*, vol. 213, no. 6, pp. 1403–1409, Jun. 2016, doi: 10.1002/pssa.201533007.

[18] N. K. Roy *et al.*, “A comprehensive study of the sintering of copper nanoparticles using femtosecond, nanosecond, and continuous wave lasers,” *Journal of Micro and Nano-Manufacturing*, vol. 6, no. 1, pp. 1–21, Mar. 2018, doi: 10.1115/1.4038455.

[19] S. Liu, S. K. Tam, and K. M. Ng, “Dual-reductant synthesis of nickel nanoparticles for use in screen-printing conductive paste,” *Journal of Nanoparticle Research 2021 23:3*, vol. 23, no. 3, pp. 1–12, Mar. 2021, doi: 10.1007/S11051-021-05191-8.

[20] N. Vaisman *et al.*, “Increased Calcium Absorption From Synthetic Stable Amorphous Calcium Carbonate: Double-Blind Randomized Crossover Clinical Trial in Postmenopausal Women,” 2014, doi: 10.1002/jbmr.2255.

[21] S. Divi and A. Chatterjee, “Generalized nano-thermodynamic model for capturing size-dependent surface segregation in multi-metal alloy nanoparticles,” *RSC Advances*, vol. 8, no. 19, pp. 10409–10424, Mar. 2018, doi: 10.1039/c8ra00945g.

[22] R. Ferrando, R. L. Johnston, and C. Louis, “Recent advances in the chemical physics of nanoalloys,” *Physical Chemistry Chemical Physics*, vol. 17, no. 42, Royal Society of Chemistry, pp. 27920–27921, 2015. doi: 10.1039/c5cp90142a.

[23] A. v. Samokhin, N. v. Alexeev, A. A. Fadeev, and Y. v. Tsvetkov, “Formation of nanoparticles of binary W-Cu and ternary W-Ni-Fe systems in thermal plasma jet,” Jan. 2013, pp. 2P-167-2P – 167. doi: 10.1109/plasma.2012.6383723.

[24] J. Y. Huh, H. Lee, and W. C. Johnson, “Particle size effects on the coherent phase equilibria of binary nanoparticles,” *Metals and Materials International*, vol. 11, no. 5, pp. 357–363, 2005, doi: 10.1007/BF03027505.

[25] A. A. Baqer *et al.*, “Synthesis and characterization of binary (CuO)0.6(CeO2)0.4 nanoparticles via a simple heat treatment method,” *Results in Physics*, vol. 9, pp. 471–478, Jun. 2018, doi: 10.1016/j.rinp.2018.02.079.

[26] K. C. Pingali, S. Deng, and D. A. Rockstraw, “DIRECT SYNTHESIS OF RU-NI NANOPARTICLES WITH CORE-AND-SHELL STRUCTURE,” *Chemical Engineering Communications*, vol. 194, no. 6, pp. 780–786, Mar. 2007, doi: 10.1080/00986440701193795.

[27] M. Benelmekki and M. Benelmekki, “Designing binary nanoparticles,” in *Designing Hybrid Nanoparticles*, Morgan & Claypool Publishers, 2014. doi: 10.1088/978-1-6270-5469-0ch3.

[28] G. Barcaro, L. Sementa, and A. Fortunelli, “Nano (Evanescent-Wave)-Particle Image Velocimetry Nanoalloy Simulation,” 2016, doi: 10.1007/978-94-017-9780-1.

[29] V. M. Samsonov, I. v. Talyzin, A. Y. Kartoshkin, and S. A. Vasilyev, “Surface segregation in binary Cu–Ni and Au–Co nanoalloys and the core–shell structure stability/instability: thermodynamic and atomistic simulations,” *Applied Nanoscience (Switzerland)*, vol. 9, no. 1, pp. 119–133, Feb. 2019, doi: 10.1007/s13204-018-0895-5.

[30] M. Cui, H. Lu, H. Jiang, Z. Cao, and X. Meng, “Phase Diagram of Continuous Binary Nanoalloys: Size, Shape, and Segregation Effects OPEN,” *Nature Publishing Group*, 2017, doi: 10.1038/srep41990.

[31] R. C. Chu, R. E. Simons, M. J. Ellsworth, R. R. Schmidt, and V. Cozzolino, “Review of cooling technologies for computer products,” *IEEE Transactions on Device and Materials Reliability*, vol. 4, no. 4, pp. 568–585, Dec. 2004, doi: 10.1109/TDMR.2004.840855.

[32] Xingcun Colin Tong, *Advanced Materials for Thermal Management of Electronic Packaging*, vol. 30. New York: Springer, 2011. [Online]. Available: http://www.springer.com/series/4076

[33] M. D. Shende and A. Mahalle, “Cooling Of Electronic Equipments with Heat Sink: A Review of Literature,” *IOSR Journal of Mechanical and Civil Engineering*, vol. 5, no. 2, pp. 56–61, Accessed: Oct. 21, 2021. [Online]. Available: www.iosrjournals.org

[34] J. Felba, “Thermally conductive adhesives in electronics,” *Advanced Adhesives in Electronics: Materials, Properties and Applications*, pp. 15–52, Jan. 2011, doi: 10.1533/9780857092892.1.15.

[35] H. W. Cui, D. S. Li, Q. Fan, and H. X. Lai, “Electrical and mechanical properties of electrically conductive adhesives from epoxy, micro-silver flakes, and nano-hexagonal boron nitride particles after humid and thermal aging,” *International Journal of Adhesion and Adhesives*, vol. 44, pp. 232–236, Jul. 2013, doi: 10.1016/J.IJADHADH.2013.03.007.

[36] S. Magdassi, A. Bassa, Y. Vinetsky, and A. Kamyshny, “Silver Nanoparticles as Pigments for Water-Based Ink-Jet Inks,” 2003, doi: 10.1021/cm021804b.

[37] S. Wang, M. Li, H. Ji, and C. Wang, “Rapid pressureless low-temperature sintering of Ag nanoparticles for high-power density electronic packaging,” *Scripta Materialia*, vol. 69, no. 11–12, pp. 789–792, Dec. 2013, doi: 10.1016/J.SCRIPTAMAT.2013.08.031.

[38] B. T. Anto, S. Sivaramakrishnan, L.-L. Chua, and P. K. H. Ho, “Hydrophilic Sparse Ionic Monolayer-Protected Metal Nanoparticles: Highly Concentrated Nano-Au and Nano-Ag ‘Inks’ that can be Sintered to Near-Bulk Conductivity at 150 °C,” *Advanced Functional Materials*, vol. 20, no. 2, pp. 296–303, Jan. 2010, doi: 10.1002/ADFM.200901336.

[39] H. M. Breitling and R. E. Hummel, “Electromigration in thin silver, copper, gold, indium, tin, lead and magnesium films,” *Journal of Physics and Chemistry of Solids*, vol. 33, no. 4, pp. 845–852, Jan. 1972, doi: 10.1016/S0022-3697(72)80101-X.

[40] X. Liu and Y. Zhou, “Electrochemical Synthesis and Room Temperature Oxidation Behavior of Cu Nanowires,” *Journal of Materials Research 2005 20:9*, vol. 20, no. 9, pp. 2371–2378, Sep. 2005, doi: 10.1557/JMR.2005.0288.

[41] S. Magdassi, M. Grouchko, and A. Kamyshny, “Copper Nanoparticles for Printed Electronics: Routes Towards Achieving Oxidation Stability,” *Materials 2010, Vol. 3, Pages 4626-4638*, vol. 3, no. 9, pp. 4626–4638, Sep. 2010, doi: 10.3390/MA3094626.

[42] K. E. J. Lehtinen and M. R. Zachariah, “Energy accumulation in nanoparticle collision and coalescence processes,” *Journal of Aerosol Science*, vol. 33, no. 2, pp. 357–368, Feb. 2002, doi: 10.1016/S0021-8502(01)00177-X.

[43] K. K. Nanda, A. Maisels, and F. E. Kruis, “Surface Tension and Sintering of Free Gold Nanoparticles,” *Journal of Physical Chemistry C*, vol. 112, no. 35, pp. 13488–13491, Sep. 2008, doi: 10.1021/JP803934N.

[44] S. Arcidiacono, N. R. Bieri, D. Poulikakos, and C. P. Grigoropoulos, “On the coalescence of gold nanoparticles,” *International Journal of Multiphase Flow*, vol. 30, no. 7–8, pp. 979–994, Jul. 2004, doi: 10.1016/J.IJMULTIPHASEFLOW.2004.03.006.

[45] W. S. Coblenz, J. M. Dynys, R. M. Cannon, and R. L. Coble, “Initial Stage Solid State Sintering Models,” *Sintering Processes*, pp. 141–157, 1980, doi: 10.1007/978-1-4899-5301-8_12.

[46] M. S, G. M, B. O, and K. A, “Triggering the sintering of silver nanoparticles at room temperature,” *ACS nano*, vol. 4, no. 4, pp. 1943–1948, Apr. 2010, doi: 10.1021/NN901868T.

[47] D. ji Yu, X. Chen, G. Chen, G. quan Lu, and Z. qiang Wang, “Applying Anand model to low-temperature sintered nanoscale silver paste chip attachment,” *Materials & Design*, vol. 30, no. 10, pp. 4574–4579, Dec. 2009, doi: 10.1016/J.MATDES.2009.04.006.

[48] K. S. Tan and K. Y. Cheong, “Physical and electrical characteristics of silver-copper nanopaste as alternative die-attach,” *IEEE Transactions on Components, Packaging and Manufacturing Technology*, vol. 4, no. 1, pp. 8–15, 2014, doi: 10.1109/TCPMT.2013.2285128.

[49] H. Zheng, G.-Q. Lu, K. D. T. Ngo, L. J. Guido, and A. O. Aning, “Die-Attachment on Copper by Nanosilver Sintering: Processing, Characterization and Reliability,” 2015.

[50] C. Weber, M. Hutter, S. Schmitz, and K. D. Lang, “Dependency of the porosity and the layer thickness on the reliability of Ag sintered joints during active power cycling,” *Proceedings - Electronic Components and Technology Conference*, vol. 2015-July, pp. 1866–1873, Jul. 2015, doi: 10.1109/ECTC.2015.7159854.

[51] T. Herboth, M. Guenther, A. Fix, and J. Wilde, “Failure mechanisms of sintered silver interconnections for power electronic applications,” *Proceedings - Electronic Components and Technology Conference*, pp. 1621–1627, 2013, doi: 10.1109/ECTC.2013.6575789.

[52] Y. MH, J. SJ, and K. HS, “Multi-pulse flash light sintering of bimodal Cu nanoparticle-ink for highly conductive printed Cu electrodes,” *Nanotechnology*, vol. 28, no. 20, Apr. 2017, doi: 10.1088/1361-6528/AA6CDA.

[53] Y. Y. Dai *et al.*, “Enhanced copper micro/nano-particle mixed paste sintered at low temperature for 3D interconnects,” *Applied Physics Letters*, vol. 108, no. 26, p. 263103, Jun. 2016, doi: 10.1063/1.4954966.

[54] S. K. Tam, K. Y. Fung, and K. M. Ng, “Copper pastes using bimodal particles for flexible printed electronics,” *Journal of Materials Science 2015 51:4*, vol. 51, no. 4, pp. 1914–1922, Oct. 2015, doi: 10.1007/S10853-015-9498-7.

[55] S. S. Anandan and V. Ramalingam, “Thermal management of electronics: A review of literature,” *Thermal Science*, vol. 12, no. 2. pp. 5–25, 2008. doi: 10.2298/TSCI0802005A.

[56] D. Wood *et al.*, “Passivated busbars from screen-printed low-temperature copper paste,” in *Energy Procedia*, Jan. 2014, vol. 55, pp. 724–732. doi: 10.1016/j.egypro.2014.08.052.

[57] P. Panek, R. P. Socha, G. Putynkowski, and A. Slaoui, “The New Copper Composite of Pastes for Si Solar Cells Front Electrode Application,” in *Energy Procedia*, Aug. 2016, vol. 92, pp. 962–970. doi: 10.1016/j.egypro.2016.07.108.

[58] B. Zhang *et al.*, “In-air sintering of copper nanoparticle paste with pressure-assistance for die attachment in high power electronics,” *Journal of Materials Science: Materials in Electronics*, vol. 32, no. 4, pp. 4544–4555, Feb. 2021, doi: 10.1007/s10854-020-05196-4.

[59] J. Lee *et al.*, “Fabrication of sinter-free conductive Cu paste using sub-10 nm copper nanoparticles,” *Journal of Materials Chemistry C*, vol. 5, no. 47, pp. 12507–12512, Dec. 2017, doi: 10.1039/c7tc02893h.

[60] Z. Zhang *et al.*, “Low-temperature and pressureless sinter joining of Cu with micron/submicron Ag particle paste in air,” *Journal of Alloys and Compounds*, vol. 780, pp. 435–442, Apr. 2019, doi: 10.1016/j.jallcom.2018.11.251.

[61] A. Zehri, L. Ye, and J. Liu, “Low-Temperature Sintering Bimodal Micro Copper-Nano Silver for Electrical Power Devices,” Nov. 2018. doi: 10.1109/ESTC.2018.8546502.

[62] K. N. Tu, “Reliability challenges in 3D IC packaging technology,” *Microelectronics Reliability*, vol. 51, pp. 517–523, 2011, doi: 10.1016/j.microrel.2010.09.031.

[63] J. Richard Culham, W. A. Khan, M. Michael Yovanovich, and Y. S. Muzychka, “The Influence of Material Properties and Spreading Resistance in the Thermal Design of Plate Fin Heat Sinks,” *Journal of Electronic Packaging*, vol. 129, no. 1, pp. 76–81, Mar. 2007, doi: 10.1115/1.2429713.

[64] T. C. Hung, Y. X. Huang, and W. M. Yan, “Thermal performance analysis of porous-microchannel heat sinks with different configuration designs,” *International Journal of Heat and Mass Transfer*, vol. 66, pp. 235–243, Nov. 2013, doi: 10.1016/J.IJHEATMASSTRANSFER.2013.07.019.

[65] K. S. Koyale, V. D. Kudale, and V. G. Talandage, “Review: Heat Transfer Coefficient in Pin-Fins,” *International Journal of Scientific & Engineering Research*, vol. 8, no. 4, 2017, Accessed: Oct. 22, 2021. [Online]. Available: http://www.ijser.org

[66] Z. Khattak and H. M. Ali, “Air cooled heat sink geometries subjected to forced flow: A critical review,” *International Journal of Heat and Mass Transfer*, vol. 130, pp. 141–161, Mar. 2019, doi: 10.1016/J.IJHEATMASSTRANSFER.2018.08.048.

[67] P. Bhandari and Y. K. Prajapati, “Thermal performance of open microchannel heat sink with variable pin fin height,” *International Journal of Thermal Sciences*, vol. 159, p. 106609, Jan. 2021, doi: 10.1016/J.IJTHERMALSCI.2020.106609.

[68] Z. Duan, H. Ma, B. He, L. Su, and X. Zhang, “Pressure Drop of Microchannel Plate Fin Heat Sinks,” *Micromachines 2019, Vol. 10, Page 80*, vol. 10, no. 2, p. 80, Jan. 2019, doi: 10.3390/MI10020080.

[69] L. H. Saw, Y. Ye, M. C. Yew, W. T. Chong, M. K. Yew, and T. C. Ng, “Computational fluid dynamics simulation on open cell aluminium foams for Li-ion battery cooling system,” *Applied Energy*, vol. 204, pp. 1489–1499, 2017, doi: 10.1016/j.apenergy.2017.04.022.

[70] J. Marx, M. Portanova, and A. Rabiei, “Ballistic performance of composite metal foam against large caliber threats,” *Composite Structures*, vol. 225, Oct. 2019, doi: 10.1016/j.compstruct.2019.111032.

[71] J. W. Paek, B. H. Kang, S. Y. Kim, and J. M. Hyun, “Effective Thermal Conductivity and Permeability of Aluminum Foam Materials 1,” 2000.

[72] D. S. Smith *et al.*, “Thermal conductivity of porous materials,” 2013, doi: 10.1557/jmr.2013.179.

[73] Y. Amani, A. Takahashi, P. Chantrenne, S. Maruyama, S. Dancette, and E. Maire, “Thermal conductivity of highly porous metal foams: Experimental and image based finite element

analysis," *International Journal of Heat and Mass Transfer*, vol. 122, pp. 1–10, Jul. 2018, doi: 10.1016/j.ijheatmasstransfer.2018.01.050.

[74] G. L. Vignoles and A. Ortona, "Numerical study of effective heat conductivities of foams by coupled conduction and radiation," *International Journal of Thermal Sciences*, vol. 109, pp. 270–278, 2016, doi: 10.1016/j.ijthermalsci.2016.06.013ï.

[75] C. Mille and R. W. Corkery, "A structural and thermal conductivity study of highly porous, hierarchical polyhedral nanofoam shells made by condensing silica in microemulsion films on the surface of emulsified oil drops," *Journal of Materials Chemistry A*, vol. 1, no. 5, pp. 1849–1859, Feb. 2013, doi: 10.1039/c2ta00451h.

[76] P. Goetze *et al.*, "Sensitivity analysis of effective thermal conductivity of open-cell ceramic foams using a simplified model based on detailed structure," *Special Topics and Reviews in Porous Media*, vol. 6, no. 1, pp. 1–10, 2015, doi: 10.1615/SpecialTopicsRevPorousMedia.v6.i1.10.

[77] I. Ghosh, "Heat transfer correlation for high-porosity open-cell foam," *International Journal of Heat and Mass Transfer*, vol. 52, no. 5–6, pp. 1488–1494, Feb. 2009, doi: 10.1016/j.ijheatmasstransfer.2008.07.047.

[78] J. Skibinski, K. Cwieka, S. H. Ibrahim, and T. Wejrzanowski, "Influence of pore size variation on thermal conductivity of open-porous foams," *Materials*, vol. 12, no. 12, Jun. 2019, doi: 10.3390/ma12122017.

[79] K. Lafdi, O. Mesalhy, and S. Shaikh, "Experimental study on the influence of foam porosity and pore size on the melting of phase change materials," *Journal of Applied Physics*, vol. 102, no. 8, 2007, doi: 10.1063/1.2802183.

[80] V. V. Calmidi and R. L. Mahajan, "The effective thermal conductivity of high porosity fibrous metal foams," *Journal of Heat Transfer*, vol. 121, no. 2, pp. 466–471, 1999, doi: 10.1115/1.2826001.

[81] W. Cheong Tan *et al.*, "Investigation of water cooled aluminium foam heat sink for concentrated photovoltaic solar cell," in *IOP Conference Series: Earth and Environmental Science*, Jul. 2019, vol. 268, no. 1. doi: 10.1088/1755-1315/268/1/012007.

[82] V. v Calmidi and R. L. Mahajan, "The Effective Thermal Conductivity of High Porosity Fibrous Metal Foams," 1999. Accessed: Oct. 09, 2019. [Online]. Available: https://asmedigitalcollection.asme.org/heattransfer/article-pdf/121/2/466/5758204/466_1.pdf

[83] A. August, A. Reiter, A. Kneer, M. Selzer, and B. Nestler, "Effective Thermal Conductivity of Composite Materials Based on Open Cell Foams," 2018. Accessed: Nov. 12, 2019. [Online]. Available: http://cansrg.com/journals/hmtrj/

[84] N. Babcsán, I. Mészáros, and N. Hegman, "Thermal and Electrical Conductivity Measurements on Aluminum Foams," *Materialwissenschaft und Werkstofftechnik*, vol. 34, no. 4, pp. 391–394, Apr. 2003, doi: 10.1002/mawe.200390081.

[85] C. Y. Zhao, "Review on thermal transport in high porosity cellular metal foams with open cells," *International Journal of Heat and Mass Transfer*, vol. 55, no. 13–14, pp. 3618–3632, 2012, doi: 10.1016/j.ijheatmasstransfer.2012.03.017.

[86] R. Chein, H. Yang, T. H. Tsai, and C. Lu, "Experimental study of heat sink performance using copper foams fabricated by electroforming," in *Microsystem Technologies*, Jul. 2010, vol. 16, no. 7, pp. 1157–1164. doi: 10.1007/s00542-009-0950-y.

[87] W. Cheong Tan *et al.*, “Investigation of water cooled aluminium foam heat sink for concentrated photovoltaic solar cell,” *IOP Conf. Ser.: Earth Environ. Sci*, vol. 268, p. 12007, 2019, doi: 10.1088/1755-1315/268/1/012007.

[88] A. Sharma, V. V. Tyagi, C. R. Chen, and D. Buddhi, “Review on thermal energy storage with phase change materials and applications,” *Renewable and Sustainable Energy Reviews*, vol. 13, no. 2, pp. 318–345, Feb. 2009, doi: 10.1016/J.RSER.2007.10.005.

[89] J. Maxa, A. Novikov, and M. Nowottnick, “Thermal Peak Management Using Organic Phase Change Materials for Latent Heat Storage in Electronic Applications,” *Materials*, vol. 11, no. 1, p. 31, Dec. 2017, doi: 10.3390/ma11010031.

[90] S. M. Sadrameli, F. Motaharinejad, M. Mohammadpour, and F. Dorkoosh, “An experimental investigation to the thermal conductivity enhancement of paraffin wax as a phase change material using diamond nanoparticles as a promoting factor,” *Heat and Mass Transfer/Waerme- und Stoffuebertragung*, vol. 55, no. 6, pp. 1801–1808, Jun. 2019, doi: 10.1007/s00231-018-02536-3.

[91] M. Karkri, M. Lachheb, D. Gossard, S. ben Nasrallah, and M. A. Almaadeed, “Improvement of thermal conductivity of paraffin by adding expanded graphite”, doi: 10.1177/0021998315612535.

[92] Tingting Qian, Jinhong Li, Xin Min, Weimin Guan, Yong Deng, and Lei Ning, “Enhanced thermal conductivity of PEG/diatomite shape-stabilized phase change materials with Ag nanoparticles for thermal energy storage,” *Journal of Materials Chemistry A*, vol. 3, no. 16, pp. 8526–8536, Apr. 2015, doi: 10.1039/C5TA00309A.

[93] S. Harikrishnan, M. Deenadhayalan, and S. Kalaiselvam, “Experimental investigation of solidification and melting characteristics of composite PCMs for building heating application,” *Energy Conversion and Management*, vol. 86, pp. 864–872, Oct. 2014, doi: 10.1016/J.ENCONMAN.2014.06.042.

[94] B. Eanest Jebasingh and A. Valan Arasu, “A detailed review on heat transfer rate, supercooling, thermal stability and reliability of nanoparticle dispersed organic phase change material for low-temperature applications,” *Materials Today Energy*, vol. 16, p. 100408, Jun. 2020, doi: 10.1016/J.MTENER.2020.100408.

[95] R. Baby and C. Balaji, “Thermal performance of a PCM heat sink under different heat loads: An experimental study,” *International Journal of Thermal Sciences*, vol. 79, pp. 240–249, May 2014, doi: 10.1016/J.IJTHERMALSCI.2013.12.018.

[96] X. Yang *et al.*, “Comparison of direct numerical simulation with volume-averaged method on composite phase change materials for thermal energy storage,” *Applied Energy*, vol. 229, pp. 700–714, Nov. 2018, doi: 10.1016/j.apenergy.2018.08.012.

[97] W. Hao Li *et al.*, “Thermal Conductivity Enhancement and Shape Stabilization of Phase-Change Materials Using Three-Dimensional Graphene and Graphene Powder”, doi: 10.1021/acs.energyfuels.9b03013.

[98] K. Chintakrinda, R. D. Weinstein, and A. S. Fleischer, “A direct comparison of three different material enhancement methods on the transient thermal response of paraffin phase change material exposed to high heat fluxes,” *International Journal of Thermal Sciences*, vol. 50, no. 9, pp. 1639–1647, Sep. 2011, doi: 10.1016/J.IJTHERMALSCI.2011.04.005.

[99] S. F. Hosseinizadeh, F. L. Tan, and S. M. Moosania, “Experimental and numerical studies on performance of PCM-based heat sink with different configurations of internal fins,” *Applied*

Thermal Engineering, vol. 31, no. 17–18, pp. 3827–3838, Dec. 2011, doi: 10.1016/J.APPLTHERMALENG.2011.07.031.

[100] R. Baby and C. Balaji, "Experimental investigations on thermal performance enhancement and effect of orientation on porous matrix filled PCM based heat sink," *International Communications in Heat and Mass Transfer*, vol. 46, pp. 27–30, Aug. 2013, doi: 10.1016/J.ICHEATMASSTRANSFER.2013.05.018.

[101] R. Kalbasi, "Introducing a novel heat sink comprising PCM and air - Adapted to electronic device thermal management," *International Journal of Heat and Mass Transfer*, vol. 169, p. 120914, Apr. 2021, doi: 10.1016/J.IJHEATMASSTRANSFER.2021.120914.

[102] Z. Chen, D. Gao, and J. Shi, "Experimental and numerical study on melting of phase change materials in metal foams at pore scale," *International Journal of Heat and Mass Transfer*, vol. 72, pp. 646–655, May 2014, doi: 10.1016/j.ijheatmasstransfer.2014.01.003.

[103] E. Fleming, S. Wen, L. Shi, and A. K. da Silva, "Experimental and theoretical analysis of an aluminum foam enhanced phase change thermal storage unit," *International Journal of Heat and Mass Transfer*, vol. 82, pp. 273–281, 2015, doi: 10.1016/j.ijheatmasstransfer.2014.11.022.

[104] C. Y. Zhao, W. Lu, and Y. Tian, "Heat transfer enhancement for thermal energy storage using metal foams embedded within phase change materials (PCMs)," *Solar Energy*, vol. 84, no. 8, pp. 1402–1412, Aug. 2010, doi: 10.1016/j.solener.2010.04.022.

[105] X. Yang, Z. Guo, Y. Liu, L. Jin, and Y. L. He, "Effect of inclination on the thermal response of composite phase change materials for thermal energy storage," *Applied Energy*, vol. 238, pp. 22–33, Mar. 2019, doi: 10.1016/j.apenergy.2019.01.074.

[106] G. Wang, G. Wei, C. Xu, X. Ju, Y. Yang, and X. Du, "Numerical simulation of effective thermal conductivity and pore-scale melting process of PCMs in foam metals," *Applied Thermal Engineering*, vol. 147, pp. 464–472, Jan. 2019, doi: 10.1016/j.applthermaleng.2018.10.106.

[107] Q. Ren, Y.-L. He, K.-Z. Su, and C. L. Chan, "Investigation of the effect of metal foam characteristics on the PCM melting performance in a latent heat thermal energy storage unit by pore-scale lattice Boltzmann modeling," *Numerical Heat Transfer, Part A: Applications*, vol. 72, no. 10, pp. 745–764, Nov. 2017, doi: 10.1080/10407782.2017.1412224.

[108] H. Ji *et al.*, "Enhanced thermal conductivity of phase change materials with ultrathin-graphite foams for thermal energy storage," *Energy and Environmental Science*, vol. 7, no. 3, pp. 1185–1192, Mar. 2014, doi: 10.1039/c3ee42573h.

[109] Z. Zhang and Y. Li, "Experimental study of a passive thermal management system using copper foam-paraffin composite for lithium ion batteries," in *Energy Procedia*, 2017, vol. 142, pp. 2403–2408. doi: 10.1016/j.egypro.2017.12.174.

[110] Z. Wang, Z. Zhang, L. Jia, and L. Yang, "Paraffin and paraffin/aluminum foam composite phase change material heat storage experimental study based on thermal management of Li-ion battery," *Applied Thermal Engineering*, vol. 78, pp. 428–436, Mar. 2015, doi: 10.1016/j.applthermaleng.2015.01.009.

[111] A. Hussain, C. Y. Tso, and C. Y. H. Chao, "Experimental investigation of a passive thermal management system for high-powered lithium ion batteries using nickel foam-paraffin composite," *Energy*, vol. 115, pp. 209–218, Nov. 2016, doi: 10.1016/j.energy.2016.09.008.

[112] H. M. Teamah, “Comprehensive review of the application of phase change materials in residential heating applications,” *Alexandria Engineering Journal*, vol. 60, no. 4, pp. 3829–3843, Aug. 2021, doi: 10.1016/J.AEJ.2021.02.053.

[113] A. Hussain, I. H. Abidi, C. Y. Tso, K. C. Chan, Z. Luo, and C. Y. H. Chao, “Thermal management of lithium ion batteries using graphene coated nickel foam saturated with phase change materials,” *International Journal of Thermal Sciences*, vol. 124, pp. 23–35, Feb. 2018, doi: 10.1016/j.ijthermalsci.2017.09.019.

[114] S. M. S. Murshed, “Introductory Chapter: Electronics Cooling — An Overview,” *Electronics Cooling*, Jun. 2016, doi: 10.5772/63321.

[115] Y. F. Maydanik, S. V. Vershinin, M. A. Korukov, and J. M. Ochterbeck, “Miniature loop heat pipes-a promising means for cooling electronics,” *IEEE Transactions on Components and Packaging Technologies*, vol. 28, no. 2, pp. 290–296, Jun. 2005, doi: 10.1109/TCAPT.2005.848487.

[116] B. A. K. Abu-Hijleh, “Enhanced solar still performance using water film cooling of the glass cover,” *Desalination*, vol. 107, no. 3, pp. 235–244, Dec. 1996, doi: 10.1016/S0011-9164(96)00165-8.

[117] M. S. Sehmbey, L. C. Chow, M. R. Pais, and T. Mahefkey, “High heat flux spray cooling of electronics,” *Proceedings*, vol. 324, pp. 903–909, 2008, doi: 10.1063/1.47084.

[118] J. Buongiorno *et al.*, “A benchmark study on the thermal conductivity of nanofluids,” *J. Appl. Phys*, vol. 106, p. 94312, 2009, doi: 10.1063/1.3245330.

[119] V. Sridhara and L. N. Satapathy, “Al2O3-based nanofluids: a review.,” *Nanoscale research letters*, vol. 6, no. 1, p. 456, Jul. 2011, doi: 10.1186/1556-276X-6-456.

[120] G. Żyła, J. Fal, S. Bikić, and M. Wanic, “Ethylene glycol based silicon nitride nanofluids: An experimental study on their thermophysical, electrical and optical properties,” *Physica E: Low-Dimensional Systems and Nanostructures*, vol. 104, pp. 82–90, Oct. 2018, doi: 10.1016/j.physe.2018.07.023.

[121] O. A. Alawi, N. A. C. Sidik, H. W. Xian, T. H. Kean, and S. N. Kazi, “Thermal conductivity and viscosity models of metallic oxides nanofluids,” *International Journal of Heat and Mass Transfer*, vol. 116, pp. 1314–1325, Jan. 2018, doi: 10.1016/j.ijheatmasstransfer.2017.09.133.

[122] L. M. Moreira *et al.*, “Thermo-optical properties of silver and gold nanofluids,” *Journal of Thermal Analysis and Calorimetry*, vol. 114, no. 2, pp. 557–564, Nov. 2013, doi: 10.1007/s10973-013-3021-7.

[123] N. A. C. Sidik, M. N. A. W. M. Yazid, and S. Samion, “A review on the use of carbon nanotubes nanofluid for energy harvesting system,” *International Journal of Heat and Mass Transfer*, vol. 111. Elsevier Ltd, pp. 782–794, Aug. 01, 2017. doi: 10.1016/j.ijheatmasstransfer.2017.04.047.

[124] F. Selimefendigil and A. J. Chamkha, “MHD mixed convection of nanofluid in a three-dimensional vented cavity with surface corrugation and inner rotating cylinder,” *International Journal of Numerical Methods for Heat & Fluid Flow*, vol. 30, no. 4, pp. 1637–1660, Apr. 2019, doi: 10.1108/HFF-10-2018-0566.

[125] W. Duangthongsuk and S. Wongwises, “Heat transfer enhancement and pressure drop characteristics of TiO2–water nanofluid in a double-tube counter flow heat exchanger,”

International Journal of Heat and Mass Transfer, vol. 52, no. 7–8, pp. 2059–2067, Mar. 2009, doi: 10.1016/J.IJHEATMASSTRANSFER.2008.10.023.

[126] Z. Uddin and S. Harmand, "Natural convection heat transfer of nanofluids along a vertical plate embedded in porous medium," *Nanoscale Research Letters*, vol. 8, no. 1, pp. 1–19, Dec. 2013, doi: 10.1186/1556-276X-8-64.

[127] R. Bubbico, G. Piero Celata, F. D'annibale, B. Mazzarotta, and C. Menale, "Comparison of the Heat Transfer Efficiency of Nanofluids," in *CHEMICAL ENGINEERING TRANSACTIONS*, 2015, vol. 43. doi: 10.3303/CET1543118.

[128] N. Ali, J. A. Teixeira, and A. Addali, "A Review on Nanofluids: Fabrication, Stability, and Thermophysical Properties," *Journal of Nanomaterials*, vol. 2018, 2018, doi: 10.1155/2018/6978130.

[129] E. v. Timofeeva, J. L. Routbort, and D. Singh, "Particle shape effects on thermophysical properties of alumina nanofluids," *Journal of Applied Physics*, vol. 106, no. 1, p. 014304, Jul. 2009, doi: 10.1063/1.3155999.

[130] A. Bhattad and J. Sarkar, "Effects of nanoparticle shape and size on the thermohydraulic performance of plate evaporator using hybrid nanofluids," *Journal of Thermal Analysis and Calorimetry*, pp. 1–13, Dec. 2019, doi: 10.1007/s10973-019-09146-z.

[131] S. A. Angayarkanni, A. K. Mishra, and J. Philip, "Effect of Polymeric Additives on Thermal and Electrical Conductivity of Nanofluids," *Journal of Nanofluids*, vol. 5, no. 5, pp. 661–668, Jul. 2016, doi: 10.1166/jon.2016.1263.

[132] G. P. Lakhawat *et al.*, "Effect of nonionic surfactant additives on the performance of nanofluid in the heat exchanger," *Int. J. Nano Dimens*, vol. 8, no. 1, pp. 18–30, Mar. 2017, doi: 10.22034/ijnd.2017.24373.

[133] P. Sudarsana Reddy and A. J. Chamkha, "Influence of size, shape, type of nanoparticles, type and temperature of the base fluid on natural convection MHD of na nofluids," *Alexandria Engineering Journal*, vol. 55, no. 1. Elsevier B.V., pp. 331–341, Mar. 01, 2016. doi: 10.1016/j.aej.2016.01.027.

[134] A. Bhattad, J. Sarkar, and P. Ghosh, "Improving the performance of refrigeration systems by using nanofluids: A comprehensive review," *Renewable and Sustainable Energy Reviews*, vol. 82. Elsevier Ltd, pp. 3656–3669, Feb. 01, 2018. doi: 10.1016/j.rser.2017.10.097.

[135] I. Gonçalves *et al.*, "Thermal Conductivity of Nanofluids: A Review on Prediction Models, Controversies and Challenges," *Applied Sciences 2021, Vol. 11, Page 2525*, vol. 11, no. 6, p. 2525, Mar. 2021, doi: 10.3390/APP11062525.

[136] E. C. Okonkwo, I. Wole-Osho, I. W. Almanassra, Y. M. Abdullatif, and T. Al-Ansari, "An updated review of nanofluids in various heat transfer devices," *Journal of Thermal Analysis and Calorimetry*. Springer Netherlands, pp. 1–56, Jun. 15, 2020. doi: 10.1007/s10973-020-09760-2.

[137] M. R. Rodríguez-Laguna *et al.*, "Mechanisms behind the enhancement of thermal properties of graphene nanofluids †," vol. 10, p. 15402, 2018, doi: 10.1039/c8nr02762e.

[138] T. P. Sarit K. Das, Stephen U. Choi, Wenhua Yu, *Nanofluids: Science and Technology*, December 2. Wiley, 2554. [Online]. Available: isbn: 978-0-470-07473-2

[139] A. R. I. Ali and B. Salam, “A review on nanofluid: preparation, stability, thermophysical properties, heat transfer characteristics and application,” *SN Applied Sciences 2020 2:10*, vol. 2, no. 10, pp. 1–17, Sep. 2020, doi: 10.1007/S42452-020-03427-1.

[140] Linghui Kong, Jianlin Sun, and Yueyue Bao, “Preparation, characterization and tribological mechanism of nanofluids,” *RSC Advances*, vol. 7, no. 21, pp. 12599–12609, Feb. 2017, doi: 10.1039/C6RA28243A.

[141] A. B *et al.*, “Determining the Effective Density and Stabilizer Layer Thickness of Sterically Stabilized Nanoparticles,” *Macromolecules*, vol. 49, no. 14, pp. 5160–5171, Jul. 2016, doi: 10.1021/ACS.MACROMOL.6B00987.

[142] A. Dadwal and P. A. Joy, “Influence of chain length of long-chain fatty acid surfactant on the thermal conductivity of magnetite nanofluids in a magnetic field,” *Colloids and Surfaces A: Physicochemical and Engineering Aspects*, vol. 555, pp. 525–531, Oct. 2018, doi: 10.1016/J.COLSURFA.2018.07.034.

[143] A. Kraynov and T. E. Müller, *Concepts for the Stabilization of Metal Nanoparticles in Ionic Liquids*. IntechOpen, 2011. doi: 10.5772/22111.

[144] K. F. Mak, L. Ju, F. Wang, and T. F. Heinz, “Optical spectroscopy of graphene: From the far infrared to the ultraviolet,” *Solid State Communications*, vol. 152, no. 15, pp. 1341–1349, Aug. 2012, doi: 10.1016/J.SSC.2012.04.064.

[145] Y. W. Sun *et al.*, “3D Strain in 2D Materials: To What Extent is Monolayer Graphene Graphite?,” *Physical Review Letters*, vol. 123, 2019, doi: 10.1103/PhysRevLett.123.135501.

[146] L. A. Jauregui *et al.*, “Thermal Transport in Graphene Nanostructures: Experiments and Simulations,” in *ECS Transactions*, Apr. 2010, vol. 28, no. 5, pp. 73–83. doi: 10.1149/1.3367938.

[147] P. Zhang *et al.*, “Fracture toughness of graphene,” *Nature Communications 2014 5:1*, vol. 5, no. 1, pp. 1–7, Apr. 2014, doi: 10.1038/ncomms4782.

[148] S. Deng and V. Berry, “Wrinkled, rippled and crumpled graphene: an overview of formation mechanism, electronic properties, and applications,” *Materials Today*, vol. 19, no. 4, pp. 197–212, May 2016, doi: 10.1016/J.MATTOD.2015.10.002.

[149] S. Homaeigohar and M. Elbahri, “Graphene membranes for water desalination,” *NPG Asia Materials 2017 9:8*, vol. 9, no. 8, pp. e427–e427, Aug. 2017, doi: 10.1038/am.2017.135.

[150] G. Yang, L. Li, W. B. Lee, and M. C. Ng, “Structure of graphene and its disorders: a review,” *Science and Technology of Advanced Materials*, vol. 19, no. 1. Taylor and Francis Ltd., pp. 613–648, Dec. 31, 2018. doi: 10.1080/14686996.2018.1494493.

[151] Y. Y. Zhang and Y. T. Gu, “Mechanical properties of graphene: Effects of layer number, temperature and isotope,” *Computational Materials Science*, vol. 71, pp. 197–200, Apr. 2013, doi: 10.1016/j.commatsci.2013.01.032.

[152] Z. Li *et al.*, “Structure-Dependent Fano Resonances in the Infrared Spectra of Phonons in Few-Layer Graphene,” *Physical Review Letters*, vol. 108, no. 15, p. 156801, Apr. 2012, doi: 10.1103/PhysRevLett.108.156801.

[153] R. Bistritzer and A. H. MacDonald, “Moiré bands in twisted double-layer graphene,” *Proceedings of the National Academy of Sciences*, vol. 108, no. 30, pp. 12233–12237, Jul. 2011, doi: 10.1073/PNAS.1108174108.

[154] L. Zhong *et al.*, “Unraveling the Influence of Metal Substrates on Graphene Nucleation from First-Principles Study,” *Journal of Physical Chemistry C*, vol. 120, no. 40, pp. 23239–23245, Oct. 2016, doi: 10.1021/acs.jpcc.6b06750.

[155] M. Batzill, “The surface science of graphene: Metal interfaces, CVD synthesis, nanoribbons, chemical modifications, and defects,” *Surface Science Reports*, vol. 67, pp. 83–115, 2012, doi: 10.1016/j.surfrep.2011.12.001.

[156] G. Zhao *et al.*, “The physics and chemistry of graphene-on-surfaces,” *Chemical Society Reviews*, vol. 46, no. 15. Royal Society of Chemistry, pp. 4417–4449, Aug. 07, 2017. doi: 10.1039/c7cs00256d.

[157] A. Dahal, R. Addou, H. Coy-Diaz, J. Lallo, and M. Batzill, “Charge doping of graphene in metal/graphene/dielectric sandwich structures evaluated by C-1s core level photoemission spectroscopy,” *APL Materials*, vol. 1, no. 4, p. 042107, Oct. 2013, doi: 10.1063/1.4824038.

[158] A. A. Balandin *et al.*, “Superior Thermal Conductivity of Single-Layer Graphene,” *Nano Letters*, vol. 8, no. 3, pp. 902–907, Mar. 2008, doi: 10.1021/NL0731872.

[159] Y. Fu *et al.*, “Graphene related materials for thermal management,” *2D Materials*, vol. 7, no. 1, p. 012001, Oct. 2019, doi: 10.1088/2053-1583/AB48D9.

[160] X. Mu, X. Wu, T. Zhang, D. B. Go, and T. Luo, “Thermal Transport in Graphene Oxide – From Ballistic Extreme to Amorphous Limit,” *Scientific Reports 2014 4:1*, vol. 4, no. 1, pp. 1–9, Jan. 2014, doi: 10.1038/srep03909.

[161] W. Lee, K. D. Kihm, and S. H. Ko, “Thermal conductivity reduction of multilayer graphene with fine grain sizes,” *JMST Advances 2019 1:1*, vol. 1, no. 1, pp. 191–195, Apr. 2019, doi: 10.1007/S42791-019-0008-Y.

[162] R. Su and X. Zhang, “Size effect of thermal conductivity in monolayer graphene,” *Applied Thermal Engineering*, vol. 144, pp. 488–494, Nov. 2018, doi: 10.1016/J.APPLTHERMALENG.2018.08.062.

[163] E. Pop, V. Varshney, and A. K. Roy, “Thermal properties of graphene: Fundamentals and applications,” *MRS Bulletin*, vol. 37, no. 12, pp. 1273–1281, Nov. 2012, doi: 10.1557/MRS.2012.203.

[164] T. Wejrzanowski, M. Grybczuk, M. Chmielewski, K. Pietrzak, K. J. Kurzydlowski, and A. Strojny-Nedza, “Thermal conductivity of metal-graphene composites,” *Materials & Design*, vol. 99, pp. 163–173, Jun. 2016, doi: 10.1016/J.MATDES.2016.03.069.

[165] K. Jagannadham, “Effect of interfacial interactions on the thermal conductivity and interfacial thermal conductance in tungsten–graphene layered structure,” *Journal of Vacuum Science & Technology A: Vacuum, Surfaces, and Films*, vol. 32, no. 5, p. 051101, Jul. 2014, doi: 10.1116/1.4890576.

[166] Y. Y. Zhang, Y. Cheng, Q. X. Pei, C. M. Wang, and Y. Xiang, “Thermal conductivity of defective graphene,” *Physics Letters A*, vol. 376, no. 47–48, pp. 3668–3672, Nov. 2012, doi: 10.1016/J.PHYSLETA.2012.10.048.

[167] X. Zhang, H. Li, and F. Ding, “Self-Assembly of Carbon Atoms on Transition Metal Surfaces-Chemical Vapor Deposition Growth Mechanism of Graphene,” *Advanced Materials*, vol. 26, no. 31, pp. 5488–5495, Aug. 2014, doi: 10.1002/adma.201305922.

[168] M. Vattur Sundaram, “Novel approaches for achieving full density powder metallurgy steels,” Gothenburg, 2019.

[169] R. Marder, C. Estournès, G. Chevallier, and R. Chaim, “Spark and plasma in spark plasma sintering of rigid ceramic nanoparticles: A model system of YAG,” *Journal of the European Ceramic Society*, vol. 35, no. 1, pp. 211–218, Jan. 2015, doi: 10.1016/J.JEURCERAMSOC.2014.08.001.

[170] A. electrodes Jiefeng Zhang *et al.*, “Characterization of spark plasma sintered Ag nanopowders ,” *Nanotechnology*, vol. 21, p. 115707, 2010, doi: 10.1088/0957-4484/21/11/115707.

[171] D. B. Kumar, B. S. babu, K. M. A. Jerrin, N. Joseph, and A. Jiss, “Review of Spark Plasma Sintering Process,” *IOP Conference Series: Materials Science and Engineering*, vol. 993, no. 1, p. 012004, Dec. 2020, doi: 10.1088/1757-899X/993/1/012004.

[172] X. Song, X. Liu, and J. Zhang, “Neck Formation and Self-Adjusting Mechanism of Neck Growth of Conducting Powders in Spark Plasma Sintering,” *Journal of the American Ceramic Society*, vol. 89, no. 2, pp. 494–500, Feb. 2006, doi: 10.1111/J.1551-2916.2005.00777.X.

[173] C. Romaric *et al.*, “Effect of current on the sintering of pre-oxidized copper powders by SPS,” *Journal of Alloys and Compounds*, vol. 692, pp. 478–484, Jan. 2017, doi: 10.1016/J.JALLCOM.2016.08.191.

[174] K. R. Anderson, J. R. Groza, M. Fendorf, and C. J. Echer, “Surface oxide debonding in field assisted powder sintering,” *Materials Science and Engineering: A*, vol. 270, no. 2, pp. 278–282, Sep. 1999, doi: 10.1016/S0921-5093(99)00197-5.

[175] M. Wu, Y. Yang, G. Yang, K. Huang, and D. Yin, “Direct evidence for surface cleaning mechanism during field-activated sintering,” *Journal of Alloys and Compounds*, vol. 784, pp. 975–979, May 2019, doi: 10.1016/J.JALLCOM.2019.01.035.

[176] S. Diouf and A. Molinari, “Densification mechanisms in spark plasma sintering: Effect of particle size and pressure,” *Powder Technology*, vol. 221, pp. 220–227, May 2012, doi: 10.1016/J.POWTEC.2012.01.005.

[177] Z. Zhaohui, W. Fuchi, W. Lin, L. Shukui, and S. Osamu, “Sintering mechanism of large-scale ultrafine-grained copper prepared by SPS method,” *Materials Letters*, vol. 62, no. 24, pp. 3987–3990, Sep. 2008, doi: 10.1016/J.MATLET.2008.05.036.

[178] G. Guenther and O. Guillon, “Models of size-dependent nanoparticle melting tested on gold,” *Journal of Materials Science*, vol. 49, no. 23. Kluwer Academic Publishers, pp. 7915–7932, Dec. 01, 2014. doi: 10.1007/s10853-014-8544-1.

[179] F. Font and T. G. Myers, “Spherically symmetric nanoparticle melting with a variable phase change temperature,” 2013.

[180] K. F. Peters, J. B. Cohen, and Y.-W. Chung, “Melting of Pb nanocrystals,” *Physical Review B*, vol. 57, no. 21, p. 13430, Jun. 1998, doi: 10.1103/PhysRevB.57.13430.

[181] F. Ding, A. Rosén, S. Curtarolo, and K. Bolton, “Modeling the melting of supported clusters,” *Applied Physics Letters*, vol. 88, no. 13, p. 133110, Mar. 2006, doi: 10.1063/1.2187950.

[182] F. Ding, A. Rosén, S. Curtarolo, and K. Bolton, “Modeling the melting of supported clusters,” *Applied Physics Letters*, vol. 88, no. 13, p. 133110, Mar. 2006, doi: 10.1063/1.2187950.

[183] K. K. Nanda, S. N. Sahu, and S. N. Behera, “Liquid-drop model for the size-dependent melting of low-dimensional systems,” *Physical Review A*, vol. 66, no. 1, p. 013208, Jul. 2002, doi: 10.1103/PhysRevA.66.013208.

[184] B. Pluis, A. W. D. van der Gon, J. W. M. Frenken, and J. F. van der Veen, “Crystal-Face Dependence of Surface Melting,” *Physical Review Letters*, vol. 59, no. 23, p. 2678, Dec. 1987, doi: 10.1103/PhysRevLett.59.2678.

[185] D. Feng, Y. Feng, S. Yuan, X. Zhang, and G. Wang, “Melting behavior of Ag nanoparticles and their clusters,” *Applied Thermal Engineering*, vol. 111, pp. 1457–1463, Jan. 2017, doi: 10.1016/j.applthermaleng.2016.05.087.

[186] R. M. German, “Thermodynamics of sintering,” in *Sintering of Advanced Materials*, Elsevier, 2010, pp. 3–32. doi: 10.1533/9781845699949.1.3.

[187] V. N. Popok, “Cluster Beam Synthesis of Polymer Composites with Nanoparticles,” *Polymer-Based Multifunctional Nanocomposites and Their Applications*, pp. 35–76, Jan. 2019, doi: 10.1016/B978-0-12-815067-2.00002-0.

[188] M. N. Rahaman, “Sintering Theory and Fundamentals,” in *Powder Metallurgy*, ASM International, 2018, pp. 205–236. doi: 10.31399/asm.hb.v07.a0006117.

[189] T. T. Molla, “Modeling Macroscopic Shape Distortions during Sintering of Multi-layers Modeling Macroscopic Shape Distortions during Sintering of Multi-layers By : Tesfaye Tadesse Molla,” 2016.

[190] Z. H. Li and D. Truhlar, “Nanothermodynamics of Metal Nanoparticles Chemical Science Nanothermodynamics of metal nanoparticles,” no. March 2016, 2014, doi: 10.1039/c4sc00052h.

[191] M. Ghasemi, Z. Zanolli, M. Stankovski, and J. Johansson, “Size- and shape-dependent phase diagram of In-Sb nano-alloys,” *Nanoscale*, vol. 7, no. 41, pp. 17387–17396, Nov. 2015, doi: 10.1039/c5nr04014k.

[192] J. Sopoušek *et al.*, “Au-Ni nanoparticles: Phase diagram prediction, synthesis, characterization, and thermal stability,” *Calphad: Computer Coupling of Phase Diagrams and Thermochemistry*, vol. 58, pp. 25–33, Sep. 2017, doi: 10.1016/j.calphad.2017.05.002.

[193] M. Wautelet, J. P. Dauchot, and M. Hecq, “Size effects on the phase diagrams of nanoparticles of various shapes,” *Materials Science and Engineering C*, vol. 23, no. 1–2, pp. 187–190, Jan. 2003, doi: 10.1016/S0928-4931(02)00266-7.

[194] F. Calvo, *Nanoalloys - From Fundamentals to Emergent Applications*, Elsevier. Elsevier, 2013. Accessed: May 21, 2020. [Online]. Available: https://app.knovel.com/hotlink/toc/id:kpNFFEA001/nanoalloys-from-fundamentals/nanoalloys-from-fundamentals

[195] R. Ferrando, J. Jellinek, and R. L. Johnston, “Nanoalloys: From theory to applications of alloy clusters and nanoparticles,” *Chemical Reviews*, vol. 108, no. 3. American Chemical Society, pp. 845–910, 2008. doi: 10.1021/cr040090g.

[196] R. L. (Roy L. Johnston and J. P. Wilcoxon, *Metal nanoparticles and nanoalloys*. Elsevier Science, 2012.

[197] A. M. El-Khatib, M. S. Badawi, Z. F. Ghatass, M. M. Mohamed, and M. Elkhatib, “Synthesize of Silver Nanoparticles by Arc Discharge Method Using Two Different Rotational Electrode

Shapes," *Journal of Cluster Science 2018 29:6*, vol. 29, no. 6, pp. 1169–1175, Jul. 2018, doi: 10.1007/S10876-018-1430-2.

[198] J. Yan, Z. Fan, and L. Zhi, "Functionalized Carbon Nanotubes and Their Enhanced Polymers," *Polymer Science: A Comprehensive Reference, 10 Volume Set*, vol. 8, pp. 439–478, Jan. 2012, doi: 10.1016/B978-0-444-53349-4.00217-X.

[199] Y. Luan *et al.*, "Arc-discharge production of high-quality fluorine-modified graphene as anode for Li-ion battery," *Chemical Engineering Journal*, vol. 392, p. 123668, Jul. 2020, doi: 10.1016/J.CEJ.2019.123668.

[200] A. Voloshko, "Nanoparticle formation by means of spark discharge at atmospheric pressure," Université Jean Monnet - Saint-Etienne, 2015. Accessed: May 19, 2020. [Online]. Available: https://tel.archives-ouvertes.fr/tel-01545174

[201] S. Chaitoglou, M. R. Sanaee, N. Aguiló-Aguayo, and E. Bertran, "Arc-discharge synthesis of iron encapsulated in carbon nanoparticles for biomedical applications," *Journal of Nanomaterials*, vol. 2014, 2014, doi: 10.1155/2014/178524.

[202] C. N. Nanev, "Theory of Nucleation," *Handbook of Crystal Growth: Second Edition*, vol. 1, pp. 315–358, Jan. 2015, doi: 10.1016/B978-0-444-56369-9.00007-1.

[203] R. Hu, M. A. Ciolan, X. Wang, and M. Nagatsu, "Copper induced hollow carbon nanospheres by arc discharge method: controlled synthesis and formation mechanism," *Nanotechnology*, vol. 27, no. 33, p. 335602, Jul. 2016, doi: 10.1088/0957-4484/27/33/335602.

[204] N. Baig, I. Kammakakam, and W. Falath, "Nanomaterials: a review of synthesis methods, properties, recent progress, and challenges," *Materials Advances*, vol. 2, no. 6, pp. 1821–1871, Mar. 2021, doi: 10.1039/D0MA00807A.

[205] A. Schiffmacher, L. Litzenberger, J. Wilde, V. Polezhaev, and T. Huesgen, "Power Electronic Assemblies on Printed Wiring Boards Mounted by Silver Sintering," *2018 7th Electronic System-Integration Technology Conference, ESTC 2018 - Proceedings*, Nov. 2018, doi: 10.1109/ESTC.2018.8546334.

[206] C.-H. Liu and X. Yu, "Silver nanowire-based transparent, flexible, and conductive thin film," *Nanoscale Research Letters 2011 6:1*, vol. 6, no. 1, pp. 1–8, Jan. 2011, doi: 10.1186/1556-276X-6-75.

[207] J. Fan, G. Li, K. Rajavel, P. Zhu, R. Sun, and C.-P. Wong, "Synergistic size and shape effect of dendritic silver nanostructures for low-temperature sintering of paste as die attach materials," *Journal of Materials Science: Materials in Electronics 2021 32:1*, vol. 32, no. 1, pp. 323–336, Jan. 2021, doi: 10.1007/S10854-020-04783-9.

[208] C.-K. Hu and H. B. Huntington, "Diffusion and electromigration of silver and nickel in lead-tin alloys," *Physical Review B*, vol. 26, no. 6, p. 2782, Sep. 1982, doi: 10.1103/PhysRevB.26.2782.

[209] R. E. Hummel and R. M. Breitling, "ON THE DIRECTION OF ELECTROMIGRATION IN THIN SILVER, GOLD, AND COPPER FILMS," *Applied Physics Letters*, vol. 18, no. 9, p. 373, Oct. 2003, doi: 10.1063/1.1653704.

[210] H. M. Breitling and R. E. Hummel, "Electromigration in thin silver, copper, gold, indium, tin, lead and magnesium films," *Journal of Physics and Chemistry of Solids*, vol. 33, no. 4, pp. 845–852, Jan. 1972, doi: 10.1016/S0022-3697(72)80101-X.

[211] M. Vattur Sundaram, “Novel approaches for achieving full density powder metallurgy steels”.

[212] M. T. Pettes, H. Ji, R. S. Ruoff, and L. Shi, “Thermal transport in three-dimensional foam architectures of few-layer graphene and ultrathin graphite,” *Nano Letters*, vol. 12, no. 6, pp. 2959–2964, Jun. 2012, doi: 10.1021/nl300662q.

[213] K. Lafdi, M. Almajali, and O. Huzayyin, “Thermal properties of copper-coated carbon foams,” *Carbon*, vol. 47, no. 11, pp. 2620–2626, Sep. 2009, doi: 10.1016/j.carbon.2009.05.014.

[214] D. Li *et al.*, “Measuring Thermal and Thermoelectric Properties of One-Dimensional Nanostructures Using a Microfabricated Device,” 2003, doi: 10.1115/1.1597619.

[215] N. Wang *et al.*, “Tailoring the Thermal and Mechanical Properties of Graphene Film by Structural Engineering,” *Small*, vol. 14, no. 29, Jul. 2018, doi: 10.1002/smll.201801346.

[216] S. Zhao *et al.*, “Heating-induced negative temperature coefficient effect in conductive graphene/polymer ternary nanocomposites with a segregated and double-percolated structure,” *Journal of Materials Chemistry C*, vol. 5, no. 32, pp. 8233–8242, 2017, doi: 10.1039/c7tc02472j.

[217] L. Zhong *et al.*, “Unraveling the Influence of Metal Substrates on Graphene Nucleation from First-Principles Study,” *Journal of Physical Chemistry C*, vol. 120, no. 40, pp. 23239–23245, Oct. 2016, doi: 10.1021/ACS.JPCC.6B06750.

[218] Y. Fu, G. Cui, and K. Jeppson, “Thermal characterization of low-dimensional materials by resistance thermometers,” *Materials*, vol. 12, no. 11. MDPI AG, Jun. 01, 2019. doi: 10.3390/ma12111740.

[219] D. Vijay, P. Goetze, R. Wulf, and U. Gross, “Forced convection through open cell foams based on homogenization approach: Steady state analysis,” *International Journal of Thermal Sciences*, vol. 98, pp. 381–394, Dec. 2015, doi: 10.1016/j.ijthermalsci.2015.07.017.

[220] C. Beckermann, S. Ramadhyani, and R. Viskanta, “Natural convection flow and heat transfer between a fluid layer and a. porous layer inside a rectangular enclosure,” *Journal of Heat Transfer*, vol. 109, no. 2, pp. 363–370, 1987, doi: 10.1115/1.3248089.

[221] Z. Zhai and Q. W. Chen Ray Herrick, “NUMERICAL DETERMINATION AND TREATMENT OF CONVECTIVE HEAT TRANSFER COEFFICIENT IN THE COUPLED BUILDING ENERGY AND CFD SIMULATION,” pp. 1000–1009, 2004.

[222] D. Wang, C. Wu, Y. Liu, P. Chen, and J. Liu, “Experimental study on the thermal performance of an enhanced-convection overhead radiant floor heating system,” *Energy and Buildings*, vol. 135, pp. 233–243, Jan. 2017, doi: 10.1016/j.enbuild.2016.11.017.

[223] L. Lizana and Z. Konkoli, “Diffusive transport in networks built of containers and tubes”, doi: 10.1103/PhysRevE.72.026305.

[224] Y. Liu *et al.*, “Surface modification of graphene for use as a structural Fortifier in water-borne epoxy coatings,” *Coatings*, vol. 9, no. 11, p. 754, Nov. 2019, doi: 10.3390/coatings9110754.

[225] S. K. Pradhan *et al.*, “Graphene-incorporated aluminum with enhanced thermal and mechanical properties for solar heat collectors,” *AIP Advances*, vol. 10, no. 6, p. 065016, Jun. 2020, doi: 10.1063/5.0008786.

[226] M. Cao *et al.*, “Ultrahigh Electrical Conductivity of Graphene Embedded in Metals,” *Advanced Functional Materials*, vol. 29, no. 17, p. 1806792, Apr. 2019, doi: 10.1002/adfm.201806792.

[227] H. Jiang, K.-S. Moon, J. Lu, and C. P. Wong, “Conductivity enhancement of nano silver-filled conductive adhesives by particle surface functionalization,” *Journal of Electronic Materials 2005 34:11*, vol. 34, no. 11, pp. 1432–1439, 2005, doi: 10.1007/S11664-005-0202-6.

[228] A. R. I. Ali and B. Salam, “A review on nanofluid: preparation, stability, thermophysical properties, heat transfer characteristics and application,” *SN Applied Sciences*, vol. 2, no. 10. Springer Nature, pp. 1–17, Oct. 01, 2020. doi: 10.1007/s42452-020-03427-1.

[229] S. Wang *et al.*, “Synthesis, growth mechanism and thermal stability of copper nanoparticles encapsulated by multi-layer graphene,” *Carbon*, vol. 50, no. 6, pp. 2119–2125, May 2012, doi: 10.1016/J.CARBON.2011.12.063.

[230] A. E. Galashev and O. R. Rakhmanova, “Mechanical and thermal stability of graphene and graphene-based materials,” *Physics-Uspekhi*, vol. 57, no. 10, pp. 970–989, Oct. 2014, doi: 10.3367/ufne.0184.201410c.1045.

[231] E. Sadeghinezhad *et al.*, “A comprehensive review on graphene nanofluids: Recent research, development and applications,” *Energy Conversion and Management*, vol. 111, pp. 466–487, Mar. 2016, doi: 10.1016/j.enconman.2016.01.004.

[232] A. Arshad, M. Jabbal, Y. Yan, and D. Reay, “A review on graphene based nanofluids: Preparation, characterization and applications,” *Journal of Molecular Liquids*, vol. 279, pp. 444–484, 2019, doi: 10.1016/j.molliq.2019.01.153.

[233] D. Rueda-García *et al.*, “From Thermal to Electroactive Graphene Nanofluids,” *Energies*, vol. 12, no. 23, p. 4545, Nov. 2019, doi: 10.3390/en12234545.

[234] M. R. Rodríguez-Laguna *et al.*, “Mechanisms behind the enhancement of thermal properties of graphene nanofluids †,” *Nanoscale*, vol. 10, p. 15402, 2018, doi: 10.1039/c8nr02762e.

[235] J. Gao, H. Wu, A. Li, Y. Yue, D. Xie, and X. Zhang, “Graphene Nanofluids as Thermal Management Materials: Molecular Dynamics Study on Orientation and Temperature Effects,” *ACS Applied Nano Materials*, vol. 2, no. 11, pp. 6828–6835, Nov. 2019, doi: 10.1021/acsanm.9b01266.

[236] D. Li, B. Li, M. Luo, C. Feng, T. Ouyang, and F. Gao, “Thermal transport properties of rolled graphene nanoribbons,” *Applied Physics Letters*, vol. 103, no. 7, p. 071908, Aug. 2013, doi: 10.1063/1.4818658.

[237] T. Ouyang, Y. Chen, Y. Xie, G. M. Stocks, and J. Zhong, “Thermal conductance modulator based on folded graphene nanoribbons,” *Applied Physics Letters*, vol. 99, no. 23, p. 233101, Dec. 2011, doi: 10.1063/1.3665184.

[238] S. A. M. Mehryan, E. Izadpanahi, M. Ghalambaz, and A. J. Chamkha, “Mixed convection flow caused by an oscillating cylinder in a square cavity filled with Cu–Al2O3/water hybrid nanofluid,” *Journal of Thermal Analysis and Calorimetry*, vol. 137, no. 3, pp. 965–982, Aug. 2019, doi: 10.1007/s10973-019-08012-2.

[239] T. Tayebi and A. J. Chamkha, “Magnetohydrodynamic Natural Convection Heat Transfer of Hybrid Nanofluid in a Square Enclosure in the Presence of a Wavy Circular Conductive Cylinder,” *Journal of Thermal Science and Engineering Applications*, vol. 12, no. 3, Jun. 2020, doi: 10.1115/1.4044857.

[240] S. A. M. Mehryan, M. Ghalambaz, A. J. Chamkha, and M. Izadi, “Numerical study on natural convection of Ag–MgO hybrid/water nanofluid inside a porous enclosure: A local thermal

non-equilibrium model," *Powder Technology*, vol. 367, pp. 443–455, May 2020, doi: 10.1016/j.powtec.2020.04.005.

[241] J. Sarkar, P. Ghosh, and A. Adil, "A review on hybrid nanofluids: Recent research, development and applications," *Renewable and Sustainable Energy Reviews*, vol. 43. Elsevier Ltd, pp. 164–177, Mar. 01, 2015. doi: 10.1016/j.rser.2014.11.023.

[242] M. Mbambo *et al.*, "Remarkable thermal conductivity enhancement in Ag-decorated graphene nanocomposites based nanofluid by laser liquid solid interaction in ethylene glycol," *Somerset West*, vol. 7129, no. 3, doi: 10.1038/s41598-020-67418-3.

[243] S. M. Hashem Zadeh, S. A. M. Mehryan, M. Ghalambaz, M. Ghodrat, J. Young, and A. Chamkha, "Hybrid thermal performance enhancement of a circular latent heat storage system by utilizing partially filled copper foam and Cu/GO nano-additives," *Energy*, vol. 213, p. 118761, Dec. 2020, doi: 10.1016/J.ENERGY.2020.118761.

[244] M. Devarajan *et al.*, "Thermophysical properties of CNT and CNT/Al2O3 hybrid nanofluid," *Micro & Nano Letters*, vol. 13, no. 5, pp. 617–621, May 2018, doi: 10.1049/MNL.2017.0029.

[245] R. L. vander Wal, S. D. Mozes, and V. Pushkarev, "Application of hybrid sphere/carbon nanotube particles in nanofluids Related content," 2007, doi: 10.1088/0957-4484/18/10/105701.

[246] C. Jin, Q. Wu, G. Yang, H. Zhang, and Y. Zhong, "Investigation on hybrid nanofluids based on carbon nanotubes filled with metal nanoparticles: Stability, thermal conductivity, and viscosity," *Powder Technology*, vol. 389, pp. 1–10, Sep. 2021, doi: 10.1016/J.POWTEC.2021.05.007.

[247] J.-M. Feng and Y.-J. Dai, "Water-assisted growth of graphene on carbon nanotubes by the chemical vapor deposition method," *Nanoscale*, vol. 5, no. 10, p. 4422, May 2013, doi: 10.1039/c3nr33855j.

[248] F. T. Johra, J. W. Lee, and W. G. Jung, "Facile and safe graphene preparation on solution based platform," *Journal of Industrial and Engineering Chemistry*, vol. 20, no. 5, pp. 2883–2887, Sep. 2014, doi: 10.1016/j.jiec.2013.11.022.

[249] A. Morais, J. P. C. Alves, F. A. S. Lima, M. Lira-Cantu, and A. F. Nogueira, "Enhanced photovoltaic performance of inverted hybrid bulk-heterojunction solar cells using TiO 2 /reduced graphene oxide films as electron transport layers," *Journal of Photonics for Energy*, vol. 5, no. 1, p. 057408, Mar. 2015, doi: 10.1117/1.jpe.5.057408.

[250] D. Li, G. Wang, L. Cheng, C. Wang, and X. Mei, "Engineering the Self-Assembly Induced Emission of Copper Nanoclusters as 3D Nanomaterials with Mesoporous Sphere Structures by the Crosslinking of Ce3+," *ACS Omega*, vol. 3, no. 11, pp. 14755–14765, Nov. 2018, doi: 10.1021/acsomega.8b02204.

[251] B. Kulyk *et al.*, "A critical review on the production and application of graphene and graphene-based materials in anti-corrosion coatings," *Critical Reviews in Solid State and Materials Sciences*. Bellwether Publishing, Ltd., 2021. doi: 10.1080/10408436.2021.1886046.

[252] J. bin Wu, M. L. Lin, X. Cong, H. N. Liu, and P. H. Tan, "Raman spectroscopy of graphene-based materials and its applications in related devices," *Chemical Society Reviews*, vol. 47, no. 5. Royal Society of Chemistry, pp. 1822–1873, Mar. 07, 2018. doi: 10.1039/c6cs00915h.

[253] D. Chen, L. Li, and L. Guo, “Temperature dependence of graphene oxide reduced by hydrazine hydrate Related content An environment-friendly preparation of reduced graphene oxide nanosheets via aminoacid,” 2011, doi: 10.1088/0957-4484/22/5/055705.

[254] L. Huang, P. Zhu, G. Li, D. Lu, R. Sun, and C. Wong, “Core-shell SiO2@RGO hybrids for epoxy composites with low percolation threshold and enhanced thermo-mechanical properties,” *Journal of Materials Chemistry A*, vol. 2, no. 43, pp. 18246–18255, Nov. 2014, doi: 10.1039/c4ta03702b.

[255] M. M. Barbooti, “Thermal behaviour of copper oxides and copper sulphate in the presence of carbon,” *Solar Energy Materials*, vol. 10, no. 1, pp. 35–40, Apr. 1984, doi: 10.1016/0165-1633(84)90005-4.

[256] K. K. Nanda, “Size-dependent melting of nanoparticles: Hundred years of Thermodynamic model,” *Pramana - Journal of Physics*, vol. 72, no. 4, pp. 617–628, Apr. 2009, doi: 10.1007/s12043-009-0055-2.

[257] Z. Osváth *et al.*, “Controlling the nanoscale rippling of graphene with SiO 2 nanoparticles,” 2014, doi: 10.1039/c3nr06885d.

[258] S. Bhowmick, A. Banerji, and A. T. Alpas, “Friction reduction mechanisms in multilayer graphene sliding against hydrogenated diamond-like carbon,” *Carbon*, vol. 109, pp. 795–804, Nov. 2016, doi: 10.1016/J.CARBON.2016.08.036.

[259] Z. Osváth *et al.*, “Mapping the nanomechanical properties of graphene suspended on silica nanoparticles,” *Journal of Experimental Nanoscience*, vol. 11, no. 13, pp. 1011–1018, 2016, doi: 10.1080/17458080.2016.1159741.

[260] H. Gao, G. Hu, and H. Liu, “Preparation of a Highly Stable Dispersion of Graphene in Water with the Aid of Graphene Oxide,” *Industrial and Engineering Chemistry Research*, vol. 58, no. 38, pp. 17842–17849, Sep. 2019, doi: 10.1021/acs.iecr.9b03771.

[261] H. S. Kim, T. J. Oweida, and Y. G. Yingling, “Interfacial stability of graphene-based surfaces in water and organic solvents,” *Journal of Materials Science*, vol. 53, no. 8, pp. 5766–5776, Apr. 2018, doi: 10.1007/s10853-017-1893-9.

[262] W. Yu, H. Xie, and W. Chen, “Experimental investigation on thermal conductivity of nanofluids containing graphene oxide nanosheets,” *Journal of Applied Physics*, vol. 107, no. 9, p. 94317, May 2010, doi: 10.1063/1.3372733.

[263] W. Yu, H. Xie, and D. Bao, “Enhanced thermal conductivities of nanofluids containing graphene oxide nanosheets,” *Nanotechnology*, vol. 21, no. 5, p. 55705, Dec. 2010, doi: 10.1088/0957-4484/21/5/055705.

[264] D. Anin Vincely and E. Natarajan, “Experimental investigation of the solar FPC performance using graphene oxide nanofluid under forced circulation,” *Energy Conversion and Management*, vol. 117, pp. 1–11, Jun. 2016, doi: 10.1016/j.enconman.2016.03.015.

[265] S. F. Huang *et al.*, “First-principles calculation of the electronic properties of graphene clusters doped with nitrogen and boron: Analysis of catalytic activity for the oxygen reduction reaction,” *Physical Review B - Condensed Matter and Materials Physics*, vol. 80, no. 23, p. 235410, Dec. 2009, doi: 10.1103/PhysRevB.80.235410.

[266] M. P. Kumar, T. Kesavan, G. Kalita, P. Ragupathy, T. N. Narayanan, and D. K. Pattanayak, “On the large capacitance of nitrogen doped graphene derived by a facile route,” *RSC Advances*, vol. 4, no. 73, pp. 38689–38697, Aug. 2014, doi: 10.1039/c4ra04927f.

[267] M. Mehrali *et al.*, “Experimental and numerical investigation of the effective electrical conductivity of nitrogen-doped graphene nanofluids,” *Journal of Nanoparticle Research*, vol. 17, no. 6, p. 267, Jun. 2015, doi: 10.1007/s11051-015-3062-x.

[268] M. Mehrali *et al.*, “Effect of nitrogen-doped graphene nanofluid on the thermal performance of the grooved copper heat pipe,” *Energy Conversion and Management*, vol. 118, pp. 459–473, Jun. 2016, doi: 10.1016/j.enconman.2016.04.028.

[269] A. Ghozatloo, M. Shariaty Niassar, and A. Rashidi, “Effect of Functionalization Process on Thermal Conductivity of Graphene Nanofluids,” *International Journal of Nanoscience and Nanotechnology*, vol. 13, no. 1, pp. 11–18, Feb. 2017, Accessed: Mar. 19, 2019. [Online]. Available: http://www.ijnnonline.net/article_24531.html

[270] M. Aziz, F. S. A. Halim, and J. Jaafar, “Preparation and characterization of graphene membrane electrode assembly,” *Jurnal Teknologi (Sciences and Engineering)*, vol. 69, no. 9, pp. 11–14, 2014, doi: 10.11113/jt.v69.3388.

[271] Z. Xing *et al.*, “One-pot hydrothermal synthesis of Nitrogen-doped graphene as high-performance anode materials for lithium ion batteries,” *Scientific Reports*, vol. 6, May 2016, doi: 10.1038/srep26146.

[272] L. S. Panchakarla *et al.*, “Synthesis, Structure, and Properties of Boron- and Nitrogen-Doped Graphene,” *Advanced Materials*, vol. 21, no. 46, pp. 4726–4730, Dec. 2009, doi: 10.1002/ADMA.200901285.

[273] J. Ederer *et al.*, “Determination of amino groups on functionalized graphene oxide for polyurethane nanomaterials: XPS quantitation vs. functional speciation,” *RSC Advances*, vol. 7, no. 21, pp. 12464–12473, Feb. 2017, doi: 10.1039/c6ra28745j.

[274] M. Mokhtar Mohamed, M. A. Mousa, M. Khairy, and A. A. Amer, “Nitrogen Graphene: A New and Exciting Generation of Visible Light Driven Photocatalyst and Energy Storage Application,” *ACS Omega*, vol. 3, no. 2, pp. 1801–1814, 2018, doi: 10.1021/acsomega.7b01806.

[275] M. Liu, W. Li, J. Rong, and C. Zhou, “Novel polymer nanocomposite hydrogel with natural clay nanotubes,” *Colloid and Polymer Science*, vol. 290, no. 10, pp. 895–905, Jul. 2012, doi: 10.1007/s00396-012-2588-z.

[276] T. Susi, T. Pichler, and P. Ayala, “X-ray photoelectron spectroscopy of graphitic carbon nanomaterials doped with heteroatoms,” *Beilstein Journal of Nanotechnology*, vol. 6, no. 1. Beilstein-Institut Zur Forderung der Chemischen Wissenschaften, pp. 177–192, Jan. 15, 2015. doi: 10.3762/bjnano.6.17.

[277] P. Lazar, R. Mach, and M. Otyepka, “Spectroscopic Fingerprints of Graphitic, Pyrrolic, Pyridinic, and Chemisorbed Nitrogen in N-Doped Graphene,” 2019, doi: 10.1021/acs.jpcc.9b02163.

[278] M. Salem, T. Meakhail, M. Bassily, and S. Torii, “Thermal Transport Phenomena of Graphene Oxide Nanofluids in Turbulent Pipe Flow.” Accessed: Jun. 27, 2019. [Online]. Available: https://www.jstage.jst.go.jp/article/aem/1/0/1_30/_pdf/-char/en

[279] M. R. Esfahani, E. M. Languri, and M. R. Nunna, “Effect of particle size and viscosity on thermal conductivity enhancement of graphene oxide nanofluid,” *International Communications in Heat and Mass Transfer*, vol. 76, pp. 308–315, Aug. 2016, doi: 10.1016/j.icheatmasstransfer.2016.06.006.

[280] S. K. Manchili *et al.*, "Surface analysis of iron and steel nanopowder," *Surface and Interface Analysis*, vol. 50, no. 11, pp. 1083–1088, Nov. 2018, doi: 10.1002/SIA.6465.

[281] J.-H. Yu, C.-S. Youn, B.-K. Kim, J.-S. Lee, and C.-J. Choi, "Characteristics and Sintering Behavior of Oxide Coated Iron Nanopowder Synthesized by Plasma Arc Discharge Process."

[282] T. Battle, U. Srivastava, J. Kopfle, R. Hunter, and J. McClelland, "The Direct Reduction of Iron," *Treatise on Process Metallurgy*, vol. 3, pp. 89–176, Jan. 2014, doi: 10.1016/B978-0-08-096988-6.00016-X.

[283] K. Prabhakaran, K. V. P. M. Shafi, A. Ulman, P. M. Ajayan, Y. Homma, and T. Ogino, "Low-temperature, carbon-free reduction of iron oxide," *Surface Science*, vol. 506, no. 1–2, pp. L250–L254, May 2002, doi: 10.1016/S0039-6028(02)01374-2.

[284] L. Leich, A. Röttger, R. Kuchenbecker, and W. Theisen, "Electro-discharge sintering of nanocrystalline NdFeB magnets: process parameters, microstructure, and the resulting magnetic properties," *Journal of Materials Science: Materials in Electronics 2020 31:22*, vol. 31, no. 22, pp. 20431–20443, Oct. 2020, doi: 10.1007/S10854-020-04562-6.

[285] J. Trapp and B. Kieback, "Fundamental principles of spark plasma sintering of metals: part I-Joule heating controlled by the evolution of powder resistivity and local current densities," 2019, doi: 10.1080/00325899.2019.1653532.

[286] T. M. Vidyuk *et al.*, "Melting at the inter-particle contacts during Spark Plasma Sintering: Direct microstructural evidence and relation to particle morphology," *Vacuum*, vol. 181, p. 109566, Nov. 2020, doi: 10.1016/J.VACUUM.2020.109566.

[287] M. Li, R. Endo, M. Akoshima, H. Tanei, H. Okada, and M. Susa, "Thermal Conductivity of Oxide Scale Thermally Grown on Iron Substrate Corrected by Temperature-dependent Interfacial Thermal Resistance in Laser Flash Measurement," *ISIJ International*, vol. 59, no. 3, pp. 398–403, Mar. 2019, doi: 10.2355/ISIJINTERNATIONAL.ISIJINT-2018-553.

[288] E. Grigoryev and P. G. Nefedova, "SPARK PLASMA SINTERING THE COMPOSITES OF BIMODAL COPPER POWDERS".

[289] S. K. Vajpai, C. Sawangrat, O. Yamaguchi, O. P. Ciuca, and K. Ameyama, "Effect of bimodal harmonic structure design on the deformation behaviour and mechanical properties of Co-Cr-Mo alloy," *Materials Science and Engineering: C*, vol. 58, pp. 1008–1015, Jan. 2016, doi: 10.1016/J.MSEC.2015.09.055.

[290] M. Ghalambaz, A. J. Chamkha, and D. Wen, "Natural convective flow and heat transfer of Nano-Encapsulated Phase Change Materials (NEPCMs) in a cavity," *International Journal of Heat and Mass Transfer*, vol. 138, pp. 738–749, Aug. 2019, doi: 10.1016/J.IJHEATMASSTRANSFER.2019.04.037.

[291] M. Ghalambaz *et al.*, "Free convective melting-solidification heat transfer of nano-encapsulated phase change particles suspensions inside a coaxial pipe," *Advanced Powder Technology*, vol. 31, no. 11, pp. 4470–4481, Nov. 2020, doi: 10.1016/J.APT.2020.09.022.

[292] M. S. Ghoghaei *et al.*, "A review on the applications of micro-/nano-encapsulated phase change material slurry in heat transfer and thermal storage systems," *Journal of Thermal Analysis and Calorimetry 2020 145:2*, vol. 145, no. 2, pp. 245–268, May 2020, doi: 10.1007/S10973-020-09697-6.